University of Southampton

FACULTY OF GEOGRAPHY AND ENVIROMENTAL SCIENCE

Geography and Environment

EXAMINING PATTERNS OF PAST ASH DISPERSAL IN DISTAL CRYPTOTEPHRA DEPOSITS

by

Alistair J Monteath

Thesis for the degree of Doctor of Philosophy

Supervisors:

Paul D.M. Hughes and Mary E. Edwards

September 2019

University of Southampton

Abstract

FACULTY OF GEOGRAPHY AND ENVIROMENTAL SCIENCE

Geography and Environment

Thesis for the of Doctor of Philosophy

EXAMINING PATTERNS OF PAST ASH DISPERSAL IN DISTAL CRYPTOTEPHRA DEPOSITS

by

Alistair J Monteath

Well dated tephra deposits provide important chronological isochrons in Quaternary Science and numerous studies have documented distal ash beds, from past eruptions, with the aim of synchronising palaeoenvironmental or archaeological sequences. These studies also generate important information on the provenance, temporal frequency and remobilisation of tephra deposits within a catchment or region; however, this evidence is often overlooked, particularly in distal settings – several hundred kilometres from the volcanic source.

As well as chronological information, tephra deposits provide a long view of volcanic ash dispersal that exceeds both instrumental and historical records. Recent studies have used these deposits to investigate wider spatial and temporal patterns in volcanic ash dispersal. To date, this approach has been confined to Europe; however, there is clearly potential to undertake further studies in regions frequently affected by ash fall. This thesis aims to investigate past changes in ash dispersal patterns using distal cryptotephra (non-visible ash) deposits. Two case studies are used to examine this: eastern North America provides an example of ultra-distal tephra dispersal and deposition, while ash clouds affecting the Falkland Islands (Islas Malvinas), South Atlantic, are likely to be strongly influenced by changes in the strength and position of the Southern Westerly Wind belt.

To maximise shard recovery rates from discrete cryptotephra deposits characterised by electron probe microanalysis, methodological experiments were undertaken to investigate the effects of the peat acid digestion protocol on diverse volcanic glass. This method has been avoided in ultra-distal settings as small highly vesicular shards are likely to be vulnerable to chemical alteration during exposure to strong acids. The results of these experiments showed samples extracted using acid digestion were geochemically indistinguishable from control samples, and therefore, acid digestion was applied throughout this thesis.

Case study I examines ultra-distal cryptotephra deposits in eastern North America. Volcanic ash fall in this region is dependent on long-distance transport processes; therefore, it is hypothesised that past changes in atmospheric circulation patterns may be recorded in the frequency or provenance of cryptotephra deposits in this region. To test this hypothesis, new cryptotephra records were developed to close spatial and temporal gaps in the existing Lateglacial and Holocene tephra framework in eastern North America. The results demonstrate a sharp increase in the frequency of cryptotephra deposits after ca. 7600 yr BP. This increase broadly coincides with early Holocene changes in atmospheric circulation, linked with the retreating Laurentide ice sheet.

Case study II investigates distal tephra deposits in the Falkland Islands with the aim of examining the effects of changes in the Southern Westerly Wind belt on tephra dispersal in the South Atlantic. Numerous cryptotephra deposits are identified, including shard peaks correlated with the Reclus R1 and Mt. Burney MB1 eruptions. However, the majority of these tephra deposits were formed of detrital glass (tephra not derived from a primary air fall event) with heterogeneous geochemical compositions and shard morphologies. This detrital glass is likely to have been remobilised from the Patagonian Steppe by aeolian processes, where tephra shards form a large component of the regional dust source. A decrease in tephra abundance is observed between 14,300–10,500 cal yr BP, which is hypothesised to be because of changes in eruption frequency, wind–strength or taphonomic processes. In order to disentangle potential taphonomic and climatic influences on the detrital glass signal in the Falkland Islands, a new multi-proxy record of wind strength is developed from the same record. Results suggest that the Southern Westerly Wind belt strengthened in intensity during the Antarctic Cold Reversal (14,700 BP-13,000 yr BP) and moved south, away from the Falkland Islands, during the Younger Dryas time period (12,900-11,700 yr BP) and Early Holocene. These findings suggest that changes in the position of the Southern Westerly Wind belt may have reduced the frequency of tephra deposition in the Falkland Islands; however, further research is needed to test this.

In summary, case study I demonstrates the potential for wider tephra frameworks to provide evidence for changes in long term patterns of tephra dispersal, as well as reiterating the need to report ‘failed’ results where tephra is absent. Case study II provides an important example of distal transport of reworked, detrital tephra. Temporal patterns in the abundance of this detrital glass can be tentatively linked with a new record of wind strength, developed in this thesis, suggesting ash fall in the Falkland Islands may have been affected by past changes in the Southern Westerly Wind belt.

Table of Contents

Table of Tables

Table of Figures

Research Thesis: Declaration of Authorship

Print name:

Title of thesis:. ……*Examining patterns of past ash dispersal in distal cryptotephra deposits*……

I declare that this thesis and the work presented in it are my own and has been generated by me as the result of my own original research.

I confirm that:

1. This work was done wholly or mainly while in candidature for a research degree at this University;
2. Where any part of this thesis has previously been submitted for a degree or any other qualification at this University or any other institution, this has been clearly stated;
3. Where I have consulted the published work of others, this is always clearly attributed;
4. Where I have quoted from the work of others, the source is always given. With the exception of such quotations, this thesis is entirely my own work;
5. I have acknowledged all main sources of help;
6. Where the thesis is based on work done by myself jointly with others, I have made clear exactly what was done by others and what I have contributed myself;
7. Parts of this work have been published as:

Monteath, A.J., Teuten, A.E., Hughes, P.D.M., Wastegård, S., 2019. The effects of the peat acid digestion protocol on geochemically and morphologically diverse tephra deposits. Journal of Quaternary Science 34, 269–274.

Monteath, A.J., Hughes, P.D.M., Wastegård, S., 2019. Evidence for distal transport of reworked Andean tephra: Extending the cryptotephra framework from the Austral Volcanic Zone. Quaternary Geochronology 51, 64–71.

Scaife, R.G., Long, A.J., Monteath, A.J., Hughes, P.D.M., Bentley, M., Stone, P., 2019. The Falkland Islands palaeoecological response to millennial scale climate perturbations during the Pleistocene-Holocene transition: implications for future vegetation stability in Southern Ocean islands. Journal of Quaternary Science, DOI: 10.1002/jqs.3150.

Signature:……Date: .....

Acknowledgements

Many thanks to all of the co-authors, funders, reviewers and general well-wishers who made this thesis happen. It was the little conversations that inspired me to dive into anything and everything during the last five years, and the most obscure ideas generally turned out to be the most interesting. In particular, this research would never have progressed without the amazing people who make up the tephrochronology community. Duane Froese, Britta Jensen, Lauren Davies, Stefan Wastegård and Chris Hayward, thank you so much for your advice, support and general interest in this project.

Paul Hughes and Mary Edwards, you have been the most enthusiastic and incredibly patient supervisors that I could have asked for. Thank you for letting me follow the research rabbit hole – from Newfoundland to the Falkland Islands and back again. And the bottomless coffees of course!

Office 1067, particularly Charlotte and Roseanna. What can I say – without using expletives? During the last four years I have got to know you both better than anyone should. We've spent weeks away together on field work, endless hours in the office and bitter weekends in the laboratory. I thought about this carefully and I've come to some considered conclusions about you both: I have never encountered such abusive, rude, narcissistic, grumpy people. You moan constantly. You are ALWAYS wrong. To put it simply: you are the worst…… and, I'm going to miss you so much. I love the pair of you, don't ever change.

Sarah. This is impossible to write. I simply don't think I could ever find the form of words to express how grateful I am to you. All that I am, and aspire to be, is because of you. Thank you for your patience, support and endless proof reading – I'm sure that this section (as the only piece you haven't covered in red pen) is riddled with mistakees!

"I think that ~~the BBC's~~ my attitude towards the ~~show~~ thesis while it was in production was very similar to that which Macbeth had towards murdering people – initial doubts, followed by cautious enthusiasm and then greater and greater alarm at the sheer scale of the undertaking and still no end in sight."

Douglas Adam, 1985 *…. with minor edits*

Chapter 1 Introduction

The study of volcanic ash (tephra) deposits has become an important research area in Quaternary Science because of the potential for tephra to provide high precision chronology and records of past volcanism (Lowe, 2011). Tephra deposits may be characterised and 'fingerprinted', based on the major-minor element compositions of volcanic glass (Smith and Westgate, 1968; Lowe *et al*., 2017), and traced between depositional environments as chronological isochrons (Dugmore *et al*., 1995; Langdon and Barber, 2004). This application of tephrochronology was pioneered by the Icelandic volcanologist Sigurdur Thórarinsson (Thórarinsson, 1944, 1981), and has been widely used in palaeoenvironmental and archaeological studies (Lowe, 2011; Lane *et al*., 2014). However, tephra deposits preserve a range of volcanic, environmental and taphonomic information that is often overlooked (Dugmore and Newton, 2012). This selective focus on the use of tephra for dating applications is particularly acute in distal settings, several hundred kilometres from the source, where ash layers are typically preserved as cryptotephra (non-visible volcanic ash) deposits.

In Europe, a region with a long history of tephrochronology and high density of study sites (Persson, 1971; Dugmore, 1989; Pilcher and Hall, 1992; Plunkett *et al*., 2004), new research has begun to use distal tephra records to investigate wider spatial and temporal patterns in volcanic ash dispersal (Wastegård and Davies, 2009; Swindles *et al*., 2011, 2018; Lawson *et al*., 2012; Sulpizio *et al*., 2014; Watson *et al*., 2017b; Plunkett and Pilcher, 2018). These studies have been energised by the 2010 eruption of Eyjafjallajökull volcano, Iceland, which caused massive disruption to air travel over Europe (Davies *et al*., 2010), at a cost of around US $1.7 billion to airline operators (Mazzocchi *et al*., 2010). Subsequent research has provided important insights into patterns of ash cloud return intervals and tephra dispersal (Swindles *et al*., 2011; Stevenson *et al*., 2015; Watson *et al*., 2017). To date such studies have been confined to Europe; however, there is clearly potential to conduct further investigations in other regions frequently affected by tephra deposition.

This thesis will investigate past changes in ash dispersal patterns throughout the Lateglacial and Holocene using distal cryptotephra deposits. In order to achieve this two case studies will be examined: eastern North America and the Falkland Islands, South Atlantic (see Chapter 2.2). Tephra dispersal over these regions is likely to have been strongly affected by past changes in wind-strength during the Lateglacial and early Holocene – temporal periods during which atmospheric conditions underwent rapid shifts (Dean *et al*., 2002; Kirby *et al*., 2002; Fletcher and Moreno, 2012; Killian and Lamy, 2013). Therefore, these case studies provide interesting examples with which to test hypotheses of long term changes in ash dispersal patterns.

In both regions the first step will be to robustly describe the pattern of tephra deposition through the development of new distal cryptotephra records. These new datasets will contribute to tephrostratigraphic frameworks emerging from southern South America (Stern, 2008; Wastegård *et al*., 2013; Fontjin *et al*., 2014, 2016) and eastern North America (Pyne-O'Donnell *et al*., 2012, 2016; Mackay *et al*., 2016). The second step will be to compare these records of ash deposition with reconstructions of eruption frequency and atmospheric conditions in order to examine the possible processes driving past changes in ash dispersal.

This thesis will seek to demonstrate that distal cryptotephra deposits can provide evidence for past changes in ash cloud dispersal, and that volcanic ash should be considered as more than just a dating point – beyond chronology.

1.1 Research aims and objectives

The primary aim of this thesis is to: *investigate past changes in ash dispersal patterns using distal cryptotephra deposits*. This aim will be addressed through two main objectives:

Objective 1. New cryptotephra records will be developed from eastern North America and the Falkland Islands, South Atlantic, to close spatial and temporal gaps in the existing tephrostratigraphic frameworks from these regions.

Objective 2. Changes in temporal frequency and provenance of cryptotephra deposits will be compared with possible drivers of ash deposition (production, transport and deposition) in order to investigate past changes in tephra dispersal patterns.

1.2 Thesis Structure

This thesis is submitted under the 'three paper thesis' structure, with methods and findings divided into four results chapters (Chapters 4-7), each formatted as a self-inclusive paper (Papers I-IV). A synthesis chapter (Chapter 8) brings together the key findings from each of these papers in order to address the research objectives of this thesis, and raises hypotheses to be tested by further research.

Chapter 1. Introduction: has provided context for the primary research aim of this thesis, and outlined the thesis structure.

Chapter 2. Literature review: the literature review is divided into three sections: 1) Reviews the literature on distal tephra deposits with focus on the dispersal of volcanic ash and applications of tephrostratigraphy beyond chronology. 2) Presents the case study regions examined in this thesis: eastern North America and the Falkland Islands, South Atlantic, including the current state of knowledge regarding tephra deposits in both of these regions. 3) Outlines research questions developed from knowledge gaps identified during this literature review.

Chapter 3. Paper rationales: outlines the research questions addressed in each results chapter (Papers I-IV), as well as providing context for study design, author contributions and funding details.

Chapter 4. Paper I: presents the results of experiments designed to test the effects of the peat acid digestion protocol (Dugmore *et al*., 1995) on diverse tephra deposits.

> Chapter 4 is published in the Journal of Quaternary Science as:
>
> Monteath, A.J., Teuten, A.E., Hughes, P.D.M., Wastegård, S., 2019. The effects of the peat acid digestion protocol on geochemically and morphologically diverse tephra deposits. Journal of Quaternary Science 34, 269–274.

Chapter 5. Paper II: Uses new and existing cryptotephra records to examine temporal patterns in volcanic ash fall over eastern North America.

Chapter 6. Paper III: Presents the first Lateglacial and early Holocene tephrostratigraphy of the Falkland Islands, South Atlantic.

Chapter 6 is published in Quaternary Geochronology as:

Monteath, A.J., Hughes, P.D.M., Wastegård, S., 2019. Evidence for distal transport of reworked Andean tephra: Extending the cryptotephra framework from the Austral Volcanic Zone. Quaternary Geochronology 51, 64–71.

Chapter 7. Paper IV: Provides a multiproxy investigation of dynamic Southern Westerly Winds in order to further investigate the controls of tephra delivery in the Falkland Islands.

Chapter 8. Synthesis and discussion: Combines the major findings of papers I-IV in order to discuss evidence for past changes in ash dispersal identified during this thesis, and outline future research questions.

Chapter 9. Conclusions: Delivers a final comment on the use of distal cryptotephra deposits to infer past changes in ash dispersal patterns.

Chapter 2 Literature review

This literature review is divided into three sections: section one provides context for the primary research aim of this thesis and reviews the current literature on distal tephra deposits with a focus on the processes affecting tephra dispersal and applications of tephrostratigraphy beyond chronology. The second section presents the two case study regions examined in this thesis: eastern North America and the Falkland Islands, South Atlantic. The current state of knowledge regarding tephra deposits in both of these regions is discussed, along with volcanic sources and environmental processes which are likely to influence ash dispersal and deposition. The third section outlines research questions developed from knowledge gaps identified throughout this literature review. These research questions are addressed in Papers I-IV (see Chapter 3) and discussed with relevance to the primary research aim in Chapter 8: Synthesis and discussion.

2.1 Tephra and cryptotephra

Tephra (from the Greek; τεφρα, meaning ashes) refers to all unconsolidated, explosive, volcanic ejectives, including crystalline minerals, volcanic glass and rock fragments (lithics) (Thorarinsson, 1944). This material forms a of range deposits, from proximal layers tens of meters thick, to cryptotephra deposits (from the Greek; *kryptein*, to hide) composed of non-visible concentrations of volcanic glass (typically <125 μm) (Thorarinsson, 1981; Lowe and Hunt, 2001). During explosive eruptions tephra may be rapidly transported (see Section 2.1.1) and deposited across a landscape, forming stratigraphic markers throughout a range of depositional environments including lakes, peat-bogs, ice-cores and ocean sediments. The spatial extents of these tephra isochrons are potentially vast, and ash plumes from historical eruptions have been observed to travel several thousand kilometres (Davies *et al*., 2010; Stevenson *et al*., 2012), while the palaeo-record holds examples of intercontinental cryptotephra deposits (Lane *et al*., 2013a; Jensen *et al*., 2014; Sun *et al.,* 2014; van der Bilt *et al*., 2017).

2.1.1 The transport and deposition of fine ash

Fine ash (<63 μm) (White and Houghton, 2006) is the principle component of distal tephra deposits (Stevenson *et al*., 2015; Watson *et al*., 2016), and comprises >30% of the total mass erupted during silicic eruptions (Rose and Durant, 2009). Unlike larger volcanic-material (centimetre to millimetre scales) which is rapidly deposited within minutes to hours of an eruption (Folch, 2012), fine ash can remain in the atmosphere for days to weeks (Robock and Matson, 1983). During this period suspended tephra may be rapidly transported over several thousand kilometres. For example, ash

from the 1980 eruption of Mt St Helens, USA, travelled around 1000 km in only 10 hours (Christiansen and Paterson, 1981), while tephra from the 2011 eruption of the Puyehue-Cordón Caulle volcanic complex, Chile, was deposited in western Antarctica within two to three weeks of eruption (Koffman *et al*., 2017).

The duration, and distance, of ash transport in the atmosphere is dictated by the eruption column height, meteorological conditions (i.e. wind velocities and uplift currents) and aggregation rates (Bonadonna *et al*., 2015). The direction of this transport will reflect the atmospheric conditions operating at the time of the eruption, crucially wind direction and atmospheric turbulence (Bursik, 2001; Folch, 2012). In regions effected by a dominant atmospheric circulation pattern ash plumes may be repeatedly dispersed in the same direction. For example, repeated easterly tephra deposition in southern South America is observed in both contemporary records (Alloway *et al*., 2015) and the palaeo archive (Stern, 2008; Fontjin *et al*., 2014) because of the strong influence of the Southern Westerly Wind belt over this region. In settings affected by more variable atmospheric circulation ash dispersal patterns may become more spatially complex, reflecting changes in the weather patterns operating during the eruption or differing wind conditions between altitudes (Lacasse, 2001). These processes can be observed in ash isopleth maps of past eruptions (e.g. the Laacher See eruption; van den Bogaard and Schmincke, 1985) and modern observations of contemporary ash fall (Davies *et al*., 2010).

Once separated from the influences of the volcanic vent, and eruption column, ash is removed from the atmosphere by dry and wet deposition processes, as well as particle aggregation (Bonadonna *et al*., 2015). Under dry conditions the fall out of volcanic ash is controlled by particle morphology and density, which is determined by the geochemical composition of the tephra and eruption style. Lighter irregular ash morphologies have lower terminal velocities than denser more-rounded particles, and so can remain airborne for longer periods, and be transported over greater distances (Wilson and Huang, 1979; Mele *et al*., 2011). Wet deposition of tephra will occur as airborne ash interacts with rain clouds and precipitation. Within rain clouds volcanic ash can act as cloud condensation nuclei or ice-nuclei, promoting rain out (rain-out) (Lathem *et al*., 2011). Beneath rain clouds tephra may be directly impacted by precipitation (wash-out). These process can lead to enhanced, and often localised, ash deposition. For example, during the 1947 eruption of Hekla, Iceland, precipitation throughout southern Finland caused some of the heaviest tephra deposition along the eruption plume route (Dugmore and Newton, 1997). Finally, particle aggregation is a key process in the deposition of fine ash (<63 μm) (Brown *et al*., 2012; Bonadonna *et al*., 2015; Durant and Brown, 2016). Tephra shards adhere to each other through electrostatic attraction, mechanical interlocking and moisture adhesion. This process will alter the aerodynamic behaviour of shards, promoting the deposition of larger shard aggregates. Aggregates from past eruptions are rarely

preserved in the geological record, as they are broken up by impact or subsequent reworking, and so the role of this process in forming distal tephra deposits it hard to observe.

2.1.2 The study of distal tephra deposits: applications

2.1.2.1 Tephrostratigraphy

'Tephrostratigraphy' (*sensu stricto*) is the study of a sequence and order of tephra (and cryptotephra) deposits (Lowe and Hunt, 2001). This technique provides the foundations for further tephra studies, and includes the characterisation of tephra deposits based on a range of information including: chronology, stratigraphy, petrology, chronology and geochemical composition (Westgate and Gorton, 1981; Lowe *et al*., 2017).

2.1.2.2 Tephrochronology

'Tephrochronology' (*sensu stricto*) is a geochronological technique that uses tephra isochrons to link depositional sequences based on the 'identification, correlation and dating of tephra layers' (Thorarinsson, 1981; Lowe and Hunt, 2001). Where tephra deposits are securely characterised, using a range of information, tephrochronology allows environmental records to be aligned and placed on a common timescale. This principle of *age transfer* can be applied as most explosive eruption episodes typically last between hours and days, and are therefore *geologically instant*, rarely exceeding the temporal resolution of a depositional environment (Lowe, 2011).

Where the numerical age of a tephra deposit is known it may be imported into the chronology of a stratigraphic record (e.g. Brooks *et al*., 2012), or used to assess the accuracy of an existing age-depth model (e.g. Blockley *et al*., 2008). However, tephrochronology is at its most powerful when used to synchronise stratigraphic records across a region (e.g. Dugmore *et al*., 1995; Langdon and Barber, 2004). Such alignment may be used to investigate environmental shifts at resolutions unavailable to traditional dating methods. For example, Lane *et al.* (2013b) demonstrated progressive climate amelioration across north-west Europe during the later Younger Dryas, using the Vedde ash to show north-south, time-transgressive, warming between Meerfelder Maar, Germany, and Lake Krakenes, Norway. On smaller spatial scales tephrochronology can be used to examine geomorphological or environmental dynamics across a landscape (Dugmore and Newton, 2012). This approach was used by Streeter and Dugmore (2014) to examine land surface stability in Iceland, where tephra isochrons were used to illustrate complex interactions between erosion rates and drivers of environmental change – both anthropogenic and climate.

2.1.2.3 Volcanic hazard assessment

Distal tephra deposits provide direct evidence of past volcanic eruptions which may not be preserved (or accessible) in proximal records due to subsequent burial or erosion (e.g. Rawson *et al*., 2015). These eruption archives provide a longer, and potentially more complete, record of tephra dispersal and deposition than historical archives (Swindles *et al*., 2013), and may include ash deposits derived from several volcanic regions (Plunkett and Pilcher, 2018). This information can be used to help estimate eruption frequencies, or styles, for the purpose of assessing volcanic hazards (Shane and Hoverd, 2002; de Fontaine *et al*., 2007; Payne *et al*., 2008; Schiff *et al*., 2010). In Western Europe regional tephrostratigraphic frameworks, composed of multiple study sites, have been used to examine the dispersal of ash clouds over the region and calculate a return interval of 44±7 years during the last millennium (Swindles *et al*., 2011; Watson *et al*., 2017b). These studies have particular implications for the aviation industry as jet aircraft are vulnerable to damage caused by airborne ash particles (Grindle and Burcham, 2003; Prata and Rose, 2015), which can cause abrasion to cockpit windows, electrical faults, and in extreme cases engine failure (e.g. Redoubt Volcano 1989-90; Casadevall, 1994). However, while these estimates provide an important 'long-view' of volcanic hazards they represent a minimum return-interval (Bourne *et al*., 2016), as tephra fall out and deposition is often patchy – exacerbated by spatial and temporal gaps in any regional tephrostratigraphy.

2.1.2.4 Eruption frequency

The use of distal tephra deposits to reconstruct past eruption frequency is closely linked with volcanic hazard assessments; however, they also provides insights into the processes controlling volcanic eruptions. Eruption frequency is determined by a range of internal (e.g. magma storage and replenishment, degassing rates, mantle melting rates) and external (e.g. earthquakes, sea level change) processes which operate on an array of time scales (Gudmundsson, 2006).

Ocean sediments and ice cores provide records of eruption frequency over Milankovitch time scales (Zielinski *et al*., 1996; Lacasse and van den Bogaard, 2002), with some evidence for interactions between climate and volcanism (Kutterolf *et al*., 2019). These climate-volcanism interactions are hypothesised to be driven by the 'unloading effect'– caused by uplift of the lithosphere and enhanced melting of the mantle following deglaciation. This process has been suggested to intensify volcanism and has been linked with increased eruption frequency in high latitudes during the end of the last Glacial (Brown *et al*., 2014). Well resolved examples of the unloading effect are reported from Iceland (Jull and McKenzie, 1996; Swindles *et al*., 2017), Alaska (Praetorius *et al*., 2016) and Kamchatka (Braitseva *et al*., 1995) during the Lateglacial and early

Holocene, and may be expressed in regions examined during this thesis (eastern North America and the Falkland Islands) which are affected by volcanism in these areas.

Evidence for intensified volcanism following deglaciation is not always present, which may reflect incomplete eruption histories, sampling bias, regional volcanic insensitivity to unloading or a rejection of the hypothesis (Watt *et al*., 2013; Cooper *et al*., 2018). In distal records any change in eruption frequency may be obscured by transport processes; however, temporal patterns may still be present in study sites immediately downwind of volcanic centres. The Falkland Islands are well positioned to examine hypotheses related to eruption frequency in the Andean Austral Volcanic Zone and the Andean Southern Volcanic Zone (see Section 2.2.2). The response of these volcanic systems to deglaciation is poorly resolved at present (Watt *et al*., 2013; Weller *et al*., 2015; 2019), where knowledge of past eruptions is based entirely on visible tephra deposits. The position of the Falkland Islands may allow for the preservation of a more regional tephra record and provide insights into changes in the eruption frequency of these volcanic zones.

2.1.2.5 Changes in atmospheric conditions

Ash from explosive volcanic eruptions may reach tropospheric and even stratospheric levels in the atmosphere. Once separated from the eruption column the transport of ash is controlled by wind direction and atmospheric turbulence (Bursik, 2001; Folch, 2012). Therefore, the deposition of tephra along the eruption plume route reflects a snapshot of the atmospheric processes operating at the time of eruption. Over Milankovitch timescales changes in the frequency and/or provenance of tephra deposits may be used to infer shifts in atmospheric circulation (Table 2.1). While the origins of this approach can be traced over 130 years (Abercromby *et al*., 1888; Brooks, 1932; Wexler, 1951; Eaton, 1963; Yoshino and Tabuchi, 1975) few studies have examined cryptotephra deposits in this way, or attempted to observe shorter millennial scale changes. This technique may provide valuable insights into long term changes in atmospheric circulation as glass shards may be correlated to their volcanic origin, and used to trace the routes of volcanic ash plumes across a landscape. At present it is unclear if distal cryptotephra deposits record a signal that consistently reflects a dominant atmospheric circulation pattern, or provide the temporal resolution needed to observe millennial scale changes. Both of the regions examined in this thesis (eastern North America and the Falkland Islands) have been affected by changes in atmospheric circulation during the lateglacial and early Holocene (Dean *et al*., 2002; Kirby *et al*., 2002; Fletcher and Moreno, 2012; Killian and Lamy, 2013), and therefore may be used to test these hypotheses – outlined in Research Objective 2.

Table 2.1: Published examples where tephra deposits have been used to infer past changes in atmospheric circulation.

Study	Region	Time Period	Observation
Coulter *et al*. (2012)	Greenland	-	The reduction in the frequency of Icelandic, basaltic tephra deposits between the Lateglacial and Holocene suggests a change in atmospheric circulation patterns.
Narcisi *et al*. (2012)	Antarctica	0-16 ka	Tephra deposits in the TALDICE ice-core suggest circumpolar westerly atmospheric circulation over Antarctica during the last 16,000 ka.
Lane *et al*. (2012)	Southern Europe	-	Identification of the Vedde Ash in northern Italy suggests polar winds were able penetrate into central and southern Europe during the Younger Dryas.
Yoshino and Tabuchi, (1975)	Japan	0-60 ka	The direction and shape of tephra deposits in Hokkaido, Japan, reflect changes in the strength of regional westerly winds.
Sigurdsson, (1990)	-	0-75 ka	Coarser shard sizes relative to distance form source suggest more vigorous atmospheric circulation during glacial periods.
Lacasse *et al*. (1998a)	North-East Atlantic	0-130 ka	Icelandic tephra deposits in the Icelandic Basin must have been transported by northerly winds during the Pleistocene. These winds are not observed in modern atmospheric circulation.
Narcisi *et al*. (2005)	Antarctica	0-200 ka	The provenance of tephra deposits in the EPICA-Dome C ice-core suggest prevailing spiralling westerly winds towards Antarctica during the last 200 ka.
Basile *et al*. (2001)	Antarctica	0-220 ka	Tephra from Southern Hemisphere volcanic centres is transported rapidly to Antarctica. This transport pathway remains the same over glacial-interglacial timescales.
Lacasse *et al*. (1998b)	North-East Atlantic	0-800 ka	Icelandic tephra deposits in the Irminger Basin must have been transported by easterly winds in the stratosphere.
Westgate *et al*. (2018)	North America	1.24 ma	The transport of Pleistocene tephra from New Mexico to Saskatchewan occurred during a southward penetration of the jet stream.
Natland, (1993)	North-West Pacific	0-3 ma	Changes in the frequency and provenance of ash deposits represent shifts in the strength of the jet stream or position of the polar front.
Lacasse, (2001)	North-East Atlantic	-	Coarser Pliocene-Pleistocene tephra deposits may reflect enhanced atmospheric circulation during these periods.
Lacasse and van den Bogaard, (2002)	North-East Atlantic	0-6 ma	A coarsening and increased frequency of tephra deposits between 3.6-3.0 ma is linked with enhanced westerly winds over the North Atlantic during this time period.

2.1.3 The study of distal tephra deposits: limitations

2.1.3.1 Site densities

Taphonomic issues mean a single record rarely provides a comprehensive regional tephrostratigraphy (Lowe, 2011; references therein). Instead, a network of sites should be used to develop a catalogue of tephra deposits across a region. At present, such detailed regional records only exist from a few areas (e.g. Europe, Japan and New Zealand), and are often temporally restricted. These limited site densities can hinder investigations of wider patterns. For example, a paucity of records prevented Swindles *et al*. (2011) and Watson *et al*. (2017) from extending studies of ash cloud reoccurrence rates beyond *ca.* 7,000 yr BP. Studies of spatial patterns are often limited in the same way, with large gaps in site coverage (Lawson *et al*., 2012). These issues are compounded by the lack of published records detailing where *no* tephra was found. Repeated reporting of these 'failed results' is crucial for establishing ash dispersal limits and testing temporal hypotheses.

While these issue remains, new research is continually closing spatial and temporal gaps in regional tephrostratigraphies. One example is eastern North America where a series of recent studies have closely examined lakes and peat-bogs throughout the region for the presence of volcanic ash (Pyne-O'Donnell *et al*., 2012, 2016; Jensen *et al*., 2014; Mackay *et al*., 2016; Spano *et al*., 2017). The results from these new studies now represent the highest density of cryptotephra records in North America, and potentially the first opportunity to examine spatial and temporal patterns within an ultra-distal tephra framework (see Q.2.3).

2.1.3.2 Taphonomic processes

The deposition, and subsequent preservation, of tephra in lake sediments and peatlands can be effected by a range of taphonomic processes (Mangerud *et al*., 1984; Boygle *et al*., 1999; Beierle and Bond, 2002; Bergman *et al*., 2004; Payne *et al*., 2005; Davies *et al*., 2007; de Fontaine *et al*., 2007; Payne and Gehrels, 2010; Pyne-O'Donnell, 2011; Watson *et al*., 2015). These mechanisms may alter the preservation of primary tephra deposits within a profile, or produce secondary tephra deposits formed of reworked or detrital glass (tephra not derived from a primary air fall event). This reworking can complicate the identification of tephra isochrons or lead to secondary deposits being incorrectly ascribed to non-existent eruptions (Davies *et al*., 2007). These complications have implications for development of robust chronologies and eruption frequencies; however, they also provide evidence for a range of external and internal processes affecting a catchment. When used in conjunction with other proxies reworked tephra can provide environmental and depositional information that might otherwise be overlooked. For example, Dugmore and Newton (2012)

illustrated post-depositional frost hummock formation using disturbed Icelandic tephra beds, while Swindles *et al*. (2013) linked reworked tephra deposits with peat erosion, following human activities in the Shetland Islands. Further examples are provided from lake sediments described by Boygle, (1999), who argued that an increase in the frequency of reworked ash beds indicated periods of vegetation disturbance within the catchment.

In both of the regions examined in this thesis reworked tephra has been linked with local and environmental processes. In eastern North America, Mackay *et al*. (2016) argued cryptotephra deposits with identical major-minor element glass compositions from the same sequence were caused by reworking of the White River Ash east, promoted by changes in peat-bog vegetation. Similar observations are reported from the Falkland Islands by Hall *et al*. (2001), who linked chaotic shard profiles with vertical reworking of primary tephra deposits. New records produced during this thesis will provide tests of these hypotheses, with wider implications for tephrochronology.

2.1.3.3 The geochemical characterisation of distal cryptotephra deposits

Correlations between distal tephra deposits are underpinned by analysis of the geochemical composition of individual shards of volcanic glass. These analyses are undertaken using both electron probe microanalysis (EPMA) (Smith and Westgate, 1968), and laser ablation inductively coupled plasma-mass spectrometry (LA-ICP-MS) (Pearce *et al*., 1996), which provide high-precision major-minor-trace element data. The compositional differences between tephra deposits may be subtle (e.g. Mt. St Helens We and Wn; Pyne-O'Donnell *et al*., 2012), and therefore correlations based on these data should be supported by a range of information including stratigraphy, petrology and chronology (Westgate and Gorton, 1981; Lowe *et al*., 2017). However, in distal settings this information is not always available as heavier crystalline mineral components rain out over longer distances, and stratigraphic evidence preserved in proximal deposits may not always be replicated. These limitations mean that correlations of distal tephra (and cryptotephra) deposits are heavily reliant on the secure geochemical characterisation of volcanic glass. In proximal and medial settings tephra deposits can be easily analysed, and studies often report >20 analyses from a single tephra deposit (e.g. Jensen *et al*., 2016). However, this is not always the case in distal and ultra-distal settings, where cryptotephra deposits are commonly composed of a few tens of shards (van der Bilt *et al*., 2017; Watson *et al*., 2017c). In these settings it is vital that shard recovery rates are maximised and glass geochemical compositions are not altered during laboratory procedures.

This thesis will examine distal and ultra-distal cryptotephra deposits in both lake sediments and peats. Glass shards for EPMA can be simply extracted from lake sediments using density separation (Turney, 1998). However, this method is less efficient in isolating tephra from peat as shards become trapped within the organic rich matrix and removed during floatation. An

alternative extraction method is acid digestion (Pilcher and Hall, 1992; Dugmore *et al*., 1995; Swindles *et al*., 2010). This protocol often achieves higher shard recovery rates from peat, relative to density separation, and has been widely used to develop a tephrostratigraphic framework across Western Europe (Pilcher and Hall, 1992; Pilcher *et al*., 1995; Plunkett *et al*., 2004). However, strong acids are known to chemically alter the structure of natural glass (Pollard and Heron, 1996), and Blockley *et al*. (2005) describe a Si leachate from tephra shards exposed to acid and alkali solutions. As a result of these findings some studies of ultra-distal cryptotephra deposits have avoided the use of acid digestion in favour of density separation (e.g. Pyne-O'Donnell *et al*., 2012; Mackay *et al*., 2016).

Several studies have examined the effects of the peat acid digestion protocol on volcanic glass using duplicate tephra samples to provide a control (Dugmore *et al*., 1992; Roland *et al*., 2015; Watson *et al*., 2016). These studies have reported consistent EPMA results between test samples; however, they have almost exclusively focussed on rhyolitic tephra deposits. This narrow sample group leaves considerable uncertainty regarding the effects of acid digestion on non-rhyolitic tephra, as the dissolution rates of natural glasses (including tephra) are determined by the chemical composition of the glass, and may be modified by surface area (Paul, 1977; Jantzen and Plodinec, 1984; Jantzen, 1992; Techer *et al*., 2001; Wolff-Boenisch et al., 2004; Conradt, 2008). In particular, SiO_2 and Al_2O_3 content determine the chemical durability of glasses, and therefore their resistance to acid solutions. The rhyolitic tephras that have been used during experiments with the peat acid digestion protocol include high SiO_2 values (>69%), and are therefore likely to be resistant to acid solutions.

Although distal cryptotephra deposits are typically composed of rhyolitic tephra shards derived from explosive Plinian eruptions (Lawson *et al*., 2012), there are numerous examples of distal ash deposits with non-rhyolitic glass compositions (Stern, 2008; Sun *et al*., 2014; Timms *et al*., 2019). Furthermore, most distal tephra deposits are characterised by small (typically *ca.* 40 µm), highly vesicular, glass shards, with high surface-area/volume ratios (Fig 2.1; Pyne-O'Donnell *et al*., 2012; Watson *et al*., 2016). Therefore, shards from distal tephra deposits may be prone to geochemical alteration during exposure to strong acids.

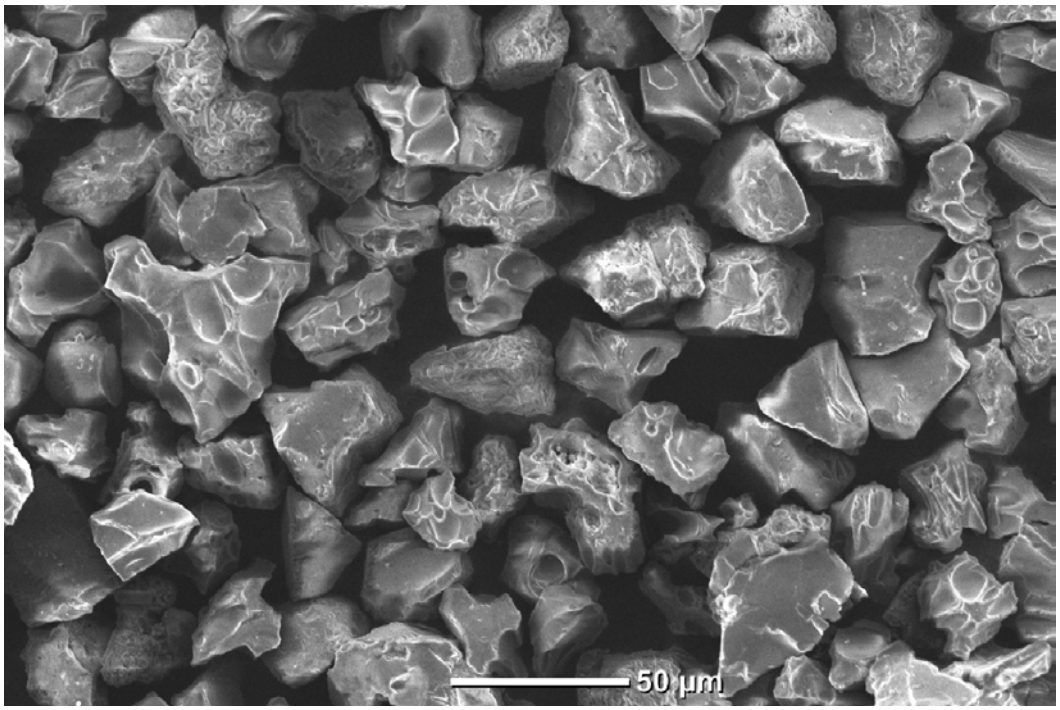

Figure 2.1: Highly vesicular glass shards from the White River Ash tephra deposit in Jan Lake, central Alaska, approximately 250 km from the source volcano – Mt. Churchill (Monteath *et al*., 2017).

This thesis will examine cryptotephra deposits derived from a range of volcanic sources (see Section 2.2) which are likely to have variable resistances to acid because of their differing geochemical compositions. Figure 2.2 shows the predicted chemical durability of widespread tephra deposits from the case study regions of this thesis (eastern North America and the Falkland Islands). These are calculated from published EPMA data and include the molar ratio of silicon to oxygen (Si:O) (Pollard and Heron, 1996), and number of non-bridging oxygen atoms (NBO) per silicon tetrahedral (White and Minser, 1984). Complete equations are given in Appendix A.3. The diagram demonstrates that although the majority of these widespread ash beds may be described as chemically durable, andesitic tephras (e.g. Hudson H_1) are likely to have a lower resistance to the strong acids used to extract tephra from peat.

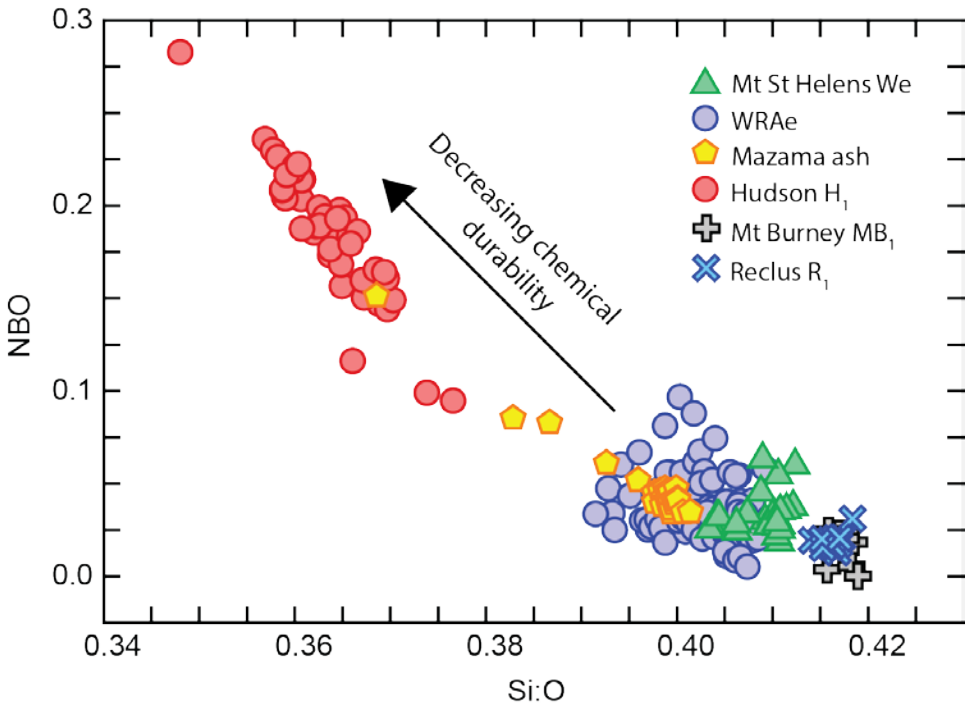

Figure 2.2: Plot of NBO and Si:O values from widespread cryptotephra deposits within study the study regions examined in thesis (full equations given in Appendix A.3). The arrow shows the direction of decreasing chemical durability. Northern Hemisphere cryptotephra include: the White River Ash eastern lobe (WRAe), Mazama ash, and Mt. St. Helens We (data from: Jensen *et al*., 2014, 2019; Mackay *et al*., 2016). Southern Hemisphere cryptotephra include: Hudson H_1, Mt Burney MB_1 and Reclus R_1 (data from Wastegård *et al*., 2013; Del Carlo *et al*., 2018).

This review of the peat acid digestion protocol demonstrates that it is still unclear if the strong acids used during tephra extraction will alter the major-minor element glass composition of highly vesicular or non-rhyolitic shards. Therefore, in order to maximise shard recovery rates from distal peat records, this thesis will examine the effects of the acid digestion protocol on a range of diverse tephra deposits. These 'case study' tephras will include a range of shard morphologies and predicted chemical durabilities to ensure that the use of acid will not affect the geochemical composition of volcanic glass, even in a *worst case scenario*: shards low predicted chemical durability and high surface-volume ratio. This methodological experiment is outline as Research Question Q.1.1.

2.2 Case studies

The primary aim of this thesis is to: *investigate past changes in patterns of ash dispersal using distal cryptotephra deposits*. In order to achieve this two case studies are examined which maximise the potential for dynamic dispersal patterns to be observed – i.e. large changes in atmospheric circulation and environmental conditions. Section 2.2 reviews the current literature on tephra deposits in both of these regions, as well as the volcanic zones and transport mechanisms affecting them. This review raises further research questions (see 2.3) which are addressed in papers I-IV (see Chapter 3.0).

Case study I examines ultra-distal cryptotephra deposits in eastern North America. This case study provides an example of long distance tephra transport which is strongly affected by atmospheric conditions because of the large distances (>4000 km) between the source volcanoes and the study region (Mackay *et al*., 2016). During the early Holocene atmospheric conditions over North America changed rapidly in response to the collapse of the Laurentide and Cordilleran ice-sheets. The effects of this atmospheric reorganisation on tephra transport are currently unknown, but are hypothesised to have enhanced distal ash dispersal over North America (Pyne-O'Donnell *et al*., 2012). Therefore, changes in the frequency and/or provenance of cryptotephra deposits in this region may provide evidence for past changes in atmospheric conditions (see Q.2.1).

The tephrostratigraphic framework of eastern North America has developed rapidly (Pyne-O'Donnell *et al*., 2012, 2016; Mackay *et al*., 2016; Spano *et al*., 2017); however, spatial and temporal gaps remain, particularly during the early Holocene. By developing new cryptotephra records throughout this period Case Study I uses this regional tephrostratigraphy to examine the atmospheric processes affecting distal tephra deposition in North America.

Case study II examines distal cryptotephra deposits in the Falkland Islands (Islas Malvinas). The archipelago lies in the South Atlantic (51-53°S, 57-61°W), approximately 540 km east of southern South America, and includes >700 islands. The Falkland Islands lie immediately downwind of the Andean Austral Volcanic Zone and the Andean Southern Volcanic zone, and have been affected by ash fall from modern eruptions in these regions. Despite this little is known about tephra deposits in the archipelago. Hall *et al*. (2001) provide the only published cryptotephra records from this region, which include high abundances of reworked volcanic glass, suggesting that the archipelago is frequently affected by ash fall.

The transport of tephra over the Falkland Islands is controlled by the Southern Westerly Wind belt, which has moved southward and strengthened since the 1970s (Marshall, 2003; Visbeck, 2009). Past changes in this atmospheric circulation pattern must have affected the dispersal of

tephra from volcanoes in southern Patagonia. Therefore, changes in the abundance of tephra deposits in the Falkland Islands, which lie beneath the core of the Southern Wind belt, may reflect variation in regional wind strengths or position.

The frequent deposition of tephra in the Falkland Islands means that tephrostratigraphic records in the archipelago are likely to be subjected to reworking processes which could be caused by changes in the local environment (e.g. vegetation cover). Therefore, these processes must be understood before beginning to investigate changes in ash dispersal patterns.

2.2.1 Case Study I: eastern North America

2.2.1.1 Tephra in eastern North America

Ultra-distal cryptotephra deposits were first reported in eastern North America by Pyne-O'Donnell *et al*. (2012), who described the tephrostratigraphy of Nordan's Pond Bog, Newfoundland. Twelve cryptotephra deposits were identified throughout the *ca.* 9,000 yr record, seven of which were linked with volcanic sources in the Cascades and Alaska (Table 2.2). This study changed perceptions of the eruption magnitude and preservation conditions needed to form ultra-distal tephra deposits, which had previously only been reported from 'exceptional' caldera forming eruptions (e.g. Mazama ash and Aniakchak CFE II) identified in the Greenland ice-cores (Zdanowicz *et al*., 1999; Pearce *et al*., 2004). Following the publication of Pyne-O'Donnell *et al*. (2012) a series of studies have closely examined the lakes and peat-bogs of eastern North America for the presence of volcanic ash (Jensen *et al*., 2014; Pyne-O'Donnell *et al*., 2016; Mackay *et al*., 2016; Spano *et al*., 2017), while further studies have identified ultra-distal cryptotephra deposits within new and existing records beyond North America (Sun *et al*., 2014; Jennings *et al*., 2014; Jensen *et al*., 2014; Blockley *et al*., 2015; Van de Blit *et al*., 2017; Watson *et al*., 2017; Plunket and Pilcher, 2018).

Cryptotephra deposits in eastern North America are typically composed of low concentrations (<100 shards/1 cm^3) of vesicular glass shards; however, some deposits may be more abundant (e.g. Mazama ash and White River Ash east) – surpassing 1000 shards/1 cm^3. This variation is not always consistent between cryptotephra derived from the same eruption. For example, the shard abundance in deposits linked with the White River Ash east is an order of magnitude greater in Saco Heath than Villagedale Bog (Mackay *et al*., 2016). These spatial inconsistencies are likely to have been caused by a combination of post depositional processes and interactions between ash clouds and variable atmospheric conditions (see Section 2.1.1). The morphology of glass shards that make up these deposits has received little attention. Pyne-O'Donnell *et al*. (2012) provide the only Holocene numerical data, which compare well with measurements from Europe described by Watson *et al*. (2016). A maximum shard length of 73 µm is reported from Nordan's Pond Bog; however, samples from this record were sieved at both 15 µm and 80 µm and so end members are likely to have been lost. In this thesis basic shard morphological descriptions are used to aid the correlation of cryptotephra deposits, although a common approach across the tephrochronological community may provide more detailed data (see Section 8.2.1).

Table 2.2: eastern North America cryptotephra deposits linked with known volcanic eruptions.

Cryptotephra deposit	Source region	Source volcano	Eruption	Reference	Age Range (yr BP)	Dating reference
FBB12-31	Cascades	Mt St Helens	Mt St Helens T	Mackay *et al*. (2016)	150-149	Yamaguchi (1983)
NDN-95	Cascades	Mt St Helens	Mt St Helens We	Pyne-O'Donnell *et al*. (2012)	*ca*. 509	Yamaguchi (1985)
VDB12-90	Mexico	Volcan Ceboruco	Jala Pumice	Mackay *et al*. (2016)	970-940	Chertkoff & Gardner (2004)
NDN-160	Alaska	Mt Churchill	White River Ash east	Pyne-O'Donnell *et al*. (2012)	1,170-1,095	Davies *et al*. (2016)
NDN-185	Cascades	Newberry Volcano	Newberry Pumice	Pyne-O'Donnell *et al*. (2012)	*ca*. 1,460	Kuehn & Foit (2006)
VDB12-176	Kamchatka	Ksudach	KS1	Mackay *et al*. (2016)	*ca.* 1,800	Braitseva *et al*. (1997)
NDN-230	Alaska	Unknown	Ruppert tephra	Pyne-O'Donnell *et al*. (2012)	2,920-2,520	Monteath *et al*. (2017)
NDN-300	Alaska	Aniakchak volcano	Aniakchak CFE II	Pyne-O'Donnell *et al*. (2012)	3,600-3,585	Davies *et al*. (2016)
NDN-490	Cascades	Newberry Volcano	East Lake tephra	Pyne-O'Donnell *et al*. (2012)	*ca.* 7,320	Kuehn & Foit (2006)
Un-reported	Kamchatka	Ksudach	KS2	Van der Bilt *et al*. (2017)	7,340-7,180	Plunkett *et al*. (2015)
NDN-545	Cascades	Crater Lake	Mazama ash	Pyne-O'Donnell *et al*. (2012)	7,680-7,580	Egan *et al*. (2015)
VL-841	Cascades	Glacier Peak	Glacier Peak	Pyne-O'Donnell *et al*. (2012)	13,710-13,410	Kuehn *et al*. (2009)
VL-846	Cascades	Mt St Helens	MSH set J	Pyne-O'Donnell *et al*. (2016)	13,800-12,800	Clyne *et al*. (2008)

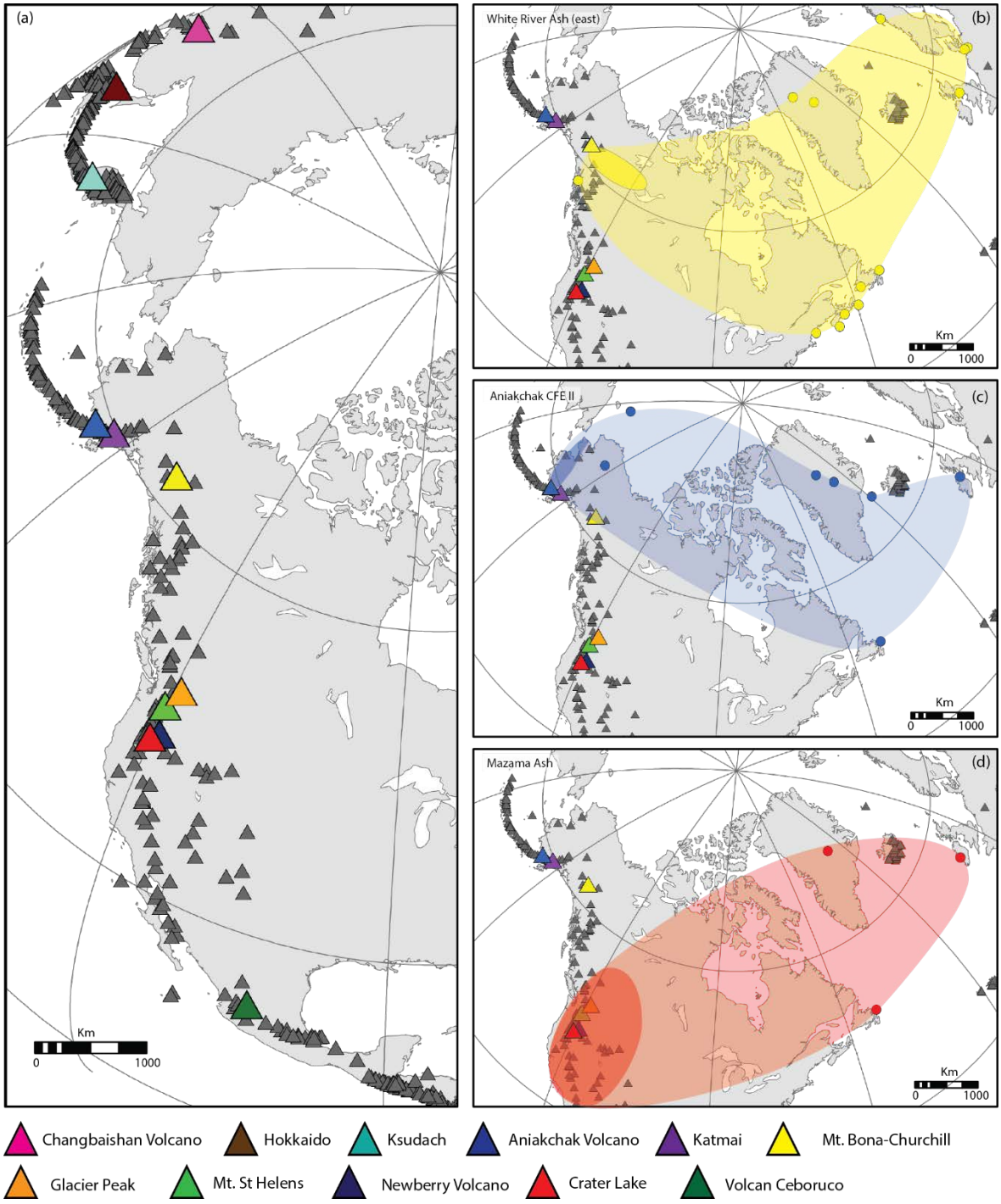

Figure 2.3: The dispersal limits of well dated ultra-distal cryptotephra deposits present in eastern North America. Sources and limits taken from Pyne-O'Donnell *et al*. (2012, 2016), Jensen *et al*. (2014), Mackay *et al*. (2016) and Plunkett and Pilcher (2018).

2.2.1.2 Volcanism affecting eastern North America

Cryptotephra deposits in eastern North America have been linked with volcanic centres in the Cascades, Alaska, Central America, Kamchatka and Japan based on glass major-minor element compositions (Pyne-O'Donnell *et al*., 2012, 2016; Mackay *et al*., 2016; Stano *et al*., 2017) (Figs. 2.3 and 2.3, Table 2.2). The Cascades volcanic chain is the most common source of cryptotephra deposits in eastern North America (Table 2.2), which is likely to be because of the proximity of the Cascade volcanoes (~4,000 km) relative to other volcanic zones affecting this region. Cryptotephra in eastern North America are typically derived from large (≥VEI 5) explosive events; however, several deposits have been linked with smaller eruptions (e.g. Mt. St Helens T; 0.4 km^3 DRE; Carey *et al*., 1995). Therefore, eruption volume alone cannot explain ultra-distal ash dispersal in North America.

Numerous large caldera forming events are known to have occurred in the volcanic regions effecting eastern North America, which are not identified in the regional tephrostratigraphy (Miller and Smith, 1987; Hildreth *et al*., 2007; Kyle *et al*., 2011; Albert *et al*., 2019). Therefore, new cryptotephra records in eastern North America are likely to reveal additional tephra isochrons from sources upwind of this region. Glass shards from eruptions in Alaska (Coulter *et al*., 2012) the Cascades (Plunket and Pilcher *et al*., 2018), Kamchatka (Cook *et al*., 2018; Plunket and Pilcher *et al*., 2018) and China (Sun *et al*., 2014) which have not been identified in eastern North America are reported from study sites in Greenland and Western Europe, and may yet be identified by further studies in this area.

Despite Iceland's comparative proximity (~2,700 km) to study sites in eastern North America, no Icelandic tephra has been identified in this region. This absence can be explained by the prevailing westerly winds and the jet stream, which favour easterly volcanic ash dispersal at these latitudes. However, the Greenland ice-cores include numerous cryptotephra deposits derived from Icelandic volcanoes (Abbot and Davies, 2012), and modelling suggests ash from the 2010 eruption of Eyjafjallajökull approached Newfoundland, Canada (Davies *et al*., 2010). Easterly winds develop in the stratosphere (>15 km) above Iceland during spring and summer months (Lacasse, 2001), which may facilitate this transport. Alternatively, higher latitudes, including areas of north-eastern North America, are likely to be affected by circum-polar ash transport (Mortensen *et al*., 2005). More northerly study sites are needed to test this hypothesis, which are unavailable here; however, modern observations of SO_2 emissions from Icelandic eruptions (e.g. Hekla 1980) have followed circum-polar transport patterns (Carn *et al*., 2008). Conversely, Icelandic ash has been described in western North America. Yalcin *et al*. (2003) link cryptotephra from the Eclipse Icefield, Alaska, with

the 1947 eruption of Hekla; however, this correlation is rejected by Davies *et al*. (2016), and seems unlikely to be robust.

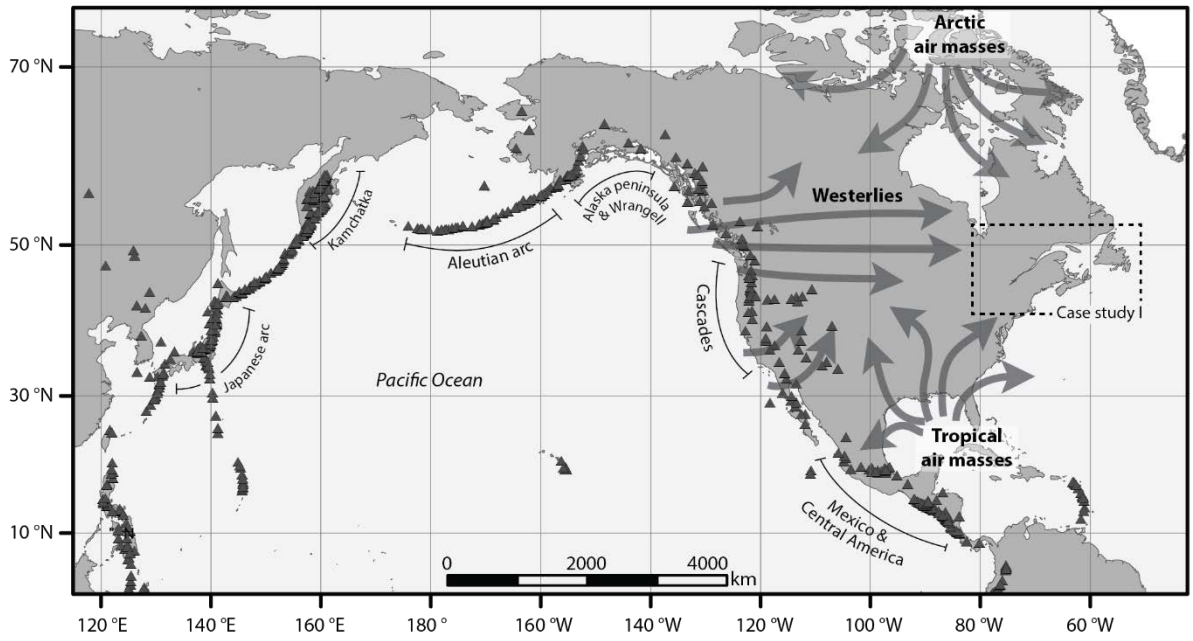

Figure 2.4: Volcanic zones linked with cryptotephra deposits in eastern North America. Volcanoes known to have been active during the Lateglacial and Holocene are shown as black triangles (Smithsonian Global Volcanism programme, 2019). The dominant air masses affecting the Case Study I region are shown as grey arrows.

2.2.1.3 Tephra transport mechanisms affecting eastern North America

The modern climate of eastern North America is affected by the polar jet and three regional air masses which control wind speed and direction: the Pacific westerly winds, Arctic air masses from the North/North-West and tropical southerly air masses (Bryson and Hare, 1974). These air masses play an important role in the delivery of tephra to eastern North America and may not have operated under the same conditions during the past. Modern ash clouds from comparatively small eruptions have been observed to pass over eastern North America. For example, the volcanic cloud from the 1992 eruption of the Crater Peak vent – Mt. Spurr (Alaska) reached the North Atlantic within three days (Fig 2.5). However, it is unclear if these events are preserved in the geological record or if heavier tephra loading is required to form a cryptotephra deposit.

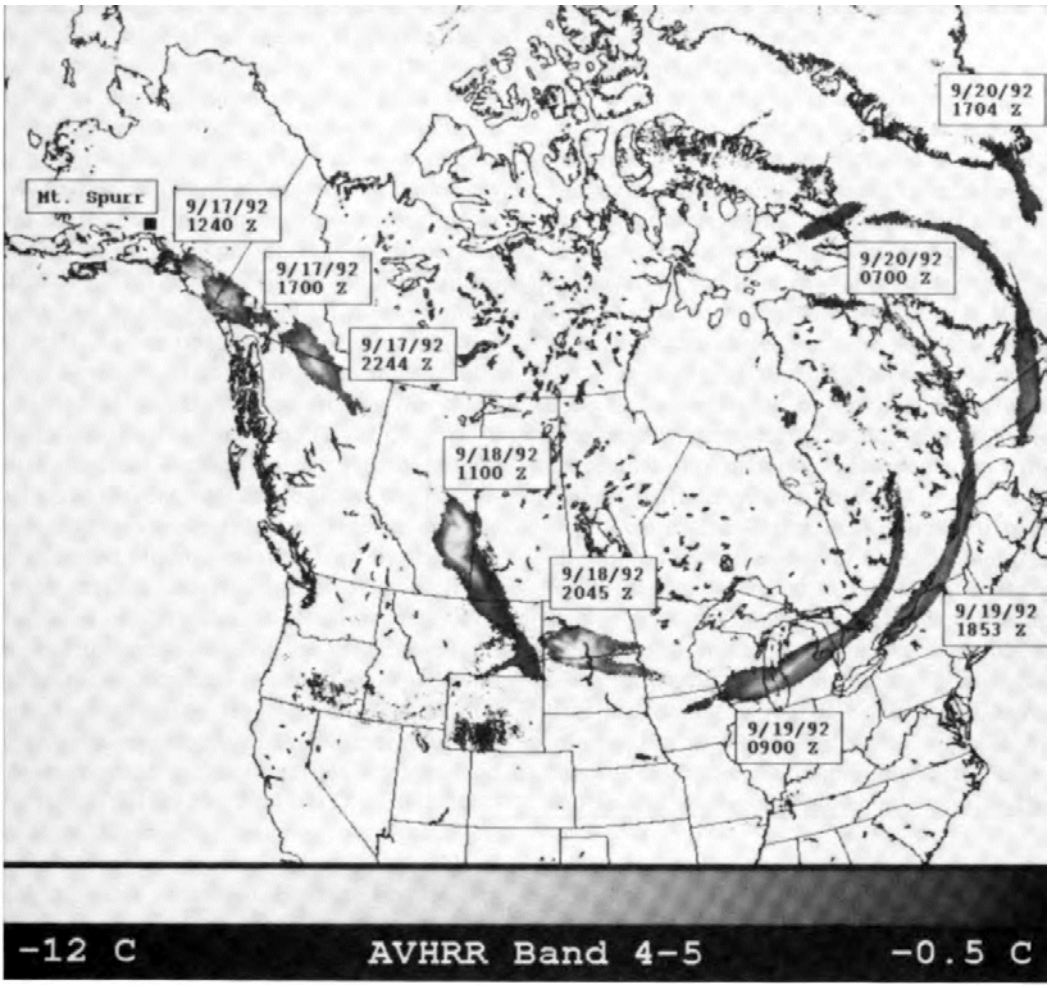

Figure 2.5: Movement of the volcanic cloud (water, volcanic ash, and sulfuric acid) from the 1992 eruption of the Crater Peak vent - Mt Spurr, Alaska (Schneider *et al*., 1995).

The White River Ash eastern lobe (WRAe) provides an important case study which highlights the effects of atmospheric circulation on distal tephra deposits. Ash from this late Holocene (1,170-1,095 cal yr BP; Davies *et al*., 2016) eruption of Mt. Churchill, Alaska, is uniquely preserved in eastern North America. It is the only cryptotephra deposit which has been identified across every Holocene study site, and is the most abundant in almost every case (Pyne-O'Donnell *et al*., 2012; Mackay *et al*., 2016; Jensen, pers coms 2019). Tephra from this eruption can be traced beyond eastern North America, into the North Atlantic and Europe, where it forms a widespread chronological marker known as the 'AD860B' tephra (Jensen *et al*., 2014). The White River Ash eastern lobe eruption was large, ejecting approximately 23 km^3 of dense-rock equivalent material (VEI 6) (Lerbekmo, 2008); however, magnitude alone cannot explain its abundance in eastern North America and Europe. Many caldera forming eruptions took place in Alaska during the Holocene which are not identified in eastern North America, despite ejecting comparable or greater volumes of material (e.g. Novarupta-Katmai, Black Peak, Okmok, Veniaminof, Akutan, Makushin and Fisher; Miller and Smith, 1987). The abundance of distal tephra deposits linked with the WRAe must, therefore, be related to atmospheric conditions and the mode of ash transport. Cryptotephra in

Poland, correlated with the WRAe, includes glass shards up to 95 µm in length despite being 7,000 km from Mt. Churchill (Watson *et al*., 2017). In order to sustain atmospheric suspension over such great distances wind speeds must have remained high throughout transport. The most plausible explanation for this ultra-distal dispersal is interaction between the eruption column and the jet stream, which can reach wind speeds in excess of 50 ms^{-1}, capable of rapidly transporting ash over large areas (Ahrens, 2012).

The atmospheric circulation patterns delivering ash to eastern North America are likely to have varied during the time period spanned by cryptotephra records in this region (*ca*. 17,000 yr BP to present). During the early Holocene these changes are suggested to have been driven by the rapid collapse of the North American ice sheets (Pausata *et al*., 2011; Ullman *et al*., 2014), which formed formidable topographic barriers during the last Glacial, >3 km thick (Peltier *et al*., 2004). How these changes affected the transport of volcanic ash across North America is currently unknown, and is the focus of Research Question 2 in this thesis (see Section 2.3). Wider ash dispersal, and coarser grain sizes, from large eruptions during glacial periods have been linked with a cooler, denser, atmosphere, under a cold climate. It's hypothesised that this would allow rising ash plumes to achieve greater heights before reaching neutral buoyancy and so affect wider areas (Sparks 1986; Sigurdsson 1990; Lacasse 2001). These processes should lead to more frequent, and more abundant, tephra deposits in Lateglacial sediments, as the effects of moderate eruptions are enhanced. However, there appears to be little evidence for this in eastern North America, where only two known tephra deposits date from this period – Mt. St Helens J and Glacier Peak (Pyne-O'Donnell *et al*., 2016). New studies sites from this thesis may help to address this hypothesis by adding to the Lateglacial tephrostratigraphic framework of eastern North America, which presently only includes three records.

Pyne-O'Donnell *et al*. (2012) noted an absence of early Holocene cryptotephra deposits prior to the Mazama ash in Nordan's Pond Bog, Newfoundland. The authors hypothesised that this absence of tephra was because of changing atmospheric circulation patterns under the diminishing effects of the Laurentide ice sheet. A similar observation is made by Dean *et al*. (2002), who argue that changes in a series of proxies from Elk Lake *ca.* 8,200 yr BP were driven by a shift from a dominant Arctic airflow to stronger westerlies as the Laurentide ice sheet retreated. At present the number of tephra records in eastern North America covering the Lateglacial and early Holocene is insufficient to address this hypothesis. Research question 2.1 aims to resolve this (see Section 2.3). New study sites combined with community data could test the hypothesised link between changes in atmospheric circulation and the frequency of ash deposition in eastern North America.

2.2.2 Case Study II: The Falkland Islands (Islas Malvinas)

2.2.2.1 Tephra in the Falkland Islands

The Falkland Islands (Islas Malvinas) lie downwind of prolific volcanic centres in Southern Patagonia (Fig. 2.6), approximately 1,000 km to the east of the archipelago. Despite this, little is known about ash deposits in the Islands. Hall *et al*. (2001) (summarised in Holmes *et al*., 2001) report undated shard profiles and limited glass electron probe microanalyses (EPMA) from the only published cryptotephra records in the archipelago: Poncho Hill Pass, Stanley Common and Fox Bay (Fig. 2.6). The authors made no attempt to correlate their data set with volcanic sources in southern South America; however, they were able to exclude Mt. Hudson as a potential source.

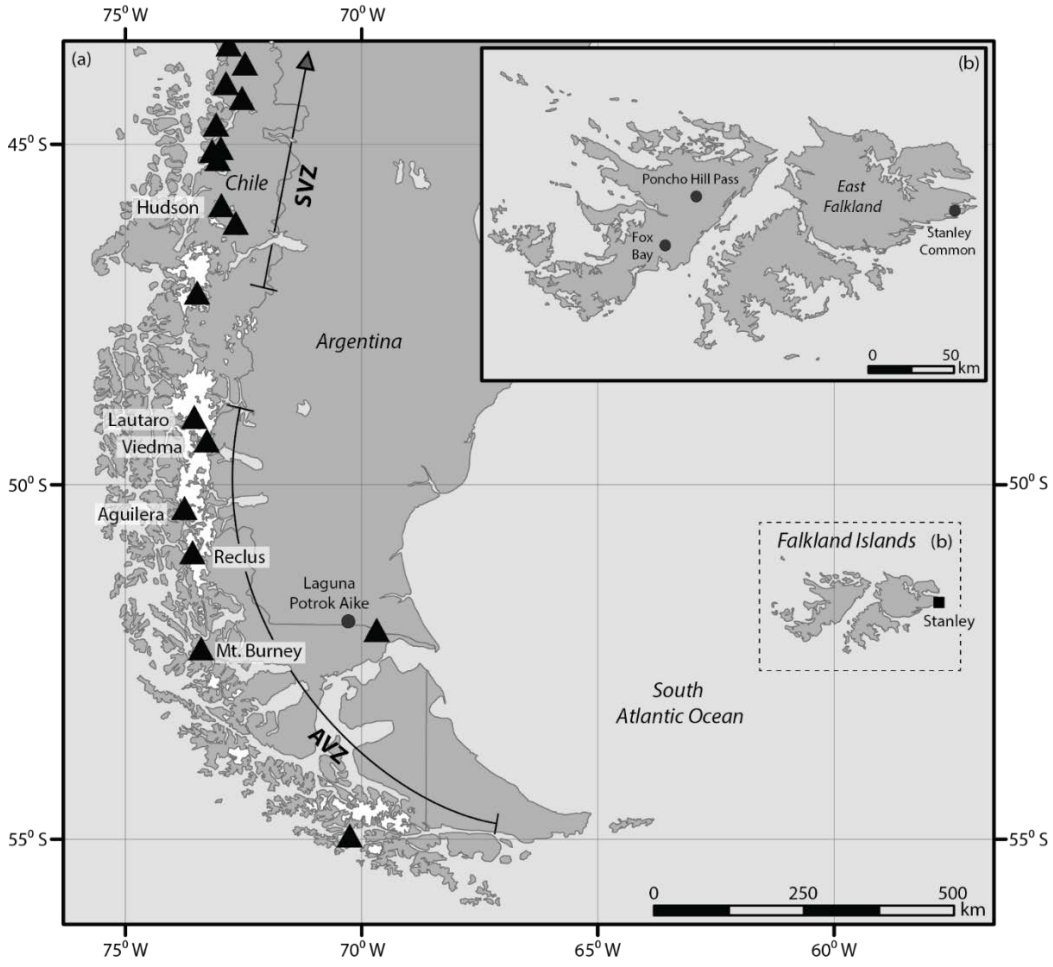

Figure 2.6: The position of sites and volcanoes described in the text. South American volcanoes known to have been active during the Holocene and Late-glacial are shown as black triangles (Smithsonian Global Volcanism programme, 2018). The extents of the Andean Southern Volcanic Zone (SVZ) and the Austral Andean Volcanic Zone (AVZ) are based on those defined by Naranjo and Stern (2004). Volcanoes linked with tephra deposits in Laguna Potrok Aike are labelled (Haberzettl *et al*., 2007, 2008; Wastegård *et al*., 2013; Smith *et al*., 2019).

2.2.2.2 Taphonomic processes affecting tephra in the Falkland Islands

The Falkland Islands cryptotephra records published by Hall *et al*. (2001) include high abundances of volcanic glass throughout the peat profiles, with occasional defined peaks (Fig. 2.7). The authors attribute this diffuse distribution of cryptotephra to vertical reworking, promoted by the fibrous plant material that made up the analysed peat sections (*Cortaderia pilosa*, *Bolax gummifera* and *Eriophorum* spp.). Further evidence for repeated tephra reworking is provided by Wilson *et al*. (2002), who report common 'tephra-like fragments' throughout large sections of a peat sequence near Lake Sulivan, West Falkland. Similar processes have been described in Northern Hemisphere peatlands (Payne *et al*., 2005; Payne and Gehrels, 2010), but rarely in the shard abundances reported by Hall *et al*. (2001) – where shard counts had to be quantified as a percentage of tephra in the inorganic fraction. This extensive reworking could reflect the disturbance of highly abundant primary tephra deposits or continued tephra delivery from the environment:

1) Different mire vegetation may allow for variable movement of tephra shards within a peat profile as the density of pore spaces and depth of root penetration changes with plant type (Payne and Gehrels, 2010; Mackay *et al*., 2016). Today, peatland surfaces in the Falkland Islands are dominated by acid-grass (*Cortaderia pilosa*) and shrub (*Empetrum rubrum*) communities (Payne *et al*., 2019); however, this may not have always been the case during the past. Hall *et al*. (2001) suggest that the fibrous peat forming vegetation in the Falkland Islands promotes a greater degree of post depositional movement of shards relative to *Sphagnum* peat-bogs, and therefore the abundant detrital tephra is derived from vertical reworking of primary tephra deposits.

2) Alternatively, tephra is a key component of dust emissions from southern South America (Gaiero *et al*., 2007). This dust is frequently transported over the Falkland Islands (Liu *et al*., 2010), and Payne *et al*. (2019) report high mineral contents in numerous peatland types in the archipelago which they suggest is derived from local, and regional, aeolian processes. This material may represent the continued deposition of Patagonian dust, including reworked tephra, and could explain the diffuse shard profiles reported by Hall *et al*. (2001).

Both of these hypotheses may be driven by wider environmental controls such as wind speed, aridity or dust abundance, and before investigating patterns of past ash dispersal it is important to understand the source of detrital glass in the Falkland Islands.

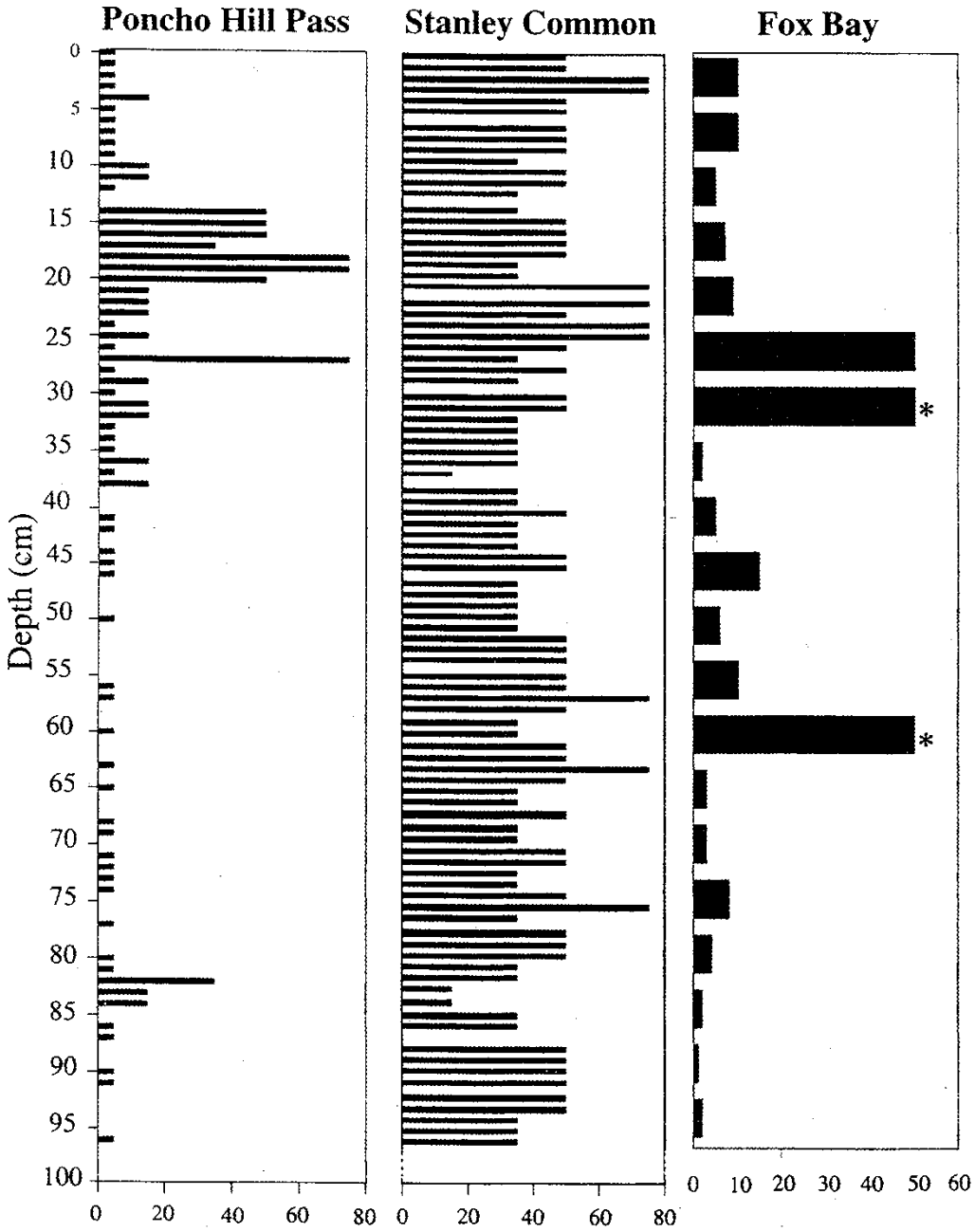

Figure 2.7: Shard profiles from published tephra records in the Falkland Islands (Hall *et al*., 2001). Shard abundance is shown as percentage of tephra in the inorganic fraction.

2.2.2.3 Volcanism affecting the Falkland Islands

Modern eruptions from the Andean Southern Volcanic Zone and the Andean Austral Volcanic Zone have strongly affected the Falkland Islands. For example, ash from the 1991 eruption of Mt. Hudson was deposited across the Islands in sufficient quantities to disrupt air traffic (Guffanti *et al.* 2009), while reworked ash from the same eruption was transported over the archipelago by wind action in the months following the final event (Wilson *et al*., 2011). More recently, ash from the 2011 eruption of Cordón Caulle (VEI 5), Chile, circum-navigated the southern Hemisphere in less than 14 days, causing air traffic disruption in South Africa, Australia and New Zealand (Alloway *et al*., 2015).

During the past the Falkland Islands were almost certainly affected by ash from both the Andean Southern Volcanic Zone and the Andean Austral Volcanic Zone, in southern South America (Fig. 2.6). Ash beds derived from both of these volcanic regions are widespread across southern Patagonia (Stern, 2008; Fontijn *et al*., 2014, 2016) and are identified in Laguna Potrok Aike, Argentina, immediately upwind from the Falkland Islands (Haberzettl *et al*., 2007, 2008; Wastegård *et al*., 2013; Smith *et al*., 2019). The regional extent of these ash deposits is largely unknown due to the scarcity of easily accessible terrestrial sites outside of southern South America. Oppedal *et al*. (2018) correlate a cryptotephra deposit in Diamond Bog, South Georgia, with the late Holocene (*ca.* 2,950 cal yr BP) Alpehue Pumice eruption of Volcan Sollipulli, Chile. This suggests Andean tephra deposits may have ultra-distal distributions, similar to examples in the Northern Hemisphere (Pyne-O'Donnell *et al*., 2012). Further Andean cryptotephra deposits are reported from the Antarctic ice-cores (Kurbatov *et al*., 2006; Narcisi *et al*., 2012). However, Del Carlo *et al*. (2018) question the strength of these correlations, and more work is needed to confidently differentiate between Patagonian and sub-Antarctic/Antarctic (e.g. South Shetlands and South Sandwich Islands) volcanic sources, which is beyond the focus of this thesis.

2.2.2.4 Transport mechanisms affecting the Falkland Islands

The transport of tephra to the Falkland Islands is controlled by the Southern Westerly Wind belt. This circum-polar wind belt is the dominant atmospheric circulation pattern between 50-55 ^{o}S, and strongly influences climate and ocean circulation in the southern mid-latitudes (Garreaud, 2009, 2013). During the Austral winter, the SWW broadens and is displaced slightly northward, whereas in the summer months the SWW contracts and strengthens, with the strongest winds recorded between 49-53°S (Lamy *et al*., 2010). The westerlies result from the pressure gradient between the Pacific/Atlantic High Pressure Cell and the Antarctic Trough, which is sensitive to changes in the southern Polar Front. Therefore, the extent of Antarctic sea-ice can result in latitudinal changes in the SWW (Purich *et al*., 2016). The westerly winds affecting the Falkland Islands are dry because of the orographic effects of the Andes, and precipitation is linked with winds from the southerly and easterly sources (Thomas *et al.*, 2018).

Changes in the position and strength of the SWW affect the dispersal of both primary ash clouds – derived directly from volcanic eruptions, and detrital, reworked tephra which forms a large component of the Patagonian dust reservoir (Gaiero *et al*., 2007). Ash clouds from volcanic eruptions in southern South America can be transported rapidly over large distances within the core of this wind belt (Alloway *et al*., 2015), while detrital glass can follow similar transport paths once remobilised by wind action (Wilson *et al*., 2011). The SWW also dictates precipitation, and consequently soil cohesion, in the Patagonian Steppe, where rainfall is associated with easterly

winds (Garreaud, 2013; Ohlendorf *et al*., 2013). Therefore, it is likely that an enhanced SWW will not only provide a greater capacity for tephra transport, but will promote higher dust emissions from the Patagonian Steppe and greater dispersal of detrital tephra.

Since the 1970s, the SWW has been observed to contract southward and strengthen (Marshall, 2003; Visbeck, 2009); however, over longer timescales the dynamics of the SWW are poorly resolved. Past reconstructions of changes in the strength and position of the SWW rely heavily on records from Patagonia, South America – the only continental landmass that intersects the core of the wind belt (e.g. Mayr *et al*., 2007; Lamy *et al*., 2010; Moreno *et al*., 2012). However, these records are not always consistent, particularly during the early Holocene (Fletcher and Moreno, 2012; Killian and Lamy, 2013), and a range of hypotheses have been presented to explain the past dynamics of the SWW (Table 2.3). These inconsistent, and often contradictory, climate records may represent: differing proxy sensitivity, chronological uncertainty, local disturbances (e.g. earthquakes, landslides or tephra loading) or real spatial and temporal variation.

Table 2.3: Palaeoenvironmental records of SWW dynamics from Patagonia.

Study	Site	Observation	Mechanism
Lamy *et al*. (2010)	Multiple	Strengthening SWW core and weaker Northern margin during the early Holocene.	Changes in the SWW driven by SST.
Mayr *et al*. (2007)	Laguna Potrok Aike	Increased wind speed post 9,200 yr BP.	Reduction in Antarctic sea ice.
Mayr *et al*. (2013)	Laguna Potrok Aike	Increased wind speed between 13,400-11,300 yr BP.	Southward movement of the SWW.
Moreno *et al*. (2012)	Multiple	Stronger SWW between 14,600-12,700 yr BP, Southward displacement of SWW between 12,700-11,000, Weaker SWW 11,000-10,000 yr BP.	None given.
Moreno *et al*. (2018a)	Lago Cipreses	Weak SWW 10,500-7,500 yr BP, Strong SWW 7,500-5,800 yr BP.	ENSO variability and SST.
Oehlerich *et al*. (2015)	Laguna Potrok Aike	Increased wind speed between 13,400-11,300 yr BP and 9200-700 yr BP.	None given.
Unkel *et al*. (2010)	Multiple	Stronger winds between 8,500-4,500 yr BP.	Southward displacement or strengthening of the SWW.
Venneste *et al*. (2015)	Harberton Bog	Increased wind speed between 14,400-11,700 yr BP.	Strengthened SWW during the ACR, a southward displacement during the YD.
Zolitschka *et al*. (2018)	Laguna Azul	Weaker winds between 11,200-10,100 yr BP, stronger winds between 10,100-8,300 yr BP.	Northward movement of the SWW between 10,000-7,500.

The divergence between records of past SWW strength and position is clear even from this limited review. Therefore, comparing tephra profiles from the Falkland Islands with records of wind speed in southern South America may not be consistent. To date, only two reconstructions of wind strength have been developed from the Falkland Islands: Turney *et al*. (2016) and Thomas *et al*. (2018). Both of these records are derived from mid–late Holocene peat in Canopus Hill, East Falkland, and describe long–distance particles (*Nothofagus* pollen and micro charcoal) which may be affected by variables other than wind–speed (e.g. local burning). In order to investigate changes in past ash dispersal patterns over the Falkland Islands an independent multi–proxy record of late glacial and early Holocene wind speed is needed. This knowledge gap is addressed by Research question Q.2.3.

2.3 Research questions

The primary aim of this thesis is to investigate past changes in ash dispersal patterns using distal cryptotephra deposits (See Chapter 1). This aim will be addressed through two main objectives which include research questions raised during the literature review, summarised in this chapter:

Objective 1. New cryptotephra records will be developed from eastern North America and the Falkland Islands, South Atlantic, to close spatial and temporal gaps in the existing tephrostratigraphic frameworks from these regions.

Q.1.1 Can the peat acid digestion protocol (Dugmore *et al*., 1995) be used to extract shards from diverse tephra deposits without causing chemical or physical alteration of the glass?

Objective 2. Changes in temporal frequency and provenance of cryptotephra deposits will be compared with possible drivers of ash deposition (production, transport and deposition) in order to investigate past changes in tephra dispersal patterns.

Q.2.1 Did early Holocene changes in atmospheric circulation enhance ash dispersal over North America?

Q.2.2 Are Lateglacial and early Holocene changes in the strength of the Southern Westerly Wind belt expressed in the abundance of tephra in the Falkland Islands?

Q.2.3 Does the Southern Westerly Wind belt strengthen or weaken over the Falkland Islands during the Lateglacial and early Holocene?

Q.2.4 Do past changes in the local environment or depositional processes coincide with changes in the abundance of reworked tephra in the Falkland Islands?

Chapter 3 Rationale for Papers I-IV

Chapter 3 outlines the rationale and study design for each research Paper (I-IV) developed during this thesis, as well as providing publication details, author contributions and acknowledgement of external funding.

3.1 Paper I

The effects of the peat acid digestion protocol on geochemically and morphologically diverse tephra deposits

A version of paper I is published as:

Monteath, A.J., Teuten, A.E., Hughes, P.D.M., Wastegård, S., 2018. The effects of the peat acid digestion protocol on geochemically and morphologically diverse tephra deposits. Journal of Quaternary Science 34, 269–274.

Paper I addresses research question:

Q.1.1 Can the peat acid digestion protocol (Dugmore *et al*., 1995) be used to extract shards from diverse tephra deposits without causing chemical or physical alteration of the glass?

3.1.1 Summary

The acid digestion protocol is the most efficient method for extracting tephra from peat for electron probe microanalysis (EPMA). However, strong acids are known to alter the chemistry of natural glasses (including tephra) (Blockley *et al*., 2005; Pollard and Heron, 1996), and so this method is often avoided in distal settings (e.g. Mackay *et al*., 2016). Several studies have examined the effects of the peat acid digestion protocol on volcanic glass geochemistry (e.g. Roland *et al*., 2015); however, these investigations have focused on a narrow sample group of rhyolitic tephra deposits which have high chemical durability (see section 2.1.3.3). Therefore, it remains unclear if acid digestion can be used to extract shards with differing geochemical compositions or high surface-area/volume ratios.

Paper I uses duplicate samples from diverse tephra deposits to examine whether the peat acid digestion protocol causes chemical or physical alteration of volcanic glass. Three case study tephra were chosen: the Changbaishan 'Millennium' tephra (B-Tm), the Saksunarvatn ash and the White River Ash eastern lobe (WRAe) – each of which has differing major-minor element glass

compositions and shard morphologies. These tephras cover a range of predicted chemical durabilities, and were separated into different size fractions to further investigate the role of shard morphology in the response of volcanic glass to strong acids. If no chemical or physical alteration of the glass is observed then the peat acid digestion protocol will be used throughout this thesis.

Further experiments (not included in the published manuscript) examined the potential for using cellulase enzymes as a method for extracting tephra from peat. These experiments were unsuccessful. The methodology used is outlined in Appendix A.6.

3.1.2 Author contributions

The study was conceived and designed by Alistair Monteath and Paul Hughes. Alistair Monteath undertook all aspects of laboratory analysis and data interpretation, including: sample extraction, shard morphological descriptions, SEM imagery and EPMA. Calculations of the predicted chemical durability of tephra deposits were under taken by Alistair Monteath and Alex Teuten. Stefan Wastegård provided reference material for the Saksunarvatn ash. The manuscript was written by Alistair Monteath including comments from all of the authors.

3.2 Paper II

Examining temporal patterns in the tephrostratigraphic framework of eastern North America

Paper II is in preparation to be submitted for publication as:

Monteath, A.J., Britta J.L. Jensen, B.J.L., Hughes, P.D.M. Davies, L.J., Mackay, H., Amesbury, M.J., Finkenbinder, M., Edwards, M.E., Booth, R.K. Examining temporal patterns in the tephrostratigraphic framework of eastern North America.

Paper II addresses research question:

Q.2.1 Are early Holocene changes in atmospheric circulation expressed in the regional tephrostratigraphy of eastern North America?

3.2.1 Summary

Tephrostratigraphic frameworks can be used to investigate spatial and temporal patterns in tephra deposits with implications for the dynamics of ash dispersal and volcanic hazards (Lawson *et al*., 2012; Swindles *et al*., 2011). Cryptotephra deposits in eastern North America are hypothesised to be have been influenced by changing atmospheric circulation patterns during the early Holocene (Pyne-O'Donnell *et al*., 2012; see Case Study I). Paper II provides a test of this hypothesis.

3.2.2 Study design and objectives

Paper II closes spatial and temporal gaps in the tephrostratigraphy of eastern North America in order to test whether past, changes atmospheric circulation are expressed in the frequency and/or provenance of cryptotephra deposits in this region.

Shard counts and EPMA analyses (Sid_128 and Sid_540) from Sidney Bog, Maine, were contributed to Jensen *et al*. (in prep) as the research objectives addressed by Paper II are focused on broader patterns of ash dispersal – not individual site tephrostratigraphy. A further five study sites analysed for ash content during this PhD were not included in Paper II as they did not include cryptotephra deposits that were likely to be linked with the Mazama ash (Fig. 3.1). The Mazama ash is dated to 7,680-7,580 cal yr BP (Egan *et al*., 2015), and is one of the most abundant, and common, tephra deposits in eastern North America (Pyne-O'Donnell *et al*., 2012; Jensen *et al*., in prep). The absence of the Mazama ash in these records suggests that they are unlikely to include early

Holocene peat strata prioritised in Paper II. Therefore, these records were not radiocarbon dated or analysed further.

The chronology and number of tephra deposits characterised using EMPA is limited in Paper II. This approach was taken as the primary aim of this study was to investigate the pattern of tephra deposition over a 17,000 year period, and so did not require a high degree of chronological precision to address research question: Q.2.1.

3.2.3 Author contributions

Alistair Monteath, Paul Hughes, Britta Jensen and Mary Edwards conceived and designed the study. Cryptotephra deposits were quantified by Alistair Monteath (Pound Cove Bog, Southwest Pond Bog, Sidney Bog and Nuangola Lake), Lauren Davies (Applemore Lake and Silverman Lake) and Matthew Amesbury (Petite Bog). EPMA was undertaken by Alistair Monteath (Pound Cove Bog, Southwest Pond Bog, Sidney Bog and Nuangola Lake), Britta Jensen (Sidney Bog) and Helen Mackay (Petite Bog). Matthew Finkenbinder and Robert Booth provided sample material and radiocarbon dating from Nuangola Lake and Long Bog, respectively. Alistair Monteath ran all age-depth models and provided radiocarbon dating for Long Pond Bog and Southwest Pond Bog. Alistair Monteath wrote the manuscript with comments from Paul Hughes and Mary Edwards.

3.2.4 Funding

Fieldwork for Paper II was supported by a Royal Geographical Society – Geographical Club Award, and an Explorers Club – Exploration Fund Grant, both awarded to Alistair Monteath. EPMA of cryptotephra deposits described in Paper II was supported by a Geologists Association – New Research Workers Award, and a World Universities Network – Research Mobility Programme Grant, both awarded to Alistair Monteath.

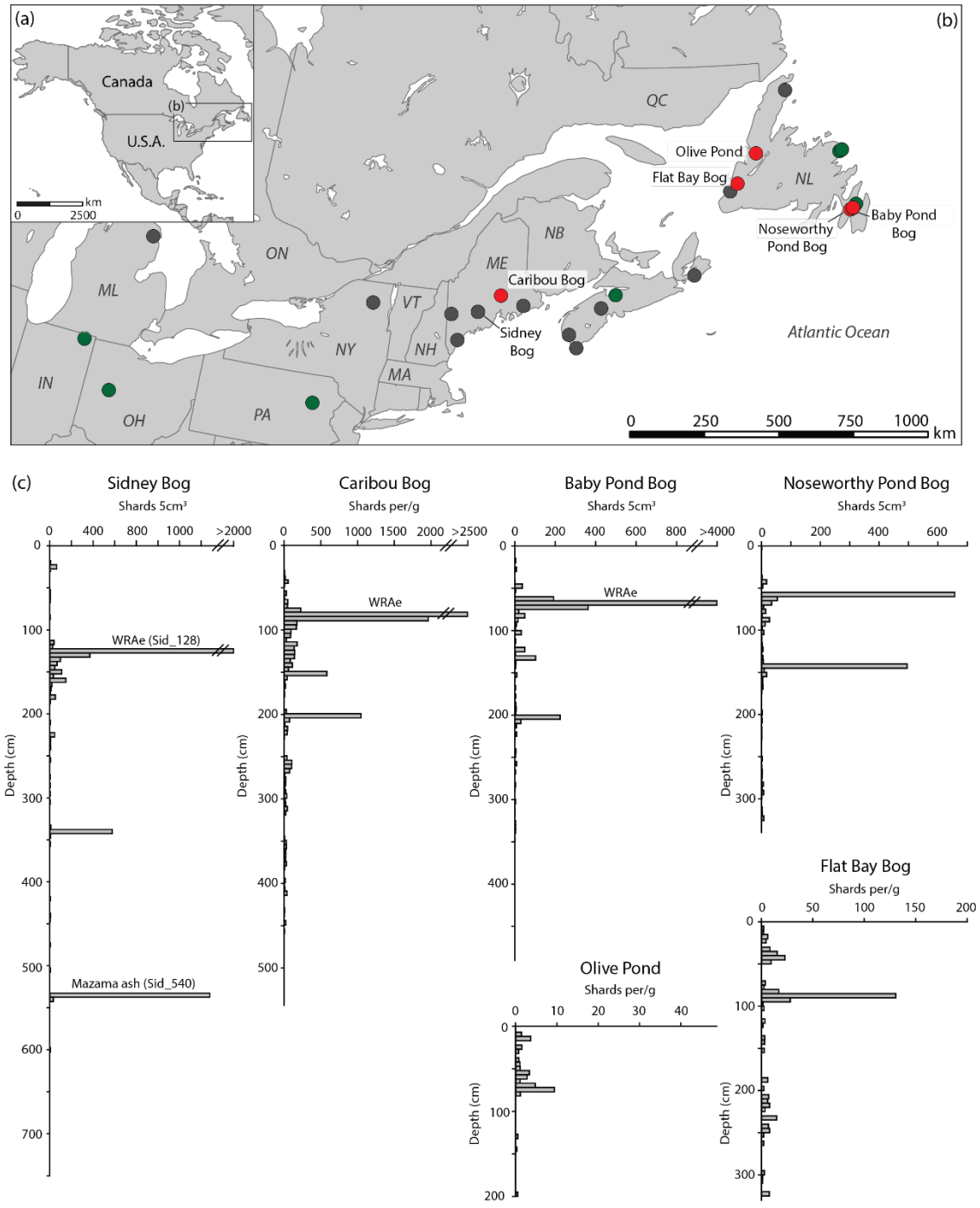

Figure 3.1: (a-b) The positions of cryptotephra records in eastern North America. Published records are indicated by dark grey circles, records presented in Paper II are shown as green circles and records developed during this thesis but not discussed in Paper II are shown as red circles and labelled. (c) Shard profiles from study sites developed during this thesis, but not discussed in Paper II. Sidney Bog is shown here as the record was analysed as part of this thesis; however, the data was contributed to Jensen *el al*. (in prep).

3.3 Paper III

Evidence for distal transport of reworked Andean tephra: Extending the cryptotephra framework from the Austral Volcanic Zone

A version of paper III is published as:

Monteath, A.J., Hughes, P.D.M., Wastegård, S., 2019. Evidence for distal transport of reworked Andean tephra: Extending the cryptotephra framework from the Austral Volcanic Zone. Quaternary Geochronology 51, 64–71.

Paper III addresses research questions:

Q.2.3 Are changes in the strength of the Southern Westerly Wind belt expressed in the abundance of tephra in the Falkland Islands?

Q.2.4 Do past changes in the local environment or depositional processes coincide with changes in the abundance of reworked tephra in the Falkland Islands?

3.3.1 Summary

The tephrostratigraphy of the Falkland Islands is poorly resolved; however, the archipelago has been strongly affected by contemporary ash clouds, and tephra deposits from past eruptions in southern South America are almost certainly present in the islands. Paper III presents the first Lateglacial and early Holocene tephrostratigraphy from the Falkland Islands. These findings are compared with records of wind-strength and environmental change in Chapter 8 (Synthesis and discussion), in order to begin to examine past patterns of tephra dispersal in the South Atlantic.

3.3.2 Study design and objectives

Shard counts were undertaken throughout the 4.65 m peat sequence from Hooker's Point, East Falkland. However, the detailed interpretation and discussion presented in Paper III is restricted to the lower 1.74 m of this record as radiocarbon dating and palaeoecological data is already available for this portion of the sequence (Scaife *et al*., 2019), which spans the lateglacial and early Holocene – time periods during which the Southern Westerly Wind belt (SWW) is likely to have been dynamic (Moreno *et al*., 2012; Vaneste *et al*., 2015).

3.3.3 Author contributions

Alistair Monteath and Paul Hughes conceived the study design. Alistair Monteath undertook all aspects of tephrostratigraphy (cryptotephra quantification, EPMA, Bayesian age-depth modelling) with the exception of radiocarbon dating, which was made available by Scaife *et al*. (2019). Stefan Wastegård provided comparative EPMA data from Laguna Potrok Aike. The manuscript was written by Alistair Monteath with comments from Paul Hughes and Stefan Wastegård.

3.3.4 Funding

EPMA results presented in Chapter III were supported by a World Universities Network – Research Mobility Programme Grant, awarded to Alistair Monteath. This grant was used to visit the University of Alberta cryptotephra laboratory, run by Prof Britta Jensen.

3.4 Paper IV

A Lateglacial and early Holocene record of dynamic Southern Westerly Winds from the Falkland Islands, South Atlantic

Paper IV is in preparation to be submitted for publication as:

Monteath, A.J., Hughes, P.D.M., Cooper, M.J., A Lateglacial-early Holocene record of dynamic Southern Westerly Winds from the Falkland Islands.

Paper III addresses research questions:

Q.2.2 Does the Southern Westerly Wind belt strengthen or weaken over the Falkland Islands during the Lateglacial and early Holocene?

Q.2.3 Are changes in the strength of the Southern Westerly Wind belt expressed in the abundance of tephra in the Falkland Islands?

3.4.1 Summary

Records of past wind strength from southern South America provide a complex and, often contradictory record, of past changes in the Southern Westerly Wind belt (Kilian and Lamy, 2013). These complexities are likely to be because of the extreme climate gradients and local disturbances (e.g. tephra loading, earthquakes, fire, etc.) which affect this region. Islands in the South Atlantic potentially provide a simpler environmental setting that can be used to develop a more regional climate signal. Paper IV presents a record of dynamic wind-strength during the Lateglacial and early Holocene, from the Falkland Islands.

3.4.2 Study design and objectives

Paper IV presents a record of past wind strength, from Hooker's Point, East Falkland. Analyses include particle size analysis, X-ray Fluorescence (XRF) core scanning and Inductively Coupled Plasma Mass Spectrometry (ICPMS) throughout the Lateglacial and early Holocene core section describe in Paper III. This study provides comparative climatic data which will be used alongside published palaeoecological data (Scaife *et al*., 2019; Appendix E), and the findings of Paper III to examine tephra dispersal in the South Atlantic (see Section 8.1.3).

3.4.3 Author contributions

Alistair Monteath and Paul Hughes conceived and designed the study. Alistair Monteath undertook particle size analysis and XRF core scanning (XRF run with technician assistance). ICPMS was conducted at the National Oceanographic Centre Southampton by Alistair Monteath and Matthew Cooper. The manuscript was written by Alistair Monteath with comments from Paul Hughes and Matthew Cooper.

3.5 Other relevant contributions

Other peer-reviewed publications and conference papers that have included data generated during this PhD are listed here.

3.5.1 Peer-reviewed publications

Scaife, R.G., Long, A.J., **Monteath, A.J.,** Hughes, P.D.M., Bentley, M., Stone, P. 2019. The Falkland Islands palaeoecological response to millennial scale climate perturbations during the Pleistocene-Holocene transition: implications for future vegetation stability in Southern Ocean islands. Journal of Quaternary Science, DOI: 10.1002/jqs.3150.

3.5.2 Conference publications

Jensen, B.J.L., Davies, L., Nolan, C., **Monteath, A.J.,** Plunkett, G., Booth, R., Ponomareva, V., Portnyagin, M., Cook, E., Pyne-O'Donnell, S., Hughes, P.D.M. 2019. A late Pleistocene to Holocene cryptotephra framework from northeastern North America: connecting the Pacific to the sub-tropics and north Atlantic. Volcanic Impacts on Climate and Society (VICS), 2019 annual meeting, Cambridge.

Mackay, H., Plunkett, G., Jensen, B.J.L., Amesbury, M., Blundell, A., Booth, R., Corona, C., Hughes, P.D.M., Ludlow, F., **Monteath, A.J.,** Newfield, T., Toohey, T., Sigl, M., Stoffel, M., Swindles, G. 2019. The AD 853 Mount Churchill eruption: examining the potential climatic and societal impacts and the timing of the Medieval Climate Anomaly in the North Atlantic region. Volcanic Impacts on Climate and Society (VICS), 2019 annual meeting, Cambridge.

Monteath, A.J., Hughes, P.D.M., Scaife, R. 2018. Lateglacial – early Holocene cryptotephra from the Falkland Islands (Malvinas). INTAV International field conference on Tephrochronology, 2018.

Jensen, B., Nolan, C., Davies, L., **Monteath, A.J.,** Booth, R., Plunkett, G., Pyne O'Donnell, S., Hughes, P.D.M. 2018. A late Pleistocene to Holocene cryptotephra framework for palaeoenvironmental records from the Midwest to east coast of North America. INTAV International field conference on Tephrochronology, 2018.

Monteath, A.J., Hughes, P.D.M., Mackay, H., Amesbury, M, J., Mallon, G., Finkenbinder, M.S. 2017. Spatial and temporal delivery of tephra to the eastern North American seaboard. Abstract V12C-07 Fall Meeting, AGU, New Orleans.

Chapter 4 Paper I

The effects of the peat acid digestion protocol on geochemically and morphologically diverse tephra deposits

4.1 Abstract

Tephra shards for electron probe microanalysis are most efficiently extracted from peat using acid digestion, which removes organic material that hinders density separation methods. However, strong acids are known to alter glass chemical compositions, and several studies have examined how acid digestion affects rhyolitic volcanic glass. The focus on rhyolitic tephra in these studies leaves considerable uncertainty, as the dissolution rates of natural glasses (including tephra) are determined by the chemical composition and surface area to volume ratio, both of which vary in tephra deposits. Here, we use duplicate samples of basaltic, trachydacitic and rhyolitic tephra to examine physical and geochemical alteration following acid digestion. Scanning electron microscope imagery reveals no discernible degradation of glass surfaces, and electron probe microanalysis results from duplicate samples are statistically indistinguishable. These findings suggest the acid digestion protocol for organic peats does not significantly alter glass geochemistry regardless of shard morphologies or geochemical compositions.

4.2 Introduction

Peatlands provide excellent settings for the application of tephrochronology, a powerful chronological tool which uses volcanic ash beds (tephras) and cryptotephra deposits (non-visible volcanic ash) as stratigraphic markers to link sediment sequences (Lowe *et al.,* 2011). This approach relies heavily on the high-precision geochemical characterisation of volcanic glass, in order to 'fingerprint' tephras by ratios of elements (Lowe *et al.,* 2017). The compositional differences between tephra deposits may be subtle (e.g. Kuehn *et al.,* 2009; Preece *et al.,* 2014), and therefore it is essential that the geochemical composition of glass shards remain unaltered during laboratory extraction processes for these analyses.

The geochemical composition of volcanic glass is typically measured using electron probe microanalysis (EPMA) or laser ablation inductively coupled plasma-mass spectrometry (LA-ICP-MS). Tephra shards for theses analyses are extracted from peat and lake sediments using density separation (Turney*,* 1998) or acid digestion (Persson, 1966; Dugmore *et al.,* 1995), as high temperatures (>350 °C) risk altering the geochemical composition of the glass (Pilcher and Hall,

1992; van den Bogaard & Schmincke, 2002). Acid digestion provides an efficient means of extracting glass shards from organic peat, and it has been widely used in the development of regional tephrostratigraphies (Pilcher *et al*., 1995; Plunkett *et al*., 2004). However, this method uses strong acids (sulphuric and nitric) which have the potential to cause ionic exchange of cations, and the formation of a leached Si gel at the glass surface (Pollard and Heron, 1996). Density separation does not risk geochemical alteration of the glass, but commonly achieves lower shard recovery rates from peat, as shards can become trapped within the macrofossil-rich solution during floatation or lost during repeated decanting steps. This problem is particularly acute in distal settings where cryptotephra deposits may be formed of a few tens of shards, often with highly vesicular, buoyant, morphologies (e.g. Pyne-O'Donnell *et al.,* 2012; Mackay *et al.,* 2016).

The protocol for the extraction of tephra from peat (Dugmore *et al*., 1995) should not require the prolonged exposure (>3 hrs) of samples to acid, and importantly does not include the use of strong alkalis which cause network dissolution in glasses (Blockley *et al.,* 2005). Therefore, there may be a lower risk of geochemical alteration during this extraction than exists for the acid digestion of minerogenic lake sediments. The effects of the peat acid digestion protocol on the geochemical composition of volcanic glass have been examined before (e.g. Dugmore *et al.,* 1992; Roland *et al.,* 2015; Watson *et al.,* 2016). However, these studies have almost exclusively focused on Icelandic rhyolitic tephras. This restricted sample group leaves considerable uncertainty, since the dissolution rates of natural glasses (including tephra) are determined by the chemical composition of the glass, and may be modified by surface area (Paul, 1977; Jantzen and Plodinec, 1984; Jantzen, 1992; Techer *et al.,* 2001; Wolff-Boenisch *et al.,* 2004; Conradt, 2008). In particular, SiO_2 and Al_2O_3 content determine the chemical durability of glasses, and therefore their resistance to acid solutions. The rhyolitic tephras that have previously been used to test the effects of the acid digestion protocol include high SiO_2 values (>69%), and so have a high predicted chemical durability. However, tephrostratigraphies may include tephra (and cryptotephra) deposits from a range of volcanic sources (Mackay *et al*., 2016; Plunkett and Pilcher, 2018) with differing geochemical compositions and shard morphologies (Newton *et al.,* 2007; Bronk Ramsey *et al.,* 2014). These diverse tephra deposits are likely to have variable resistance to the acid solutions used in the acid digestion protocol. Therefore, further tests are needed to ensure the acid digestion protocol does not affect the glass geochemical composition of tephra deposits composed of shards with low chemical durability and/or high surface-volume ratios.

Here, we use electron probe microanalysis (EPMA) and scanning electron microscope (SEM) imagery to test for geochemical and physical alteration in duplicate tephra samples following acid digestion extraction. We use control and test samples from three widespread tephra isochrons with contrasting glass geochemical compositions, shard sizes and morphologies: the (1) White River Ash

eastern lobe (WRAe), the Changbaishan (Baitoushan) 'Millennium' tephra (B-Tm), and the Saksunarvatn ash (Fig 4.1.). Together these case study tephra deposits provide new tests of the effects of acid digestion on tephras with low chemical durability and/or high surface-volume ratios.

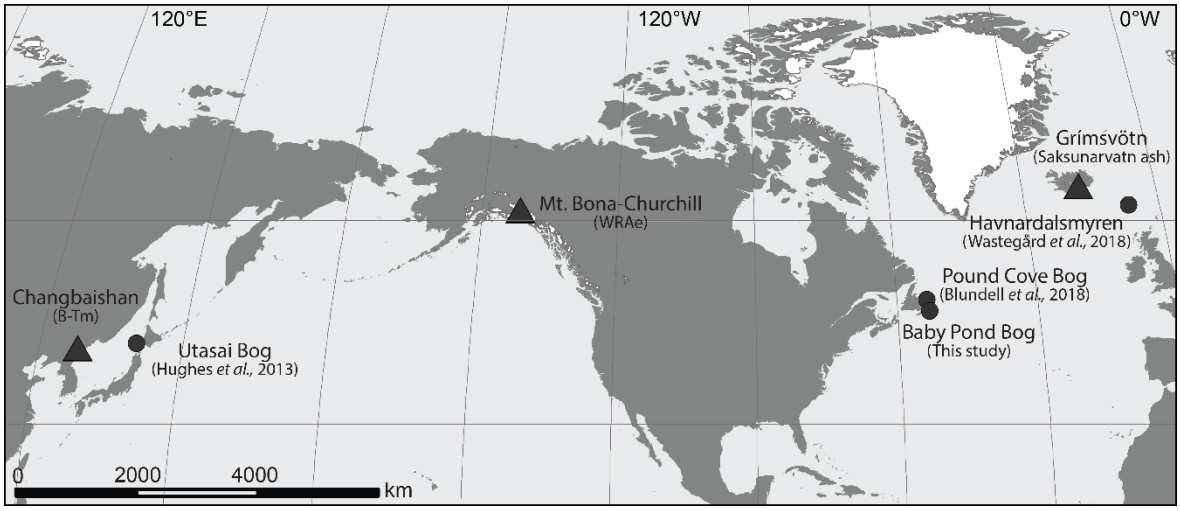

Figure 4.1 Study site(s) (circles) and source volcano (triangles) for each case study tephra (B-Tm tephra from Utasai Bog; WRAe from Pound Cove Bog and Baby Pond Bog; Saksunarvatn ash from Havnardalsmyren Lake.

4.3 Methods

4.3.1 Predicted chemical durability and morphological descriptions

The theoretical chemical durability of each case study tephra was quantified using the empirical approaches applied by Pollard *et al.* (2003) (Fig. 4.2). These include calculations of the (Si:O) ratio (Pollard and Heron, 1996) and number of non-bridging oxygen atoms (NBO) per silicon tetrahedral (White and Minser, 1984) for each tephra deposit. Complete equations are shown in Appendix A.3.

Shard morphological descriptions were based on long axis measurements, which were taken from 100 glass shards for each sample. These samples were extracted from the host material using ashing (Pilcher and Hall, 1992) and sieving (at 15 µm), as they were not analysed for their geochemical composition.

4.3.2 Tephra extraction procedures

Acid digestion (Dugmore *et al*., 1995): samples were placed in 50 mL of concentrated (98 %) H_2SO_4, thoroughly mixed, and left to settle for 30 minutes. Three mL of concentrated HNO_3 was then added to the solution, which was left for 15 minutes while the reaction subsided. This process was repeated twice more, until no further reaction took place. The samples were then boiled until the

solution turned a translucent pale yellow colour, which was diluted with 100 mL of distilled water and left for one hour. Finally, samples were decanted into 1500 mL of distilled water to remove excess acid, and sieved at 15 µm. To assess the effects of acid digestion on differing shard sizes, samples from the B-Tm tephra and Saksunarvatn Ash were sieved at 15 µm and 63 µm following acid digestion. These large (> 63 µm) and small (15-63 µm) fractions were mounted separately for electron probe microanalysis.

Density separation (Eden *et al.,* 1996; Turney*,* 1998; Blockley *et al.,* 2005): samples were subjected to stepped floatation using sodium polytungstate ($Na_6(H_2W_{12}O_{40}).H_2O$) at 2.0 g/cm^3 and 2.5 g/cm^3. In order to separate the glass shards from organic matter the 2.0 g/cm^{-3} float was retained in the test tube and carefully stirred between additional centrifuge runs (e.g. Blockley *et al.,* 2015; Roland *et al*., 2015). This process was repeated five times to maximise shard recovery.

4.3.3 Electron probe microanalysis

Glass shards were analysed by electron probe microanalysis (EPMA), with wavelength dispersive spectrometry, on a Cameca SX100 electron probe micro-analyser at the Tephra Analytical Unit, University of Edinburgh. Shards were mounted in epoxy resin stubs and polished to expose the internal glass surface, before carbon coating (Hall and Hayward, 2014). A suite of 11 elements (Si, Ti, Al, Fe, Mn, Mg, Ca, Na, K, P, Cl) were measured using 3 µm and 5 µm beam diameters, with a 10 KeV accelerating voltage, and 5 nA current (Hayward, 2012). Three secondary standards of known composition were run alongside case study samples to check for instrumental drift: i) Lipari rhyolitic obsidian, ii) Old Crow tephra and iii) BHVO-2g basalt (Kuehn *et al.,* 2011). Results are presented as normalised weight percent (wt %) oxides for geochemical composition bi-plots. Raw major-minor oxide data and associated standard measurements are reported in Appendix A.1 and A.2.

4.3.4 Case study tephra deposits: morphologies and chemical durability

Three Holocene tephra deposits with differing predicted chemical durability (Fig. 4.2), and shard morphologies (Table 4.1) were selected as case studies to test the effects of acid digestion on volcanic glass geochemistry: the Changbaishan 'Millennium' tephra (B-Tm), from Utasi Bog, Japan (42°38'00.32"N, 140°18'26.79"E; Hughes *et al*., 2013), the Saksunarvatn ash from Havnardalsmyren, Faroe Islands (62°00'57.5"N, 6°51'17.0"W; Wastegård *et al.,* 2018), and the White River Ash eastern lobe (WRAe), from Pound Cove Bog (53°35'44"W, 49°9'59"N; Blundell *et al*., 2018) and Baby Pond Bog (47°25'16.1"N, 53°32'47.2"W; this study), Newfoundland. These case studies are representative of the range of tephra deposits commonly used to construct peatland

tephrostratigraphies (Lawson *et al*., 2012), and include both visible tephra beds and ultra-distal cryptotephra.

Table 4.1: Details of each case study tephra including shard population statistics. Descriptions include: dominant shard morphology (shard type), minimum (Min), maximum (Max) and mean ($\bar{x}$) long axis length (µm), as well as standard deviation (σ).

Tephra	B-Tm	WRAe	Saksunarvatn Ash
Source volcano	Changbaishan	Mt Bona-Churchill	Grímsvötn
Age (b2k)	1055±4	1147±1	10,347±45
Reference(s)	Sun *et al.* (2014)	Coulter *et al.* (2012) Jensen *et al.* (2014)	Rasmussen *et al.* (2006)
Geochemical composition	Rhyolitic-Trachydacite	Rhyolitic	Basaltic
$\bar{x}$	77	42	75
σ	31	15	41
Max	183	93	238
Min	28	15	25
Shard type	Cuspate/platy	Vesicular/ foamy	Blocky/ cuspate

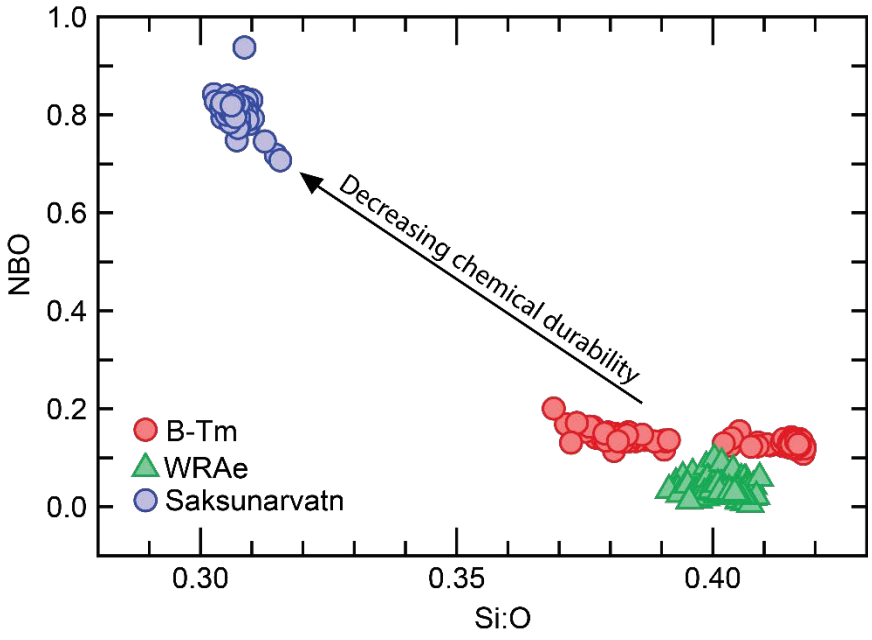

Figure 4.2 Plot of NBO and Si:O values from the case study tephra deposits. The arrow shows the direction of decreasing chemical durability. Glass major-minor element (wt%) data used to generate Figure 4.2 includes: (B-Tm) this study; Hughes *et al*. (2013); McLean *et al*. (2016); (WRAe), Pyne-O'Donnell *et al*., 2012; Jensen *et al*., 2014; Davies *et al*., 2016; (Saksunarvatn ash) This study; Wastegård *et al*. (2018).

4.4 Results and Discussion

4.4.1 Geochemical outliers

Analyses with analytical totals of <94% were removed from data sets (B-Tm acid >63 µm, n=1; WRAe acid, n=5; WRAe float, n=2) used for bivariate plots and principle component analysis (PCA), although the majority of these became consistent with remaining data set after normalisation (Appendix A.1). While analyses with analytical totals as low 90% may be acceptable in some tephra deposits (Pearce *et al*., 2008), we use 94% as a cut-off point as it represents an approximate 5% departure from the average analytical totals of the case study tephra deposits (97.5-99%). The majority of these analyses are from WRAe samples, and are likely due to the small shard sizes ($\bar{x}$ 42 µm) and highly vesicular shard morphologies. Seven outlier analyses were also removed from the *B-Tm float* population because of extremes in the glass major-minor element compositions, which are likely due to partial analysis of mineral inclusions during EPMA. Outlying data points are present in all data sets; however, with the exception of *B-Tm float*, the number of these outliers is consistent between duplicate samples, and there are no observable differences in analytical totals (Appendix A.1).

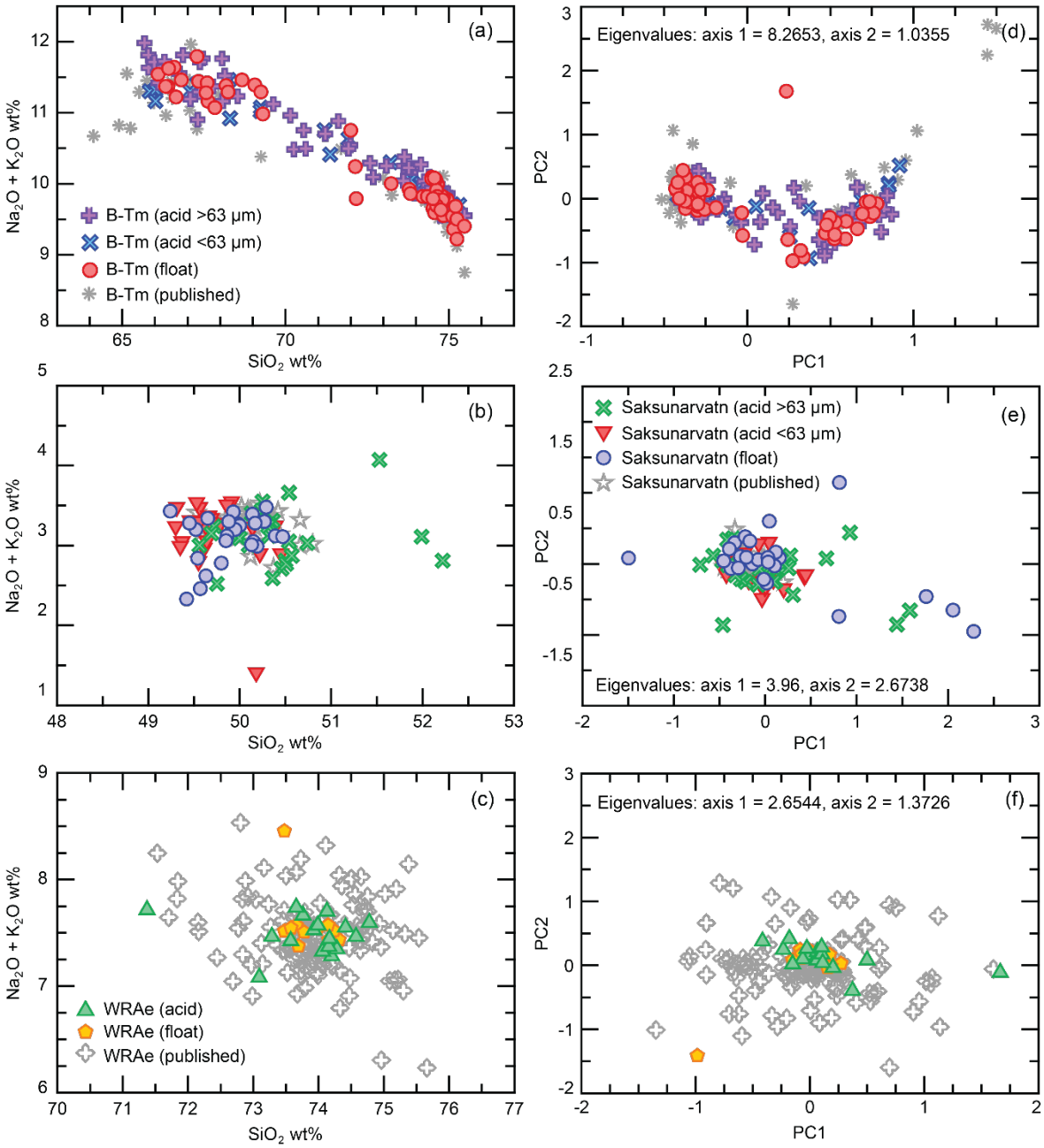

Figure 4.3 : (a,b,c) Bivariate plots of selected major oxide totals (wt%) from case study tephras and comparative published values (B-Tm, Hughes *et al*., 2013; McLean *et al*., 2016, Saksunarvatn ash, Wastegård *et al*., 2018, WRAe, Pyne-O'Donnell *et al*., 2012; Jensen *et al*., 2014; Davies *et al*., 2016). (d,e,f) Scores for principal components analysis.

4.4.2 Data interpretation

Bivariate plots of major-minor element glass compositions show no observable difference between duplicate samples extracted using either acid digestion or density separation (Fig. 4.3a,b,c; Fig. A1). To test for any statistical differences between these samples the datasets were compared using principle component analysis (PCA) (Fig. 4.2d,e,f) and similarity coefficients (SC; Borchardt *et al.,* 1972) (Appendix A.5). The use of multi-variate statistics have been advocated (in addition to

bivariate plots) as a means of discriminating between tephra deposits (Gonzalez *et al*., 1999; Pollard *et al.,* 2006; Pouget *et al*., 2014), and can be rapidly run using freely available software (e.g. VEGAN, Oksanen *et al.,* 2013; as used here). The results from these analyses show there is no statistical difference between duplicate datasets, and outliers identified using bivariate plots are also identified as outliers by PCA (Fig. 4.3). These results suggest that the acids used during the digestion protocol are not sufficiently aggressive to alter the geochemical composition of glass shards to a degree that is recordable during EPMA.

During the early stages of glass dissolution the outer surface of the glass is degraded (Jantzen *et al.,* 2010) and gel layer formation, re-crystallisation of leached material and pitting corrosion can be observed on the glass surface (e.g. Blockley *et al.,* 2005). Visual inspection of tephra shards from this study using a high-power microscope, and SEM imagery revealed no discernible damage to outer surfaces of the volcanic glass extracted using either acid digestion or density separation (e.g. Fig. 4.4). Absence of these features in any of the case study samples suggests the extraction methods used here were unable to cause degradation of the glass surfaces.

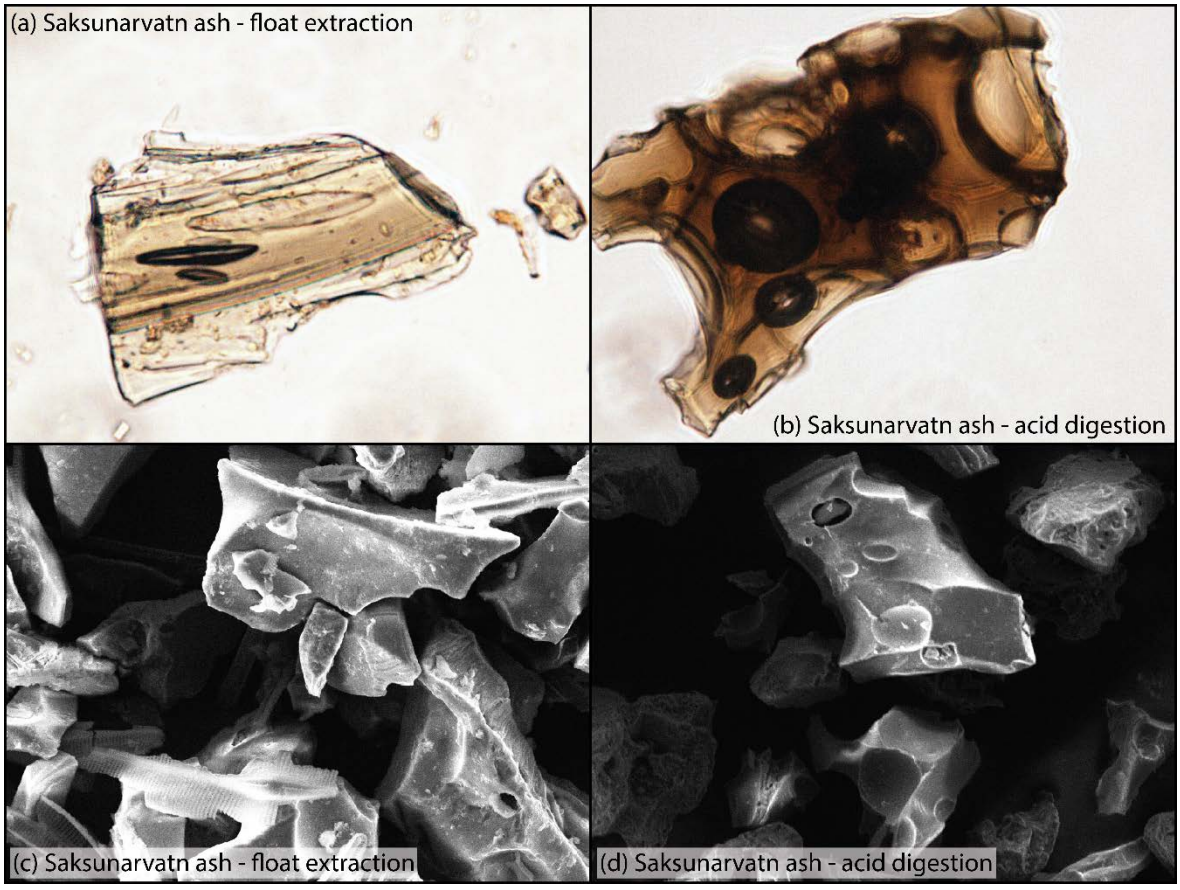

Figure 4.4: Microscope imagery and SEM images from duplicate samples of the Saksunarvatn ash.

4.5 Conclusions

This study found duplicate samples of tephra deposits, with differing predicted chemical durability and shard morphologies, were geochemically indistinguishable following either acid digestion or density separation shard extraction methods. Furthermore, visual inspection of the glass surface revealed no evidence of glass degradation. These findings suggest that the acid solutions used during the extraction of tephra from peat are not sufficiently aggressive to significantly alter glass major-minor element geochemistry to a degree that is recordable during EPMA. Therefore, acid digestion can be safely applied in distal settings where cryptotephra deposits are composed of small highly-vesicular glass shards, or in regions where tephra deposits include low silica geochemical compositions.

4.6 Acknowledgments

We would like to thank Dr Chris Hayward and Mr Mike Hall at the Tephrochronology Analytical Unit, University of Edinburgh, for their help and advice with electron probe microanalysis and stub preparation. Dr Rhys Timms kindly supplied materials for tephra separation, and Dr Sandra Nogue and Prof Mary Edwards provided helpful feedback on an earlier draft of the manuscript. Miss Roseanna Mayfield provided field assistance during the coring of Baby Pond Bog. The helpful comments of Dr Tom Roland and an anonymous reviewer improved both clarity and focus of this manuscript.

Chapter 5 Paper II

Examining temporal patterns in the tephrostratigraphic framework of eastern North America

5.1 Abstract

Tephrostratigraphic frameworks can be used to provide a long view of tephra dispersal with implications for understanding the dynamics of ash clouds and volcanic hazards. To date, studies of wider patterns in continental tephra records have been confined to Europe; however, the rapid global expansion of tephrochronology means there is now potential to use this approach in new areas. The number of cryptotephra (non-visible ash deposits) records from eastern North America is unique in the continent, and provides an opportunity to investigate the controls of ultra-distal ash dispersal and deposition. Here, we present the results of eight new cryptotephra records, alongside previous findings, in order to examine temporal patterns in the eastern North American tephrostratigraphy between 17,000 cal yr BP and the present day. An increase in the frequency of cryptotephra deposits is observed after *ca.* 7,600 cal yr BP, beginning with the deposition of the Mazama ash. This change in the frequency of tephra deposition is discussed in relation to volcanic and environmental controls of fine ash dispersal, and hypotheses regarding the mechanisms of tephra delivery to eastern North America. We reject hypotheses relating to eruption frequency or taphonomic processes in favour of dynamic atmospheric controls of regional tephra dispersal - possibly caused by the retreat of the Laurentide Ice Sheet and associated changes in atmospheric circulation.

5.2 Introduction

The study of cryptotephra deposits (non-visible ash deposits) has become a valuable chronological tool in Quaternary Science (Lowe, 2011; Davies, 2015), and detailed tephrostratigraphic frameworks have been developed from diverse regions around the world (Lowe *et al*., 2008; Fontjin *et al*., 2014; Timms *et al*., 2019). These frameworks combine tephra records from multiple study sites and provide a regional tephrostratigraphy (the sequence of tephra deposits: Thorarinsson, 1981; Lowe and Hunt, 2001), which may be used to refine chronology in palaeoenvironmental, or archaeological, sequences. Recent studies have used these datasets to investigate spatial and temporal patterns in tephra deposition, in order to better understand (and predict) ash dispersal and volcanic hazards (Wastegård and Davies, 2009; Swindles *et al*., 2011, 2018; Lawson *et al*., 2012;

Sulpizio *et al*., 2014; Watson *et al*., 2017b; Plunkett and Pilcher, 2018). To date, such studies have been confined to Europe, a region with a long history of cryptotephra research and a high density of study sites (Persson, 1971; Dugmore, 1989; Pilcher *et al*., 1995; Plunkett *et al*., 2004); however, there is clearly potential to use this approach in other regions frequently affected by tephra deposition.

Pyne-O'Donnell *et al*. (2012) reported numerous ultra-distal cryptotephra deposits from Nordan's Pond Bog, Newfoundland (Fig. 5.1). These ash deposits were correlated with volcanic eruptions in Alaska and the Cascades, up to 7000 km from Newfoundland, and began a renewed interest in ultra-distal cryptotephra deposits. Since the publication of this first record a series of studies have closely examined the lakes and peat-bogs of eastern North America for the presence of volcanic ash (Jensen *et al*., 2014; in prep; Pyne-O'Donnell *et al*., 2016; Mackay *et al*., 2016; Spano *et al*., 2017; Hughes *et al*., in prep). These studies have identified numerous ultra-distal cryptotephra deposits sourced from volcanoes in the Pacific northwest and central America, many of which have also been found in the Greenland ice-cores (Zdanowicz *et al*., 1999; Pearce *et al*., 2004) and into Europe (Jensen *et al*., 2014; Watson *et al*., 2017a; Plunkett and Pilcher, 2018; Timms *et al*., 2019). The number of cryptotephra records developed from eastern North America is unique in the continent, and provides the first opportunity to explore wider patterns in distal cryptotephra deposits outside of Europe.

Here, we present the results from eight new cryptotephra records (Fig. 5.1), alongside the findings of previous studies, in order to examine temporal patterns in the occurrence of cryptotephra deposits in eastern North America between 17,000 cal yr BP and the present day. These patterns are discussed in relation to wider volcanic and environmental controls of tephra deposition, which raise hypotheses regarding the production, transport and preservation of fine ash in eastern North America.

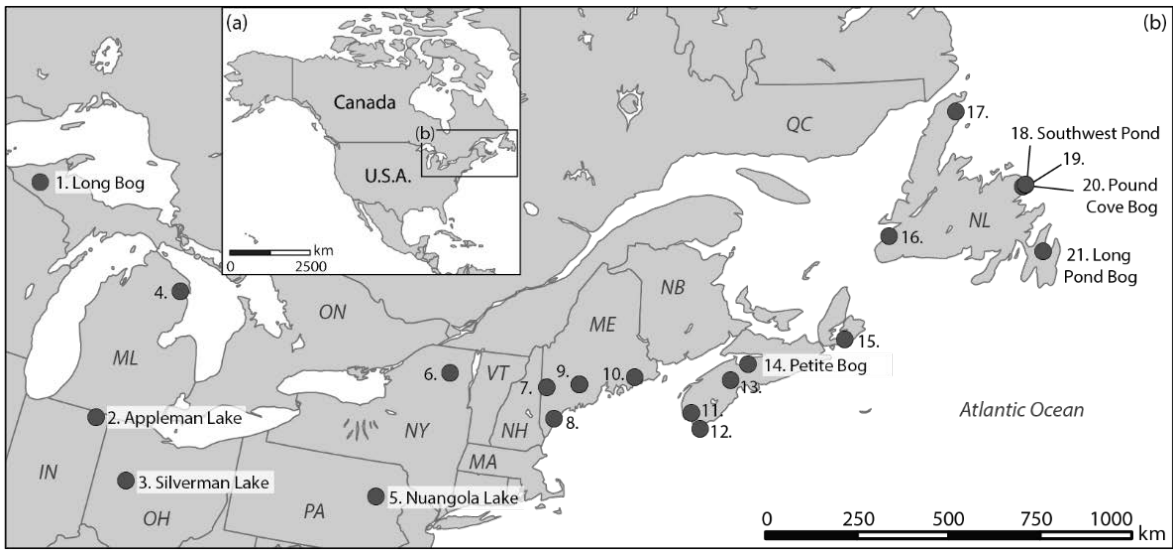

Figure 5.1: The location of study sites from this investigation shown in relation to published cryptotephra records in eastern North America. Sites are numbered east to west and include records from this study (labelled) as well as 4. Irwin Smith Bog, 6. Bloomingdale Bog, 7. Crocker Pond, 8. Saco Heath, 9. Sidney Bog, 10. Great Heath Bog, 11. Thin-ice Pond, 12. Villagedale Bog, 13. Veinot Lake, 15. Framboise Bog, 16. Jeffrey's Bog, 17. Burnt Village Bog and 18. Nordan's Pond Bog. State/province abbreviations include: Newfoundland and Labrador (NL), Ontario (ON), Quebec (QC), Indian (IN), Massachusetts (MA), Maine (ME), New Brunswick (NB), New Hampshire (NH), Ohio (OH), Pennsylvania (PA) and Vermont (VT).

5.3 Study sites and methods

5.3.1 Tephrostratigraphy

To close spatial and temporal gaps in the existing tephrostratigraphy of eastern North America (Pyne-O'Donnell *et al*., 2012, 2016; Jensen *et al*., 2014, in prep; Mackay *et al*., 2016; Hughes *et al*., in prep) eight new study sites from this region were examined for presence of cryptotephra deposits (Fig. 5.1): Long Pond Bog (47°29'50.10"N, 53°16'9.42"W), Pound Cove Bog (49°10'10.3"N, 53°35'35.3"W), Southwest Pond Bog (49°7'43.60"N, 53°43'18.30"W), Petite Bog (45°08'31.4"N 63°56'02.7"W), Nuangola Lake (41°09'32.7"N, 75°58'26.0"W), Appleman Lake (41°37'25.3"N, 85°12'49.0"W), Silverman Lake (40°21'15.0"N, 83°48'45.0"W) and Long Bog (46°00'04.1"N 89°43'02.7"W). In order to identify cryptotephra deposits in peat sequences; continuous samples spanning five cm were taken throughout the cores and processed using ashing methodology (Pilcher and Hall, 1992), followed by emersion in 10 % Hydrochloric acid (HCL) and sieving at either 15 µm or 25 µm. More minerogenic material from basal peat sections and lake sediments was

subjected to additional sieving at 80 µm and heavy liquid floatation, to extract glass shards from the host material (Turney *et al*., 1998). Where higher concentrations of tephra shards were identified samples were processed in the same manner at one or two centimeter intervals to refine the stratigraphic position of any cryptotephra deposits.

Glass shards from cryptotephra deposits were extracted for EPMA using heavy liquid floatation with lake sediments and acid digestion for peat samples (Dugmore *et al*., 1995). Some previous studies of ultra-distal tephrostratigraphy have avoided using acid digestion because of fears that the small, highly vesicular, shards could be susceptible to geochemical alteration during exposure to acid (Pyne-O'Donnell *et al*., 2012; Mackay *et al*., 2016). However, recent comparative studies have reported consistent EPMA results between shards extracted using acid digestion and control samples (Roland *et al*., 2015; see Paper I). Therefore, acid digestion was applied to peat samples during this study in order to maximise shard recovery rates for EPMA. Glass shards from all extractions were mounted in epoxy resin stubs and polished to expose the internal glass surfaces before carbon coating (Kuehn and Froese, 2010; Hall and Hayward, 2014).

Glass shards were analysed by electron probe microanalysis (EPMA), with wavelength dispersive spectrometry, on either a JEOL 8900 superprobe at the University of Alberta, or a Cameca SX100 electron probe micro-analyser at the Tephra Analytical Unit, University of Edinburgh. A suite of 11 elements (Si, Ti, Al, Fe, Mn, Mg, Ca, Na, K, P, Cl) were measured using a 5 µm beam diameter. Analyses were undertaken at the University of Alberta using a 15 keV accelerating voltage, and 6 nA beam current (Jensen *et al*., 2008), while a 10 KeV accelerating voltage, and 5 nA current was used at the University of Edinburgh (Hayward, 2012). Three secondary standards of known composition were run alongside eastern North American samples to check for instrumental drift: i) Lipari rhyolitic obsidian, ii) Old Crow tephra and iii) BHVO-2g basalt (Kuehn *et al.,* 2011). The major-minor element composition of glass shards are presented as normalised weight percent (wt %) oxides in comparative diagrams. Raw data and associated standard measurements are reported in Appendix B.2, B.3 and B.4.

5.3.2 Chronology

To standardise chronological methodology new Bayesian age-depth models were developed from radiocarbon dates for both new study sites and published records using OxCal 4.2.3 (Bronk Ramsey, 2017). *P_Sequence* depositional models were run with outlier detection (Bronk Ramsey 2008, 2009) and a variable *k* factor (depositional events per unit length: cm^{-1}) (Bronk Ramsey and Lee, 2013), using the IntCal13 calibration curve (Reimer *et al*., 2013). Where applicable the sampling date of the uncut peat surface was used to further constrain the age-depth models. As limited radiocarbon

dating was available the known ages of the White River Ash east (1170-1095 cal yr BP; Davies *et al*., 2016) and Mazama ash (7680-7580 cal yr BP; Egan *et al*., 2015) tephra deposits were used to develop the age-depth model. Age ranges are reported at 95.4 % level confidence throughout the manuscript and new radiocarbon dates are reported in Appendix B.1.

5.3.3 Defining primary ash fall events

EPMA data are not available for all of the cryptotephra deposits identified by previous research and this study. These uncharacterised cryptotephra deposits are considered as primary ash fall events when shard abundances are ≥10 per cm^3, and are distinct from background concentrations. Where these parameters are met, the number of cryptotephra deposits present within any time interval is expressed as 'minimum' and 'maximum' values. This approach is taken because an uncharacterised cryptotephra deposit, occurring within the chronological uncertainty at a study site, could represent either a repeat of an observed tephra resulting from taphonomic processes, or a distinct tephra deposit – derived from a primary ash fall event.

5.4 Results

5.4.1 The tephrostratigraphy of new study sites

Twenty seven cryptotephra deposits are reported from the eight new study sites analysed as part of this study (Fig. 5.2). Ten glass geochemical populations from these deposits may be correlated with tephra isochrons previously identified in eastern North America based on chronology, shard morphology and major-minor element glass compositions. Two further cryptotephra populations have glass major-minor element compositions that differ from all tephra deposits previously described in eastern North America.

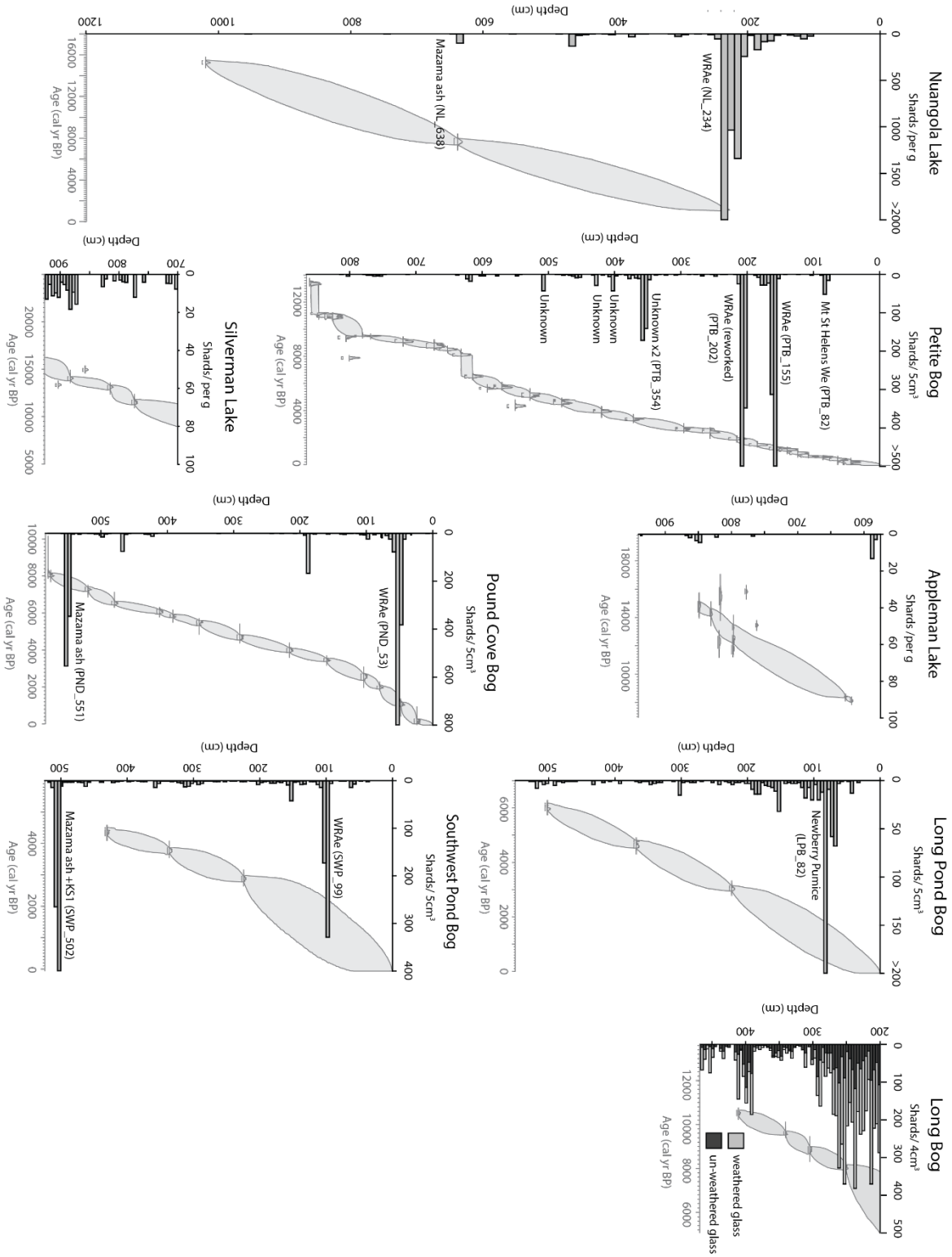

Figure 5.2: Tephrostratigraphies and Oxcal age-depth models (shown at 2σ age uncertainty) from the eight new study sites presented in this study.

Table 5.1: Normalised major-minor element compositions of correlated (a) and uncorrelated (b) cryptotephra deposits from this study. Major-minor element compositions of reference material from correlative tephra deposits is highlighted in grey. Data sources: MSH-We: Pyne-O'Donnell *et al*. (2012); WRAe: Jensen *et al*. (2014); Newberry Pumice: Pyne-O'Donnell *et al*. (2012); Mazama ash: this study. n. = number of analyses.

(a)

Sample		SiO_2	TiO2	Al_2O_3	FeO_T	MnO	MgO	CaO	Na_2O	K_2O	P_2O_5	Cl	H_2O Diff
MSH-We	Mean	75.89	0.25	13.51	1.5	0.04	0.26	1.44	4.5	2.5	-	0.1	2.61
n. 66	StDev	0.5	0.04	0.27	0.08	0.03	0.03	0.12	0.19	0.09	-	0.03	1.94
PTB_82	Mean	75.96	0.22	13.46	1.46	0.03	0.27	1.49	4.49	2.54	0.03	0.21	1.27
n. 13	StDev	0.47	0.02	0.37	0.12	0.01	0.03	0.12	0.17	0.21	0.01	0.15	1.57
WRAe	Mean	73.89	0.21	14.49	1.52	0.05	0.36	1.83	4.13	3.19	-	0.34	2.73
n. 107	StDev	0.63	0.04	0.32	0.20	0.02	0.07	0.18	0.16	0.17	-	0.04	1.48
PTB_155	Mean	73.31	0.24	14.44	1.51	0.06	0.42	1.88	4.62	3.24	-	0.36	2.08
n. 9	StDev	0.29	0.04	0.17	0.08	0.03	0.03	0.03	0.27	0.05	-	0.02	1.06
NL_234	Mean	73.74	0.21	14.20	1.57	0.05	0.41	1.95	4.31	3.15	0.06	0.35	1.25
n. 15	StDev	0.29	0.01	0.17	0.08	0.01	0.05	0.11	0.10	0.08	0.01	0.03	0.87
SWP_99	Mean	74.25	0.16	14.30	1.37	0.04	0.32	1.64	4.23	3.48	0.04	0.35	3.16
n. 9	StDev	0.76	0.03	0.52	0.24	0.01	0.07	0.22	0.24	0.61	0.02	0.03	2.20
Newberry Pumice	Mean	72.84	0.23	14.24	2.06	0.06	0.18	0.86	5.28	4.10	-	0.15	1.63
n. 20	StDev	0.67	0.13	0.69	0.44	0.27	0.14	0.15	0.25	0.48	-	0.05	0.88
LPB_82	Mean	73.68	0.22	13.83	1.93	0.06	0.18	0.89	5.03	3.98	0.04	0.16	2.00
n. 10	StDev	0.24	0.00	0.23	0.08	0.01	0.02	0.05	0.11	0.09	0.01	0.03	1.63
Mazama ash	Mean	72.37	0.44	14.73	2.05	0.06	0.51	1.64	5.25	2.81	-	0.19	1.90
n. 25	StDev	1.33	0.08	0.26	0.49	0.03	0.22	0.35	0.19	0.12	-	0.02	0.89
PND_551	Mean	72.64	0.42	14.57	1.87	0.05	0.47	1.59	5.37	2.87	-	0.18	1.90
n. 24	StDev	0.44	0.04	0.16	0.05	0.02	0.03	0.06	0.34	0.15	-	0.02	1.40
NL_638	Mean	73.13	0.43	14.12	1.88	0.05	0.48	1.66	5.22	2.77	0.07	0.19	0.94
n. 15	StDev	0.50	0.02	0.25	0.13	0.01	0.05	0.09	0.11	0.09	0.01	0.01	1.21
SWP_502(a)	Mean	72.71	0.43	14.71	1.88	0.04	0.47	1.55	5.18	2.89	-	0.19	2.43
n. 12	StDev	0.29	0.03	0.17	0.05	0.02	0.03	0.04	0.23	0.21	-	0.02	1.28

(b)

Sample		SiO_2	TiO2	Al_2O_3	FeO_T	MnO	MgO	CaO	Na_2O	K_2O	P_2O_5	Cl	H_2O Diff
PTB_354a	Mean	75.37	0.45	12.83	2.44	0.11	0.54	2.61	3.83	1.76	0.07	0.15	0.65
n. 15	StDev	0.54	0.01	0.39	0.13	0.01	0.04	0.15	0.13	0.08	0.01	-	1.12
PTB_354b	Mean	75.02	0.16	13.95	1.34	0.04	0.31	1.69	4.07	3.37	0.04	-	5.25
n. 7	StDev	0.85	0.04	0.46	0.16	0.01	0.08	0.22	0.23	0.17	0.01	-	2.90
SWP_502(b)	Mean	71.07	0.45	14.78	3.61	0.16	0.65	2.75	5.11	1.28	-	0.18	1.05
n. 3	StDev	0.26	0.06	0.09	0.09	0.03	0.05	0.09	0.21	0.06	-	0.01	0.39

5.4.2 Correlated cryptotephra deposits

Correlations between new cryptotephra deposits identified in this study and volcanic sources are based on glass geochemical compositions, similarity coefficients (SC) (Borchardt *et al*., 1972), shard morphologies and modelled age ranges. All of the newly identified cryptotephra deposits correlated with known tephra deposits have previously been identified in eastern North America, and can be confidently ascribed to eruption events in the Cascades and Alaska.

5.4.2.1 Mt St Helens We

Tephra deposit PTB_82 is composed of platy, vesicular glass shards with a modelled age range of 640-390 cal yr BP. The major-minor element glass compositions and modelled age range of PTB_82 closely overlap those of Mt. St Helens set We, which has been identified across eastern North America (Pyne-O'Donnell *et al*., 2012; Mackay *et al*., 2016; Jensen *et al*., in prep), and is dated to *ca.* AD 1482 (468 yr BP) using dendrochronology (Yamaguchi, 1983, 1985).

5.4.2.2 The White River Ash eastern lobe

Cryptotephra deposits that correlate with the White River Ash eastern lobe (WRAe) are identified in Pound Cove Bog, Southwest Pond Bog and Nuangola Lake. This cryptotephra is characterised by pumiceous, highly vesicular shards, derived from a large (VEI 6) Plinian eruption of Mt. Churchill (Alaska) between 1170-1095 cal yr BP (Lerbekmo, 2008; Preece *et al*., 2014; Davies *et al*., 2016). Cryptotephra deposits associated with this eruption are common throughout eastern North America (Mackay *et al*., 2016; Jensen *et al*., 2019), and extend into Europe as far as Poland (Pilcher *et al*., 1995; Jensen *et al*., 2014; Watson *et al*., 2017a).

5.4.2.3 Newberry Pumice

LPB_82 is formed of platy, vesicular, glass shards and was deposited in Long Pond Bog between 1790-330 cal yr BP. The major-minor element glass compositions and modelled age range of LPB_82 are consistent with the Newberry Pumice, derived from Newberry Volcano (Oregon) during the Big Obsidian Eruptive Episode *ca.* 1460 cal yr BP (MacLeod *et al.*, 1995; Kuehn, 2002; Keuhn and Foit, 2006). The Newberry Pumice was deposited eastward, and cryptotephra deposits associated with this eruption have been identified across eastern North America (Pyne-O'Donnell *et al*., 2012; Jensen *et al*., in prep).

5.4.2.4 The Mazama Ash

Cryptotephra deposits in Pound Cove Bog, Southwest Pond Bog and Nuangola Lake can be correlated with the Mazama ash, based on the close overlap in glass chemical compositions and modelled age ranges (Fig. 5.3). The Mazama ash is derived from Crater Lake (Oregon), and was produced between 7680-7580 cal yr BP (Egan *et al*., 2015), during one of the largest eruptions to take place during the Holocene (VEI: 7), which ejected up to 50 km^3 of mainly rhyodacitic magma (Bacon and Lanphere, 2006). Distal cryptotephra deposits linked with this eruption are found throughout eastern North America (Pyne O'Donnell *et al.,* 2012; Spano *et al*., 2017; Jensen *et al*., 2019), and extend across Greenland (Zdanowicz *et al.,* 1999) and possibly into Europe (Plunkett and Pilcher, 2018).

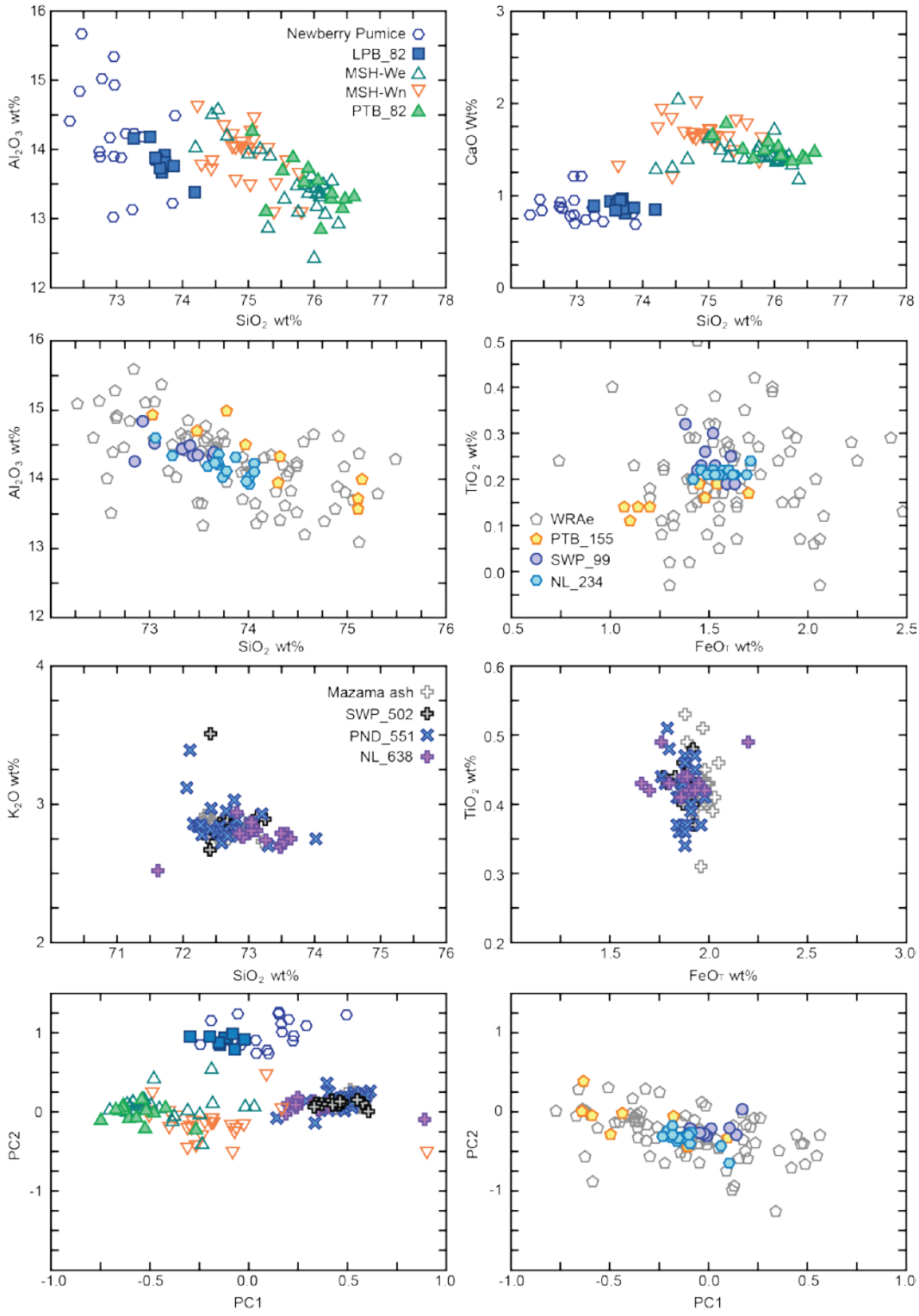

Figure 5.3: Selected bivariate plots of major-minor element glass compositions of correlated cryptotephra deposits. Comparative data is sourced from: MSH-We: Pyne-O'Donnell *et al*. (2012); WRAe: Jensen *et al*. (2014); Newberry Pumice: Pyne-O'Donnell *et al*. (2012). Reference material from the Mazama ash (UA 1573) was run alongside SWP_502 and PND_551 at the University of Alberta. P_2O_5 and Cl were removed for PCA calculations, from which the WRAe is plotted seperately for clarity.

5.4.3 Potential tephra correlations

Tephra deposit SWP_502b can potentially be correlated with a known volcanic eruption; however, should be treated with caution there are insufficient analyses to confirm this. Further side by side EPMA of SWP_502b and reference material and/or trace-element analysis could be used to confirm this correlation.

5.4.3.1 SWP_502b

Major-minor element glass compositions from a sub population of SWP_502 (n=3) closely overlap higher SiO_2 analyses of the KS_2 tephra (7350-7210 cal yr BP; Plunkett *et al.,* 2015), derived from Ksudach volcano, Kamchatka (Fig. 5.4). Visible tephra beds from this large (7-8 km^3 of ejecta; Kyle *et al.,* 2011) eruption extend north >900 km across Kamchatka, and cryptotephra deposits in Nova Scotia and Svalbard have been linked with this event (van der Bilt *et al.,* 2017). It is likely that a cryptotephra deposit produced during this eruption is obscured by the Mazama ash in Southwest Pond Bog; however, further analyses are need to confirm this.

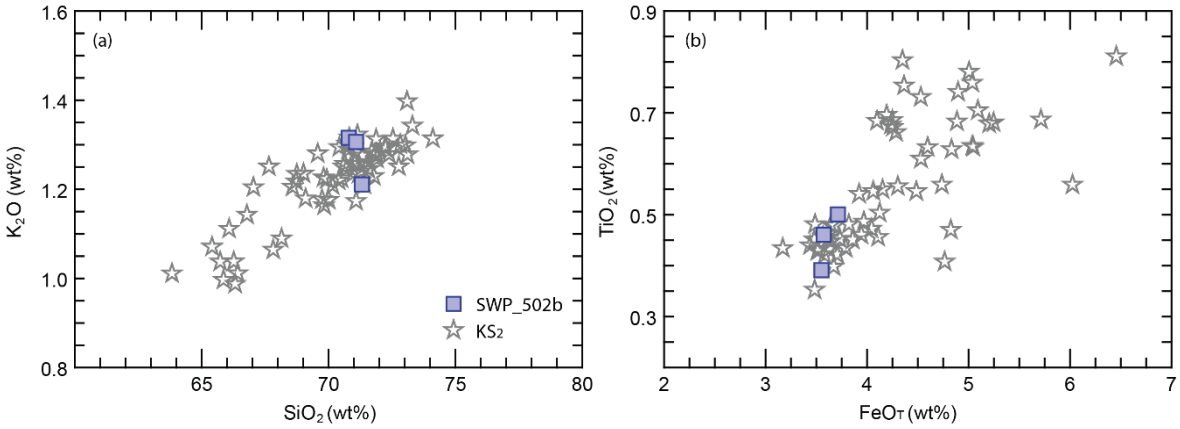

Figure 5.4: Selected bivariate plots of major-minor element glass compositions from SWP_502b and KS2 (Plunket *et al*., 2015; Ponomareva *et al*., 2017).

5.4.4 Uncorrelated cryptotephra deposits

Tephra deposit PTB_354 cannot yet be linked with any volcanic centre known to affect eastern North America. This uncertainty reflects the large number of eruptions capable of reaching eastern North America, under the right atmospheric conditions, within the age range associated with PTB_354. As the limits of ash dispersal are continually extended this issues is likely to become more common in tephrochronology in the future.

5.4.4.1 PTB_354

Tephra PTB_354 was deposited between 3430-2870 cal yr BP, and includes two distinct, geochemical populations (PTB_354a and PTB_354b), which are likely to have been derived from two separate volcanic sources. The major-minor element glass compositions of PTB_354a and PTB_354b do not consistently overlap with published EPMA data from large eruptions in the Cascades, Alaska or Kamchatka that took place within 500 years of the modelled age range for PTB_354 (Fig. 5.5). PTB_354a does overlap with analyses from historical eruptions of Hokkaido-Komagatake (Ko-c1, Ko-c2 and Ko-d) (Fig 5.5d), Japan; however, no large eruptions are known from this volcano during the time period associated with PTB_354 (Hughes *et al*., 2013; Yoshimoto *et al*., 2008). Although further identification is being sort, we cannot confidently link either glass population from PTB_354 with a volcanic region. Tephra deposits derived from past eruptions in Kamchatka, the Aleutian Arc and Japan share geochemical similarities with PTB_354, while the study of tephra deposits is at an early stage in Central America and the Kurile Islands.

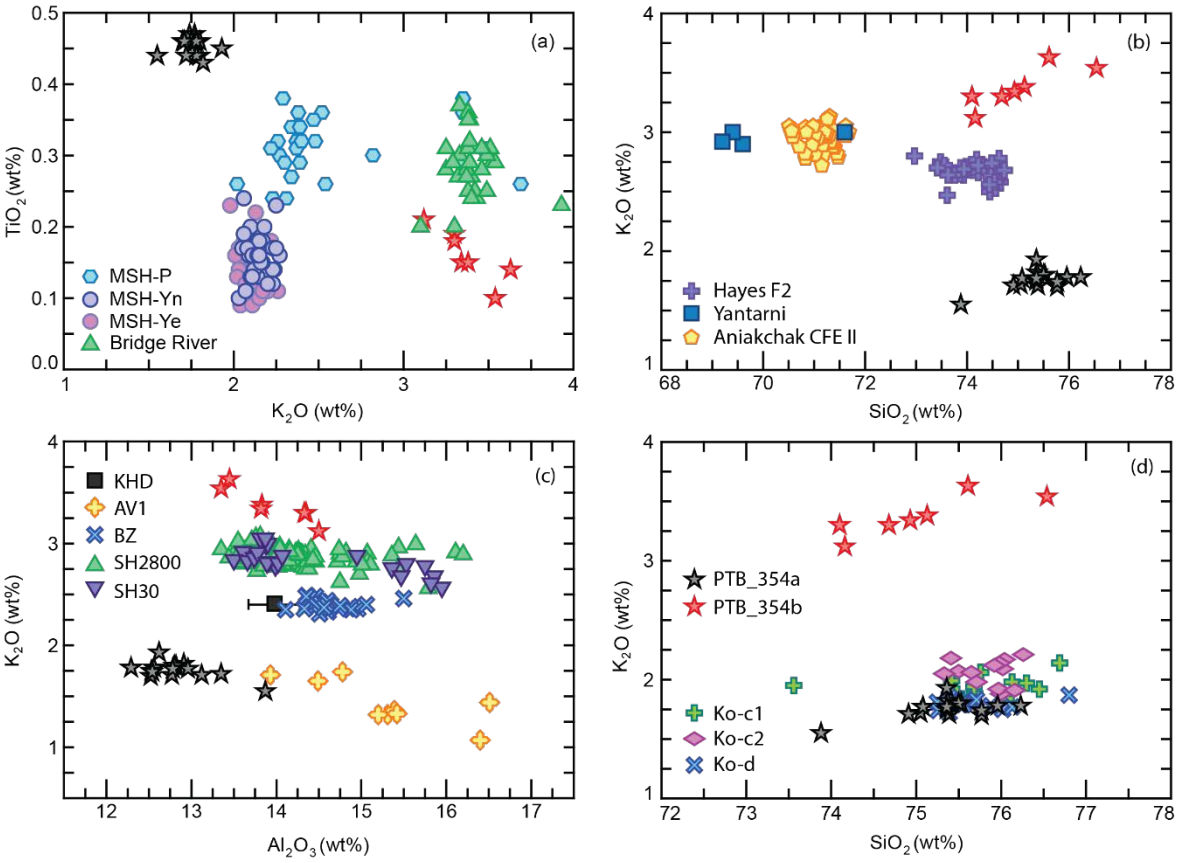

Figure 5.5: Selected bivariate plots of major-minor element glass compositions from PTB_354 and large (≥VEI 4) volcanic eruptions producing rhyolitic tephra between 4000-2300 yr BP. Comparative data includes analyses from Mt St Helens (Yn,Ye,Yb and P), Mt Meager (Bridge River) (Jensen *et al*., 2019), Yantarni (Riehle *et al*., 1999), Hayes (F2) (Wallace *et al*., 2014), Aniakchak (CFE II) (Kaufman *et al*., 2012), Sheveluch (SH2800, SH30), Bezymianny (BZ) (Ponomareva *et al*., 2017), Avachinsky (AVI), Khodutka (KHD) (Kyle *et al*., 2011) and Hokkaido-Komagatake (Ko-c1, Ko-c2 and Ko-d) (Hughes *et al*., 2013).

5.4.5 Detrital tephra

Abundant detrital tephra shards (tephra shards not derived from primary air fall events) are present throughout large sections of Long Bog (Fig. 5.2). These shards are larger than glass from primary tephra deposits and are often visibly weathered. Jensen *et al*. (in prep) report similar findings from Irwin Smith Bog, Michigan, which they attribute to the remobilisation of tephra previously held within loess deposits in the American Midwest. Reworked tephra can be transported several hundreds of kilometres by wind action (see Paper III), and it is possible that the detrital glass in Long Bog could obscure less abundant cryptotephra deposits derived from primary air fall events.

5.5 Discussion

5.5.1 Temporal patterns in cryptotephra deposits

Based on the available chronology and glass EPMA data we find evidence for between 42 and 56 unique cryptotephra deposits from 21 study sites in eastern North America (Appendix B.6). The vast majority of these events occur during the period 7600 cal yr BP to present, while only two predate this: Glacier Peak (13,710-13,410 cal yr BP; Kuehn *et al*., 2009) and Mt St Helens J (13,800-12,800 cal yr BP; Clynne *et al*., 2008), both reported by Pyne-O'Donnell *et al*. (2016). The frequency of cryptotephra deposition events undergoes a step-change beginning with the deposition of the Mazama ash (Fig. 5.6) (7,682-7,584 cal yr BP; Egan *et al*., 2015): from one air fall events per 4,700 years between 7600-17,000 cal yr BP to one air fall event per 200 years between 7600 cal yr BP to present. Sections 5.5.2-5.5.4 discuss this change in the frequency of tephra deposition over eastern North America and raise three hypotheses which may explain it.

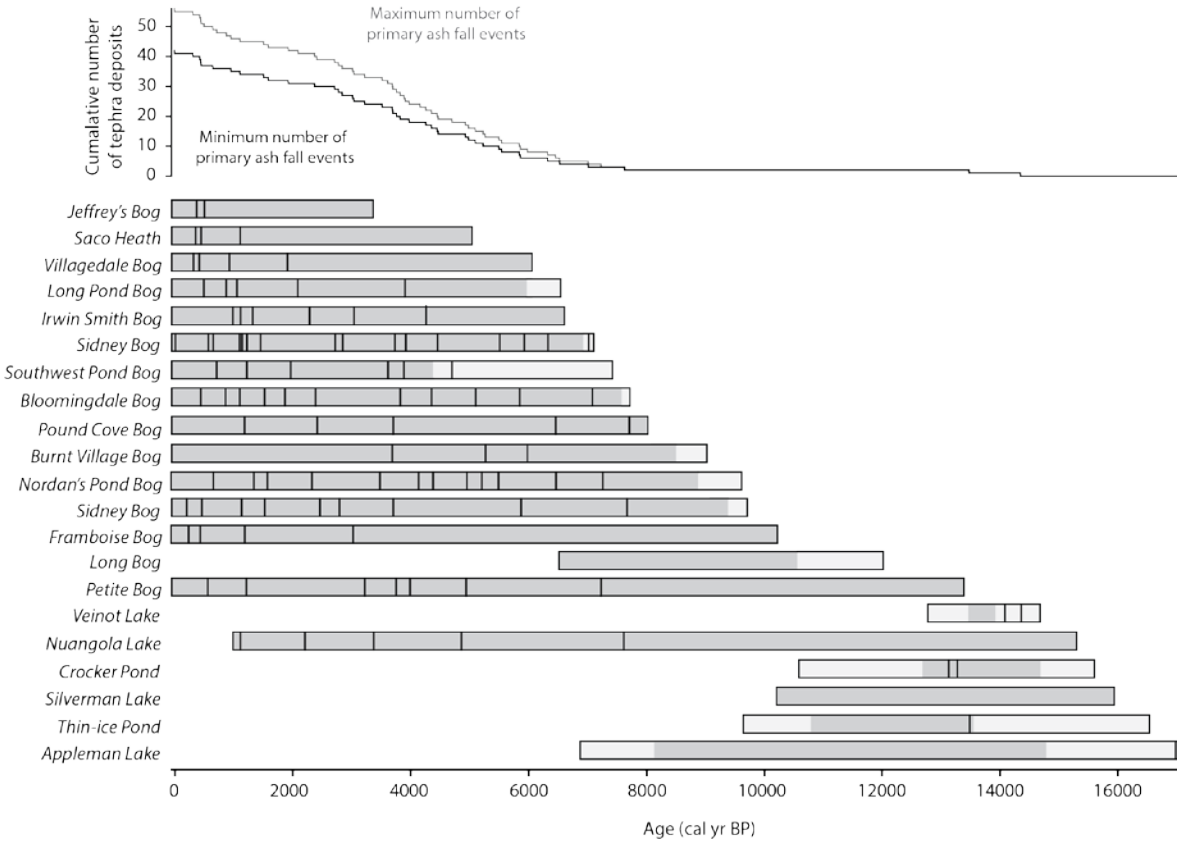

Figure 5.6: The cumulative number of cryptotephra deposits plotted against temporal site coverage. The position of cryptotephra deposits in each record is indicated by a black line. Sections of core that have been analysed for ash content, but not directly dated are indicated by lighter grey bar extensions – estimated by age-depth model projections.

5.5.2 Hypothesis 1: The increase in the frequency of cryptotephra deposits is due to an increase in eruption frequency

The increase in the frequency of cryptotephra deposits after *ca.* 7,600 cal yr BP could be explained by an uptake in the number of large explosive eruptions during this period. However, studies of proximal tephra deposits from the regions affecting eastern North America demonstrate numerous large eruptions took place throughout the entire time period spanned by our records (*ca.* 17,000 cal yr BP to present) (Miller and Smith, 1987; Mullineaux, 1996; Hildreth *et al*., 2007; Kyle *et al*., 2011; Albert *et al*., 2019). Wider databases of large volcanic eruptions (LaMEVE; Crosweller *et al*., 2012; Global Volcanism Program, 2019) do show an upturn in volcanism following the onset of the Holocene (Fig. 5.7), and again during the late Holocene; however, these increases are likely to reflect a bias in the recording of evidence for past eruptions rather than physical processes (Brown *et al*., 2014). Conversely, the SO_4^{2-} record from the Greenland ice cores suggest more intensive volcanism during the Lateglacial and early Holocene (Zielinski *et al*., 1996, 1997), which is not reflected in the tephrostratigraphy of eastern North America. This increase is suggested to be driven by crustal unloading as Pleistocene ice-sheets retreated (Jull and McKenzie, 1996), and there is evidence for intensified volcanism in several of the high latitude volcanic regions affecting eastern North America (Alaska and Kamchatka) (Braitseva *et al*., 1995; de Fontaine *et al*., 2007; Brown *et al*., 2014; Praetorius *et al*., 2016) (Fig. 5.7). Therefore, the available evidence does not support *Hypothesis 1*, and the temporal pattern of tephra deposition evident in the eastern North America is unlikely to represent an increase in volcanic activity after *ca.* 7,600 yr BP.

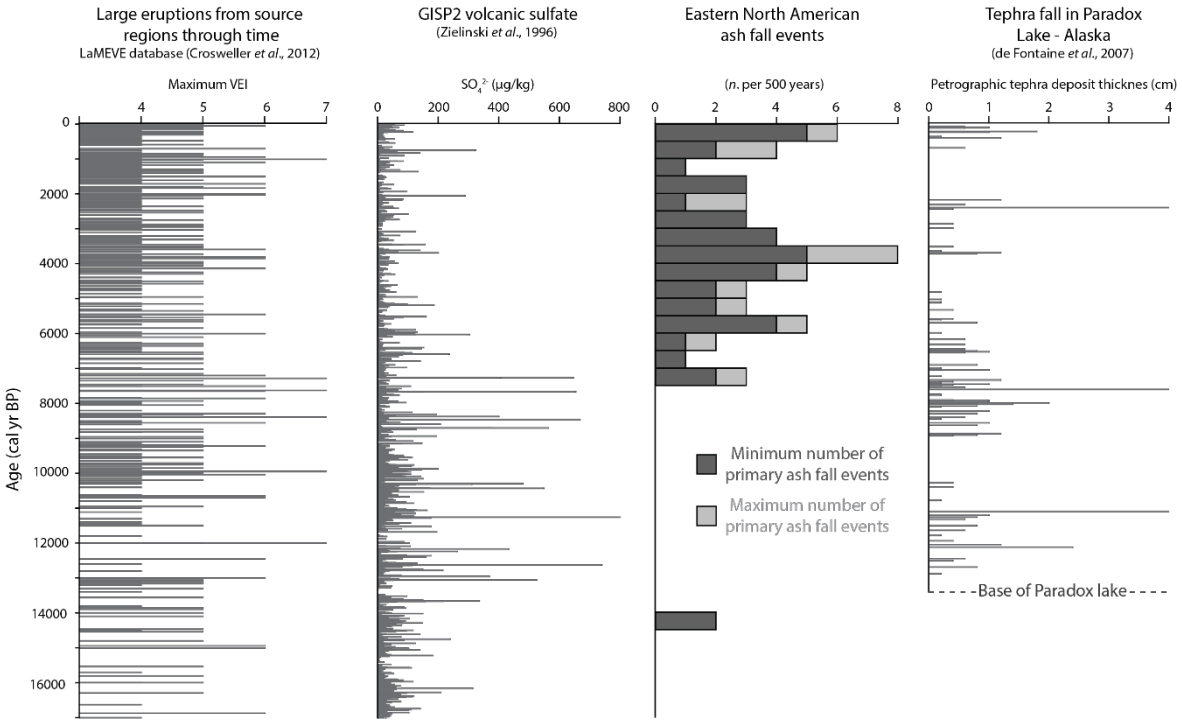

Figure 5.7: Temporal patterns in tephra fall from key regional sources and datasets plotted against tephra occurance in eastern North America.

5.5.3 Hypothesis 2: The increase in the frequency of cryptotephra deposits is due to the number and type of available study sites

The cryptotephra framework in eastern North America was not developed with the aim of interpreting temporal patterns. While we have analysed new study sites for this purpose (principally through the investigation of Lateglacial and early Holocene sediments), a bias towards mid-late Holocene records remains (Fig. 5.6). It is possible that the higher frequency of cryptotephra deposits between *ca.* 7,600 cal yr BP to present day reflects the increased study-site density throughout this period. This seems unlikely however, as the inflection point, and upturn in the frequency of ash fall, occurs sometime after the increase in the number of study sites (Fig. 5.6). Furthermore, the minimum site coverage between 14,500 cal yr BP and 7,600 cal yr BP is six records and which include tephra deposits from two eruption sequences. During the mid-late Holocene no combination of two or more records extends beyond 484 years without including more than two cryptotephra deposits (East Lake Tephra and SB-13), and only one record covers a period of more than 4,500 years (Framboise Bog). The Lateglacial and early Holocene records are therefore distinct from younger periods, and it is unlikely that the step-change in cryptotephra deposition frequency is due to site density.

The Holocene tephrostratigraphy of eastern North America is primarily derived from peat records; however, the temporal limits of peat initiation in this region mean the Lateglacial and early Holocene tephrostratigraphy is developed from lake sediments (Pyne-O'Donnell *et al*., 2016; this study). This change in depositional environment or sedimentation rate could alter the efficiency of tephra preservation, and cause an apparent reduction in the frequency of cryptotephra deposits. This hypothesis is not supported by the published literature, as lake sediments have been repeatedly shown to provide good archives of distal cryptotephra deposits (Watson *et al*., 2016). This includes Nuangola Lake (from this study) which preserves multiple, concise cryptotephra deposits, as well as an abundant WRAe isochron – composed of >2000 shards per gram. While taphonomic influences, such as frozen lake surfaces (Boygle, 1999), or snow drifts (Bergman *et al*., 2004), may have affected individual sites during the Lateglacial and early Holocene, it is implausible that taphonomic processes can explain the absence/reduction of cryptotephra deposits across all of the study sites during this period. Therefore, we do not support the *Hypothesis 2*.

5.5.4 Hypothesis 3: The increase in the frequency of cryptotephra deposits is because of changes in atmospheric circulation

The increase in the frequency of cryptotephra deposits after *ca.* 7,600 cal yr BP may be explained by a change in the transport efficiency of tephra in the atmosphere. The first Holocene deposition of cryptotephra in eastern North America (the Mazama ash) occurs shortly after inferred regional changes in atmospheric circulation (Dean *et al*., 2002; Finkenbinder *et al*., 2016), and precipitation patterns (Williams *et al*., 2010), around the time of the early-mid Holocene transition, *ca.* 8,200 yr BP. The lag between this atmospheric shift and the first deposition of cryptotephra is likely to be because of the intermittent supply of tephra affecting eastern North America – related to the natural intervals between large eruptions. Evidence for regional atmospheric changes and shifts in aridity *ca.* 8,200 yr BP are expressed in lake-sediment geochemistry (Dean *et al*., 2002; Nelson and Hu, 2008) and regional pollen records (Shuman *et al*., 2002; Williams *et al*., 2010), summarised in Figure 5.8. The rapid collapse of the Laurentide Ice Sheet is often suggested as a driver for these changes in atmospheric circulation patterns and airflow strength, and was advocated by Pyne-O'Donnell *et al*. (2012) to explain the absence of early Holocene cryptotephra deposits in Nordan's Pond Bog, Newfoundland. Modelling studies, loess deposits and mapping of sand spits from palaeo-lakes at the margins of the former Laurentide Ice Sheet provide evidence for anticyclonic winds over the ice sheet (Bromwich *et al*., 2004; Pausata *et al*., 2011; Schaetzl *et al*., 2016). However, these winds are likely to have been restricted to a narrow belt (~150 km) around the ice sheet margin (Arbogast *et al*., 2015), and may not have affected more southerly study sites from our

dataset. Dean *et al*. (2002) and Kirby *et al*. (2002) both suggest the position of the winter-polar front lay further south than present day during the early Holocene, and this may have enhanced intrusions of tephra free, arctic air masses into eastern North America, as well as pushing the jet stream south, away from study sites. A disruption of tephra delivery may have occurred 'up stream' of our study region and affected ash plumes extending from Alaska or Kamchatka. This partial disruption would explain the presence of tephra deposits associated with Glacier Peak and Mt St Helens J, both sourced from the Cascades, during the Lateglacial (Pyne O'Donnell *et al*., 2016).

Based on the available data and supporting literature discussed above we favour *Hypothesis 3: the increase in the frequency of cryptotephra deposits is because of changes in atmospheric circulation.* This is the only hypothesis which we cannot confidently refute; however, there is insufficient evidence to conclude a driving mechanism for this change. Recent carbonate $\delta^{18}O$ records from lake sediments, as well as dust flux and *Sphagnum* $\delta^{18}O$ records from ombrotrophic peat-bogs, have demonstrated dynamic atmospheric conditions over eastern North America during the mid-late Holocene (Daley *et al*., 2016; Finkenbinder *et al*., 2016; Pratte *et al*., 2017a, 2017b), and future studies using these techniques may provide insight into the atmospheric processes operating during the early Holocene.

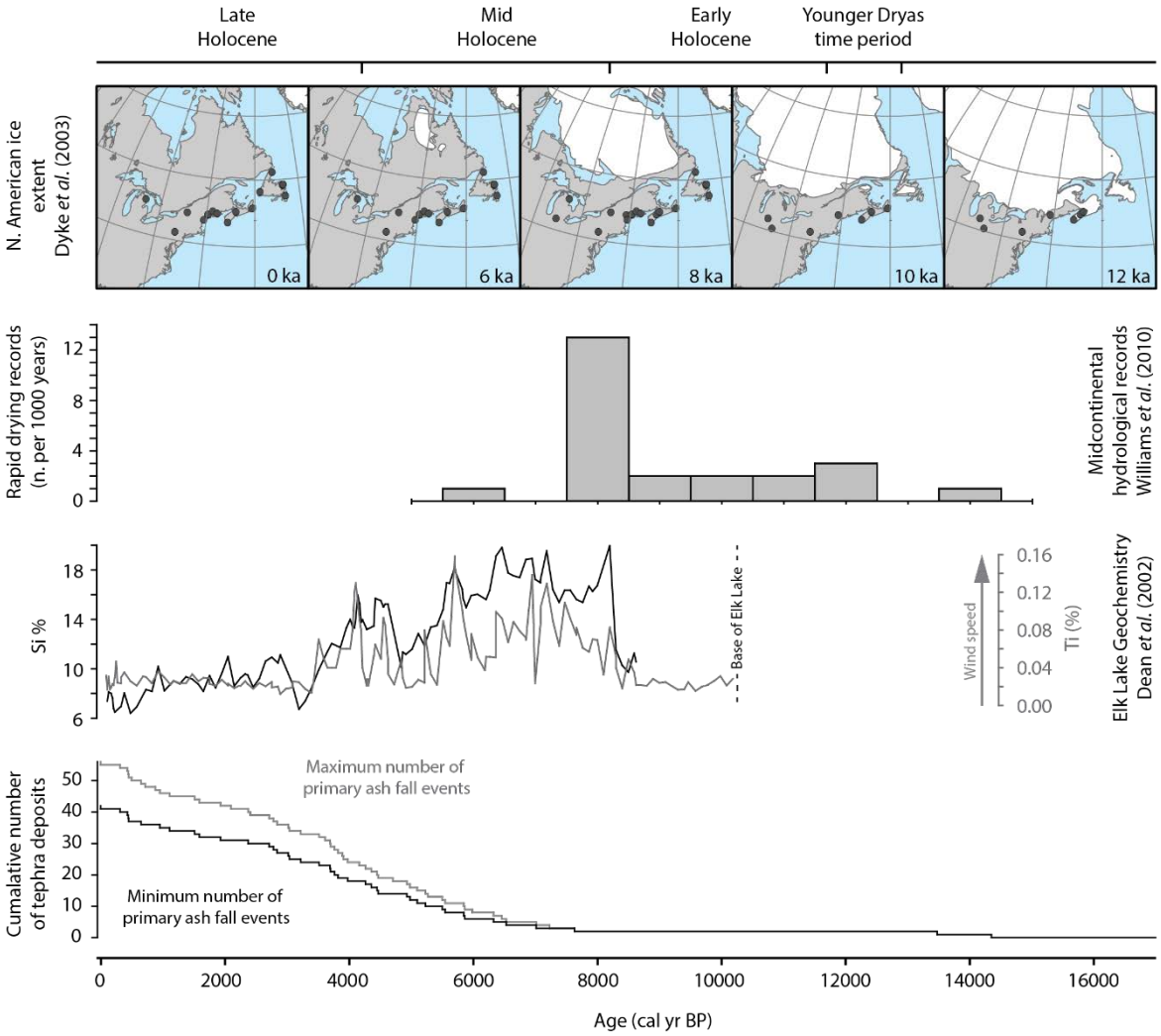

Figure 5.8: The cumulative number of eastern North American cryptotephra deposits plotted against North American ice extent (shown with cryptotephra study sites), number of rapid response drying records and Elk Lake, Minnesota, geochemistry – where increasing Ti and Si represent elevated dust levels and strengthening wind speed.

5.6 Conclusions

A network of tephrostratigraphic records, can be used to investigate wider temporal patterns in tephra deposits with implications for ash dispersal and volcanic hazards. This approach has largely been confined to European data sets; however, there is clearly potential to examine regional tephrostratigraphic frameworks from other areas frequently affected by ash deposition.

We report further occurrences of well characterised and wide spread cryptotephra deposits in eastern North America (Mt St Helens We, WRAe, Newberry Pumice and Mazama ash). Two geochemical populations from the sample PTB_354 do not correlate with any glass major-minor element datasets published from this region, and cannot be correlated with a volcanic source at this time.

For the first time we use a North American cryptotephra framework to investigate temporal patterns in tephra delivery to this region. Our results demonstrate an upturn in the frequency of cryptotephra deposits during the mid-late Holocene, beginning with the deposition of the Mazama ash (7,682-7,584 cal yr BP; Egan *et al*., 2015). The available evidence suggests this upturn is unlikely to have been caused by an increase in volcanic activity or changes in taphonomy, and it is best explained by changes in atmospheric circulation.

This study presents results from cryptotephra investigations that were previously considered to have been unsuccessful due to the absence of primary air fall tephra deposits (Appleman Lake, Silver Lake, Long Bog). However, these studies become important sources of information when considered as part of a wider pattern. This reiterates the importance of reporting 'failed' results. Such results not only contribute to temporal patterns, but provide important data points in constraining tephra isopach maps.

5.7 Acknowledgements

We would like to thank Chris Hayward and Mike Hall at the Tephrochronology Analytical Unit, University of Edinburgh, for their help and advice with microprobe analysis and stub preparation. This research includes study sites and radiocarbon dating that was supported by a Natural Environment Research Council (NERC) grant: PRECIP project (grant numbers NE/G019851/1, NE/G02006X/1; NE/G020272/1; NE/G019673/1). Further field work and analytical investigation was supported by grants from the Royal Geographical Society (Geographical Club Award), the Explorers Club (The Exploration Fund Grant) and the Geologists Association (New Research Workers award), awarded to Ali Monteath. Charlotte Clarke and Roseanna Mayfield helped with fieldwork in Newfoundland.

Chapter 6 Paper III

Evidence for distal transport of reworked Andean tephra: Extending the cryptotephra framework from the Austral Volcanic Zone

6.1 Abstract

Cryptotephra deposits (non-visible volcanic ash beds) may extend thousands of kilometres and provide valuable chronological isochrons. Here, we present a Lateglacial-early Holocene (*ca*. 16,500 cal yr BP-6000 cal yr BP) tephrostratigraphy from Hooker's Point, East Falkland, South Atlantic. This period spans the last glacial termination across the southern mid-latitudes, a time period during which the palaeoenvironmental record is poorly resolved in southern South America and the South Atlantic. The development of a regional tephrostratigraphy will provide chronological constraint for palaeoenvironmental records from this period. Two cryptotephra deposits from Hooker's Point are linked with Mt. Burney, including the early-Holocene MB_1 tephra, while a third is likely to be derived from the R_1 eruption of Reclus volcano. The high shard abundance of these cryptotephra deposits suggests they extend further into the Southern Ocean, and may act as regional stratigraphic markers during the Lateglacial. Further peaks in shard abundance are composed of detrital glass (tephra not derived from primary air fall events), with mixed shard morphologies and geochemically heterogeneous glass populations. This detrital glass is likely to have been repeatedly reworked by wind action in the Patagonian Steppe before final deposition in the Falkland Islands. The high abundance of detrital glass in the Hooker's Point sequence suggests long distance transport of reworked tephra is common in this region, and highlights the need to carefully analyse cryptotephra deposits in order to avoid incorrectly describing reworked tephra as new isochrons. A temporal pattern of shard abundance is apparent in the Hooker's Point sequence with a reduction /absence of shards between 14,300-10,500 cal yr BP.

6.2 Introduction

Cryptotephra deposits (non-visible volcanic ash beds) provide valuable chronological isochrons, and insights into tephra transport and dispersal (Jensen *et al.,* 2014; Bronk Ramsey *et al.,* 2015; Plunkett and Pilcher, 2018). However, few cryptotephras deposits have been described from southern South America and the South Atlantic; a region affected by strong atmospheric circulation patterns and frequent explosive volcanism. Contemporary observations suggest tephra from this region may be deposited across wide areas. For example, ash from the 2011 eruption of the Puyehue-Cordón

Caulle volcanic complex in Chile (Volcanic Explosivity Index; VEI 5) reached the Western Antarctic Ice Sheet (Koffman *et al.,* 2017), and caused air traffic disruption in Australia and New Zealand (Klüser *et al.,* 2012; Alloway *et al.*, 2015). It is therefore likely that the palaeoenvironmental record holds further examples of distal cryptotephra deposits that may be used to synchronise climate archives and refine volcanic hazard assessments.

Here, we describe the Lateglacial and early Holocene (*ca*. 16,500-6000 cal yr BP) tephrostratigraphy from Hooker's Point (HP) (51°42'S, 57°47'W), an exposed peat cliff on East Falkland near Port Stanley (Fig. 6.1). This period spans the last glacial termination across the southern mid-latitudes, which was punctuated by abrupt climate events and changes in latitudinal positon and strength of the Southern Westerly Wind belt (SWW) (Vanneste *et al.,* 2015; Mayr *et al*., 2013; Moreno *et al.,* 2012). The palaeoenvironmental record from southern South America and the South Atlantic is poorly resolved during this period (Kilian and Lamy, 2013), with some sites recording uninterrupted warming (Haberle and Bennett, 2004), while others show dynamic osilations in temperature or precipitation (García *et al*., 2012; Mansilla *et al.,* 2018). This inconsistent, often contradictory, climate-record may reflect: i) differing proxy sensitivities, ii) real spatial-temporal climate variability or iii) chronological uncertainty, and the establishment of a regional tephrochronological framework will provide chronological constraint in addressing palaeoenvironmental questions.

The Falkland Islands (Islas Malvinas) are well placed to extend the tephrostratigraphy of southern South America as they lie beneath the central jet of the SWW (50-55^{o}S), and downwind of the Andean Southern Volcanic Zone (SVZ; 33-46 °S) and the Austral Andean Volcanic Zone (AVZ; 49-55°S). Since the last glacial period 74 volcanic centres in these zones are known to have been active (Fontijn *et al.,* 2014, 2016), and cryptotephra deposits in Isla de los Estados (Unkel *et al.*, 2008), the Falkland Islands (Hall *et al.,* 2001), South Georgia (Oppedal *et al.,* 2018) and the Antarctic ice cores (Kurbatov *et al.,* 2006; Narcisi *et al.,* 2012) have been linked with Andean volcanoes. The Falkland Islands are therefore ideally placed to study palaeo-ash clouds extending from the Southern Andes during the Lateglacial-Holocene transition.

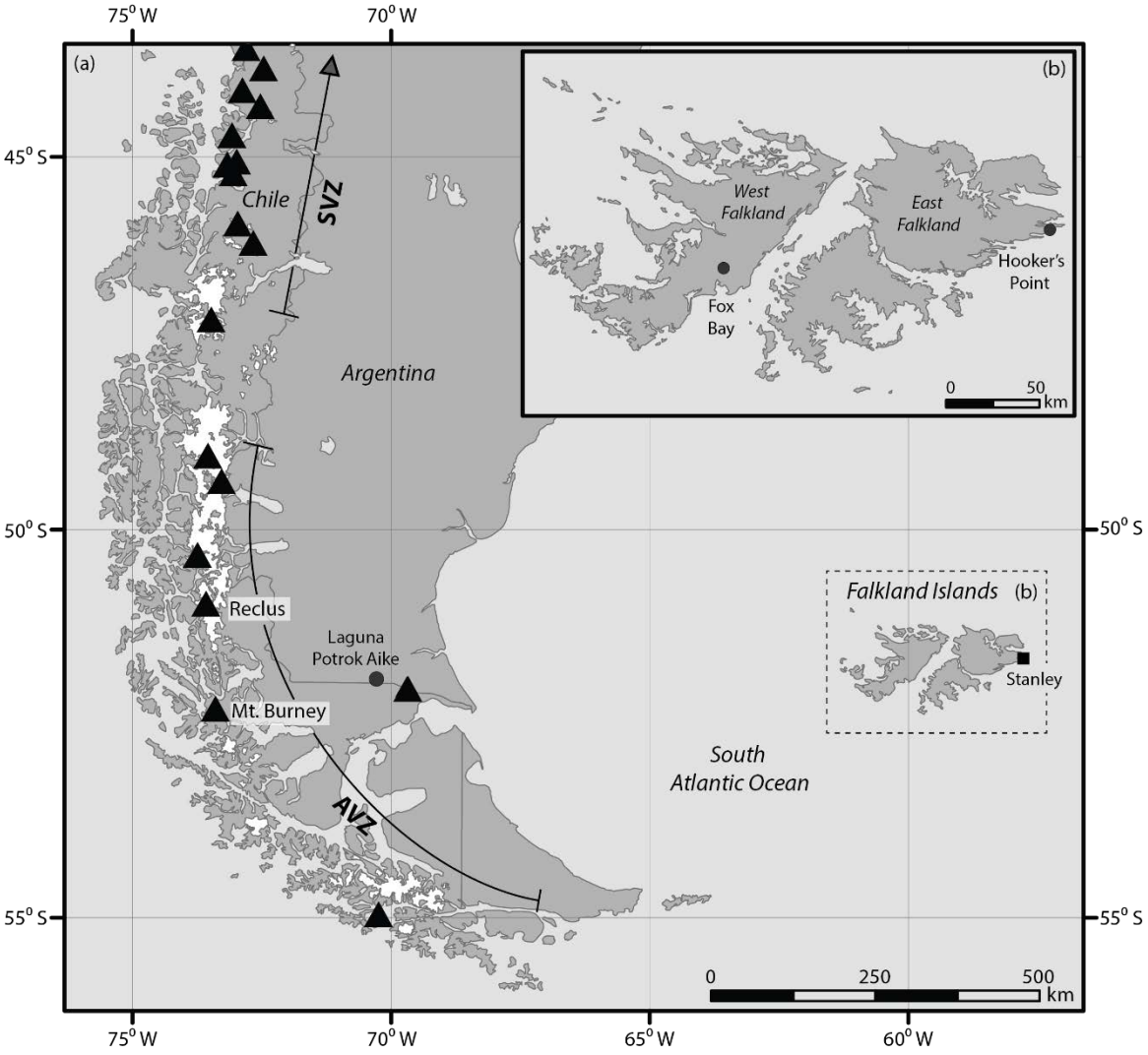

Figure 6.1: The position of sites and volcanoes described in the text. South American volcanoes known to have been active during the Holocene and Late-glacial are shown as black triangles (Smithsonian Global Volcanism programme, 2018). The extents of the Andean Southern Volcanic Zone (SVZ) and the Austral Andean Volcanic Zone (AVZ) are based those defined by Naranjo and Stern, (2004).

6.3 Materials and methods

6.3.1 The Hooker's Point section

The Hooker's Point peat sequence (51°42'S, 57°47'W) is situated in East Falkland, 3.5 km east of Port Stanley. The exposed section lies adjacent to Hooker's Point, immediately behind a small beach, and extends from around 3 metres a.s.l. to the cliff top at around 8 metres a.s.l. The peat profile was sampled using a series of 50 cm and 25 cm monolith tins which were pushed into overlapping, cleaned, cliff sections. Samples beneath the present beach level were obtained using a hand gouge to a depth of 2 metres.

6.3.2 Tephrostratigraphy

Cryptotephra deposits were identified from continuous 5 cm samples, concentrated using ashing (Pilcher and Hall, 1992), emersion in 10 % Hydrochloric acid (HCl), and sieving (80 µm and 15 µm). Heavy liquid flotation at 2.0 g/cm^{-3} and 2.55 g/cm^{-3}, was used to extract glass shards from the remaining host material (Turney *et al.,* 1998), and residues were mounted in Canada Balsam and counted under a high power microscope. Shard abundance was quantified against the dried sample weight (shards/gram), as sample densities varied with organic content. Where peaks in shard abundance were identified, further 1 cm samples were processed and quantified in the same manner to refine the stratigraphic position of the cryptotephra deposit. The morphological characteristics of 100 glass shards from each cryptotephra deposit were recorded (colour, morphology and long axis length) and measured using an eyepiece graticule mounted in the high power microscope.

Glass shards from peak cryptotephra concentrations were extracted for electron probe microanalysis (EPMA) using heavy liquid flotation (Turney *et al.,* 1998) with minor modifications to the method; i) 10 % HCl was not applied as no carbonates were present in the samples, and ii) cleaning floats at 2.0 g/cm^3 were retained and subjected to additional centrifuge cycles. Between these cycles samples were carefully stirred to separate glass shards from the organic material. Additional material from cryptotephra deposit HP_32 was subjected to acid digestion (Dugmore *et al.,* 1992) to increase the number of shards available for EPMA. Glass shards extracted for geochemical analysis were mounted in an epoxy resin stub and polished to expose internal glass surfaces before being carbon coated for EPMA.

The geochemical composition of glass shards were analysed following established protocols (Jensen *et al.,* 2008) at the University of Alberta, using wavelength dispersive spectrometry (WDS) on a JEOL 8900 superprobe and a Cameca SX-100 electron microprobe. Ten major-minor elements

(Si, Ti, Al, Fe, Mn, Mg, Ca, Na, K, Cl) were measured using a 5 µm beam, with 15 keV accelerating voltage, and 6 nA beam current to minimise Na and K migration during analyses. Two secondary standards, of known composition, were run concurrently during EPMA to assess analytical accuracy and precision: i) ID3506, Lipari rhyolitic obsidian, and ii) Old Crow tephra (Kuehn *et al.,* 2011). Results were normalized to 100 % and are presented as weight percent oxides (wt %) in bi-plot diagrams. Raw major-minor element glass compositions and associated standard measurements are reported in Appendix C.1 and C.2.

6.3.3 Chronology

A Bayesian age-depth model (Fig. 6.2) was developed from eight radiocarbon dates (Table 6.1) using OxCal 4.2.3 (Bronk Ramsey, 2017), and the SHCal13 calibration curve (Hogg *et al.,* 2013). A *P_Sequence* depositional model was run with outlier detection (Bronk Ramsey, 2009a, 2009b), and a variable *k* factor (depositional events per unit length: cm^{-1}) (Bronk Ramsey and Lee, 2013). One radiocarbon date (Beta-241336) suggested a slight age reversal; however, it did not reduce the overall model agreement to <60 %, and so was retained in the final age-depth model (Bronk Ramsey, 2009a). Calibrated dates and age ranges are reported at two sigma (95.4 %) confidence throughout this study.

Table 6.1: Radiocarbon dates from the Hooker's Point sediment sequence with calibrated two sigma age ranges. Ages were calibrated using OxCal 4.2.3 (Bronk Ramsey, 2017), and the SHCal13 calibration curve (Hogg et al., 2013).

Laboratory ID Code	Material	Depth (cm)	Radiocarbon age (^{14}C yr BP)	$^{13}\delta$C (‰)	Calibrated age range (95.4 %) (cal yr BP)
Beta-193400	Bulk (peat)	0-2	5700±40	-27.0	6628-6405
Beta-241334	Plant Macro	42-43	7390±40	-29.7	8341-8055
Beta-193401	Bulk (peat)	76	9250±80	-26.7	10650-10241
Beta-241335	Plant Macro	90-91	10030±40	-25.0	11749-11330
Beta-241336	Wood	94-95	9940±40	-27.0	11602-11242
Beta-193402	Bulk (peat)	100	10370±60	-27.3	12517-12000
Beta-241338	Plant Macro	154-155	13320±50	-27.1	16217-15822
Beta-193403	Bulk (peat)	168	13630±140	-27.7	16923-16055

6.4 Results and Discussion

High numbers of glass shards were found throughout large sections of the Hooker's Point sediment sequence, with increased tephra abundance between 65-75 cm and 130-174 cm (Fig. 6.2, A3). Samples from eight peaks in shard concentration were analysed by EPMA, all of which are composed of high SiO_2 rhyolitic glass (Table 6.2a). Three cryptotephra deposits are linked with volcanic centres in the Andean Austral volcanic zone (AVZ) based on the major-minor element composition of volcanic glass and modelled age ranges (Section 6.4.1). Analyses from further cryptotephra deposits are geochemically heterogeneous with low analytical totals (not reflected in secondary standards), low Na_2O and high SiO_2 (Table 6.2b, Fig. 6.3). These characteristics are found in heavily weathered detrital glasses (glass shards not derived from primary air fall events) which are susceptible to Na loss during analysis (Jensen *et al.,* 2016), and suggest a large amount of reworked glass is present in the Hooker's Point record.

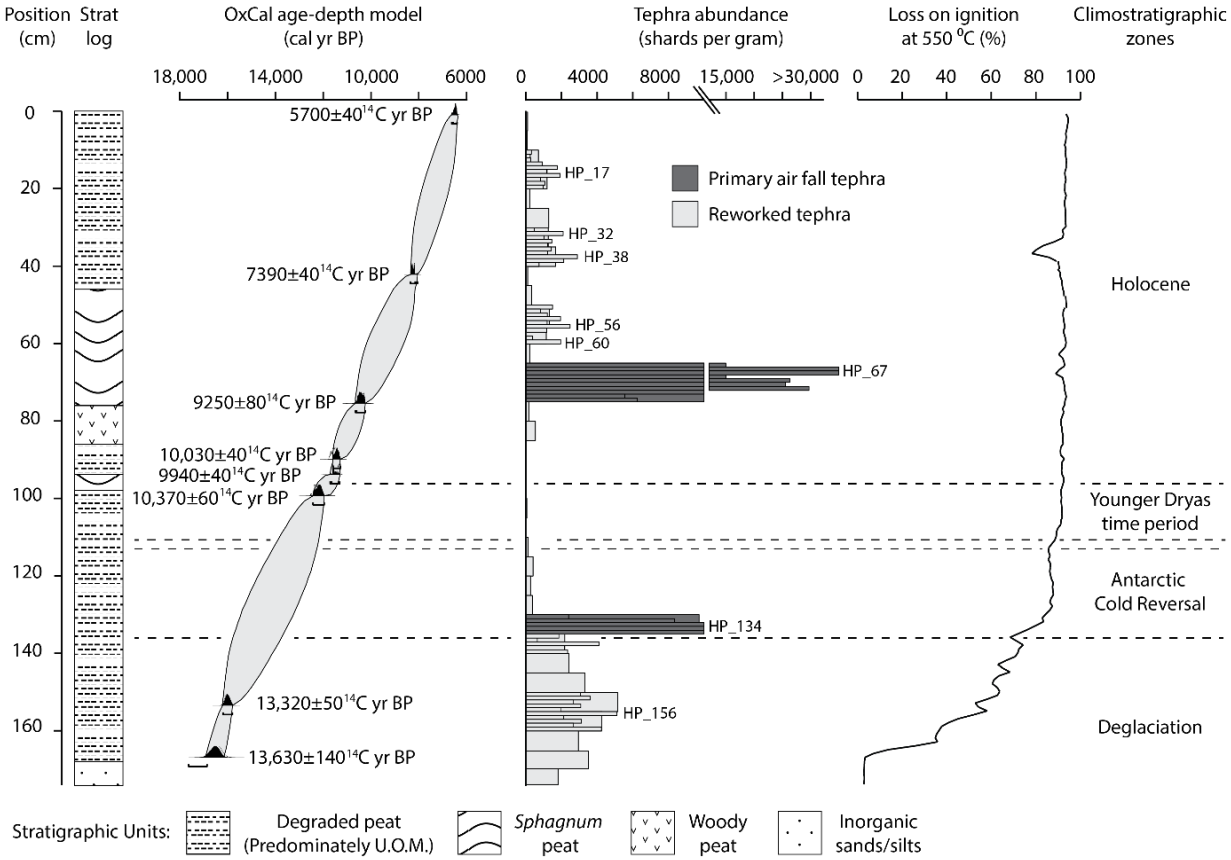

Figure 6.2: Summary lithostratigraphy, radiocarbon dates, OxCal age-depth model, tephra abundance, loss on ignition (LOI) and broad climatic zones from Hooker's Point, Falkland Islands.

Table 6.2: Major-minor element composition (non-normalised) of primary (a) and reworked (b) cryptotephra deposits from Hooker's Point, shown as mean and one standard deviation (StDev) (n = number of analyses). (c) Bracketing analyses and recommended values (Kuehn et al., 2011) for secondary standards. (*) Recommended value.

(a)

Sample	n		SiO_2	TiO_2	Al_2O_3	FeO_T	MnO	MgO	CaO	Na_2O	K_2O	Cl	Total
HP_14-17	10	Mean	75.58	0.17	12.81	1.02	0.03	0.26	1.18	4.15	1.96	0.20	97.32
Pop b.		StDev	*1.39*	*0.03*	*0.22*	*0.10*	*0.02*	*0.03*	*0.13*	*0.27*	*0.17*	*0.03*	*1.79*
HP_67	27	Mean	74.94	0.16	12.61	1.04	0.05	0.24	1.18	4.58	1.80	0.19	96.74
		StDev	*0.94*	*0.04*	*0.19*	*0.09*	*0.02*	*0.03*	*0.12*	*0.23*	*0.12*	*0.02*	*1.09*
HP_134	33	Mean	74.51	0.13	12.64	1.18	0.04	0.20	1.42	3.80	2.58	0.18	96.65
		StDev	*1.07*	*0.03*	*0.28*	*0.11*	*0.02*	*0.03*	*0.09*	*0.20*	*0.13*	*0.02*	*1.32*

(b)

Sample	n		SiO_2	TiO_2	Al_2O_3	FeO_T	MnO	MgO	CaO	Na_2O	K_2O	Cl	Total
HP_14-17	30	Mean	72.44	0.19	12.24	1.28	0.05	0.14	0.91	2.56	3.69	0.16	93.63
Detrital glass		StDev	*2.13*	*0.11*	*0.79*	*0.52*	*0.03*	*0.12*	*0.36*	*0.84*	*0.92*	*0.05*	*2.59*
HP_32	33	Mean	72.46	0.13	12.05	1.15	0.04	0.11	0.86	2.80	3.52	0.17	93.26
Detrital glass		StDev	*1.80*	*0.07*	*0.47*	*0.35*	*0.03*	*0.08*	*0.27*	*0.81*	*0.70*	*0.05*	*2.12*
HP_38	35	Mean	72.81	0.14	12.15	1.18	0.05	0.11	0.90	2.85	3.58	0.16	93.90
Detrital glass		StDev	*1.77*	*0.10*	*0.73*	*0.37*	*0.02*	*0.10*	*0.34*	*0.79*	*0.75*	*0.07*	*2.49*
HP_56	34	Mean	72.53	0.14	12.33	1.32	0.06	0.13	0.99	2.84	3.43	0.14	93.87
Detrital glass		StDev	*1.72*	*0.10*	*0.65*	*0.47*	*0.02*	*0.10*	*0.35*	*0.96*	*0.72*	*0.04*	*2.31*
HP_60	32	Mean	72.63	0.14	12.39	1.10	0.06	0.15	0.98	3.04	3.42	0.15	94.03
Detrital glass		StDev	*2.33*	*0.07*	*0.74*	*0.52*	*0.03*	*0.14*	*0.45*	*1.06*	*0.97*	*0.05*	*2.99*
HP_156	55	Mean	71.33	0.18	12.00	1.36	0.05	0.14	0.95	3.19	3.60	0.19	92.96
Detrital glass		StDev	*1.58*	*0.08*	*0.48*	*0.48*	*0.03*	*0.07*	*0.30*	*0.40*	*0.59*	*0.06*	*1.67*

(c)

Sample	n		SiO_2	TiO_2	Al_2O_3	FeO_T	MnO	MgO	CaO	Na_2O	K_2O	Cl	Total
Lipari	50	Mean	74.04	0.08	13.10	1.55	0.07	0.03	0.72	4.08	5.19	0.33	99.11
		StDev	*0.55*	*0.02*	*0.11*	*0.07*	*0.02*	*0.01*	*0.03*	*0.19*	*0.10*	*0.02*	*0.74*
Old Crow	41	Mean	72.1	0.3	12.62	1.61	0.06	0.29	1.40	3.78	3.63	0.27	95.99
		StDev	*0.83*	*0.04*	*0.14*	*0.07*	*0.02*	*0.03*	*0.05*	*0.19*	*0.15*	*0.02*	*1.11*
Lipari*	33	Mean	74.1	0.07	13.1	1.55	0.07	0.04	0.73	4.07	5.11	0.34	99.18
		StDev	*0.96*	*0.03*	*0.34*	*0.06*	*0.03*	*0.02*	*0.05*	*0.28*	*0.26*	*0.03*	
Old Crow*	18	Mean	72.1	0.3	12.5	1.62	0.05	0.28	1.43	3.66	3.56	0.27	95.77
		StDev	*1.7*	*0.05*	*0.3*	*0.12*	*0.02*	*0.02*	*0.05*	*0.38*	*0.28*	*0.05*	

Table 6.3: Shard morphology statistics for Hooker's Point cryptotephra deposits. Descriptions include: minimum (Min), maximum (Max) and mean ($\bar{x}$) long axis lengths (µm), as well as standard deviation (σ) and shard morphologies (SM). Descriptions are based on 100 measurements (n).

HP_17	**HP_32**	**HP_38**	**HP_56**	**HP_60**	**HP_67**	**HP_134**	**HP_156**
$\bar{x}$: 40	$\bar{x}$: 38	$\bar{x}$: 38	$\bar{x}$: 40	$\bar{x}$: 41	$\bar{x}$: 45	$\bar{x}$: 37	$\bar{x}$: 42
σ: 13	σ: 13	σ: 12	σ: 13	σ: 14	σ: 19	σ: 12	σ: 13
Max: 75	Max: 75	Max: 80	Max: 80	Max: 100	Max: 138	Max: 83	Max: 98
Min: 18	Min: 15	Min: 18	Min: 15	Min: 15	Min: 18	Min: 23	Min: 18
SM: mixed	SM: mixed	SM: mixed	SM: mixed	SM: mixed	SM: cuspate	SM: cuspate/platy	SM: mixed
n: 100	*n*: 100	*n*: 100	*n*: 100	*n*: 100	*n*: 100	*n*: 100	*n*: 100

6.4.1 Tephra correlations

Correlations between Hooker's Point cryptotephra deposits and Andean volcanoes are based on glass geochemical compositions, similarity coefficients (SC) (Borchardt *et al.,* 1972) and modelled age ranges; however, they should be considered as working correlations, to be continually tested by future studies. A future tephra framework for southern South America and the Southern Ocean should be based on a range of information including; glass geochemical compositions (major, minor and trace elements), petrology, chronology and stratigraphic context (Lowe *et al.,* 2017). This work is at an early stage in southern South America and there are few comparative datasets; however, recent studies are beginning to address this (Fontjin *et al.,* 2016; Del Carlo *et al.,* 2018; Mansilla *et al.,* 2018).

A consistent minor offset in SiO_2 and Al_2O_3 values is evident in tephras correlated between Hooker's Point and Laguna Potrok Aike (Fig. 6.3). This offset is also apparent in the Lipari standard measurements (Fig. A3), which show no sign of Na loss (Tables B2, B4). The differences in SiO_2 and Al_2O_3 values are therefore likely to reflect differing instrumental conditions during EPMA. Future work could use side-by-side analysis of both samples to eliminate such analytical differences (Westgate *et al.,* 2013; Monteath *et al.,* 2017).

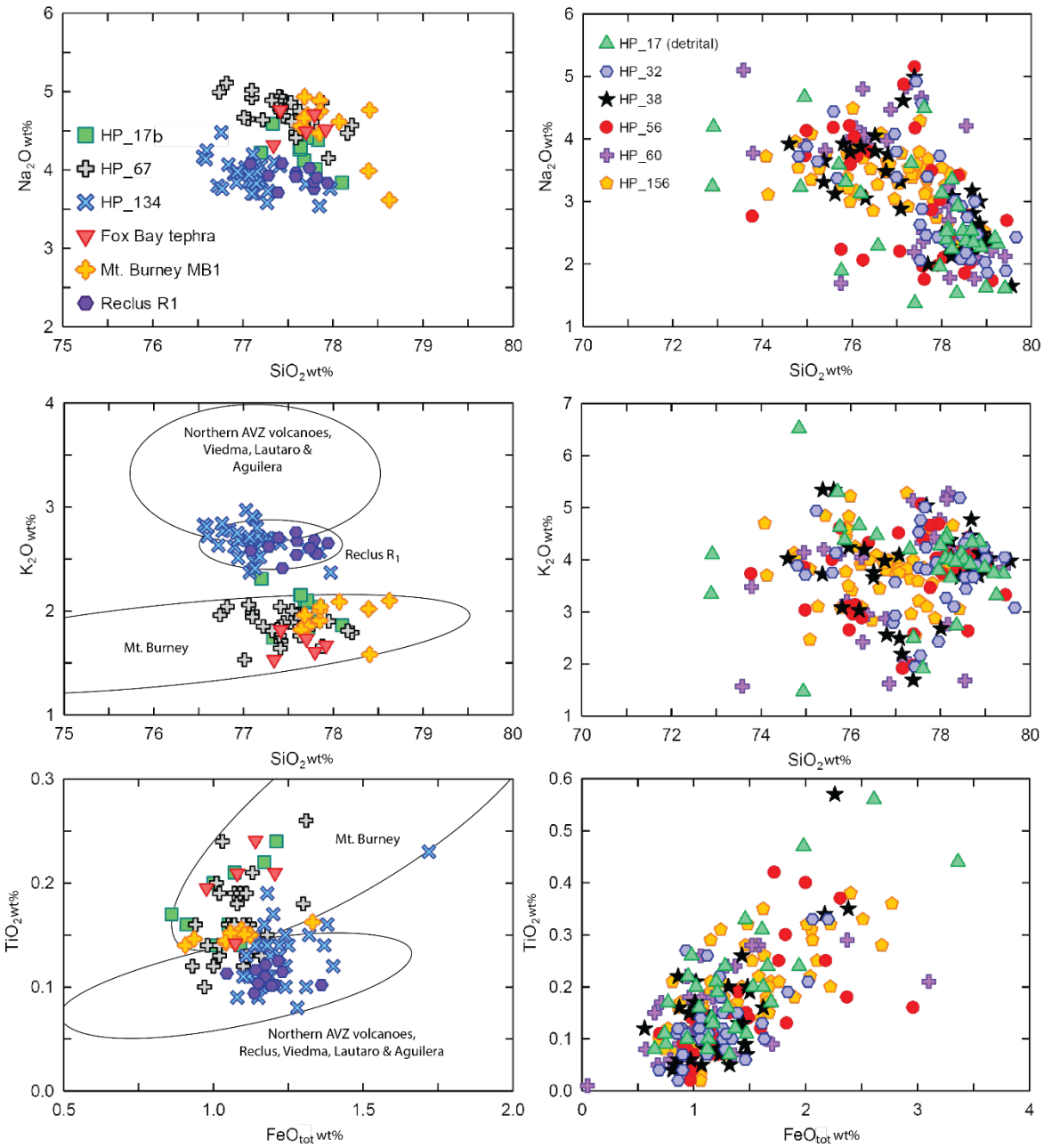

Figure 6.3: Bivariate plots of glass geochemical compositions (normalised major and minor element data) from Falkland Islands cryptotephra deposits (this study; Hall *et al*., 2001) and the Mb_1 and Reclus R_1 tephras from Laguna Potrok Aike (Wastegård *et al*., 2013). Geochemical envelopes are redrawn from Wastegård *et al*., (2013), and overlap previous studies of AVZ tephras (e.g. Kilian et al., 2003; Haberzettl *et al*., 2009; Stern, 2008).

6.4.2 Cryptotephra deposit HP_17 (14-17 cm)

HP_17 is composed of clear glass shards with mixed morphologies (Table 6.3, Fig. C.3) and heterogeneous geochemical compositions (Fig. 6.3), suggesting that the majority of the cryptotephra deposit is formed of detrital glass. However, a sub-population (n=10) (hereafter

referred to as HP_17b) with low K_2O values (1.74-2.31 wt %) relative to other HP_17 analyses, plots consistently as a discrete group, and may be derived from a primary air fall event (Fig. 6.3). Analyses from this group closely overlap those from HP_67 except for marginally lower Na_2O values (Fig. 6.3).The two-sigma modelled age range of HP_17 is 7,680-6,610 cal yr BP. However, the age range of HP_17b cannot be precisely determined as consistent geochemical analyses only account for 25% (n=10) of the deposit, and the exact stratigraphic position of the cryptotephra may be obscured by detrital glass.

Glass geochemical compositions from HP_17b consistently plot as Mt. Burney 'type' and may be separated from other volcanic centres in SVZ and AVZ by high SiO_2 (77.2-78.1 wt%) and low K_2O values (1.74-2.31 wt%) (Kilian *et al.,* 2003; Haberzettl *et al.,* 2009; Stern, 2008; Wastegård *et al.,* 2013; Del Carlo *et al.,* 2018). No large eruptions of Mt. Burney are known from the modelled age range of HP_17, and HP_17b may represent a previously unknown eruption of this volcano. Alternatively, Kilian *et al.,* (2003) describe a Mt. Burney 'type' tephra bed stratigraphically between the MB_1 (9950-8850 cal yr BP; Stern *et al.,* 2008) and MB_2 (3820-4710 cal yrs BP; Del Carlo *et al*., 2018) tephras, also derived from Mt. Burney. The best age constraint for this eruption is a radiocarbon date (4420±40 ^{14}C yr BP) 17 cm above the tephra. Based on sediment accumulation rates, Kilian *et al.* (2003) suggest an age of around 5691±11 cal yr BP for the described tephra bed. Given the dating uncertainties associated with both tephras, it's plausible that they may be derived from the same eruption; however, further understanding of the Mt. Burney eruptive history is needed to test both of these hypotheses.

6.4.3 Cryptotephra deposit HP_67 (67 cm)

HP_67 is a highly abundant cryptotephra deposit (>30,000 shards per gram), formed of clear, cuspate glass shards (Table 6.2, Figs. A2, A5). Glass geochemical compositions occur in a narrow SiO_2 range (76.7-78.2 wt%), and have low K_2O values (1.53-2.06 wt%), relative to other cryptotephra deposits present in Hooker's Point, with the exception of HP_17b (Fig. 6.3). The two-sigma modelled age range of HP_67 is 10,490-9,190 cal yr BP.

Glass major-minor elements from HP_67 plot in high SiO_2 Mt. Burney envelopes (Fig. 6.3), and closely overlap the MB_1 tephra in Laguna Potrok Aike (Wastegård *et al.,* 2013) (SC: 0.96; Table B3) . The MB_1 tephra was deposited eastward from a large (VEI 5) early Holocene eruption of Mt. Burney (Fontijn *et al.,* 2014), radiocarbon dated to 9950-8850 cal yr BP by Stern *et al.,* (2008). This age estimate overlaps with the modelled age range of HP_67, and HP_67 may be correlated with the MB_1 tephra. This correlation extends the known distribution of this ash deposit >1000 km east from Mt. Burney.

6.4.4 Cryptotephra deposit HP_134 (132-135 cm)

HP_134 forms an abundant (>12,000 shards per gram) cryptotephra deposit composed of clear, cuspate, platy shards (Table 6.3, Figs. C.3, C.4). Glass shard geochemical compositions fall in a tight high SiO_2 range (76.5-78 wt%), with intermediate K_2O values (2.37-2.97 wt%) relative to other Hooker's Point cryptotephra deposits. The two-sigma modelled age range of the cryptotephra deposit is 15,640-13,550 cal yr BP.

The geochemical composition of glass analyses from HP_134 consistently plot in major-minor element envelopes for Reclus volcano (Fig. 6.3), and closely overlap the Reclus R_1 tephra in Laguna Potrok Aike (Wastegård *et al.,* 2013) (SC: 0.95; Table B3). Published age ranges for the Reclus R_1 tephra (15,510-14,350 cal yr BP; McCulloch *et al.,* 2005; 15,260-14,370 cal yr BP; Stern *et al.,* 2008) overlap the modelled age range of HP_134, and it is likely that HP_134 may be correlated with Reclus R_1. This tephra was deposited to the southeast of Reclus Volcano, towards the Falkland Islands, and is derived from one of the largest eruptions known from the AVZ (VEI 6) (Stern *et al.,* 2011; Fontijn *et al.,* 2014). Identification of the Reclus R_1 tephra in East Falkland extends the known distribution of this ash deposit >1100 km from Reclus volcano.

6.4.5 Fox Bay cryptotephra deposit 60-65 cm

Comparison between published EPMA data from Fox Bay, West Falkland (Hall *et al.,* 2001), and analyses from Laguna Potrok Aike (Wastegård *et al.,* 2013) and Hooker's Point (Fig. 6.3), show a strong geochemical overlap between an uncorrelated cryptotephra deposit in Fox Bay at 60-65 cm, and Mt. Burney 'type' analyses. The Fox Bay cryptotephra deposit is undated and so cannot be linked with an eruption event; however, the analyses suggest Mt. Burney 'type' cryptotephra deposits may be present across the Falkland Islands.

6.5 Detrital glass abundance

The majority of cryptotephra deposits analysed from Hooker's Point are composed of detrital glass (glass shards not derived from primary air fall events) with heterogeneous glass geochemistries (Fig. 6.3). No visible tephra beds have been reported from the Falkland Islands (Hall *et al.,* 2001) that could act as sources of reworked glass, and it is likely that detrital glass present in Hooker's Point is reworked from deposits in southern South America. Prevailing westerly winds and outwash plains mean tephra from volcanic eruptions in the SVZ and the AVZ is widely deposited over the Patagonian steppe. In this semi-arid, sparsely vegetated environment tephra may be repeatedly reworked by wind action where it forms a large component of regional dust emissions (Gaiero *et al*., 2007). Unconsolidated tephra can be suspended by relatively low winds speeds (6-9 km/h)

(Fowler and Lopushinsky, 1986), and once remobilised tephra from southern South America may be transported and deposited over large distances (including the Falkland Islands). For example, in the aftermath of the 1991 eruption of Volcán Hudson (VEI 5) plumes of remobilised ash extended >1000 km over Argentina and the western Atlantic Ocean (Wilson *et al.,* 2011). The discovery of abundant detrital glass throughout the Hooker's Point sediment sequence suggests that distal transport of reworked tephra is a common occurrence in this region, and that cryptotephra deposits must be carefully analysed in order to avoid incorrectly describing reworked material as new primary air fall events.

A temporal pattern of detrital glass abundance is apparent in the Hooker's Point sediment sequence, with an absence/reduction of tephra during the time periods associated with the Antarctic Cold Reversal (ACR; 14,700-13,000 cal yr BP; Pedro *et al*., 2011), Younger Dryas (YD; 12,900-11,700 cal yr BP; Walker *et al*., 2009), and early-Holocene (Fig. 6.2). This pattern could reflect: i) changes in position and/or strength of the Southern Westerly Winds (SWW), with stronger winds delivering more detrital glass to the study site. However, while the dynamics of the SWW are poorly resolved during the Lateglacial, palaeoenvironmental records from latitudes both North and South of the Falkland Islands suggest an increase in SWW velocities during the ACR (Moreno *et al.,* 2012; Vanneste *et al.,* 2015), which is not reflected in the detrital glass record from Hooker's Point. Alternatively, tephra abundance could indicate ii) changes in eruption frequency from the SVZ and AVZ. Several studies have discussed a link between deglaciation and increasing volcanism (Watt *et al.,* 2013; Fontijn *et al.,* 2016; Weller *et al.,* 2018); however, the low Na_2O and high SiO_2 values in detrital tephra from Hooker's Point suggest that the glass has been subjected to extensive weathering prior to deposition. This weathering indicates a lag between the eruptive event and final burial of the glass at Hooker's Point. Therefore the tephra delivery pattern may not reflect the eruption sequence as primary air fall events are rapidly transported and deposited. Finally, the temporal pattern may be derived from iii) site specific taphonomic processes and changes in the efficiency of tephra entrapment. Each of these hypotheses could explain the temporal pattern of tephra abundance in Hooker's Point, and further investigation of the sedimentary (e.g. grain size analysis) and dust (e.g. rare earth elements) records from Hooker's Point are needed to disentangle potential taphonomic and climatic influences on the detrital glass signal.

The abundant detrital glass present in Hooker's Point is likely to obscure a more comprehensive tephrostratigraphy. Numerous large explosive eruptions are known to have taken place in the SVZ and AVZ since deglaciation, which were deposited eastward across large areas (Fontijn *et al.,* 2014, 2016). Tephra from these eruptions is likely to be present in Hooker's Point, but are obscured by the influx of detrital tephra. Morphological descriptions of the Hooker's Point cryptotephra deposits show that although there is little variance in shard size (Fig. C.4) primary air

fall events (HP_67 and HP_134) have more consistent shard morphologies than detrital glass deposits (Fig. C.3). Mclean *et al.* (2018) used shard morphologies to differentiate between reworked tephra and primary air fall events in Japan, and this approach may allow detection of further cryptotephra deposits in the Falkland Islands.

6.6 Conclusions

Modern observations and palaeo-records suggest that the study of cryptotephra deposits originating from Andean volcanoes is likely to provide valuable chronological isochrones across southern South America and the South Atlantic islands. The development of a Lateglacial tephrostratigraphy from this region will help answer questions of abrupt climate change during this period, which are poorly resolved at present.

Cryptotephra deposits in Hooker's Point are linked with the widespread MB_1 and R_1 tephras, which are likely to extend beyond the Falkland Islands, and may act as key regional markers. An additional Mt. Burney type cryptotephra, deposited during the mid-Holocene, may represent a minor eruption of Mt. Burney described by Kilian *et al.* (2003), or a previously unknown eruption from the same source.

A high abundance of detrital glass is present throughout large sections of the Hooker's Point sediment sequence. This glass is likely to have been sourced from reworked deposits in southern South America, suggesting distal transport of reworked glass is common in this region, and care must be taken to avoid interpreting reworked deposits as new primary air fall events. A temporal pattern of detrital glass abundance is apparent in Hooker's Point, with a reduction in the concentration of shards throughout the ACR, YD period and early-Holocene. This pattern may reflect: i) variability in the strength and/or position of the SWW, ii) changes in eruption frequency, or iii) site-specific taphonomic processes; however, further work is needed to test these hypotheses.

Further primary cryptotephra deposits are likely to be obscured by detrital glass, and future studies of cryptotephra in the Falklands may benefit from a morphology-based approach to shard quantification.

6.7 Acknowledgements

We are grateful to Prof Robert Scaife, Prof Anthony Long and Prof Mike Bentley for access to the Hooker's Point peat sequence and radiocarbon dating. We would also like to thank Dr Lauren Davies and Prof Britta Jensen for their help with sample preparation and EPMA analysis at the University of Alberta. Fieldwork for this project was funded by the Shackleton trust, and was supported by the Falkland Islands Bureau of Mineral Resources. Alex Blake assisted in sample collection from Hooker's Point and tephrochronology was supported by a World Universities Network Research Mobility Programme grant, awarded to Ali Monteath. We are also grateful to Peter Abbott and a second anonymous reviewer for their helpful comments on an earlier version of this manuscript.

Chapter 7 Paper IV

A Lateglacial and early Holocene record of dynamic Southern Westerly Winds from the Falkland Islands, South Atlantic

7.1 Abstract

The Southern Westerly Wind belt is a major feature of Southern Hemisphere, mid-latitude, climate, that is closely linked with the ventilation and draw down of CO_2 in the Southern Ocean. Past changes in the strength and/or position of this wind belt are poorly resolved, particularly during the Lateglacial and early Holocene, time periods associated with rapid fluctuations in global temperature and atmospheric conditions. Here, we use geochemistry (XRF and ICPMS analysis) and particle size analyses from a peat sequence in the Falkland Islands (Islas Malvinas), South Atlantic, to reconstruct wind strength across the Pleistocene-Holocene transition (*ca.* 16,500-6,450 cal yr BP). Wind strength is observed to be at its strongest between 14,400-13,000 cal yr BP, before declining sharply and reaching a minimum between 12,900-11,000 cal yr BP. Our findings suggest the Southern Westerly Wind belt strengthened during the Antarctic Cold Reversal, before moving southward, away from the Falkland Islands, during the Younger Dryas time period and early Holocene. A gradual resumption of high wind speeds between 10,400-8000 cal yr BP is in good agreement with published records east of the Andes; however, our Falkland Islands record contrasts with those west of the Andes Mountains which show a strengthening of the Southern Westerly Wind belt at this time.

7.2 Introduction

The Southern Westerly Wind belt (SWW) is the dominant atmospheric circulation pattern between 50-55 ^{o}S, and strongly influences regional climate and ocean circulation (Garreaud, 2009, 2013). Variations in the strength and/or position of the SWW are linked with changes in sea ice extent, ocean productivity and deep water upwelling in the Southern Ocean (Lovenduski *et al*., 2008; Hodgson and Sime, 2010; Purich *et al*., 2016). In turn, these changes influence the ventilation and draw-down of CO_2 by the Southern Ocean, which accounts for ~40% of the global ocean carbon sink (Anderson *et al*., 2009; Toggweiler, 2009; Frölicher *et al*., 2015).

Modern observations show a southward contraction and strengthening of the SWW since the mid-1970s (Marshall, 2003; Visbeck, 2009); however, these records are of insufficient length to separate short term fluctuations from long-term trends. Reconstructions of past changes in the

strength and position of the SWW rely heavily on records from Patagonia, South America – the only continental landmass that intersects the core of the wind belt (e.g. Mayr *et al*., 2007; Lamy *et al*., 2010; Moreno *et al*., 2012). These studies have provided important insights into the dynamics of the SWW during the Lateglacial; however, the timing and magnitude of reconstructed changes in wind-strength are often inconsistent, or even contradictory (Killian and Lamy, 2013). These differences are likely to be due to the complex climatic patterns that exist throughout Patagonia because of the latitudinal range and orographic effects of the Andes. Further complexity is caused by local disturbances (e.g. tephra loading, fire, mass movements) which strongly influence records from this region, compounded by multifaceted proxies and chronological uncertainty.

Recent studies of past changes in the SWW have investigated peat sequences and lake deposits from South Atlantic islands (Unkel *et al*., 2008, 2010; Björck *et al*., 2012; Strother *et al*., 2015). These islands are potentially simpler environmental settings than southern Patagonia, with shallower precipitation and temperature gradients. Therefore, records from these islands may provide a more regional climate signal. The Falkland Islands (Islas Malvinas) lie beneath the core of the SWW, and changes in the abundance of long-distance pollen (*Nothofagus* – Southern Beach) and micro-charcoal have been linked with dynamic wind patterns affecting the archipelago (Turney *et al*., 2016; Thomas *et al*., 2018). Peatlands in the Falkland Islands have the potential to provide long records of environmental change, including the Pleistocene-Holocene transition (Wilson *et al*., 2002; Scaife *et al*., 2019). These systems include a higher mineral component than most global peatlands, and peat rarely exceeds 95% organic content, even in sites that are clearly ombrotrophic. This inorganic material is derived from a combination of local aeolian processes and far-travelled dust (including tephra) from southern South America (Payne *et al*., 2019; see Paper III). The abundance of mineral material in Falkland Islands mires make them ideal records for investigating past changes in peat geochemistry. This approach has been successfully used to reconstruct regional wind patterns and storm frequency (Unkel *et al*., 2008, 2010); however, remains under used (Longman *et al*., 2018).

Here, we present a multiproxy Lateglacial-early Holocene (*ca.* 16,500-6,450 cal yr BP) record of wind-strength, from a peat sequence in Hooker's Point (51°42'S, 57°47'W), Falkland Islands, South Atlantic. Particle size analysis and inorganic geochemistry are used together with previous analyses from this site (see Paper III; Scaife *et al*., 2019) to reconstruct past dynamics of the SWW.

7.2.1 The study site

The Falkland (Islas Malvinas) archipelago (51°-52°55'S, 57°40'-61°30'W) includes over 750 islands, and lies around 540 km east of southern South America, in the South Atlantic Ocean (Fig 7.1.). The islands lie beneath the core of the Southern Westerly Wind belt (SWW) (49-53^{o}S) and are affected by high monthly and annual wind speeds (mean values of 216-324 km/hr), which are dominated (74%) by westerlies from the sector 200-340° (Clark and Wilson, 1992; Upton and Shaw 2002; Lister and Jones, 2015).

The Hooker's Point sequence lies 3.5 km east of Stanley (Fig. 7.1), behind an active beach, and includes 4.65 m of peat strata. The lowermost 1.7 m of this sequence, analysed here, spans the Lateglacial and early Holocene time periods (*ca.* 16,500-6,450 cal yr BP). Wave action has caused partial erosion of the Hooker's Point peatland and prevents full topographical and basal surveys that would help establish the mire hydrological functioning. There is no evidence that the peatland in Hooker's Point became solely ombrotrophic during the past; however, the site lies in an area of low vertical relief and is unlikely to have been affected by fluvial transport processes (Fig. A4.1). Peat initiation began *ca.* 16,500 cal yr BP, over a former shallow lake-basin, and plant macrofossil, diatom and pollen analyses indicate that locally damp, sub-aerial, conditions continued almost throughout the Lateglacial. The pollen and plant macrofossil assemblage represents a local vegetation community dominated by *Empetrum rubrum*, Poaceae and monocotyledons (*Astelia pumila* in the modern setting) (Scaife *et al*., 2019), typical of peatlands in the Falkland Islands (Moore, 1968). Changes in the abundance of *Sphagnum* macrofossil remains and Poaceae pollen occur between 12,200-8,020 cal yr BP, indicating wetter conditions at the site during this time period (Scaife *et al*., 2019). The plant macrofossil assemblage is composed of freshwater peat taxa throughout the record, suggesting that the coring-site was unaffected by marine transgression during the Lateglacial and early Holocene.

The geomorphological setting and lack of fluvial influence at Hooker's Point means mineral content in the peat is almost entirely delivered through aeolian processes. Payne *et al*. (2019) suggest similar mechanisms affect a range of peatlands in the Falkland Islands which are characterised by a substantial (>5 %) inorganic, wind-borne component, derived from a combination of local and distal sources. The mineral content in Hooker's Point therefore provides a record of past wind strength affecting the study site.

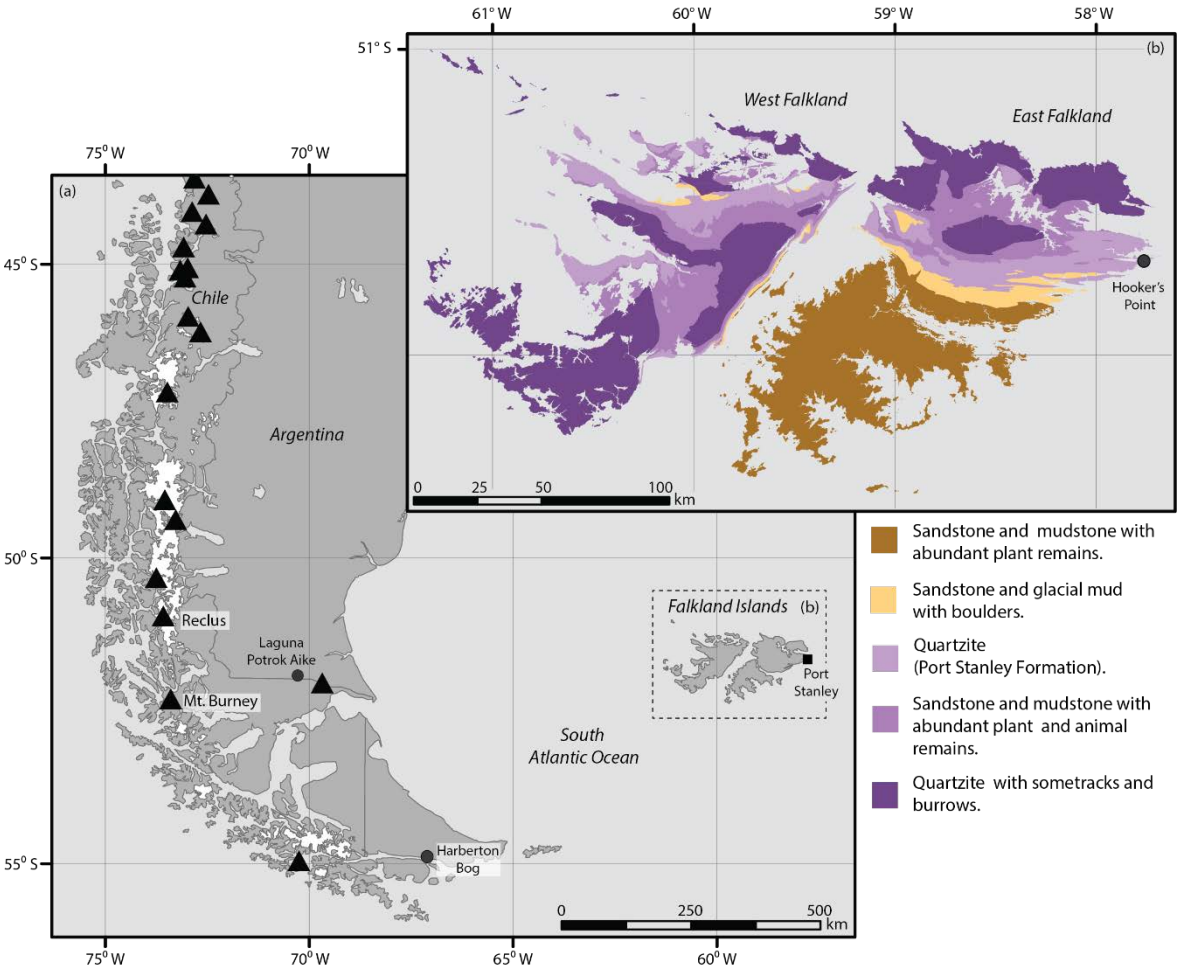

Figure 7.1: (a) The position of the Falkland Islands shown in relation to study sites and volcanoes (black triangles) described in the text. (b) The position of Hooker's Point and the major geological formations in the Falkland Islands.

7.3 Methods

7.3.1 Chronology

The chronology of the Hooker's Point sequence (Fig. 7.2) was first presented by Scaife *et al.* (2019), and is established from eight radiocarbon dates (Appendix D.1). An age-depth model was developed in the Bayesian statistical program OxCal v4.3 (Bronk Ramsey, 2017), using the SHCal13 calibration curve (Hogg *et al.,* 2013). A *P_Sequence* depositional model was run (Bronk Ramsey, 2009a) with a variable *k* factor (Bronk Ramsey and Lee, 2013) and outlier analysis (Bronk Ramsey, 2009b). The final age-depth model was tested against the published age ranges of the Mt. Burney MB_1 and Reclus volcano R_1 tephra beds (Fig. 7.2), which are identified in Hooker's Point as cryptotephra deposits (see Paper III).

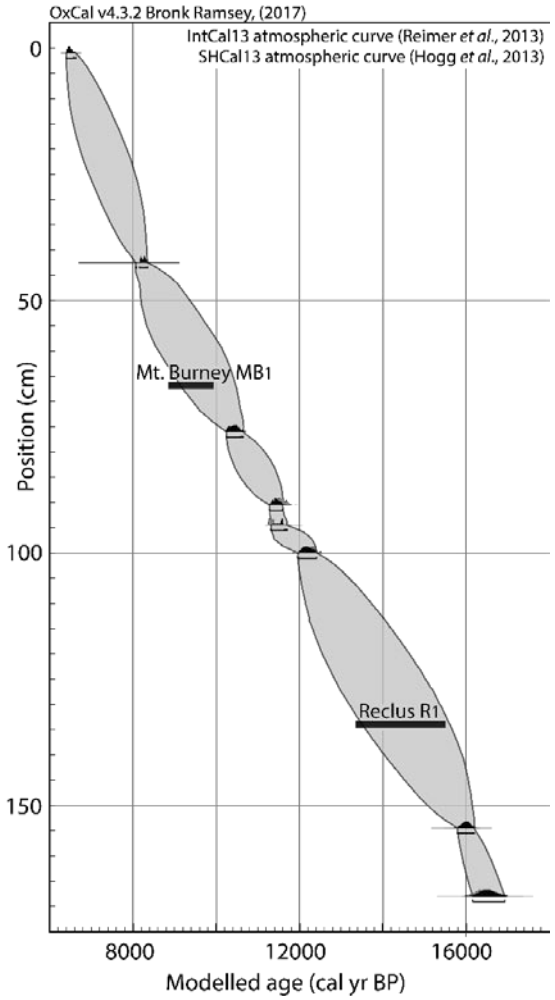

Figure 7.2: Oxcal age-depth model from the Hooker's Point sequence shown with 2σ calibrated error range. The published age ranges for the Mt. Burney MB_1 (9950-8850 cal yr BP; Stern *et al*., 2008) and Reclus R_1 (15,510-14,350 cal yr BP; McCulloch *et al*., 2005) tephra beds are shown as black bars, and provide an independent test of the age-depth model. The position of the cryptotephra deposits are taken from Paper III.

7.3.2 Particle size analysis

Particle size analyses were performed on contiguous four cubic centimetre peat samples taken at one centimetre intervals throughout the core. These were heated at 550 ^{o}C for two hours to remove organic material, and mixed with a weak dispersant solution of 5 % Sodium hexametaphosphate (Calgon) to form a homogenous paste. Particle size distribution measurements were made using laser diffraction on a Malvern Mastersizer 3000 and are reported as average values derived from five repeated measurements. For each analysis settings were adjusted so that the standard deviations of these five measurements were below 5 % for the D10, D50 and D90 values. These adjustments included adding more sample material to increase obscuration and/or the application of ultrasound.

7.3.3 X-ray Fluorescence core scanning

X-ray Fluorescence (XRF) core scanning was conducted on continuous peat samples taken at one centimetre intervals using a mounted Niton XL3 XRF analyser. Before XRF analysis was undertaken, samples were freeze-dried, ground, and covered with film to homogenise the material, reduce surface roughness, and remove water content, which can negatively affect the data quality of XRF core scanning results (Croudace and Rothwell, 2015). Data are presented as percentage values and are considered as semi-quantitative because of the difficulties in analysing highly organic peats. We restrict our discussion to elements which occurred in high abundance or compared well with loss on ignition or Inductively Coupled Plasma Mass Spectrometry (ICP-MS) analyses (Si, Al, Ti, K, Ca, Cl, S and Sr) (Figure A4.3). A single peat sample from Hooker's Point (HP_14) was used as an internal standard and repeatedly run every 15 analyses to check for instrumental drift (Appendix D.2 Fig. D.2).

7.3.4 Inductively Coupled Plasma Mass Spectrometry

Forty one bulk peat samples were processed for element geochemistry using Inductively Coupled Plasma Mass Spectrometry (ICP-MS). Samples were taken at 3-6 centimetre intervals, based on the results from particle size analysis and XRF core scanning. Analyses were conducted using a ThermoFisher X Series 2 Inductively Coupled Plasma Mass Spectrometer at the National Oceanography Centre, Southampton. Dried peat samples were burnt for two hours at 550°C and placed in glass vials. Following burning, these samples were transferred to acid-washed Teflon® bombs and digested in HNO_3/HF/H_2O_2 overnight. The digested samples were made up to a mother solution in HCl. Metal elemental analyses were made for Ca, Ti, Fe, Sr, Zr, Ba, Th, U and 14 Rare Earth Elements (REE).

Rock standards CBlk, BHVO2, BIR-1, JB-1a, JGB-1, JB-3, JB-2, AGV-2, BCR-2, JA-2, BRR-1 and BAS206 were run alongside samples from Hooker's Point in order to monitor analytical performance. Standard measurements typically varied by no more than 5 % relative standard deviation (%RSD) across all measured elements. For example, measurements of BIR-1 varied between 4.70 %RSD in Li and 0.59 %RSD in Ti. Four blank samples were also run during ICPMS analysis in order to assess the reproducibility of the acid digestion method – measurements were <1 ppb for REEs and <1 ppm for Ca, Ti, Fe, Sr, Zr, Ba, Th, U.

7.3.5 Dust flux quantification

The dust flux rate (FR) (g m^{-2} yr^{-1}) for each sample analysed with ICPMS was calculated from the REE concentrations measured in the peat using the following equations:

$$Total\ REE\ AR\ (\mu g cm^{-2}\ yr^{-1}) = \sum (REE)_t \times peat\ AR\ \times density \qquad (1)$$

$$Dust\ FR = total\ REE\ AR / \sum (REE)_{UCC}\ \times 10{,}000 \qquad (2)$$

where the sum of REE concentrations (REE_t) in the upper continental crust (UCC) is taken as 148 µg/g (Rudnick and Gao, 2003) and the peat accumulation rate (AR) is derived from the chronology of the Hooker's Point sequence. The bulk density of each peat sample was determined by weighing measured (1 cm^3) samples, which were dried overnight at 105 ^{o}C.

7.4 Results and discussion

7.4.1 Particle size analysis

Particle size analysis indicates that the mineral component of the Hooker's Point peat sequence is predominately comprised of silt (2-63 µm), with a secondary fraction of very fine sand (63-125 µm). Clay content declines early in the record, from a maximum of six percent, and remains low throughout the analysed section (Fig. 7.3). The sand component (>63 µm) present in Hooker's Point must be derived from local sources because of the distance between South America and the Falkland Islands (~540 km); however, the silt fraction (2-63 µm) is likely to include dust from reworked loess, tephra deposits and desiccated lake beds in southern Patagonia (Bullard *et al*., 2016). These sources supply ~30 × 10^6 t yr^{-1} of dust to the South Atlantic shelf (Gaiero *et al*., 2003), which is observed in the atmosphere over the Falkland Islands (Li *et al*., 2010; Neff and Bertler, 2015).

Two periods of raised particle size occur in the Hooker's Point sequence, between 133-114 cm (14,470-13,080 cal yr BP), and 37-35 cm (*ca.* 8000 cal yr BP) (Fig. 7.3). The first event, 133-114 cm, includes high abundances of very fine sand (maximum 21 %) and fine sand (maximum 12 %) relative to background values. This increase in particle size is interpreted as a strengthening of the wind speed affecting Hooker's Point and coincides with the Antarctic Cold Reversal (14,700-13,000 yr BP; Pedro *et al*., 2011). The second event, between 37-35 cm (*ca.* 8000 cal yr BP), is characterised by a sharp influx of medium sand (250-500 µm). The size distribution of the mineral content at this depth is distinct from any period in the Hooker's Point sequence (Fig. 7.4). Strong winds are likely to have affected Hooker's Point throughout the Lateglacial and early Holocene, however; these were insufficient to transport medium sand to the study site during any other time period. Therefore, event 37-35 cm must have been deposited during an extremely high energy event. The proximity to the ocean, and low topographical relief surrounding Hooker's Point, suggests that the sand influx between 37-35 cm is likely to have been derived from a storm event. Similar sand (>250 µm) influxes in coastal peat-bogs have been used to examine past storm frequencies in southern Sweden during the mid-late Holocene (Björckl and Clemmensen, 2004; De Jong *et al*., 2006), and younger peat deposits at Hooker's Point may preserved a similar record. Prior to 'event 37-35 cm' the study site is likely to have been protected from storm events by an extended foreshore caused by lower sea levels, which rose around 90 m during the study period, peaking *ca.* 7000 cal yr BP (Ponce *et al*., 2011; Newton, 2017).

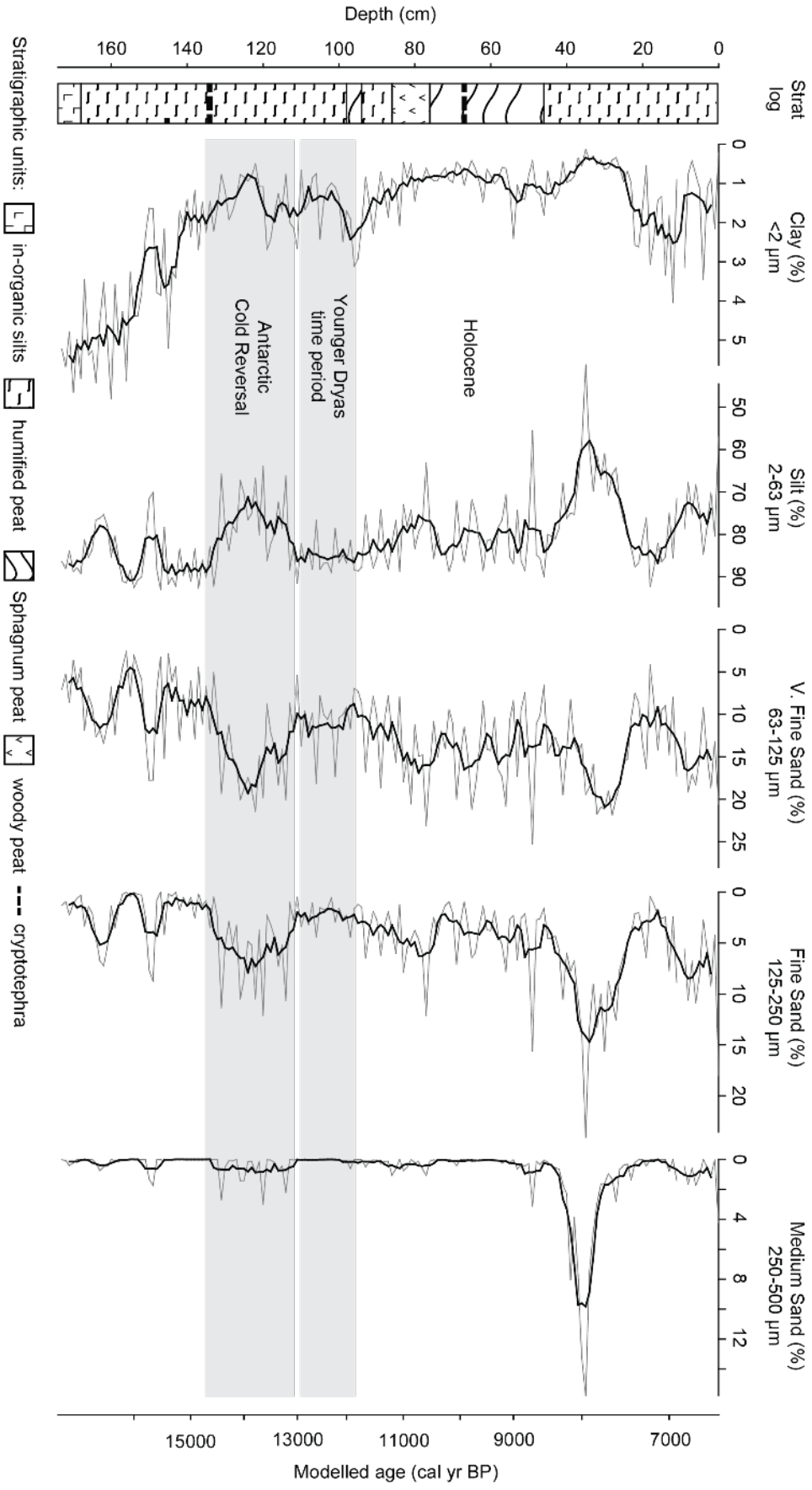

Figure 7.3: Particle size analysis results from Hooker's Point plotted alongside plant macrofossil stratigraphy from Scaife *et al*. (2019). The position of cryptotephra deposits are reported in Paper III.

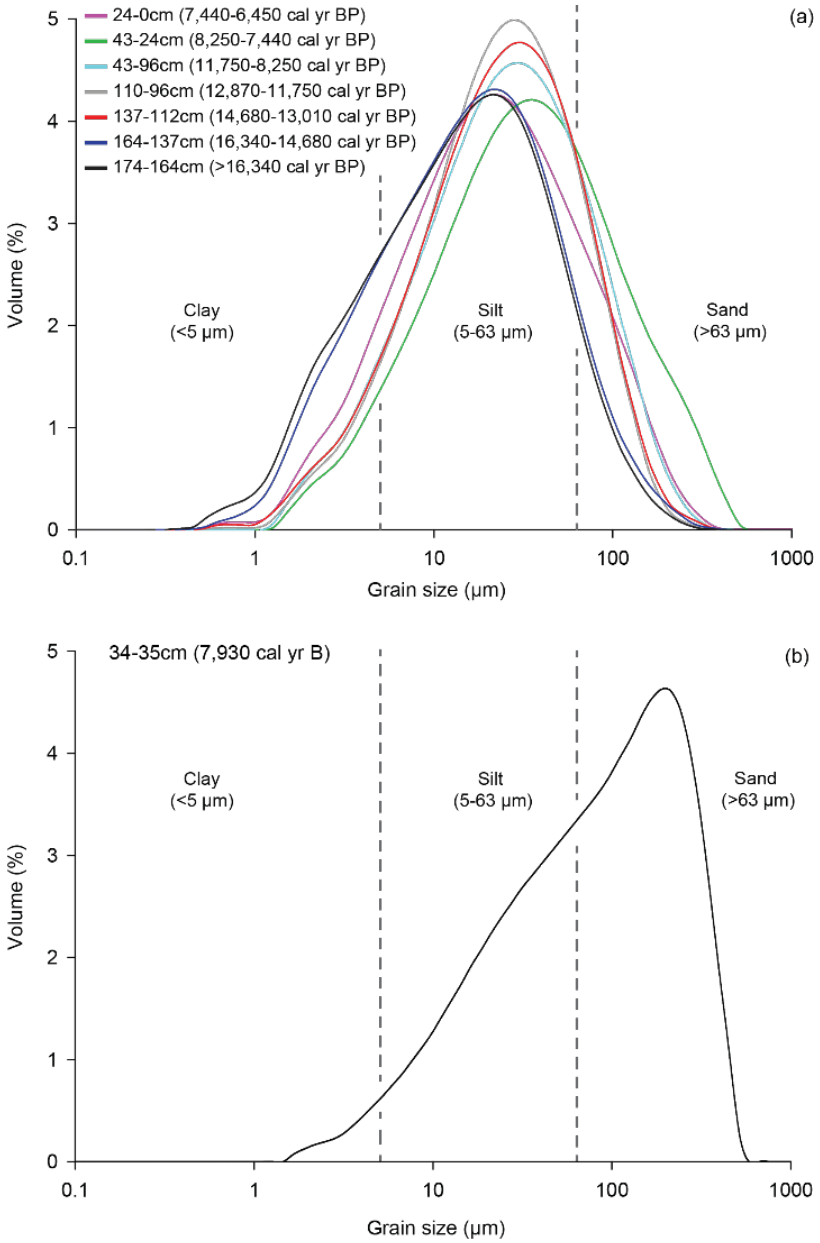

Figure 7.4: Averaged (mean) particle size analysis results from the Hooker's Point sequence.

7.4.2 Interpretation of geochemical data

In the Hooker's Point sequence, lithogenic elements Si, Al, Ti and K are closely linked with the abundance of mineral material in the peat. Si, in particular, follows an inverse pattern to variability in organic content throughout the record and is unaffected by other environmental changes (Fig. 7.6). Hooker's Point lies within the Port Stanley geological formation (Fig. 7.1), a 400 million year old sedimentary unit formed of quartz-rich sandstone (Aldiss and Edwards 1999; Stone, 2010). Modern beach sands in Hooker's Bay and Surf Bay (adjacent to Hooker's Point) are derived from this unit, and are composed of >98 % Si (Greenway, 1972). Therefore, Si values within the peat sequence analysed here are most likely to reflect the deposition of local material eroded from the parent bed rock.

Fe is commonly used as an indicator of terrigenous input to peatlands (Longman *et al*., 2018); however, it is prone to remobilisation in wet conditions (Croudace and Rothwell, 2015). In the Hooker's Point record Fe loosely follows the declining trend observed in other lithogenic elements (Si, Al, Ti, and K) (Fig 7.5.), although with a greater degree of variability, which is likely to be caused by remobilisation of the element in the damp peat. This relationship breaks down between 13,000-10,500 cal yr BP, where the abundance of Fe increases despite a reduction in Si and Ti, suggesting that Fe is unrelated to terrigenous input at this time. Schittek *et al*. (2015) used the ratio of Fe/Ti to infer changes in redox conditions in a peatland from the Peruvian Andes, and in Hooker's Point this ratio coincides with changes in the plant macrofossil assemblage, suggesting that Fe is driven by a similar process here (Fig. 7.6).

Ca does not change with lithogenic elements, but co-varies closely with Sr in the Hooker's Point record, suggesting that both elements have a biogenic origin (Croudace and Rothwell, 2015). Biogenic Ca is linked with $CaCO_3$, as organic accumulation leads to higher consumption of CO_2, and higher pH, leading to precipitation of $CaCo_3$. (Boyle, 2001). In peatlands where Ca has been shown to have a biogenic origin the ratio of Ca/Ti has been used to infer organic productivity (e.g. Turner *et al*., 2015) and trophic status (e.g. Poto *et al*., 2013), and it is likely that in the Hooker's Point record Ca variability reflects similar processes.

Ca XRF data does not agree with ICPMS analyses from the earliest deposits in Hooker's Point (Fig. A4.3). This apparent divergence is caused by the abundance of other elements during this period as the XRF analyses are presented as percentage data, which are allowed to act more independently later in the record because of the high abundance of organic C, which is not measured during XRF core scanning. The effects of this are removed where Ca XRF analyses are used as part of a ratio with a lithogenic element (Fig. 7.5).

XRF analyses of Cl show two prominent rises between 16,000-14,000 cal yr BP and 12,800-11,600 cal. yr BP (Fig. 7.5). Maximum values reach 7 % making Cl one of the most abundant elements in Hooker's Point during these time periods. Cl has been used (along with Br) to infer marine influences on coastal peatlands – particularly storm frequency (Schofield *et al*., 2010). However, in the Hooker's Point sequence Cl is unaffected by both the storm event *ca*. 8000 cal yr BP, and rising sea levels (Fig. 7.7), suggesting that in this record Cl is unlikely to have a marine origin. The initial phase of elevated Cl occurs during the Lateglacial, when precipitation in the Falkland Islands was likely to have been lower because of an enhanced precipitation gradient over the Patagonian ice-sheet. This aridity may have caused high levels of evaporation leaving sodium chloride on the landscape – increasing Cl abundance in Hooker's Point. The second period of raised Cl occurs with elevated Ca, previously attributed to organic productivity. Halogens, including Cl, have been linked with peat decomposition using C:N ratios (Biester *et al*., 2004), and it is possible that the second phase of Cl deposition is linked with these processes.

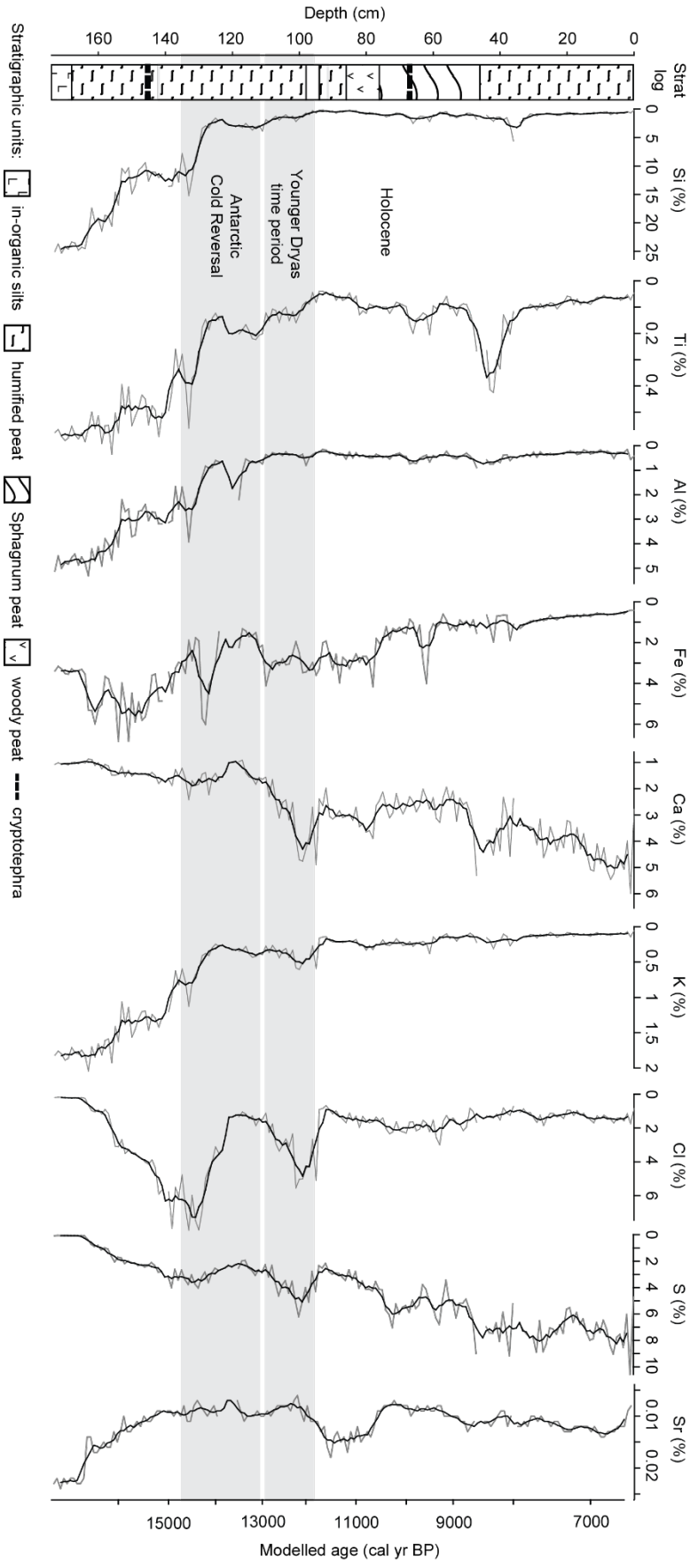

Figure 7.5: XRF results from Hooker's Point plotted alongside the plant macrofossil stratigraphy from Scaife *et al*. (2019).

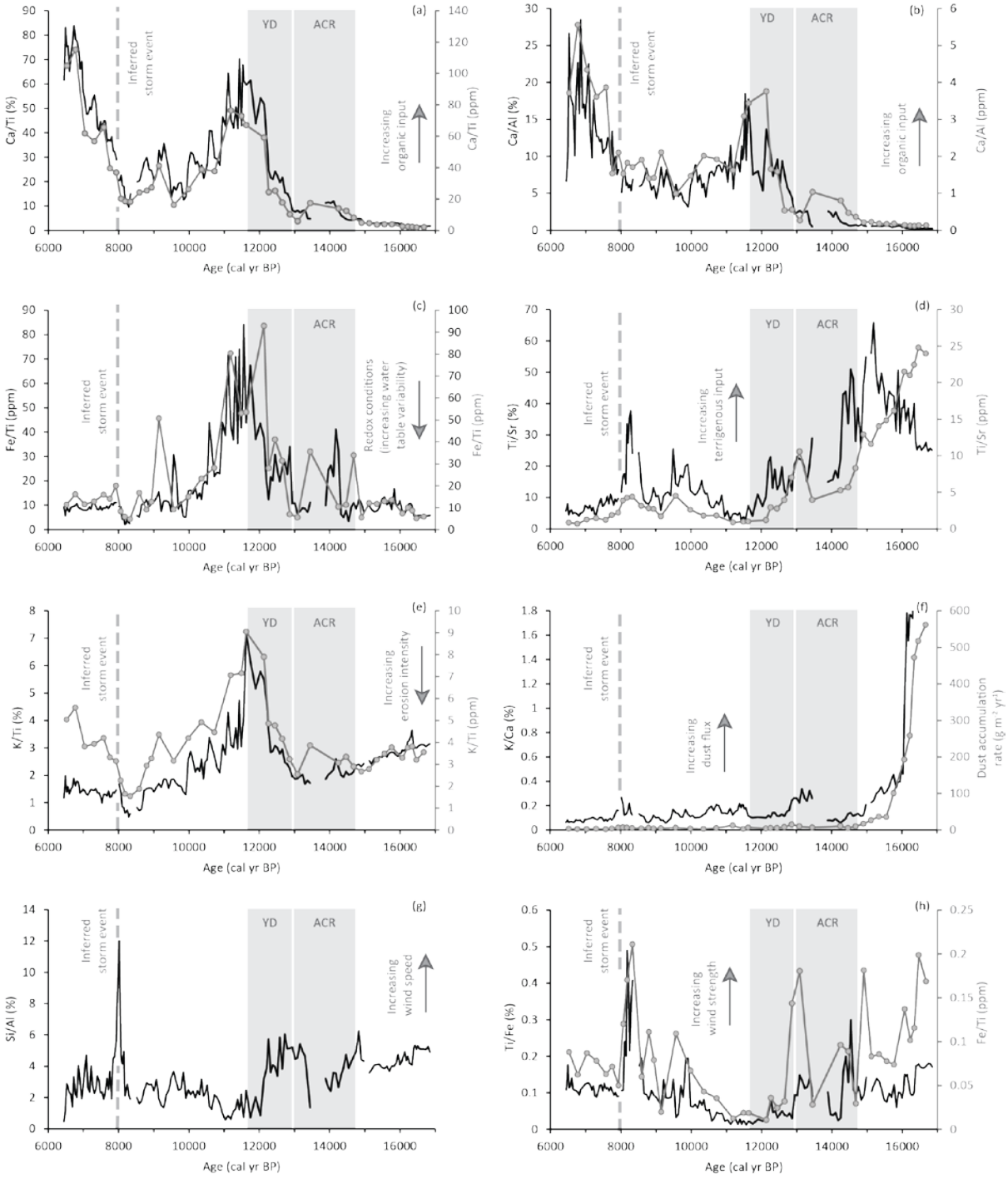

Figure 7.6: Element ratios associated with aeolian deposition and wind speed plotted using XRF and ICPMS analyses from the Hooker's Point sequence. These ratios were developed in (a) Turner *et al*. (2015), (b) Blanchet *et al*. (2009), (c) Schittek *et al*. 2015), (d) Zaragosi *et al*. (2006), (e) Piva *et al*. (2008), (f and g) Hanebuth and Henrich (2009) and (h) Zarriess and Mackensen (2010).

7.4.3 Palaeoenvironmental interpretation

7.4.3.1 16,850-16,000 cal yr BP

The earliest period of the Hooker's Point record is strongly influenced by factors unrelated to wind strength. Particle size analyses indicate a low energy system; however, inorganic content and Si values are elevated suggesting considerable input of local material (Fig. 7.5). During the earliest stages of peat accumulation this local mineral material may have been delivered to Hooker's Point through fluvial processes as the peatland underwent paludification. Aeolian material is also likely to be more abundant during this period, as lower sea levels exposed greater areas of the continental shelf to wind erosion (Fig. 7.8), which may have been enhanced by surface instability because of reduced vegetation cover in what was a dry, cold, steppe environment (Scaife *et al*., 2019).

The Hooker's Point record is also likely to have been affected by elevated dust production in Patagonia at this time (Lambert *et al*., 2008). Throughout glacial periods the Antarctic ice cores preserve dust concentrations 20-50 times higher than during interglacials, which are linked with the terminal positions of Patagonian glaciers (Sugden *et al*., 2009). Although Antarctic dust concentrations fall rapidly during the Lateglacial, as glaciers retreat into proglacial lakes, values remain high during the earliest time period spanned by the Hooker's Point sequence (Fig. 7.8).

7.4.3.2 16,000-14,400 cal yr BP

Between 16,000-14,400 cal yr BP the abundance of organic matter increases in two stepped intervals (*ca*. 16,000 cal yr BP and *ca*. 14,680 cal yr BP), closely mirrored by decreases in lithogenic elements (S, Al, Ti and K) (Figs. 7.5 and 7.7). These shifts suggest that the transport processes depositing inorganic material in the Hooker's Point peatland altered at these times, and it is likely that these change represent the end of fluvial influence at the study site.

7.4.3.3 14,400-13,000 cal yr BP

The minerogenic content in Hooker's Point coarsens and includes a higher percentage of sand-sized particles between 14,450-12,870 cal yr BP, suggesting greater wind speeds affected the study site during this period (Fig. 7.3). This increased transport capacity is also apparent in several elemental ratios linked with aeolian input and wind-strength at this time (Fig. 7.6). Regionally, this period is associated with the Antarctic Cold Reversal (ACR) (14,700-13,000 yr BP), a pause in Southern Hemisphere warming expressed as (0.5°C) cooling, and local drying, in the Falkland Islands (Pedro *et al*., 2011, 2016).

7.4.3.4 13,000-10,400 cal yr BP

From *ca*. 13,000 cal yr BP the abundance of lithogenic elements (Si and Ti), and element ratios linked with aeolian input, decline to minima between 11,750-10,950 cal yr BP (Figs. 7.5 and 4.5). This decline is also evident in the record of particle size from Hooker's Point, which includes lower sand abundances during this period, and a rise in the percentage of clay *ca*. 11,750 cal yr BP (Fig. 7.3). Together, these changes indicate a reduction in wind speed over the Falkland Islands at this time, which is supported by the palaeoecological record from Scaife *et al*. (2019): Poaceae abundance declines sharply from *ca*. 12,180 cal yr BP, reaching a minimum *ca*. 11,680 cal yr BP. While *Sphagnum* enters the record for the first time *ca.* 12,200 cal yr BP, indicating wetter peatland surface conditions at the study site. This change suggests that the balance between precipitation and evaporation (P-E) shifted towards a smaller water deficit or water surplus in the Hooker's Point peatland, which is likely to be because of a reduction in the dominance of westerly winds, allowing more frequent moisture bearing easterly winds to affect the archipelago.

7.4.3.5 10,400-8000 cal yr BP

The time period 10,400-8000 cal yr BP is characterised by a gradual rise in lithogenic elements (Si and Ti), and a return to a grass dominated local environment (Scaife *et al*., 2019), indicating the return of strong winds over the Falkland Islands. A second increase in *Sphagnum* abundance occurs in the plant macrofossil record independently of pollen and geochemical analyses during this period. This divergence between the local vegetation and more regional proxies suggests that these wetter conditions were driven by peatland functioning, and not a wider climatic driver. The latest part of this period of increased wind speed is obscured by a storm event *ca*. 8000 cal yr BP, where input of local material overrides the influence of wind on the palaeoenvironmental record. Downward reworking of fine material from this storm event causes Ti values to rise early, before being obscured by Si from the larger sand grains derived from this event (Fig. 7.5).

7.4.3.6 8000-6450 cal yr BP

Particle size data return to values similar to those preceding the storm event from *ca.* 7450 cal yr BP. Lithogenic elements remain low from this time, and element ratios linked with increasing biogenic sedimentation increase, suggesting a reduction in the abundance of aeolian material in the Hooker's Point record.

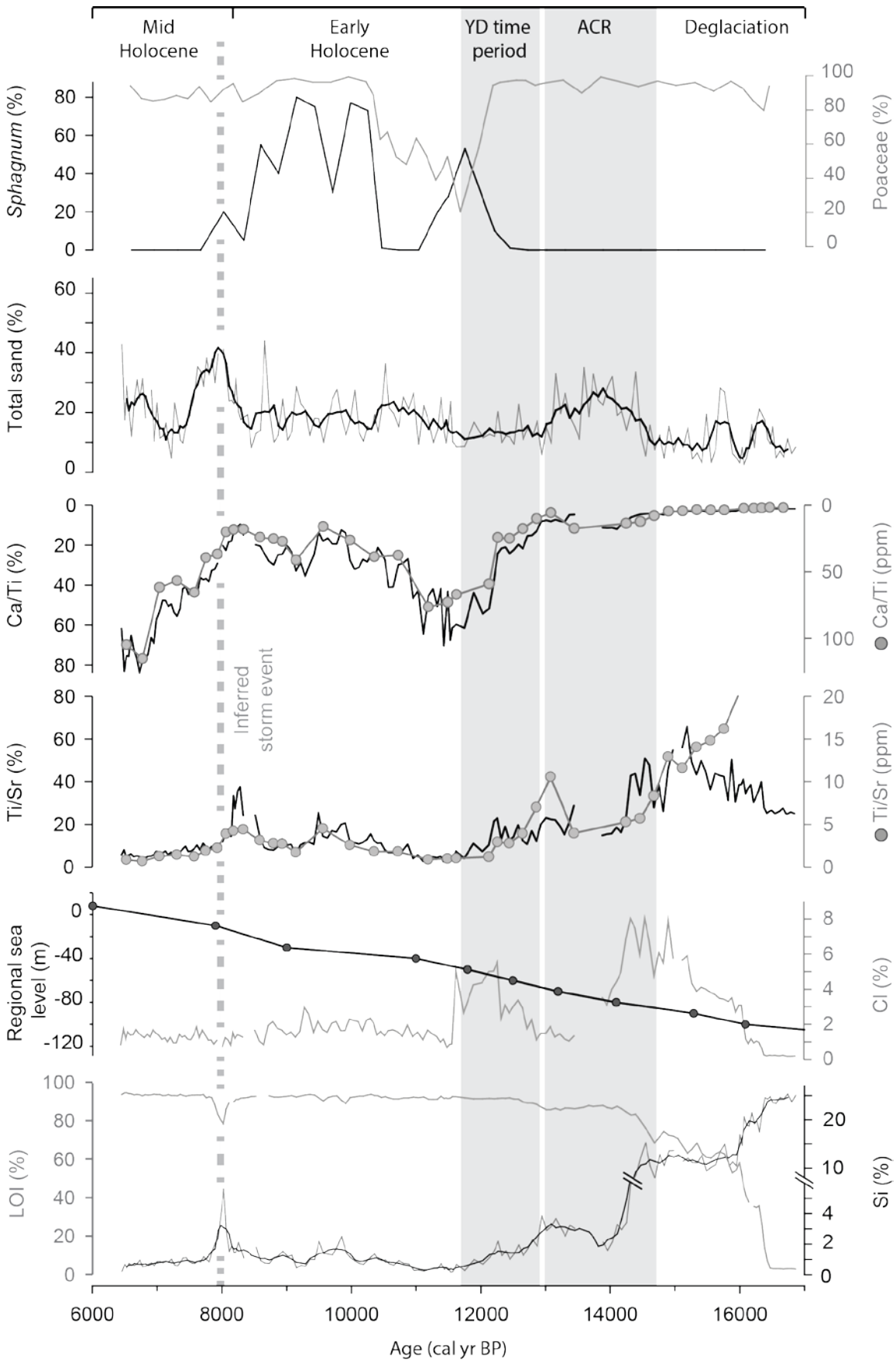

Figure 7.7: Palaeoenvironmental data from Hooker's Point. Plant macrofossil data and pollen data (*Sphagnum* and Poaceae) first published by Scaife *et al*. (2019). Regional sea level curve is taken from Ponce *et al*. (2011).

7.4.4 Dynamics of the Southern Westerly Wind belt

Lithogenic input and the abundance of sand in the Hooker's Point record increase from *ca*. 14,400 cal yr BP, and remain elevated throughout the Antarctic Cold Reversal (14,700-13,000 yr BP) (Fig. 7.7). This time period has been associated with a strengthening of the Southern Westerly Wind belt in palaeoenvironmental records throughout Patagonia, and our new study extends this observation into the South Atlantic (Moreno *et al*., 2012; Garcia *et al*., 2012; Vanneste *et al*., 2015). Conversely, wind strength proxies and Poaceae abundance decline in Hooker's Point during the Younger Dryas time period and early Holocene (12,900-11,700 yr BP), suggesting that the SWW either weakened or shifted latitude, away from the Falkland Islands, at this time. It has been hypothesised that a southern movement of the atmospheric intertropical convergence zone (ITCZ) displaced the SWW southward during the Younger Dryas time period (Fig. 7.8) (Anderson *et al*., 2009; Schneider *et al*., 2014; Buizert *et al*., 2018), and records to the South of Hooker's Point continue to record high wind speeds throughout this period, supporting this assertion (Vanneste *et al*., 2015). However, this pattern is not consistently expressed throughout Patagonian, and wind proxies in the Laguna Potrok Aike record (Mayr *et al*., 2013), Argentina, remain elevated in contrast to Hooker's Point, despite negligible difference in latitude between the two study sites. These differences may be because of real spatial variability in the strength of the SWW, proxy insensitivy or chronological uncertainty. The Mt. Burney M_1 tephra deposit is identified in both records (Haberzettl *et al*., 2007; see Paper III), and demonstrates a chronological offset of around 500 years between Hooker's Point and Laguna Potrok Aike (core PTA03) at this tie point. A similar offset during the Lateglacial would help to resolve the apparent divergence in wind strength between Hooker's Point and Laguna Potrok Aike.

Aeolian proxies in the Hooker's Point sequence record a gradual increase in wind strength over the Falkland Islands from *ca*. 10,400 cal yr BP, culminating in a storm event *ca*. 8000 yr BP. A similar increase in wind speed is observed in the long distance pollen record from Laguna Potrok Aike, where the abundance of Andean forest taxa pollen (mostly *Nothofagus*) rises between 9200-7000 cal yr BP (Mayr *et al*., 2007; Oehlerich *et al*., 2015). In Hooker's Point the period of strengthening SWW ends shortly after *ca.* 8000 cal yr BP, where it is obscured by the storm event; however continues until *ca.* 7000 cal yr BP in Laguna Potrok Aike. Conversely, palaeoenvironmental records from West of the Andes indicated lower wind speeds during the early Holocene (Lamy *et al*., 2010). This contrast between records either side of the Andes is hard to resolve; however, may suggest the SWW was more meridional during periods in the past, and that changes in the position of the core flow where more complex than consistent hemispheric latitudinal shifts (Fletcher and Moreno, 2012; Turney *et al*., 2018).

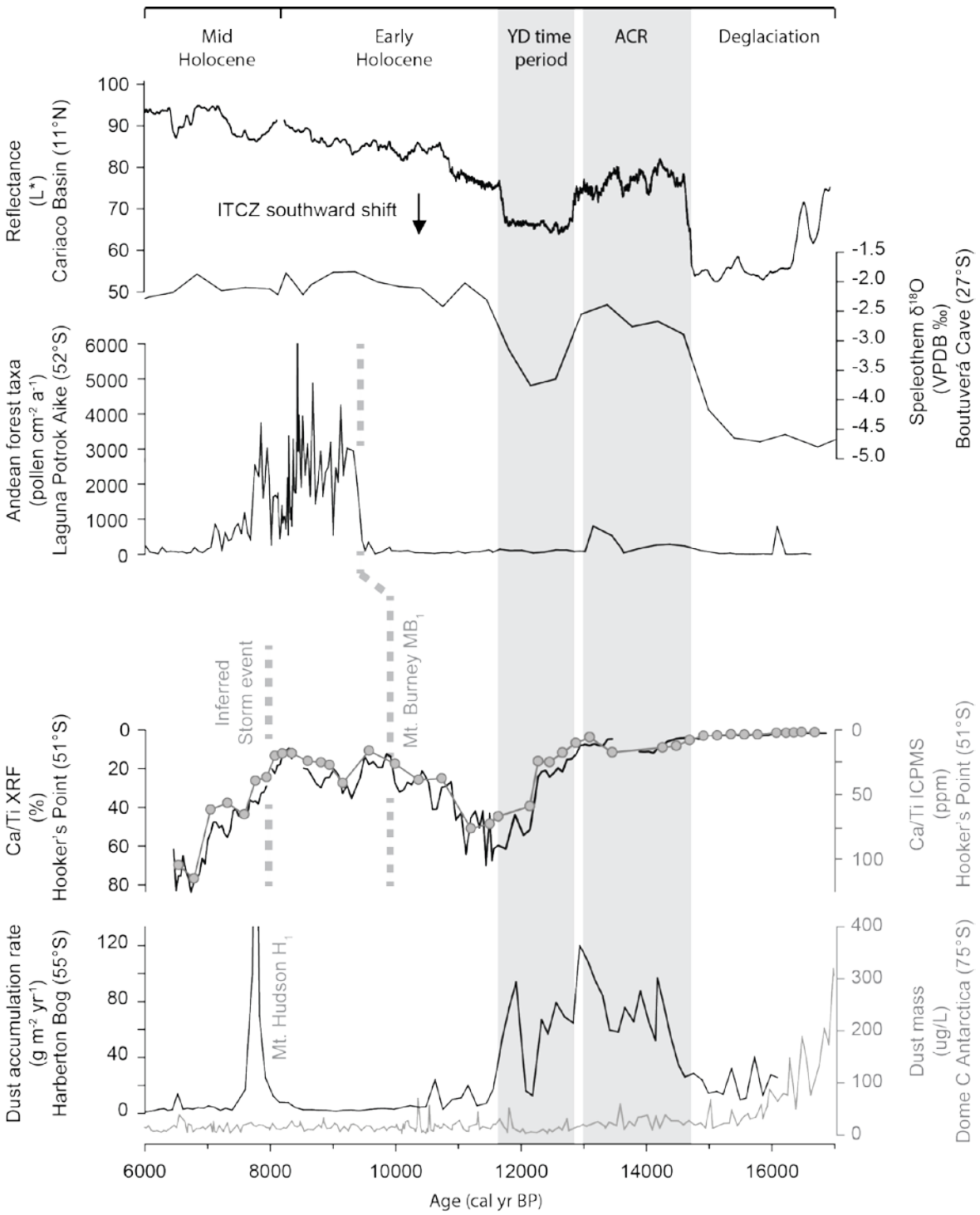

Figure 7.8: Palaeoenviromental data from Hooker's Point, the Cariaco Basin (Deplazes *et al*., 2013), Boutuverá Cave (Wang *et al*., 2007), Laguna Potrok Aike (Mayr et al., 2007; Oehlerich *et al*., 2015) and Harberton Bog (Vanneste *et al*., 2015) The positions of the Mt. Burney Mb_1 tephra is reported in the Hooker's Point record by Paper III and Laguna Potrok Aike record by Haberzettl *et al*. (2007).

7.5 Conclusions

Changes in lithogenic elements and particle size can be used to infer strong wind speeds over Hooker's Point during the Antarctic Cold Reversal (14,700-13,000 yr BP). This finding is well supported by records of glacial advances, vegetation composition and dust flux in southern South America, linked with a strengthening of the core SWW at this time (Moreno *et al*., 2012; Garcia *et al*., 2012; Vanneste *et al*., 2015).

Wind speeds fall rapidly during the Younger Dryas time period (12,900-11,700 yr BP), reaching a minimum *ca.* 11,650 cal yr BP. Comparison with regional records from eastern and southern Patagonia (Fig. 7.8) suggests that this reduction in wind speed is linked with a southward displacement of the SWW, away from the Falkland Islands.

Wind speed increases again during the latter part of the early Holocene. This strengthening of the SWW belt is also observed at Laguna Potrok Aike (Mayr *et al*., 2007; Oehlerich *et al*., 2015); however, it is in antiphase with records to the west of the Andes (Lamy *et al*., 2010). The difference between records either side of the Andes highlights the complexity of the past climate gradients that existed across the Andes and the South Atlantic Ocean. Recognition of these climate differences and the ability to distinguish them from measurement error provides the basis for building a detail picture of past climate variability. Only when these gradients are well understood in the southern hemisphere will we be able to use palaeoclimate records to provide an accurate baseline for distinguishing between modern climate variability and climate change. To separate changes in the intensity of the SWW belt from changes in the latitudinal position, a series of well-dated, multi-proxy records – independent of temperature and/or precipitation are needed across a broad longitudinal and latitudinal range.

7.6 Acknowledgements

We are grateful to Prof Robert Scaife, Prof Anthony Long and Prof Mike Bentley for access to the Hooker's Point peat sequence and radiocarbon dating. Fieldwork for this project was funded by the Shackleton Trust, and was supported by the Falkland Islands Bureau of Mineral Resources. Alex Blake assisted in sample collection from Hooker's Point. Dr Christoph Mayr kindly provided comparative Andean forest taxa data, and chronology, from Laguna Potrok Aike.

Chapter 8 Synthesis and discussion

Chapter 8 will synthesise the key findings from Papers I-IV in order to address the research objectives of this thesis. A second section in this chapter presents future research directions which were raised during the literature review and Papers I-IV - including new pilot data.

8.1 Investigating past ash dispersal patterns

The primary aim of this thesis is to: *investigate past changes in ash dispersal patterns using distal cryptotephra deposits*. In order to achieve this two case studies were examined: eastern North America and the Falkland Islands, South Atlantic. Both of these regions are likely to have been affected by changes in atmospheric circulation patterns during the past, which must have influenced the dispersal of volcanic ash.

8.1.1 Case Study I: eastern North America

Paper II uses new study sites and community data to answer research question Q.2.1: *Did early Holocene changes in atmospheric circulation enhance ash dispersal over North America*? This question was first raised by Pyne-O'Donnell *et al*. (2012), who noted an absence of cryptotephra deposits below the Mazama ash in Nordan's Pond Bog, Newfoundland. The authors hypothesised that the absence of early Holocene cryptotephra deposits was because of the influence of the Laurentide ice-sheet on regional atmospheric circulation. By combining new cryptotephra records from this thesis (Long Pond Bog, Pound Cove Bog, Sidney Bog, Southwest Pond Bog and Nuangola Lake) with unpublished community data, and the existing regional tephrostratigraphy (Pyne-O'Donnell *et al*., 2012, 2016; Mackay *et al*., 2016; Hughes *et al*., in prep; Jensen *et al*., in prep), Paper II was able to address this hypothesis.

The results from Paper II demonstrate an upturn in the frequency of ash fall events over eastern North America after *ca.* 7,600 cal yr BP, beginning with the Mazama ash (7,680-7,580 cal yr BP; Egan *et al*., 2015). Three hypotheses are raised to explain this upturn in ash delivery; however, only one cannot be refuted: *Change in the frequency of tephra deposits in eastern North America is caused by shifts in atmospheric circulation*. It is difficult to provide a detailed mechanism for this shift as the atmospheric conditions over eastern North America are poorly resolved during the early Holocene, and appear to have been spatially and temporally complex (Dean *et al*., 2002; Wilson *et al*., 2010; Finkenbinder *et al*., 2016). However, the collapse of the Laurentide ice sheet must have led to a reorganisation of atmospheric circulation because of the dramatic change in topography

across North America (Pausata *et al*., 2011). And therefore it is likely that this glacial retreat lead to enhanced tephra dispersal over North America after *ca*. 7,600 cal yr BP.

Paper II provides the first evidence that changes in the frequency and provenance of ultra-distal cryptotephra deposits may record dynamic tephra dispersal patterns over millennial timescales, and that in some cases tephra records may be used to support investigations of past changes in atmospheric circulation. This finding also demonstrates that the atmospheric conditions affecting ash cloud dispersal should be considered by studies using cryptotephra deposits to provide estimates of ash fall reoccurrence intervals, as they may be affected by process other than eruption frequency (e.g. Swindles *et al*., 2013; Watson *et al*., 2017).

The density of cryptotephra records in eastern North America also provides the first opportunity to examine spatial patterns in ash fall over this region. There appears to be a reduction in both the number of cryptotephra deposits, and their shard abundance, in north-western Newfoundland during the Holocene (Fig. 8.1). This pattern may represent the northern margin of the Jet stream's typical position, which is likely to play a key role in the dispersal of tephra over North America (see Section 2.1.1.). More study sites are needed to test this hypothesis; however, using tephra deposits in this way may help to support studies of past air mass change.

The dispersal of past ash clouds can now begin to be reconstructed using the dataset developed during this thesis. For example, none of the new study sites contain a cryptotephra deposit linked with the Aniakchak CFE II eruption, suggesting that Nordan's Pond Bog, Newfoundland, marks the southern limit of this ash cloud (Pyne-O'Donnell *et al*., 2012). Continued development of the regional tephrostratigraphy will allow for further examinations of spatial patterns in ultra-distal tephra deposits, similar to those undertaken in Europe (Wastegård and Davies, 2009; Lawson *et al*., 2012).

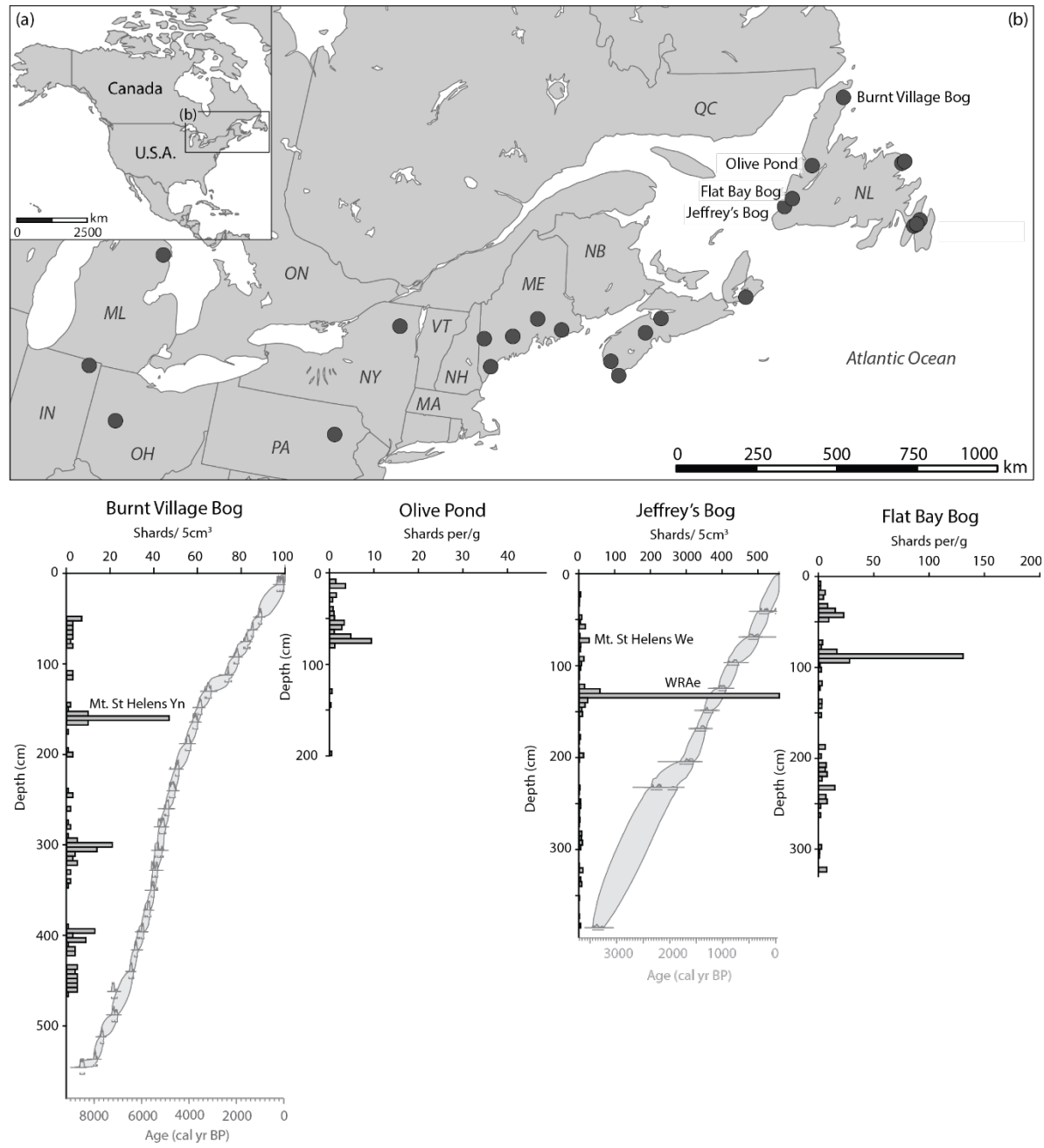

Figure 8.1: Shard profiles and locations of cryptotephra records from north-western Newfoundland, characterised by low shard abundances. The positon of published, and new, study sites presented in chapter II are shown as unlabelled grey circles.

8.1.2 Case Study II: The Falkland Islands

The Falkland Islands provide a more complex example of ash dispersal than Case Study I. Paper III demonstrated that the record of primary ash fall in the Falkland Islands is obscured by detrital glass, reworked from the Patagonian Steppe. However, temporal patterns are observed in the Hooker's Point sequence, with a reduction in the abundance of tephra between 14,300-10,500 cal yr BP. Therefore, detrital glass in the Falkland Islands may provide evidence for past changes in the dispersal of volcanic ash over this region. Before investigating ash dispersal patterns it is important to interpret the environmental processes controlling the abundance of detrital glass in the Falkland Islands. This section combines the tephrostratigraphy of Hooker's Point with records of wind-strength (Paper IV) and past vegetation change (Scaife *et al*., 2019) in order to understand these processes. In doing so two research questions from this thesis are addressed:

> Q.2.2 Are Lateglacial and early Holocene changes in the strength of the Southern Westerly Wind belt expressed in the abundance of tephra in the Falkland Islands?
>
> Q.2.4 Do past changes in the local environment or depositional processes coincide with changes in the abundance of reworked tephra in the Falkland Islands?

Hall *et al*. (2001) report chaotic shard profiles from three study sites in the Falkland Islands that are strongly affected by reworked volcanic glass. The authors suggest that these deposits are likely to have developed following vertical reworking of *in-situ* primary tephra deposits – promoted by the plant communities forming the peat (C*ortaderia pilosa*, *Bolax gummifera* and *Eriophorum* sp.). This hypothesis can be rejected using data from Paper III which shows that reworked tephra deposits in the Falkland Islands are formed of chemically and morphologically heterogeneous glass shards, which must have been heavily weathered before burial.

The earliest deposits from Hooker's Point (17,200-15,780 cal yr BP) include a high abundance of reworked glass, before the signal is obscured by primary ash fall from the Reclus R_1 eruption (*ca.* 15,530 cal yr BP at Hooker's Point). This period is characterised by low organic content and high Si values, relative to the rest of the Hooker's Point record (Fig. 8.2), caused by the deposition of local mineral material (see Paper IV). During this early period of peat development in Hooker's Point the record is strongly affected by input from the local region. Lower sea levels exposed large areas of the continental shelf to wind erosion during the Lateglacial, which is likely to have been vegetated by restricted plant cover in what was a dry, cold, steppe environment (Scaife *et al*., 2019). Repeated deposition of both primary and detrital tephra in this landscape means that volcanic ash is likely to form a significant mineral component of soils and aeolian deposits in the Falkland Islands. Therefore, the abundant detrital tephra in the Hooker's Point record is likely to have been derived from enhanced erosion of these deposits during this period.

The link between detrital glass abundance and local mineral input appears to break down later in the Hooker's Point record where shard counts vary despite limited changes in the abundance of organic material or lithogenic (Si, Al and Ti) elements (Fig. 8.2). The lowest shard abundances occur between 14,300-10,500 cal yr BP, with almost no detrital glass recorded during the period 12,830-11,070 cal yr BP. This reduction in detrital tephra spans periods characterised by both dry (Poaceae) and wet vegetation (*Sphagnum*) communities (Scaife *et al*., 2019), as well as changes in wind-speed proxies, and so cannot be simply interpreted by either record (Fig. 8.2). Interestingly the near absence of detrital glass between 12,830-11,070 cal yr BP coincides with a reduction in wind-strength over Hooker's Point, associated with a southern movement of the SWW (Fig. 8.2). This could suggest a link between the strength of the SWW and the delivery of detrital tephra to the Falkland Islands, or reflect further stabilising of the environment under wetter, more productive, conditions.

One hypothesis which cannot yet be tested using the current data set is the influence of fire on the abundance of detrital glass. Charred plant macrofossils occur regularly in the Hooker's Point palaeoecological record (Scaife *et al*., 2019), and burning is common in the contemporary setting, where it occurs naturally and during agricultural practices. Local burning could promote the remobilisation of tephra from the surrounding catchment as vegetation cover is removed leading to elevated shard counts. Holocene fire histories have been developed from the Falkland Islands (Groff, 2019); however, a charcoal record from Hooker's Point is needed to test this hypothesis.

From this discussion it cannot be concluded that abundance of detrital tephra in the Hooker's Point record is driven solely by changes in wind-strength. However, the near absence of tephra between 12,830-11,070 cal yr BP, a period associated with a drop in wind-speed affecting Hooker's Point, suggests that the SWW may play some role. Further sites across the Falkland Islands are needed to more comprehensively resolve this question, before the past dispersal of volcanic ash can be understood in this region.

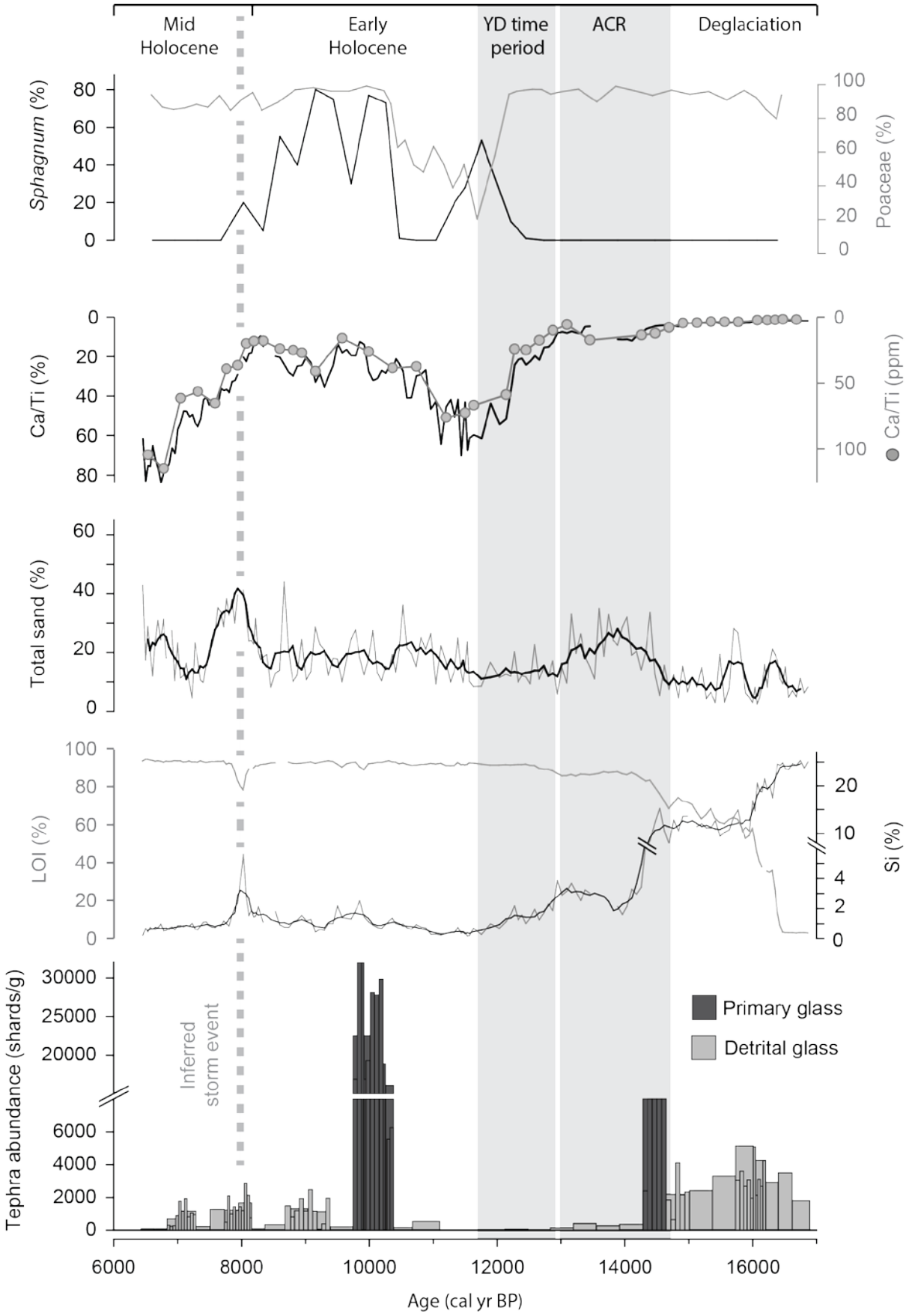

Figure 8.2: The abundance of tephra shards in the Hooker's Point record plotted against paleaoecological data (Scaife *et al*. 2019), particle size and geochemical analyses from the site (Paper IV).

8.1.3 Implications for hazards posed by volcanic ash clouds

Paper II demonstrates an uptake in the frequency of cryptotephra deposits found in eastern North America after *ca*. 7600 cal yr BP. This change in the frequency of ash fall events is likely to have been caused by a shift in position and/or strength of the westerlies – linked with the retreating North American ice sheets. The finding demonstrates that over millennial time scales hazards associated with ash clouds are closely linked with changes in atmospheric circulation, and raises the question: are long term investigations of ash cloud return intervals (e.g. Swindles *et al*., 2011; Watson *et al*., 2017) representative of modern hazards if atmospheric conditions have changed?

Volcanic ash clouds have been observed to travel several thousand kilometres in the Southern mid-latitudes and have repeatedly affected air traffic in this region (Guffanti *et al*., 2009; Alloway *et al*., 2015). Paper III confirms that ash clouds from past eruptions in Austral Andean Volcanic Zone reached the Falkland Islands and are likely to have extended further into the South Atlantic. This study also reports abundant tephra deposits composed of reworked volcanic glass derived from detrital tephra in the arid Patagonian steppe. It is possible that this detrital ash may pose a hazard to aircraft if suspended in sufficient quantities. There is evidence that tephra deposits can form a secondary hazard following large eruptions, for example, in the months following the AD 1991 eruption of Mt. Hudson ash clouds composed of tephra re-suspended by wind action extended across southern South America and into the South Atlantic (Wilson *et al*., 2011). Similar processes have been observed over older deposits in Alaska where tephra from the AD 1912 eruption of Novarupta-Katmai (VEI 7) continues to pose a hazard to aircraft a century after the event. During periods of dry weather and strong winds pyroclastic deposits from this eruption are re-suspended from the Valley of Ten Thousand Smokes, forming ash plumes that extend into the Gulf of Alaska (Hadley *et al*., 2003). It is possible that a mix both dust and tephra from the Patagonian steppe could pose similar hazards.

8.2 Developing regional tephrostratigraphic frameworks

The first objective of this thesis is to develop new cryptotephra records from eastern North America and the Falkland Islands, South Atlantic, to close spatial and temporal gaps in tephrostratigraphic frameworks from these regions. The establishment of a Lateglacial and early Holocene tephrostatigraphy is at an early stage in both of these regions, and new cryptotephra records were needed in order to resolve the primary research aim of this thesis: *to investigate past changes in ash dispersal patterns using distal cryptotephra deposits*. Objective one is addressed by Papers I-III which included methodological experiments as well as chronology, shard counts and electron probe microanalyses (EPMA) from new study sites – summarised here.

8.2.1 Eastern North America

By examining the effects of the peat acid digestion protocol (Dugmore *et al*., 1995) on diverse tephra deposits, Paper I provides an important methodological step in robustly analysing the major-minor element composition of ultra-distal cryptotephra deposits (Q.1.1). Strong acids are known to affect the chemical composition of natural glasses (including tephra) at different rates depending on the chemical durability of the glass and its surface-area/volume ratio (see Section: 2.1.3.3). Previous experimental studies examining the alteration of volcanic ash during exposure to acid (Dugmore *et al*., 1992; Roland *et al*., 2015) have focussed on a narrow geochemical and morphological sample group. Therefore, further study was needed before using the peat acid digestion protocol, as ultra-distal tephra deposits are often composed of highly vesicular shards with variable major-minor element glass compositions. Paper I found no discernible evidence for physical or chemical alteration of diverse samples of volcanic glass following extraction using the peat acid digestion protocol. Therefore, it was concluded that this process does not alter the major-minor element composition of tephra to a degree that is recordable during EPMA. Following this study acid digestion was used to extract tephra for EPMA in both Paper II and Paper III.

Paper II presents the findings from eight new ultra-distal cryptotephra records in eastern North America, as part of a wider study examining temporal changes in ash fall frequency during the lateglacial and early Holocene. These include unpublished tephrochronology community data and original study sites developed during this thesis. Cryptotephra deposits from new study sites were correlated with tephra isochrons previously identified in eastern North America (Pyne-O'Donnell *et al*., 2012; Mackay *et al*., 2016), including: Mt. St Helens We, White River Ash east, Newberry Pumice and Mazama ash, confirming that these tephras form widespread chronological markers in this region.

Paper II also demonstrates the value of apparently 'failed results' where no tephra deposits are identified. Reporting these findings not only provides useful data which may demonstrate a wider pattern, but helps to constrain the spatial limits of past ash clouds. This practice is not common, despite the benefits of such data, and there is clearly a need for a community discussion on how to make these 'failed' results publically available.

8.2.2 The Falkland Islands

Paper III presents the first detailed study of cryptotephra deposits from the Falkland Islands and provides the foundations of a Lateglacial and early Holocene tephrostratigraphy for the archipelago. Shard peaks in Hookers Point, East Falkland, are correlated with the Reclus volcano R_1 and Mt. Burney MB_1 eruptions, confirming the presence of these important chronological isochrons in the South Atlantic (see Paper III). The detection of these cryptotephra deposits in the Hooker's Point sequence allows this record to be linked with the key regional climate archive from Laguna Potrok Aike, Argentina, and is used in Paper IV to identify an apparent chronological offset between the two records. The abundance of these tephra deposits (>10,000 shards/g) suggests that they extend further into the South Atlantic and may be used to synchronise island palaeoenvironmental records throughout this region (see Section 8.2.3). As noted in Paper III further discrete cryptotephra deposits are likely to be present in the Hooker's Point sequence; however, they are obscured by the high abundance of detrital glass in this record. This smothering of cryptotephra deposits in the Falkland Islands highlights the difficulties in developing a comprehensive terphrostratigraphic framework for Patagonia and the South Atlantic region. It may be that records beyond the Falkland Islands (e.g. South Georgia) are unaffected by detrital glass from the Patagonian Steppe, which could help to refine the South American tephrostratigraphy.

8.3 Recommendations for future research

This thesis has demonstrated that distal cryptotephra deposits can be used to provide environmental and taphonomic information beyond chronology. However, it has also raised further questions which should be the subject of future research. Section 8.2 outlines some of these knowledge gaps and presents new pilot data aimed at addressing them.

8.3.1 Maximising morphological data from distal tephra deposits

The spatial patterns of past ash clouds are beginning to be pieced together by the continued development of regional tephrostratigraphic frameworks (Wastegård and Davies, 2009; Lawson *et al*., 2012). However, the morphological properties of tephra from these ash clouds have been largely ignored. For example, Plunkett and Pilcher (2018) summarise chronology and EPMA from 161 middle and early Holocene tephra records in North-West Europe alone, whereas Stevenson *et al*. (2015) found just 33 published examples of shard measurements from distal tephra deposits, globally.

This thesis has recorded basic shard morphological types and long axis measurements in order to examine the effects of the peat acid digestion protocol on diverse volcanic glass, and differentiate between primary and reworked tephra deposits (see Paper I and Paper III). While these measurements have helped to resolve the research questions of this thesis, further, more detailed, shard morphological investigations have the potential to provide quantitative data on the aerodynamic behaviour of volcanic ash.

The initial findings from a pilot study are presented here to demonstrate the range of morphological information that can be rapidly retrieved from distal cryptotephra deposits. Freely available software (ImageJ) was used in conjunction with scanning electron microscope (SEM) images, produced during this thesis, to undertake the measurements outlined in Figure 8.3.

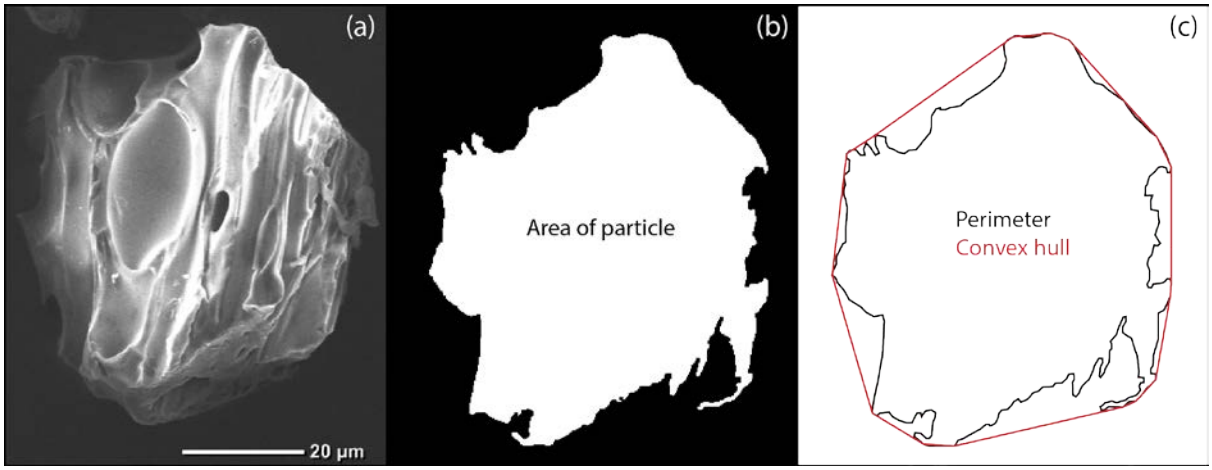

Figure 8.3: (a) SEM image of a vesicular tephra shard. (b) 2D projection of the same tephra shard produced using ImageJ software, following methodology outlined by Liu et al. (2015). (c) The perimeter and convex hull of the 2D image.

The results from limited measurements of glass shards (n=23) extracted from ultra-distal cryptotephra deposits, correlated with the Mazama ash and White River Ash east, are presented in Figure 8.4. The Mazama ash appears to include a wider range of shard sizes relative to the White River Ash east, when the two are compared using both long axis length and shard perimeter. Interestingly the morphological populations can be separated by subtle differences in circularity, even when long axis measurements closely overlap (Fig. 8.4b). These very basic measurements demonstrate the potential to separate cryptotephra deposits based on shard morphology. Further more comprehensive studies could use shard morphological measurements to calculate a range of variables, including terminal velocity (Wilson and Huang, 1979). By combining this data with knowledge of the eruption conditions and the provenance of distal tephra deposits it should be possible to provide estimates of the wind speeds affecting past ash clouds.

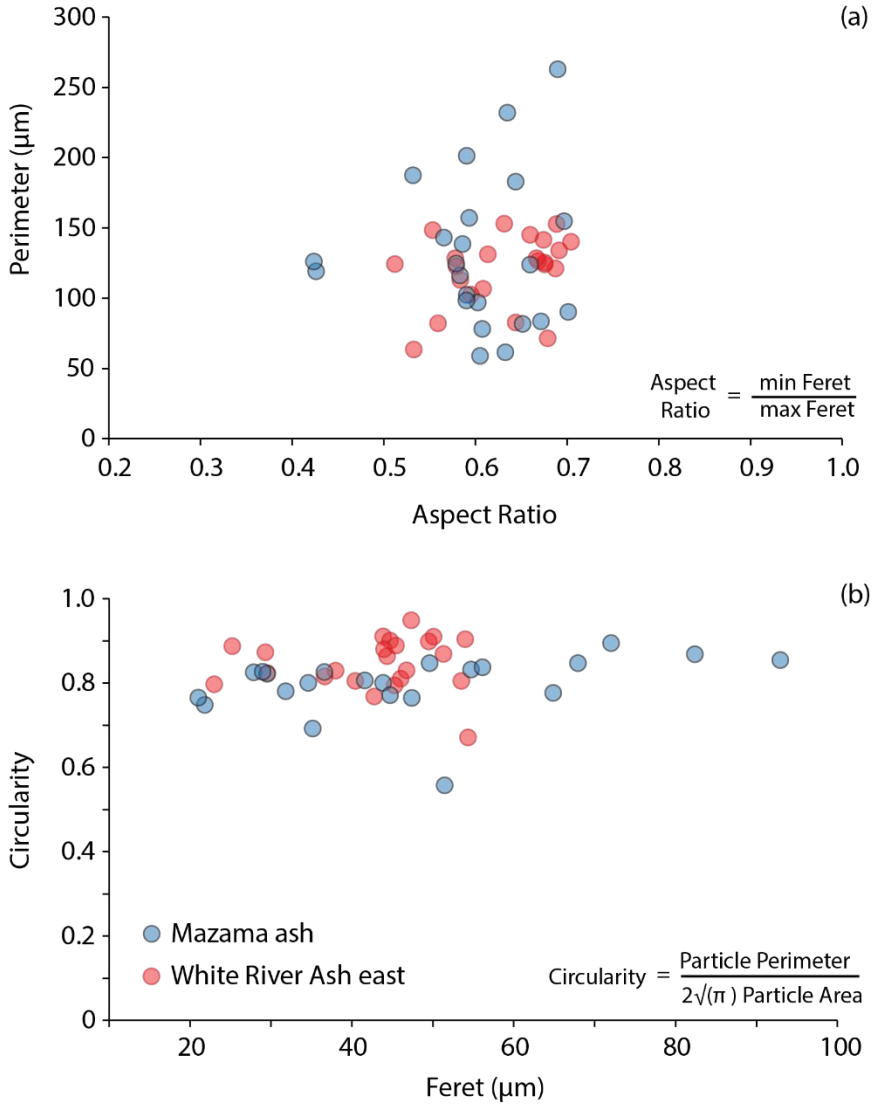

Figure 8.4: Bi-plots of basic shard morphological measurements and ratios. Mazama ash sample is taken from Sidney Bog, Maine, while the White River Ash east sample is taken from Baby Pond Bog, Newfoundland. Feret = long axis.

As well increasing the number of studies which record shard measurements, a standardised more detailed, approach is needed in order to maximise the use of this data between disciplines (Stevenson *et al.*, 2015). This approach may vary between depositional settings. Ombrotrophic peat bogs may provide more consistent records of tephra morphology than lake sediments, which can be biased by the selective input of tephra from the surrounding catchment, and require more intensive laboratory procedures to isolate volcanic ash (e.g. sieving at 25 µm and 80 µm). However, Watson *et al*. (2016) report differing long axis measurements (median values 40-50 µm) from 14

cryptotephra deposits in the same peatland, derived from the Hekla 1510 eruption. This variability demonstrates that tephra is selectively deposited across a peat surface according to size, and clearly a number of records are needed to reliably represent the physical compositions of past ash clouds.

8.3.2 A new proxy of wind strength in the Falkland Islands

Paper IV has demonstrated that a combination of proxies is needed to interpret the palaeoenvironmental record from peat in the Falkland Islands. Therefore, developing new proxies for wind strength is important if we are to better understand past changes in the SWW.

Beaches in East Falkland are typically formed of sand eroded from the Port Stanley geological formation. This formation is mostly comprised of quartzite; however, also includes a small component of red garnet. Garnets are denser and heavier than the Si rich quartzite, and so beach sands formed of this mineral require more energy to be transported than those derived from quartzite. Following storms, this difference in transport rates means that beaches affected by strong wind or wave action can turn 'pink' as the quartz is selectively removed, leaving the red garnet grains behind (Stone *et al*., 2005). This relationship means that the ratio of Si grains to red garnet grains, deposited on the surface of coastal peatlands by aeolian processes, may change with wind strength in the Falkland Islands, and provide a proxy that could be used to reconstruct past changes in the SWW.

8.3.3 Understanding past dynamics of the Southern Westerly Wind belt

Both the literature review (see Section 2.2.2.4) and Paper IV discuss the discrepancies between records of past changes in the SWW from southern South America. Understanding the dynamics of this circum-polar atmospheric system is important because of its role in regional climate and CO_2 sequestration in the Southern Oceans (Anderson *et al*., 2009; Garreaud *et al*., 2013).

Paper IV demonstrated that island settings can preserve long records of past wind strength which are unaffected by the strong orographic effects that complicate records from southern Patagonia. This study continues a recent interest in South Atlantic islands (Unkel *et al*., 2008, 2010; Björck *et al*., 2012; Strother *et al*., 2015; Turney *et al*., 2016; Thomas *et al*., 2018), and helps to describe changes in the wind strength affecting the Falkland Islands during the Lateglacial and early Holocene time periods. However, it remains difficult to reconcile differing proxy sensitivities and chronological offsets with records of wind strength from southern South America. As a result, only limited inferences can be made about past changes in the strength and/or position of the SWW from this new dataset.

By developing a network of island study sites, across a latitudinal transect it may be possible to separate changes in the core strength of the SWW from northern or southern shifts in its position. There are several islands in the latitudes affected by the SWW which became deglaciated early in the Lateglacial and contain long peat sequences that could be analysed using a methodology similar to Paper IV (Hall *et al*., 2004; Hodgson *et al*., 2014). The chronology of these sites would be crucial as minor offsets could appear as time transgressive shifts; however, it is likely that tephra isochrons could be used to link these records. The discovery of abundant cryptotephra deposits in the Falkland Islands, derived from the Mt. Burney MB_1 and Reclus R_1 eruptions, demonstrates that these isochrons extend into the South Atlantic. Further evidence from modern observations (Alloway *et al*., 2015), and description of Patagonian tephra in South Georgia (Oppedal *et al*., 2018), support this finding, and suggest that Southern Hemisphere ash deposits may have ultra-distal distributions, similar to those described in the Northern Hemisphere (Pyne-O'Donnell *et al*., 2012; Ponomareva *et al*., 2015). These distal cryptotephra deposits are likely to provide important isochrons which may be used to synchronise regional records of past SWW dynamics.

A network of island wind strength records which span the latitudinal range of the SWW, and are synchronised using tephra isochrons, would represent a major step forward in understanding the past dynamics of this major climate feature.

Chapter 9 Conclusions

The primary aim of this thesis is to *investigate past changes in ash dispersal patterns using distal cryptotephra deposits*. The findings from this study demonstrate that tephra dispersal is strongly affected by changes in atmospheric circulation, and that a long view of ash fall is needed in order to identify millennial scale changes in the pattern of tephra dispersal. For example, Paper II found that in eastern North America changes in the frequency of ash fall events can be linked with shifts in atmospheric circulation, caused by the collapse of the Laurentide ice-sheet. The situation in the Falkland Islands proved to be more complex, and despite comparing multiple palaeoecological (Scaife *et al*., 2019) and geochemical proxies (Paper IV) with the tephra record from Hooker's Point (Paper III), the temporal pattern of tephra dispersal over the Falkland Islands remains largely unresolved. Despite these complexities, future work should continue to consider the implications for ash dispersal when examining distal cryptotephra deposits. It was only after the incremental addition of new records that the atmospheric pattern in eastern North America became apparent, and there is some evidence for changing tephra abundance in response to a southern movement of the SWW in the Hooker's Point peat sequence.

Further studies of distal tephra deposits should include detailed shard morphological descriptions. Paper III used basic long axis measurements and shard descriptions to separate detrital glass from primary ash fall events; however, more detailed descriptions could be used to better understand the movement of tephra in the atmosphere with implications for projections of ash cloud dispersal.

The key scientific findings of this thesis include:

- The peat acid digestion protocol does not chemically or physically alter diverse volcanic glass, and therefore can be safely used to extract highly vesicular, ultra-distal tephra shards, for EPMA.

- By combining a network of cryptotephra records, an upturn in the frequency of volcanic ash fall over eastern North America is demonstrated after *ca*. 7,600 cal yr BP. This increase in tephra deposition is linked with the collapse of the Laurentide ice-sheet, and associated changes in atmospheric circulation.

- The first Lateglacial and early Holocene tephrostratigraphy from the Falkland Islands is developed from a peat sequence in Hooker's Point, east Falkland. Cryptotephra deposits are correlated with key regional isochrons: Reclus R_1 and Mt. Burney MB_1.

- A high abundance of detrital glass is observed throughout the Hooker's Point peat sequence with is derived from repeatedly reworked tephra deposits in the Patagonian Steppe.

- A multi-proxy record of Lateglacial and early Holocene wind-strength is developed from Hooker's Point. Changes in particle size and peat geochemistry suggest the Southern Westerly Wind belt move south, away from the Falkland Islands, during the Younger Dryas time period.

In summary, tephrochronology provides an important tool in Quaternary Science; however, this is not the limit of information preserved in tephra deposits. This thesis has demonstrated that distal tephra deposits can provide evidence for past changes in the dispersal of volcanic ash, and that tephra should be considered as more than just a dating point – beyond chronology.

Appendix A Paper I

A.1 EPMA glass shard analyses included in Paper I

Appendix A.1 includes major-minor oxide concentrations (wt%) of individual glass shards from the case study tephra deposits described in Paper I. Shards were analysed at the Tephra Analytical Unit, University of Edinburgh, using a Cameca SX100 electron probe microanalyser. 3 µm and 5 µm focused beams were used, with a 10 KeV accelerating voltage, and 5 nA current (Hayward, 2012).

Table A.1: Individual, glass, major-minor oxide concentrations from tephra deposits (wt%) analysed in Paper I.

Sample	SiO_2	TiO2	Al_2O_3	FeO_T	MnO	MgO	CaO	Na_2O	K_2O	P_2O_5	Cl	Total	Date	Beam width
BTm-Float	75.51	0.23	10.11	4.01	0.08	0.01	0.24	5.17	4.24	0.01	0.44	100.04	21/03/2018	5 µm
BTm-Float	75.28	0.23	10.34	4.17	0.08	0.05	0.21	5.07	4.16	0.01	0.43	100.04	21/03/2018	5 µm
BTm-Float	75.26	0.24	10.47	4.30	0.09	0.03	0.27	5.46	4.42	0.02	0.44	100.99	21/03/2018	5 µm
BTm-Float	74.96	0.23	10.07	3.99	0.09	-0.02	0.26	5.29	4.36	0.00	0.44	99.67	21/03/2018	5 µm
BTm-Float	74.72	0.24	10.45	4.21	0.08	-0.03	0.22	5.28	4.34	0.00	0.43	99.95	21/03/2018	5 µm
BTm-Float	74.65	0.22	10.13	4.09	0.07	0.00	0.18	5.06	4.37	0.00	0.45	99.21	21/03/2018	5 µm
BTm-Float	74.53	0.23	10.27	4.06	0.09	0.02	0.26	5.52	4.55	0.01	0.42	99.96	21/03/2018	5 µm
BTm-Float	74.39	0.23	10.35	3.83	0.08	0.00	0.27	5.09	4.35	0.00	0.44	99.03	21/03/2018	5 µm
BTm-Float	74.29	0.23	10.44	4.09	0.09	0.00	0.20	5.25	4.23	0.01	0.43	99.26	21/03/2018	5 µm
BTm-Float	74.17	0.24	10.46	4.10	0.08	0.01	0.27	5.41	4.22	0.00	0.42	99.39	21/03/2018	5 µm
BTm-Float	74.11	0.23	10.13	4.14	0.09	0.02	0.23	5.06	4.18	0.01	0.43	98.62	21/03/2018	5 µm
BTm-Float	74.11	0.23	10.25	4.06	0.08	0.01	0.21	5.41	4.27	0.01	0.45	99.06	21/03/2018	5 µm
BTm-Float	73.98	0.24	10.32	4.08	0.09	0.00	0.22	5.25	4.42	0.01	0.44	99.05	21/03/2018	5 µm

BTm-Float	73.87	0.23	10.34	4.07	0.09	-0.02	0.21	5.34	4.38	0.01	0.44	98.95	21/03/2018	5 µm
BTm-Float	73.85	0.25	10.39	4.18	0.09	0.02	0.35	5.10	4.40	0.01	0.40	99.03	21/03/2018	5 µm
BTm-Float	73.83	0.24	10.56	3.98	0.09	0.02	0.33	5.28	4.29	0.03	0.43	99.07	21/03/2018	5 µm
BTm-Float	73.78	0.24	10.28	3.98	0.09	0.04	0.23	5.41	4.39	0.00	0.43	98.86	21/03/2018	5 µm
BTm-Float	73.68	0.23	10.23	4.00	0.08	0.00	0.29	4.81	5.15	0.00	0.44	98.92	21/03/2018	5 µm
BTm-Float	73.63	0.23	10.30	3.96	0.08	0.04	0.23	5.23	4.35	0.00	0.45	98.50	21/03/2018	5 µm
BTm-Float	73.50	0.24	10.32	3.85	0.08	-0.01	0.23	5.38	4.28	0.00	0.42	98.29	21/03/2018	5 µm
BTm-Float	73.36	0.24	10.33	3.98	0.08	0.04	0.21	5.24	4.23	0.01	0.43	98.16	21/03/2018	5 µm
BTm-Float	73.22	0.22	9.90	4.11	0.09	0.01	0.23	5.12	4.48	0.00	0.46	97.84	21/03/2018	5 µm
BTm-Float	73.14	0.26	10.90	4.12	0.09	0.01	0.34	5.22	4.55	0.02	0.41	99.07	21/03/2018	5 µm
BTm-Float	72.97	0.23	10.34	4.18	0.08	0.03	0.25	5.20	4.44	0.01	0.43	98.15	21/03/2018	5 µm
BTm-Float	72.95	0.23	9.84	4.05	0.08	0.03	0.19	5.18	4.34	0.00	0.44	97.34	21/03/2018	5 µm
BTm-Float	72.93	0.30	12.27	4.23	0.10	0.01	0.59	5.61	4.74	0.02	0.29	101.10	21/03/2018	5 µm
BTm-Float	72.79	0.24	10.48	4.17	0.07	0.01	0.26	5.29	4.34	0.01	0.43	98.09	21/03/2018	5 µm
BTm-Float	72.76	0.25	11.17	4.36	0.10	0.00	0.40	5.37	4.56	0.00	0.38	99.34	21/03/2018	5 µm
BTm-Float	72.74	0.25	10.91	4.04	0.09	0.03	0.34	5.52	4.26	0.00	0.40	98.57	21/03/2018	5 µm
BTm-Float	72.62	0.22	9.94	4.17	0.09	0.02	0.24	5.06	4.35	0.01	0.44	97.15	21/03/2018	5 µm
BTm-Float	72.57	0.23	10.07	4.11	0.07	0.00	0.25	5.22	4.26	0.00	0.44	97.22	21/03/2018	5 µm
BTm-Float	72.49	0.24	9.82	4.05	0.09	0.01	0.30	5.33	4.44	0.00	0.41	97.17	21/03/2018	5 µm
BTm-Float	71.99	0.23	9.83	3.94	0.08	0.02	0.25	5.24	4.40	0.01	0.43	96.41	21/03/2018	5 µm
BTm-Float	71.58	0.24	9.90	3.88	0.08	0.00	0.30	5.39	4.31	0.01	0.41	96.11	21/03/2018	5 µm
BTm-Float	71.53	0.44	11.05	4.67	0.09	0.28	0.91	4.55	5.16	0.06	0.37	99.12	21/03/2018	5 µm
BTm-Float	70.28	0.28	11.50	4.12	0.10	0.03	0.45	5.92	4.57	0.01	0.35	97.61	21/03/2018	5 µm
BTm-Float	69.20	0.34	14.03	4.25	0.13	0.03	0.70	5.82	5.14	0.01	0.19	99.84	21/03/2018	5 µm
BTm-Float	68.29	0.32	13.52	4.23	0.11	0.03	0.70	6.41	4.72	0.03	0.25	98.61	21/03/2018	5 µm
BTm-Float	67.93	0.33	13.46	4.38	0.12	0.03	0.69	6.00	5.21	0.02	0.20	98.37	21/03/2018	5 µm
BTm-Float	67.89	0.39	14.08	4.48	0.15	0.10	0.96	5.93	5.30	0.03	0.17	99.48	21/03/2018	5 µm
BTm-Float	67.64	0.39	14.63	4.77	0.15	0.04	1.02	5.92	5.38	0.03	0.14	100.10	21/03/2018	5 µm

BTm-Float	67.50	0.36	13.94	4.61	0.14	0.07	0.91	5.90	5.37	0.03	0.17	99.00	21/03/2018	5 µm
BTm-Float	67.27	0.37	14.32	4.84	0.14	0.07	0.94	6.05	5.32	0.03	0.17	99.50	21/03/2018	5 µm
BTm-Float	67.14	0.39	14.29	4.75	0.13	0.07	1.04	5.60	5.36	0.03	0.16	98.97	21/03/2018	5 µm
BTm-Float	67.05	0.43	14.92	5.28	0.14	0.12	1.21	5.88	5.40	0.04	0.13	100.59	21/03/2018	5 µm
BTm-Float	66.91	0.33	13.63	4.32	0.13	0.04	0.71	6.01	5.16	0.01	0.20	97.44	21/03/2018	5 µm
BTm-Float	66.88	0.45	14.67	4.96	0.16	0.16	1.18	5.80	5.67	0.05	0.12	100.10	21/03/2018	5 µm
BTm-Float	66.73	0.40	14.40	4.65	0.14	0.09	1.06	5.76	5.25	0.03	0.14	98.66	21/03/2018	5 µm
BTm-Float	66.31	0.39	14.19	4.76	0.14	0.09	1.06	5.94	5.33	0.05	0.20	98.46	21/03/2018	5 µm
BTm-Float	65.40	0.38	13.87	4.67	0.13	0.08	0.99	5.95	5.51	0.04	0.17	97.19	21/03/2018	5 µm
BTm-Float	65.25	0.45	14.63	4.80	0.14	0.14	1.22	5.90	5.52	0.06	0.13	98.23	21/03/2018	5 µm
BTm-Float	65.24	0.46	15.12	4.68	0.14	0.17	1.33	5.76	5.63	0.06	0.12	98.71	21/03/2018	5 µm
BTm-Float	65.19	0.42	14.93	4.90	0.14	0.12	1.20	5.55	5.62	0.06	0.15	98.28	21/03/2018	5 µm
BTm-Float	64.73	0.43	14.52	5.00	0.15	0.08	1.29	5.84	5.24	0.06	0.14	97.48	21/03/2018	5 µm
BTm-Float	64.56	0.40	14.43	4.79	0.15	0.07	1.08	5.70	5.58	0.03	0.15	96.95	21/03/2018	5 µm
Mean:	73.50	0.24	10.40	4.09	0.09	0.02	0.29	5.26	4.41	0.01	0.42	98.73		
StDev:	1.14	0.04	0.49	0.15	0.01	0.05	0.13	0.23	0.22	0.01	0.03	1.13		
Mean:	66.69	0.39	14.30	4.69	0.14	0.08	1.02	5.88	5.35	0.04	0.16	98.74		
StDev:	1.31	0.04	0.48	0.27	0.01	0.04	0.20	0.18	0.22	0.02	0.03	1.03		
BTm-Float	*68.26*	*0.03*	*18.76*	*0.79*	*0.00*	*-0.02*	*0.02*	*7.32*	*6.88*	*0.00*	*0.00*	*102.05*	21/03/2018	5 µm
BTm-Float	*71.52*	*0.37*	*14.92*	*5.00*	*0.13*	*0.08*	*0.99*	*0.21*	*1.53*	*0.04*	*0.17*	*94.97*	21/03/2018	5 µm
BTm-Float	*67.13*	*0.01*	*18.39*	*0.38*	*0.00*	*-0.01*	*0.08*	*7.27*	*6.73*	*0.01*	*0.00*	*100.00*	21/03/2018	5 µm
BTm-Float	*65.80*	*0.02*	*18.35*	*0.40*	*0.00*	*-0.01*	*0.13*	*7.48*	*6.52*	*0.00*	*0.00*	*98.69*	21/03/2018	5 µm
BTm-Float	*66.82*	*0.01*	*18.30*	*0.50*	*0.00*	*0.00*	*0.05*	*7.61*	*6.09*	*0.00*	*0.00*	*99.37*	21/03/2018	5 µm
BTm-Float	*65.40*	*0.00*	*17.82*	*0.71*	*0.00*	*0.02*	*0.00*	*6.85*	*6.93*	*0.00*	*0.00*	*97.73*	21/03/2018	5 µm

Sample	SiO_2	TiO2	Al_2O_3	FeO_T	MnO	MgO	CaO	Na_2O	K_2O	P_2O_5	Cl	Total	Date	Beam width
BTm-acid->63um	75.07	0.23	10.13	4.19	0.07	0.02	0.18	5.27	4.25	0.00	0.44	99.86	21/03/2018	5 µm
BTm-acid->63um	74.42	0.23	10.24	3.97	0.08	0.01	0.22	5.34	4.43	0.00	0.44	99.37	21/03/2018	5 µm
BTm-acid->63um	74.40	0.22	10.18	4.21	0.09	0.02	0.23	5.16	4.33	0.00	0.45	99.28	21/03/2018	5 µm
BTm-acid->63um	74.15	0.23	10.03	4.43	0.09	0.02	0.40	4.73	4.75	0.00	0.38	99.22	21/03/2018	5 µm
BTm-acid->63um	74.03	0.23	10.02	4.15	0.07	0.04	0.22	5.03	4.47	0.00	0.43	98.68	21/03/2018	5 µm
BTm-acid->63um	73.52	0.23	9.52	4.00	0.08	0.00	0.28	5.15	4.16	0.01	0.44	97.39	21/03/2018	5 µm
BTm-acid->63um	73.51	0.22	10.10	4.03	0.06	0.01	0.21	5.27	4.30	0.00	0.45	98.15	21/03/2018	5 µm
BTm-acid->63um	73.25	0.23	10.06	3.92	0.07	0.02	0.21	5.26	4.26	0.00	0.44	97.74	21/03/2018	5 µm
BTm-acid->63um	73.16	0.23	9.70	4.10	0.09	0.01	0.20	5.07	4.55	0.01	0.46	97.59	21/03/2018	5 µm
BTm-acid->63um	73.03	0.23	9.69	4.13	0.09	0.02	0.24	5.29	4.34	0.01	0.44	97.50	21/03/2018	5 µm
BTm-acid->63um	72.95	0.25	10.58	4.22	0.10	0.04	0.38	4.88	4.84	0.00	0.38	98.62	21/03/2018	5 µm
BTm-acid->63um	72.80	0.24	10.14	4.01	0.08	0.01	0.20	5.13	4.49	0.01	0.44	97.55	21/03/2018	5 µm
BTm-acid->63um	72.60	0.22	9.71	4.35	0.09	0.03	0.21	5.17	4.34	0.00	0.46	97.19	21/03/2018	5 µm
BTm-acid->63um	72.58	0.24	10.16	4.15	0.10	0.03	0.24	4.69	4.82	0.00	0.44	97.44	21/03/2018	5 µm
BTm-acid->63um	72.39	0.26	10.86	4.06	0.10	0.01	0.40	5.46	4.41	0.01	0.38	98.34	21/03/2018	5 µm
BTm-acid->63um	72.31	0.24	9.94	3.79	0.08	0.02	0.21	5.15	4.22	0.01	0.44	96.39	21/03/2018	5 µm
BTm-acid->63um	72.27	0.23	9.54	4.28	0.08	0.04	0.22	5.00	4.40	0.00	0.44	96.49	21/03/2018	5 µm
BTm-acid->63um	72.24	0.23	10.12	3.98	0.08	0.01	0.26	5.21	4.42	0.00	0.43	96.98	21/03/2018	5 µm
BTm-acid->63um	72.23	0.23	9.95	3.79	0.08	0.03	0.25	4.94	4.47	0.01	0.44	96.42	21/03/2018	5 µm
BTm-acid->63um	72.22	0.24	10.28	3.91	0.08	0.01	0.23	5.43	4.26	0.00	0.42	97.09	21/03/2018	5 µm
BTm-acid->63um	72.17	0.21	9.45	4.20	0.08	0.03	0.20	5.22	4.09	0.01	0.47	96.13	21/03/2018	5 µm
BTm-acid->63um	72.08	0.23	10.22	3.98	0.08	0.01	0.21	5.56	4.43	0.01	0.42	97.21	21/03/2018	5 µm
BTm-acid->63um	72.03	0.22	9.72	4.16	0.08	0.01	0.21	5.19	4.44	-0.01	0.43	96.48	21/03/2018	5 µm
BTm-acid->63um	71.69	0.23	10.34	4.02	0.08	-0.01	0.21	5.25	4.31	0.00	0.44	96.55	21/03/2018	5 µm
BTm-acid->63um	71.62	0.27	11.95	3.85	0.10	0.02	0.40	5.39	4.55	0.02	0.37	98.53	21/03/2018	5 µm
BTm-acid->63um	71.32	0.23	10.03	4.06	0.08	0.01	0.22	5.25	4.38	0.01	0.44	96.03	21/03/2018	5 µm

BTm-acid->63um	71.31	0.23	9.92	4.08	0.09	0.00	0.17	5.35	4.26	0.00	0.44	95.85	21/03/2018	5 µm
BTm-acid->63um	71.16	0.26	11.04	4.02	0.08	0.05	0.37	5.47	4.51	0.01	0.41	97.36	21/03/2018	5 µm
BTm-acid->63um	71.05	0.26	10.42	3.89	0.09	0.05	0.29	5.56	4.45	0.02	0.40	96.47	21/03/2018	5 µm
BTm-acid->63um	71.00	0.24	10.29	4.09	0.08	0.02	0.25	5.37	4.47	0.01	0.42	96.23	21/03/2018	5 µm
BTm-acid->63um	70.96	0.23	9.60	4.16	0.08	0.01	0.25	5.34	4.29	0.00	0.44	95.37	21/03/2018	5 µm
BTm-acid->63um	70.83	0.27	11.27	4.19	0.11	0.02	0.55	5.40	4.64	0.00	0.29	97.58	21/03/2018	5 µm
BTm-acid->63um	70.53	0.22	9.98	4.12	0.08	0.03	0.21	5.32	4.42	0.00	0.44	95.36	21/03/2018	5 µm
BTm-acid->63um	70.18	0.32	12.88	4.45	0.12	0.03	0.67	5.48	4.94	0.03	0.27	99.37	21/03/2018	5 µm
BTm-acid->63um	70.02	0.32	12.28	4.13	0.10	0.05	0.60	5.69	4.82	0.02	0.28	98.32	21/03/2018	5 µm
BTm-acid->63um	69.98	0.24	9.92	4.25	0.10	0.03	0.38	5.28	4.47	0.02	0.39	95.06	21/03/2018	5 µm
BTm-acid->63um	69.77	0.40	12.93	4.46	0.11	0.12	0.82	5.54	4.86	0.04	0.25	99.31	21/03/2018	5 µm
BTm-acid->63um	69.61	0.29	11.36	4.37	0.10	0.04	0.50	6.10	4.48	0.00	0.33	97.19	21/03/2018	5 µm
BTm-acid->63um	69.41	0.26	11.22	4.36	0.09	0.04	0.61	5.39	4.73	0.06	0.32	96.50	21/03/2018	5 µm
BTm-acid->63um	69.36	0.27	11.54	4.14	0.10	0.03	0.43	5.52	4.63	0.01	0.32	96.35	21/03/2018	5 µm
BTm-acid->63um	68.28	0.34	12.43	4.45	0.12	0.07	0.73	5.80	4.87	0.02	0.23	97.34	21/03/2018	5 µm
BTm-acid->63um	68.23	0.39	14.36	4.49	0.14	0.11	1.12	5.78	5.40	0.03	0.16	100.22	21/03/2018	5 µm
BTm-acid->63um	68.19	0.30	12.19	4.37	0.12	0.04	0.77	5.39	5.00	0.02	0.26	96.64	21/03/2018	5 µm
BTm-acid->63um	67.80	0.36	14.09	4.45	0.13	0.04	0.98	5.74	5.72	0.02	0.16	99.50	21/03/2018	5 µm
BTm-acid->63um	67.62	0.43	14.92	4.90	0.14	0.15	1.17	5.92	5.35	0.04	0.15	100.78	21/03/2018	5 µm
BTm-acid->63um	67.53	0.37	13.57	4.63	0.11	0.09	0.92	5.63	5.43	0.03	0.20	98.52	21/03/2018	5 µm
BTm-acid->63um	66.73	0.48	14.65	4.78	0.13	0.17	1.18	5.73	5.08	0.06	0.15	99.13	21/03/2018	5 µm
BTm-acid->63um	66.59	0.40	14.58	4.60	0.14	0.09	1.09	5.68	5.48	0.05	0.15	98.85	21/03/2018	5 µm
BTm-acid->63um	66.51	0.35	13.74	4.35	0.13	0.05	0.90	6.18	5.31	0.03	0.17	97.73	21/03/2018	5 µm
BTm-acid->63um	66.41	0.32	12.33	4.36	0.12	0.10	0.82	5.25	5.36	0.03	0.27	95.37	21/03/2018	5 µm
BTm-acid->63um	66.36	0.49	15.10	5.04	0.15	0.20	1.40	5.94	5.53	0.06	0.11	100.37	21/03/2018	5 µm
BTm-acid->63um	65.80	0.37	14.00	4.55	0.13	0.05	0.95	5.82	5.22	0.02	0.18	97.07	21/03/2018	5 µm
BTm-acid->63um	65.60	0.31	14.43	4.34	0.12	0.05	0.91	5.80	5.60	0.03	0.16	97.35	21/03/2018	5 µm
BTm-acid->63um	65.27	0.37	13.91	4.41	0.13	0.05	1.04	5.73	5.64	0.03	0.15	96.75	21/03/2018	5 µm

BTm-acid->63um	64.89	0.47	14.71	4.61	0.14	0.16	1.22	6.11	5.37	0.06	0.14	97.89	21/03/2018	5 µm
BTm-acid->63um	64.84	0.47	14.79	4.89	0.15	0.17	1.29	5.86	5.65	0.05	0.11	98.27	21/03/2018	5 µm
BTm-acid->63um	64.73	0.47	14.94	4.62	0.15	0.13	1.22	5.83	5.56	0.05	0.12	97.81	21/03/2018	5 µm
BTm-acid->63um	64.55	0.49	14.94	4.83	0.14	0.15	1.23	5.78	5.81	0.06	0.13	98.10	21/03/2018	5 µm
BTm-acid->63um	64.47	0.40	14.12	4.84	0.13	0.12	1.16	5.69	5.47	0.04	0.14	96.59	21/03/2018	5 µm
BTm-acid->63um	64.24	0.41	13.92	4.57	0.14	0.10	1.16	5.75	5.60	0.03	0.15	96.09	21/03/2018	5 µm
BTm-acid->63um	63.53	0.47	14.51	5.09	0.17	0.14	1.23	5.99	5.24	0.06	0.12	96.54	21/03/2018	5 µm
BTm-acid->63um	62.93	0.44	14.64	4.65	0.13	0.14	1.25	5.91	5.57	0.05	0.12	95.81	21/03/2018	5 µm
Mean:	71.98	0.25	10.43	4.12	0.09	0.02	0.31	5.28	4.47	0.01	0.41	97.36		
StDev:	1.48	0.04	0.87	0.17	0.01	0.02	0.15	0.25	0.20	0.01	0.06	1.24		
Mean:	65.96	0.41	14.13	4.63	0.14	0.11	1.08	5.79	5.42	0.04	0.16	97.85		
StDev:	1.58	0.06	0.85	0.23	0.01	0.05	0.18	0.20	0.23	0.02	0.04	1.50		
BTm-acid->63um	*68.76*	*0.23*	*10.05*	*3.79*	*0.08*	*-0.01*	*0.26*	*5.07*	*4.39*	*0.01*	*0.41*	*93.05*	*21/03/2018*	*5 um*

Sample	SiO_2	TiO2	Al_2O_3	FeO_T	MnO	MgO	CaO	Na_2O	K_2O	P_2O_5	Cl	Total	Date	Beam width
BTm-acid-<63um	73.89	0.24	10.13	4.02	0.08	-0.01	0.23	5.17	4.36	0.00	0.43	98.52	22/03/2018	5 µm
BTm-acid-<63um	73.71	0.23	9.98	4.31	0.06	0.03	0.25	5.20	4.34	0.00	0.44	98.55	23/03/2018	5 µm
BTm-acid-<63um	73.65	0.24	10.36	4.16	0.09	-0.01	0.27	5.28	4.27	0.00	0.44	98.75	23/03/2018	5 µm
BTm-acid-<63um	73.56	0.24	10.42	3.82	0.08	0.02	0.22	5.30	4.46	0.00	0.42	98.54	23/03/2018	5 µm
BTm-acid-<63um	73.56	0.22	9.88	3.77	0.08	0.03	0.20	5.25	4.22	0.00	0.45	97.67	22/03/2018	5 µm
BTm-acid-<63um	73.37	0.21	9.66	4.18	0.09	0.02	0.19	5.06	4.41	0.00	0.45	97.64	23/03/2018	5 µm
BTm-acid-<63um	73.28	0.24	10.40	4.22	0.10	0.00	0.30	5.49	4.39	0.00	0.41	98.82	22/03/2018	5 µm
BTm-acid-<63um	73.15	0.26	10.98	3.87	0.08	0.03	0.37	5.23	4.72	0.01	0.37	99.08	22/03/2018	5 µm
BTm-acid-<63um	72.81	0.23	10.04	3.99	0.09	0.03	0.28	5.18	4.39	0.01	0.44	97.50	23/03/2018	5 µm
BTm-acid-<63um	72.20	0.27	11.07	3.94	0.09	0.02	0.48	5.37	4.79	0.01	0.35	98.60	22/03/2018	5 µm
BTm-acid-<63um	71.85	0.23	9.62	3.95	0.08	0.01	0.18	5.01	4.28	0.01	0.44	95.66	23/03/2018	5 µm
BTm-acid-<63um	71.76	0.25	10.63	4.01	0.08	0.04	0.32	5.16	4.44	0.01	0.41	97.10	23/03/2018	5 µm
BTm-acid-<63um	71.32	0.24	10.43	4.02	0.11	0.02	0.28	5.20	4.45	0.01	0.42	96.50	23/03/2018	5 µm

BTm-acid-<63um	70.70	0.28	11.97	4.12	0.09	0.00	0.31	5.30	5.15	0.01	0.35	98.29	22/03/2018	5 µm
BTm-acid-<63um	70.62	0.32	12.82	3.85	0.07	0.04	0.44	5.29	5.37	0.01	0.35	99.18	23/03/2018	5 µm
BTm-acid-<63um	70.25	0.30	12.41	4.16	0.11	0.07	0.56	5.51	4.74	0.02	0.30	98.43	22/03/2018	5 µm
BTm-acid-<63um	68.48	0.38	14.28	4.86	0.14	0.04	0.91	5.86	5.08	0.05	0.18	100.26	23/03/2018	5 µm
BTm-acid-<63um	67.93	0.37	13.40	4.24	0.11	0.08	0.91	5.58	5.24	0.04	0.20	98.11	23/03/2018	5 µm
BTm-acid-<63um	67.77	0.33	13.65	4.17	0.12	0.06	0.72	5.68	5.16	0.01	0.20	97.86	23/03/2018	5 µm
BTm-acid-<63um	67.77	0.35	14.30	4.20	0.13	0.05	0.93	6.14	5.23	0.01	0.16	99.27	22/03/2018	5 µm
BTm-acid-<63um	67.14	0.45	14.76	4.73	0.16	0.16	1.21	5.83	5.48	0.05	0.13	100.09	22/03/2018	5 µm
BTm-acid-<63um	66.81	0.38	14.39	4.88	0.13	0.10	1.08	5.72	5.60	0.04	0.16	99.29	23/03/2018	5 µm
BTm-acid-<63um	66.62	0.53	15.39	5.16	0.14	0.21	1.43	5.87	5.40	0.06	0.10	100.90	22/03/2018	5 µm
BTm-acid-<63um	65.38	0.53	14.87	4.88	0.14	0.29	1.52	5.77	5.44	0.08	0.13	99.04	23/03/2018	5 µm
BTm-acid-<63um	64.80	0.47	15.10	5.09	0.14	0.21	1.30	5.60	5.52	0.07	0.12	98.42	23/03/2018	5 µm
Mean:	72.48	0.25	10.68	4.02	0.09	0.02	0.31	5.25	4.55	0.01	0.40	98.05		
StDev	1.24	0.03	0.96	0.16	0.01	0.02	0.11	0.13	0.33	0.01	0.04	0.97		
Mean:	66.97	0.42	14.46	4.69	0.13	0.13	1.11	5.78	5.35	0.05	0.15	99.25		
StDev	1.22	0.08	0.65	0.39	0.01	0.09	0.27	0.17	0.18	0.02	0.04	1.03		

Sample	SiO_2	TiO2	Al_2O_3	FeO_T	MnO	MgO	CaO	Na_2O	K_2O	P_2O_5	Cl	Total	Date	Beam width
Saksun_>63	50.42	3.26	13.67	16.95	0.22	3.86	8.82	2.52	0.77	0.38	0.02	100.89	22/03/2018	3 µm
Saksun_>63	49.86	2.67	10.48	15.72	0.24	7.85	10.96	2.49	0.36	0.26	0.01	100.91	22/03/2018	3 µm
Saksun_>63	49.45	2.89	13.39	14.26	0.23	5.59	10.06	2.84	0.44	0.30	0.02	99.45	22/03/2018	3 µm
Saksun_>63	49.30	3.03	11.81	14.68	0.24	6.51	9.83	2.52	0.44	0.33	0.02	98.71	22/03/2018	3 µm
Saksun_>63	49.29	3.07	12.52	14.82	0.22	5.28	9.61	2.81	0.43	0.33	0.02	98.40	22/03/2018	3 µm
Saksun_>63	49.25	3.13	12.93	14.13	0.24	5.28	9.56	2.93	0.49	0.33	0.02	98.29	22/03/2018	3 µm
Saksun_>63	49.24	2.92	12.69	14.54	0.22	5.58	9.98	2.51	0.42	0.31	0.02	98.43	22/03/2018	3 µm
Saksun_>63	49.17	2.89	13.89	14.25	0.24	5.61	10.12	2.82	0.44	0.30	0.01	99.73	22/03/2018	3 µm
Saksun_>63	49.07	1.67	14.26	12.05	0.20	7.35	12.37	2.14	0.17	0.16	0.01	99.46	22/03/2018	3 µm
Saksun_>63	48.45	2.98	12.98	14.77	0.24	5.75	9.85	2.89	0.49	0.34	0.02	98.75	22/03/2018	3 µm

Saksun_>63	48.31	1.89	12.84	12.50	0.20	7.31	11.73	2.26	0.29	0.15	0.01	97.51	22/03/2018	5 µm
Saksun_>63	49.75	2.90	12.83	14.78	0.23	5.66	10.02	2.62	0.41	0.28	0.02	99.51	22/03/2018	5 µm
Saksun_>63	49.32	1.76	13.64	12.69	0.21	6.95	12.48	2.27	0.19	0.14	0.01	99.64	22/03/2018	5 µm
Saksun_>63	48.71	3.09	12.47	14.57	0.24	5.24	9.90	2.83	0.51	0.29	0.02	97.85	22/03/2018	5 µm
Saksun_>63	49.44	2.92	13.19	14.42	0.25	5.84	10.08	2.64	0.39	0.27	0.02	99.45	22/03/2018	5 µm
Saksun_>63	49.13	2.88	13.00	14.81	0.23	5.76	10.22	2.77	0.41	0.27	0.01	99.50	22/03/2018	5 µm
Saksun_>63	50.03	3.08	12.54	14.85	0.24	5.50	9.81	2.69	0.39	0.28	0.02	99.44	22/03/2018	5 µm
Saksun_>63	49.09	3.10	12.74	14.96	0.25	5.57	9.69	2.65	0.42	0.30	0.02	98.78	22/03/2018	5 µm
Saksun_>63	48.83	2.96	12.84	14.05	0.23	5.69	10.01	2.64	0.49	0.27	0.03	98.03	22/03/2018	5 µm
Saksun_>63	50.03	2.41	13.86	12.64	0.22	6.23	10.79	2.77	0.33	0.21	0.01	99.50	22/03/2018	5 µm
Saksun_>63	48.74	2.95	12.87	14.60	0.23	5.66	9.85	2.82	0.46	0.29	0.02	98.47	22/03/2018	5 µm
Saksun_>63	49.35	3.10	12.73	14.95	0.25	5.25	9.86	2.75	0.46	0.28	0.02	98.99	22/03/2018	5 µm
Saksun_>63	49.59	2.98	12.93	14.80	0.22	5.73	10.56	2.30	0.47	0.27	0.02	99.86	22/03/2018	5 µm
Saksun_>63	48.94	3.12	12.86	14.53	0.24	5.43	9.60	2.77	0.43	0.28	0.02	98.22	22/03/2018	5 µm
Saksun_>63	49.45	3.11	13.11	14.46	0.23	5.36	9.56	2.87	0.47	0.28	0.02	98.93	22/03/2018	5 µm
Mean:	49.29	2.83	12.92	14.39	0.23	5.83	10.21	2.64	0.42	0.28	0.02	99.07		
StDev	0.49	0.43	0.73	1.03	0.01	0.83	0.86	0.22	0.11	0.06	0.00	0.85		

Sample	SiO_2	TiO2	Al_2O_3	FeO_T	MnO	MgO	CaO	Na_2O	K_2O	P_2O_5	Cl	Total	Date	Beam width
Saksun_control	48.94	2.08	13.82	12.46	0.21	6.61	11.68	2.70	0.27	0.21	0.01	98.97	22/03/2018	3 µm
Saksun_control	49.15	2.96	12.92	13.96	0.21	5.46	9.86	2.72	0.44	0.30	0.02	98.00	22/03/2018	3 µm
Saksun_control	49.81	3.08	13.04	14.54	0.23	5.27	9.78	2.95	0.46	0.34	0.02	99.51	22/03/2018	3 µm
Saksun_control	48.58	2.01	13.86	12.36	0.21	6.88	11.27	2.21	0.25	0.18	0.01	97.83	22/03/2018	3 µm
Saksun_control	48.37	2.91	13.36	13.97	0.23	5.41	10.02	2.59	0.48	0.30	0.02	97.66	22/03/2018	3 µm
Saksun_control	49.83	2.64	13.98	13.13	0.23	5.71	10.19	2.39	0.45	0.29	0.02	98.83	22/03/2018	3 µm
Saksun_control	50.29	3.07	12.78	13.29	0.24	4.83	9.22	2.56	0.45	0.34	0.02	97.10	22/03/2018	3 µm
Saksun_control	49.36	3.11	12.08	14.59	0.23	5.26	9.46	3.08	0.50	0.34	0.02	98.03	22/03/2018	3 µm
Saksun_control	49.83	2.90	13.00	14.18	0.22	5.37	10.08	2.63	0.38	0.22	0.02	98.83	22/03/2018	5 µm

Saksun_control	49.43	3.08	13.15	14.43	0.22	5.11	9.59	2.82	0.40	0.26	0.02	98.51	22/03/2018	5 µm
Saksun_control	49.51	3.37	12.36	15.06	0.22	4.79	9.72	2.97	0.53	0.26	0.03	98.81	22/03/2018	5 µm
Saksun_control	49.31	2.76	13.21	13.95	0.24	5.71	10.29	2.55	0.40	0.21	0.02	98.65	22/03/2018	5 µm
Saksun_control	48.65	2.88	12.80	14.18	0.23	5.72	10.21	2.74	0.43	0.23	0.02	98.09	22/03/2018	5 µm
Saksun_control	49.33	2.60	12.95	13.73	0.23	5.99	10.59	2.21	0.33	0.20	0.01	98.16	22/03/2018	5 µm
Saksun_control	49.61	3.12	12.43	15.08	0.24	5.52	9.58	2.81	0.48	0.27	0.02	99.16	22/03/2018	5 µm
Saksun_control	49.68	3.10	12.41	14.67	0.25	5.41	9.88	2.78	0.49	0.26	0.02	98.93	22/03/2018	5 µm
Saksun_control	50.26	2.96	13.12	14.03	0.24	5.44	10.01	2.63	0.37	0.26	0.02	99.34	22/03/2018	5 µm
Saksun_control	49.77	2.89	13.12	14.44	0.24	5.56	9.81	2.72	0.36	0.24	0.02	99.17	22/03/2018	5 µm
Saksun_control	49.72	2.90	12.76	13.90	0.23	5.85	10.34	2.31	0.41	0.25	0.01	98.69	22/03/2018	5 µm
Saksun_control	50.51	2.91	11.61	13.36	0.23	7.43	11.33	2.35	0.36	0.26	0.02	100.38	22/03/2018	5 µm
Saksun_control	49.03	2.88	12.99	14.36	0.22	5.58	9.97	2.58	0.45	0.25	0.01	98.32	22/03/2018	5 µm
Saksun_control	49.08	3.09	12.97	14.46	0.23	5.26	9.50	2.86	0.47	0.29	0.02	98.23	22/03/2018	5 µm
Saksun_control	49.76	2.72	12.96	14.38	0.22	5.58	10.14	2.35	0.42	0.23	0.02	98.79	22/03/2018	5 µm
Saksun_control	50.64	2.89	13.01	13.19	0.22	5.01	9.29	2.29	0.44	0.28	0.02	97.29	22/03/2018	5 µm
Saksun_control	48.50	2.85	12.90	14.10	0.21	5.63	9.91	2.65	0.40	0.25	0.02	97.44	22/03/2018	5 µm
Saksun_control	50.58	3.13	12.95	12.52	0.22	5.11	9.65	3.53	0.47	0.30	0.02	98.47	22/03/2018	5 µm
Mean:	49.52	2.88	12.94	13.94	0.23	5.60	10.05	2.65	0.42	0.26	0.02	98.51		
StDev	0.63	0.30	0.51	0.74	0.01	0.59	0.60	0.30	0.07	0.04	0.00	0.74		

Sample	SiO_2	TiO2	Al_2O_3	FeO_T	MnO	MgO	CaO	Na_2O	K_2O	P_2O_5	Cl	Total	Date	Beam width
Saksun_acid_<63	49.00	2.88	13.83	13.73	0.23	5.58	10.13	2.77	0.47	0.31	0.02	98.96	22/03/2018	3 µm
Saksun_acid_<63	49.97	2.93	13.14	14.44	0.23	5.74	10.24	3.08	0.44	0.30	0.02	100.53	22/03/2018	3 µm
Saksun_acid_<63	48.96	3.09	13.07	14.84	0.24	5.51	9.81	2.82	0.44	0.34	0.02	99.13	22/03/2018	3 µm
Saksun_acid_<63	49.28	2.91	13.36	14.15	0.23	5.53	9.83	2.45	0.40	0.32	0.02	98.47	22/03/2018	3 µm
Saksun_acid_<63	49.02	2.87	13.14	13.59	0.23	5.64	10.13	2.72	0.44	0.31	0.02	98.10	22/03/2018	3 µm
Saksun_acid_<63	48.58	2.98	13.20	14.69	0.23	5.62	10.06	2.75	0.44	0.34	0.02	98.90	22/03/2018	3 µm
Saksun_acid_<63	48.40	2.67	13.31	14.13	0.22	6.13	10.29	2.55	0.39	0.27	0.01	98.37	22/03/2018	3 µm

Saksun_acid_<63	48.78	2.93	13.35	14.26	0.24	5.68	10.25	3.00	0.45	0.31	0.01	99.25	22/03/2018	3 µm
Saksun_acid_<63	48.87	3.14	13.35	14.62	0.24	5.25	9.64	2.82	0.50	0.32	0.02	98.77	22/03/2018	3 µm
Saksun_acid_<63	49.62	2.90	12.89	13.99	0.21	5.70	10.19	2.85	0.47	0.30	0.02	99.14	22/03/2018	3 µm
Saksun_acid_<63	49.40	2.88	13.16	14.81	0.24	5.73	10.08	2.79	0.44	0.32	0.02	99.86	22/03/2018	3 µm
Saksun_acid_<63	49.91	2.91	14.22	14.35	0.22	5.72	10.11	2.85	0.48	0.32	0.01	101.11	22/03/2018	3 µm
Saksun_acid_<63	49.33	3.12	13.22	14.51	0.23	5.34	9.56	3.03	0.47	0.31	0.02	99.16	22/03/2018	3 µm
Saksun_acid_<63	49.94	2.88	14.19	14.43	0.23	5.66	10.19	2.72	0.36	0.29	0.02	100.91	22/03/2018	3 µm
Saksun_acid_<63	49.16	3.10	12.79	14.30	0.24	5.35	9.45	2.74	0.44	0.36	0.02	97.95	22/03/2018	3 µm
Saksun_acid_<63	49.61	3.14	13.00	14.64	0.23	5.29	9.60	2.36	0.49	0.34	0.02	98.71	22/03/2018	3 µm
Saksun_acid_<63	48.79	3.17	13.06	14.68	0.23	5.31	9.68	2.81	0.47	0.36	0.01	98.56	22/03/2018	3 µm
Saksun_acid_<63	48.91	3.15	13.24	14.88	0.24	5.47	10.07	2.32	0.44	0.33	0.02	99.08	22/03/2018	3 µm
Saksun_acid_<63	49.18	2.90	13.71	14.42	0.23	5.67	10.03	2.83	0.46	0.31	0.02	99.76	22/03/2018	3 µm
Saksun_acid_<63	49.17	2.96	13.28	14.55	0.23	5.68	9.88	3.05	0.47	0.33	0.02	99.61	22/03/2018	3 µm
Saksun_acid_<63	49.08	3.09	13.46	14.67	0.24	5.42	9.62	2.92	0.53	0.32	0.02	99.37	22/03/2018	3 µm
Saksun_acid_<63	49.12	2.87	13.31	14.99	0.25	5.78	10.14	2.60	0.43	0.32	0.02	99.84	22/03/2018	3 µm
Saksun_acid_<63	49.84	3.11	5.26	17.09	0.33	10.05	12.25	1.07	0.33	0.34	0.02	99.68	22/03/2018	3 µm
Saksun_acid_<63	49.24	3.08	12.87	14.38	0.24	5.23	9.64	2.88	0.45	0.36	0.03	98.42	22/03/2018	3 µm
Saksun_acid_<63	49.41	2.92	13.54	14.15	0.22	5.67	10.08	2.79	0.47	0.31	0.02	99.58	22/03/2018	3 µm
Saksun_acid_<63	48.62	2.72	13.57	13.81	0.23	5.81	10.34	2.56	0.35	0.27	0.01	98.29	22/03/2018	3 µm
Saksun_acid_<63	48.87	2.87	13.57	13.90	0.24	5.74	9.95	2.83	0.45	0.32	0.02	98.77	22/03/2018	3 µm
Mean:	49.19	2.97	13.04	14.48	0.24	5.75	10.05	2.70	0.44	0.32	0.02	99.19		
StDev	0.42	0.13	1.59	0.64	0.02	0.88	0.51	0.38	0.04	0.02	0.00	0.80		

Sample	SiO_2	TiO2	Al_2O_3	FeO_T	MnO	MgO	CaO	Na_2O	K_2O	P_2O_5	Cl	Total	Date	Beam width
BPB_acid	72.60	0.21	13.38	1.44	0.05	0.39	1.65	4.26	3.11	0.07	0.30	97.46	09/08/2018	5 µm
BPB_acid	72.56	0.20	13.71	1.51	0.04	0.46	1.87	4.40	3.14	0.08	0.34	98.31	09/08/2018	5 µm
BPB_acid	70.99	0.20	13.75	1.43	0.05	0.40	1.78	4.02	3.11	0.06	0.34	96.11	09/08/2018	5 µm
BPB_acid	74.21	0.21	13.96	1.36	0.05	0.37	1.93	4.40	3.02	0.06	0.36	99.94	09/08/2018	5 µm

BPB_acid	73.29	0.19	14.02	1.34	0.05	0.38	1.78	4.32	3.12	0.06	0.38	98.93	09/08/2018	5 µm
BPB_acid	72.28	0.21	14.13	1.52	0.05	0.41	1.93	4.34	3.25	0.06	0.34	98.53	09/08/2018	5 µm
BPB_acid	72.79	0.20	14.21	1.34	0.04	0.38	1.97	4.46	2.99	0.05	0.36	98.80	09/08/2018	5 µm
BPB_acid	73.08	0.20	14.26	1.51	0.05	0.42	1.90	4.40	3.04	0.08	0.41	99.36	09/08/2018	5 µm
BPB_acid	73.85	0.21	14.67	1.44	0.05	0.36	1.88	4.47	3.20	0.06	0.35	100.53	09/08/2018	5 µm
BPB_acid	71.80	0.21	15.52	1.49	0.04	0.42	1.80	3.98	2.98	0.06	0.35	98.65	09/08/2018	5 µm
Mean:	72.75	0.20	14.16	1.44	0.05	0.40	1.85	4.30	3.10	0.06	0.35	98.66		
StDev	0.94	0.01	0.59	0.07	0.00	0.03	0.09	0.17	0.09	0.01	0.03	1.24		
BPB_acid	*67.98*	*0.21*	*13.27*	*1.41*	*0.05*	*0.39*	*1.82*	*4.24*	*2.91*	*0.10*	*0.41*	*92.79*	*09/08/2018*	*5 um*
BPB_acid	*69.53*	*0.20*	*13.43*	*1.30*	*0.04*	*0.34*	*1.71*	*4.07*	*2.86*	*0.08*	*0.35*	*93.89*	*09/08/2018*	*5 um*

Sample	SiO_2	TiO2	Al_2O_3	FeO_T	MnO	MgO	CaO	Na_2O	K_2O	P_2O_5	Cl	Total	Date	Beam width
BPB_float	69.30	0.22	13.56	1.44	0.04	0.43	1.89	4.10	2.95	0.08	0.36	94.37	09/08/2018	5 µm
BPB_float	71.26	0.20	13.80	1.33	0.03	0.39	1.82	4.12	3.16	0.08	0.39	96.58	09/08/2018	5 µm
BPB_float	73.56	0.20	14.02	1.56	0.04	0.38	1.87	4.35	3.10	0.06	0.34	99.48	09/08/2018	5 µm
BPB_float	72.33	0.21	14.02	1.49	0.04	0.41	1.78	4.18	3.07	0.08	0.38	97.98	09/08/2018	5 µm
BPB_float	73.72	0.21	14.13	1.47	0.04	0.37	1.89	4.33	3.04	0.07	0.36	99.63	09/08/2018	5 µm
BPB_float	70.25	0.20	14.14	1.43	0.04	0.35	1.86	4.19	3.02	0.06	0.33	95.87	09/08/2018	5 µm
BPB_float	73.39	0.21	14.23	1.48	0.05	0.41	1.85	4.25	3.07	0.06	0.39	99.40	09/08/2018	5 µm
BPB_float	71.22	0.20	14.39	1.48	0.04	0.39	1.80	4.16	2.97	0.07	0.36	97.07	09/08/2018	5 µm
BPB_float	72.67	0.21	14.40	1.64	0.03	0.38	1.87	4.35	3.12	0.07	0.33	99.06	09/08/2018	5 µm
BPB_float	72.03	0.21	14.67	1.38	0.05	0.35	1.97	4.33	3.03	0.07	0.37	98.48	09/08/2018	5 µm
Mean:	71.97	0.21	14.13	1.47	0.04	0.39	1.86	4.24	3.05	0.07	0.36	97.79		
StDev	1.47	0.01	0.32	0.09	0.01	0.03	0.05	0.10	0.07	0.01	0.02	1.78		
BPB_float	*66.63*	*0.18*	*12.82*	*1.45*	*0.03*	*0.37*	*1.68*	*4.05*	*2.94*	*0.13*	*0.43*	*90.71*	*09/08/2018*	*5 µm*
BPB_float	*68.11*	*0.20*	*12.83*	*1.22*	*0.04*	*0.32*	*1.60*	*3.42*	*2.75*	*0.13*	*0.39*	*91.01*	*09/08/2018*	*5 µm*

Sample	SiO_2	TiO2	Al_2O_3	FeO_T	MnO	MgO	CaO	Na_2O	K_2O	P_2O_5	Cl	Total	Date	Beam width
PND_acid	69.64	0.20	13.29	1.58	0.05	0.36	1.86	4.09	2.83	0.09	0.36	94.35	09/08/2018	5 µm
PND_acid	72.82	0.19	13.97	1.53	0.04	0.39	1.90	4.19	3.01	0.08	0.37	98.48	09/08/2018	5 µm
PND_acid	73.10	0.20	14.22	1.62	0.05	0.41	1.87	4.24	2.99	0.06	0.33	99.10	09/08/2018	5 µm
PND_acid	73.12	0.20	14.35	1.38	0.03	0.38	1.91	4.24	2.93	0.06	0.39	98.99	09/08/2018	5 µm
PND_acid	73.24	0.21	14.86	1.45	0.05	0.41	1.94	4.28	3.11	0.05	0.32	99.91	09/08/2018	5 µm
PND_acid	72.06	0.19	14.90	1.14	0.04	0.34	2.32	4.41	2.93	0.06	0.31	98.70	09/08/2018	5 µm
PND_acid	71.45	0.17	16.54	1.26	0.04	0.28	2.65	5.10	2.62	0.06	0.27	100.43	09/08/2018	5 µm
Mean:	72.20	0.19	14.59	1.42	0.04	0.37	2.06	4.36	2.92	0.06	0.34	98.57		
StDev	1.31	0.02	1.02	0.17	0.01	0.04	0.30	0.34	0.16	0.01	0.04	1.98		
PND_acid	*67.96*	*0.20*	*12.76*	*1.30*	*0.04*	*0.33*	*1.73*	*3.70*	*2.78*	*0.14*	*0.37*	*91.30*	*09/08/2018*	*5 µm*
PND_acid	*67.64*	*0.20*	*12.80*	*1.50*	*0.04*	*0.35*	*1.64*	*3.93*	*2.91*	*0.10*	*0.39*	*91.51*	*09/08/2018*	*5 µm*
PND_acid	*67.56*	*0.19*	*13.40*	*1.58*	*0.05*	*0.40*	*1.82*	*4.17*	*2.79*	*0.10*	*0.43*	*92.49*	*09/08/2018*	*5 µm*

Sample	SiO_2	TiO2	Al_2O_3	FeO_T	MnO	MgO	CaO	Na_2O	K_2O	P_2O_5	Cl	Total	Date	Beam width
PND3_Float_1	69.85	0.22	13.52	1.47	0.04	0.37	1.83	4.08	3.03	0.09	0.33	94.83	09/08/2018	5 µm
PND3_Float_1	72.64	0.20	13.96	1.39	0.05	0.40	1.97	4.27	3.01	0.11	0.42	98.41	09/08/2018	5 µm
PND3_Float_1	72.62	0.18	14.11	1.35	0.04	0.38	1.79	3.31	5.05	0.12	0.45	99.40	09/08/2018	5 µm
Mean:	71.70	0.20	13.86	1.40	0.04	0.39	1.86	3.89	3.70	0.11	0.40	97.55		
StDev	1.61	0.02	0.31	0.06	0.00	0.01	0.09	0.51	1.17	0.02	0.06	2.40		

A.2 EPMA secondary standards included in Paper I

Appendix A.2 includes major-minor oxide concentrations (wt%) of secondary glass standards described in Paper I. Shards were analysed at the Tephra Analytical Unit, University of Edinburgh, using a Cameca SX100 electron probe microanalyser. 3 µm and 5 µm focused beams were used, with a 10 KeV accelerating voltage, and 5 nA current (Hayward, 2012).

Table A.2: Individual major-minor oxide concentrations (wt%) from secondary glass standards included in Paper I.

Run start (21/03/18)	SiO_2	TiO2	Al_2O_3	FeO_T	MnO	MgO	CaO	Na_2O	K_2O	P_2O_5	Cl	Total	Date	Beam width
BCR2g	54.52	2.26	13.69	12.51	0.20	3.60	7.23	3.40	1.83	0.34	-	99.57	21/03/2018	5 µm
BCR2g	54.81	2.25	13.37	12.29	0.19	3.70	7.10	3.34	1.79	0.34	-	99.18	21/03/2018	5 µm
BCR2g	54.92	2.27	13.52	13.00	0.20	3.67	7.32	2.78	1.79	0.34	-	99.81	21/03/2018	5 µm
Lipari	73.85	0.08	12.71	1.62	0.07	0.04	0.74	4.17	5.16	0.00	-	98.45	21/03/2018	5 µm
Lipari	74.04	0.07	13.06	1.55	0.06	0.06	0.74	4.14	5.10	0.00	-	98.81	21/03/2018	5 µm
Lipari	73.77	0.08	13.24	1.63	0.07	0.04	0.78	4.19	5.33	0.00		99.13	21/03/2018	5 µm

Run end (21/03/18)	SiO_2	TiO2	Al_2O_3	FeO_T	MnO	MgO	CaO	Na_2O	K_2O	P_2O_5	Cl	Total	Date	Beam width
BCR2g	54.63	2.29	13.42	12.26	0.20	3.59	7.34	3.23	1.83	0.33	0.01	99.13	21/03/2018	5 µm
BCR2g	54.37	2.28	13.50	12.66	0.20	3.63	7.31	3.26	1.83	0.35	0.01	99.41	21/03/2018	5 µm
BCR2g	54.02	2.28	13.64	12.44	0.20	3.45	7.31	3.27	1.78	0.33	0.01	98.73	21/03/2018	5 µm
BCR2g	54.69	2.29	13.61	12.62	0.20	3.61	7.27	3.27	1.93	0.34	0.01	99.83	21/03/2018	5 µm
BCR2g	54.60	2.28	13.58	12.54	0.19	3.66	7.47	3.08	1.71	0.35	0.01	99.46	21/03/2018	5 µm
BCR2g	55.03	2.28	13.21	12.74	0.20	3.57	7.20	3.34	1.91	0.34	0.00	99.82	21/03/2018	5 µm
BCR2g	54.08	2.29	13.13	12.30	0.20	3.67	7.17	3.25	1.85	0.34	0.01	98.28	21/03/2018	5 µm
Lipari	74.24	0.08	13.29	1.66	0.06	0.02	0.72	3.98	5.20	0.00	0.36	99.61	21/03/2018	5 µm

Lipari	74.15	0.08	13.18	1.55	0.07	0.03	0.76	4.07	5.26	0.02	0.37	99.54	21/03/2018	5 µm
Lipari	73.59	0.08	12.70	1.43	0.08	0.03	0.80	4.21	5.25	0.01	0.37	98.54	21/03/2018	5 µm
Lipari	74.02	0.08	13.06	1.76	0.07	0.05	0.78	4.04	5.14	0.00	0.37	99.38	21/03/2018	5 µm
Lipari	74.20	0.09	13.11	1.65	0.07	0.03	0.85	4.30	5.20	0.00	0.35	99.86	21/03/2018	5 µm
Lipari	73.87	0.09	13.14	1.42	0.07	0.03	0.79	4.08	5.25	0.00	0.36	99.10	21/03/2018	5 µm

Run start (22/03/18)	**SiO_2**	**TiO2**	**Al_2O_3**	**FeO_T**	**MnO**	**MgO**	**CaO**	**Na_2O**	**K_2O**	**P_2O_5**	**Cl**	**Total**	**Date**	**Beam width**
Lipari	73.47	0.08	12.78	1.50	0.06	0.04	0.71	4.08	5.15	0.00	0.35	98.22	22/03/2018	5 µm
Lipari	73.35	0.07	12.68	1.44	0.07	0.05	0.76	4.18	5.19	0.00	0.36	98.16	22/03/2018	5 µm
Lipari	74.04	0.08	13.98	1.56	0.06	0.07	0.76	4.68	5.19	0.00	0.37	100.79	22/03/2018	5 µm
BCR2g	54.59	2.27	13.04	11.95	0.22	3.57	7.06	4.21	1.89	0.33	0.00	99.12	22/03/2018	5 µm
BCR2g	55.44	2.30	13.87	12.75	0.19	3.52	7.11	3.21	1.82	0.34	0.01	100.56	22/03/2018	5 µm
BCR2g	54.60	2.29	14.26	12.70	0.18	3.59	6.96	3.42	1.85	0.36	0.01	100.23	22/03/2018	5 µm
Lipari	75.09	0.08	12.01	1.49	0.07	0.03	0.78	3.97	5.19	0.00	0.37	99.08	22/03/2018	3 µm
Lipari	75.45	0.08	12.90	1.42	0.07	0.03	0.68	3.94	5.09	0.00	0.36	100.03	22/03/2018	3 µm
Lipari	75.03	0.07	12.72	1.58	0.07	0.05	0.71	3.92	5.16	0.01	0.35	99.68	22/03/2018	3 µm
Lipari	74.78	0.08	13.95	1.54	0.07	0.04	0.68	4.14	5.12	0.01	0.37	100.78	22/03/2018	3 µm
BCR2g	55.18	2.26	13.15	12.37	0.22	3.52	7.21	3.26	1.73	0.32	0.01	99.23	22/03/2018	3 µm
BCR2g	55.44	2.25	12.86	12.61	0.20	3.55	7.24	2.96	1.76	0.31	0.01	99.18	22/03/2018	3 µm
BCR2g	55.49	2.23	13.85	12.20	0.20	3.60	6.97	3.20	1.73	0.34	0.01	99.82	22/03/2018	3 µm
BCR2g	54.48	2.26	13.99	12.71	0.19	3.58	7.09	2.99	1.72	0.34	0.01	99.36	22/03/2018	3 µm

Run end (22/03/18)	SiO_2	TiO2	Al_2O_3	FeO_T	MnO	MgO	CaO	Na_2O	K_2O	P_2O_5	Cl	Total	Date	Beam width
Lipari	73.55	0.08	13.29	1.57	0.08	0.04	0.81	4.19	5.12	0.01	0.36	99.11	22/03/2018	3 µm
Lipari	73.76	0.08	13.46	1.62	0.06	0.05	0.76	4.50	5.07	0.01	0.36	99.72	22/03/2018	3 µm
Lipari	74.00	0.09	13.13	1.73	0.07	0.05	0.81	4.18	5.19	0.00	0.36	99.61	22/03/2018	3 µm
Lipari	74.00	0.08	13.23	1.63	0.07	0.05	0.81	4.25	5.02	0.01	0.38	99.53	22/03/2018	3 µm
Lipari	73.72	0.07	13.80	1.86	0.07	0.04	0.74	3.85	5.08	0.01	0.36	99.61	22/03/2018	3 µm
Lipari	73.74	0.08	13.65	1.50	0.06	0.05	0.82	4.35	5.09	0.01	0.36	99.70	22/03/2018	3 µm
BCR2g	54.21	2.29	13.59	12.52	0.20	3.58	7.16	3.44	1.78	0.32	0.01	99.10	22/03/2018	3 µm
BCR2g	54.63	2.26	13.78	12.16	0.19	3.57	6.83	3.29	1.88	0.33	0.01	98.92	22/03/2018	3 µm
BCR2g	54.63	2.27	13.87	12.70	0.21	3.60	7.07	3.79	1.79	0.33	0.01	100.26	22/03/2018	3 µm
BCR2g	53.88	2.26	13.35	12.43	0.19	3.51	7.19	3.64	1.78	0.30	0.00	98.55	22/03/2018	3 µm
BCR2g	54.82	2.28	14.07	12.24	0.19	3.44	7.09	3.83	1.89	0.32	0.01	100.18	22/03/2018	3 µm
BCR2g	54.33	2.26	13.63	12.77	0.20	3.53	7.22	3.42	1.80	0.31	0.00	99.48	22/03/2018	3 µm
Lipari	74.51	0.08	12.96	1.52	0.06	0.06	0.74	3.98	5.16	0.01	0.38	99.47	22/03/2018	5 µm
Lipari	73.47	0.08	12.84	1.72	0.07	0.04	0.82	4.00	4.98	-0.01	0.36	98.36	22/03/2018	5 µm
Lipari	73.76	0.08	12.99	1.39	0.07	0.08	0.77	3.99	5.24	0.00	0.37	98.74	22/03/2018	5 µm
Lipari	75.03	0.07	13.00	1.43	0.06	0.05	0.75	3.95	5.05	-0.01	0.36	99.74	22/03/2018	5 µm
Lipari	73.96	0.08	13.32	1.59	0.06	0.03	0.71	3.92	5.02	0.00	0.36	99.05	22/03/2018	5 µm
Lipari	78.64	0.08	13.47	1.69	0.06	0.04	0.81	0.11	1.87	0.00	0.38	97.15	22/03/2018	5 µm
BCR2g	54.74	2.26	13.64	12.82	0.21	3.64	7.17	3.29	1.89	0.26	0.01	99.94	22/03/2018	5 µm
BCR2g	55.26	2.26	13.54	12.19	0.20	3.54	6.95	3.22	1.71	0.24	0.01	99.12	22/03/2018	5 µm
BCR2g	54.38	2.27	13.24	12.24	0.21	3.65	7.18	3.24	1.88	0.25	0.01	98.55	22/03/2018	5 µm
BCR2g	54.66	2.28	13.29	12.73	0.19	3.57	7.20	3.46	1.91	0.27	0.01	99.56	22/03/2018	5 µm
BCR2g	54.65	2.27	13.07	12.12	0.19	3.51	7.09	3.13	1.85	0.26	0.01	98.15	22/03/2018	5 µm
BCR2g	54.74	2.28	13.66	12.24	0.20	3.60	7.20	3.22	1.85	0.25	0.01	99.25	22/03/2018	5 µm

Run end (23/03/18)	SiO_2	TiO2	Al_2O_3	FeO_T	MnO	MgO	CaO	Na_2O	K_2O	P_2O_5	Cl	Total	Date	Beam width
Lipari	73.64	0.08	12.92	1.47	0.07	0.05	0.70	4.26	5.14	0.01	0.36	98.70	23/03/2018	3 µm
Lipari	77.84	0.08	13.57	1.68	0.06	0.04	0.78	0.22	1.64	0.01	0.35	96.28	23/03/2018	3 µm
Lipari	73.74	0.08	13.01	1.33	0.06	0.05	0.74	4.24	5.26	0.00	0.37	98.88	23/03/2018	3 µm
Lipari	73.62	0.08	12.66	1.46	0.06	0.05	0.78	4.20	5.22	0.00	0.37	98.51	23/03/2018	3 µm
Lipari	73.52	0.08	12.91	1.57	0.08	0.04	0.79	3.86	5.23	0.00	0.36	98.44	23/03/2018	3 µm
Lipari	73.57	0.08	11.89	1.57	0.07	0.09	0.73	3.94	5.25	0.01	0.36	97.55	23/03/2018	3 µm
BCR2g	53.97	2.25	13.39	12.46	0.21	3.54	7.13	3.26	1.84	0.34	0.01	98.40	23/03/2018	3 µm
BCR2g	53.62	2.27	13.63	12.62	0.20	3.68	7.08	2.82	1.78	0.37	0.01	98.07	23/03/2018	3 µm
BCR2g	53.72	2.24	13.01	12.51	0.20	3.48	7.13	3.15	1.81	0.36	0.01	97.62	23/03/2018	3 µm
BCR2g	54.12	2.26	12.59	12.20	0.20	3.56	6.96	2.98	1.82	0.35	0.01	97.05	23/03/2018	3 µm
BCR2g	54.96	2.25	12.55	12.80	0.20	3.58	7.02	2.96	1.75	0.36	0.01	98.43	23/03/2018	3 µm
BCR2g	54.53	2.25	13.08	12.14	0.18	3.66	7.04	3.39	1.85	0.36	0.01	98.49	23/03/2018	3 µm
Lipari	75.10	0.08	13.10	1.41	0.07	0.03	0.71	3.86	5.12	0.01	0.36	99.84	23/03/2018	5 µm
Lipari	74.06	0.08	13.01	1.45	0.07	0.01	0.70	4.03	5.22	0.01	0.36	99.00	23/03/2018	5 µm
Lipari	74.90	0.08	13.17	1.50	0.06	0.04	0.72	4.13	5.23	0.01	0.36	100.20	23/03/2018	5 µm
Lipari	74.53	0.08	12.93	1.51	0.06	0.04	0.75	4.13	5.14	0.01	0.36	99.55	23/03/2018	5 µm
Lipari	74.03	0.08	13.19	1.60	0.07	0.03	0.68	3.93	5.06	0.00	0.37	99.04	23/03/2018	5 µm
Lipari	74.15	0.08	12.99	1.62	0.08	0.04	0.76	4.04	5.30	0.01	0.36	99.42	23/03/2018	5 µm
BCR2g	55.34	2.25	13.46	12.12	0.20	3.47	6.93	3.36	1.79	0.36	0.01	99.29	23/03/2018	5 µm
BCR2g	54.60	2.25	13.44	12.33	0.20	3.60	7.02	3.28	1.84	0.34	0.01	98.90	23/03/2018	5 µm
BCR2g	54.22	2.23	13.66	12.45	0.21	3.54	7.09	3.34	1.82	0.35	0.01	98.93	23/03/2018	5 µm
BCR2g	54.74	2.25	13.86	12.67	0.21	3.46	6.97	3.02	1.77	0.36	0.01	99.31	23/03/2018	5 µm
BCR2g	54.88	2.27	13.42	12.67	0.20	3.57	7.28	2.83	1.82	0.34	0.01	99.30	23/03/2018	5 µm

BCR2g	54.68	2.27	13.57	12.39	0.18	3.52	7.09	3.32	1.85	0.36	0.01	99.24	23/03/2018	5 µm

Run start (09/08/18)	**SiO_2**	**TiO2**	**Al_2O_3**	**FeO_T**	**MnO**	**MgO**	**CaO**	**Na_2O**	**K_2O**	**P_2O_5**	**Cl**	**Total**	**Date**	**Beam width**
Old Crow	72.30	0.27	12.12	1.71	0.06	0.29	1.43	3.72	3.53	0.06	0.37	95.86	09/08/2018	5 µm
Old Crow	71.00	0.27	12.18	1.66	0.04	0.25	1.48	3.61	3.71	0.06	0.37	94.64	09/08/2018	5 µm
Old Crow	73.23	0.28	12.25	1.78	0.06	0.29	1.48	3.69	3.59	0.04	0.29	96.98	09/08/2018	5 µm
Old Crow	72.03	0.27	12.41	1.72	0.05	0.28	1.43	3.96	3.64	0.03	0.27	96.10	09/08/2018	5 µm
Old Crow	72.36	0.28	12.86	1.70	0.06	0.28	1.49	3.84	3.67	0.04	0.28	96.86	09/08/2018	5 µm
Lipari	74.67	0.08	12.97	1.70	0.06	0.07	0.76	4.25	4.99	0.01	-	99.5429	09/08/2018	5 µm
Lipari	74.05	0.08	12.98	1.61	0.06	0.05	0.72	4.00	5.18	0.01	-	98.736	09/08/2018	5 µm
Lipari	74.79	0.08	13.41	1.51	0.06	0.04	0.74	3.97	5.16	0.01	-	99.7777	09/08/2018	5 µm
BCR2g	54.38	2.25	13.23	12.55	0.19	3.71	7.33	3.14	1.71	0.36	-	98.8383	09/08/2018	5 µm
BCR2g	54.82	2.25	13.44	12.81	0.18	3.66	7.44	3.29	1.74	0.36	-	99.9673	09/08/2018	5 µm
BCR2g	54.74	2.24	13.07	12.70	0.18	3.67	7.20	3.23	1.75	0.37	-	99.1558	09/08/2018	5 µm

Run end (09/08/18)	**SiO_2**	**TiO2**	**Al_2O_3**	**FeO_T**	**MnO**	**MgO**	**CaO**	**Na_2O**	**K_2O**	**P_2O_5**	**Cl**	**Total**	**Date**	**Beam width**
Old Crow	73.19	0.28	12.18	1.52	0.05	0.31	1.42	3.56	3.66	0.04	0.28	96.51	09/08/2018	5 µm
Old Crow	72.64	0.29	12.20	1.56	0.06	0.30	1.42	3.86	3.48	0.03	0.28	96.11	09/08/2018	5 µm
Old Crow	73.33	0.28	12.22	1.61	0.05	0.29	1.43	3.87	3.55	0.03	0.27	96.94	09/08/2018	5 µm
Old Crow	71.87	0.28	12.41	1.61	0.05	0.26	1.44	3.94	3.58	0.03	0.28	95.74	09/08/2018	5 µm
Lipari	74.37	0.07	12.27	1.41	0.05	0.06	0.73	3.99	5.01	0.01	-	97.97	09/08/2018	5 µm
Lipari	74.12	0.08	12.26	1.55	0.07	0.02	0.74	4.02	5.15	0.01	-	98.02	09/08/2018	5 µm
BCR2g	54.48	2.22	12.96	11.96	0.19	3.55	7.20	3.39	1.79	0.38	-	98.10	09/08/2018	5 µm
BCR2g	54.34	2.25	13.18	12.33	0.19	3.68	7.24	3.22	1.68	0.36	-	98.47	09/08/2018	5 µm

A.3 The equations used to derive estimates of glass chemical durability

$$Si{:}\,O = \frac{fsi}{60.08 \sum \frac{n_m \times f_m}{W_m}} \qquad Equation\ 1$$

Equation A.1. The molar ratio of silicon to oxygen (Huggins and Sun, 1943; Pollard and Heron, 1996).

fsi = the weight fraction of SiO_2 (= wt%/100)
n_M = the number of oxygens in the formula of each oxide
W_m = the molecular weight of each oxide
f_M = the weight fraction of each oxide

$$NBO = \frac{2(Na_2O + K_2O + CaO + MgO + FeO - Al_2O_3 - Fe_2O_3)}{\left(SiO_2 + 2(Al_2O_3) + 2(Fe_2O_3)\right)} \qquad Equation\ 2$$

Equation A.2. The number of non-bridging oxygens (NBO) (White and Minser, 1984). All Fe was represented as Fe_2O_3 as the ratio between the FeO and redox Fe_2O_3 states is not known in the case study volcanic glasses used here. Oxide formulas represent the molar fraction of each oxide (converted using values in Table A1).

Table A.3: The factors used for converting weight percentages to molar fractions in Paper I.

Oxide	SiO_2	Al_2O_3	TiO_2	Fe_2O_3	FeO	MnO	MgO	CaO	Na2O	K_2O	P_2O_5	Cl
Molar mass factor	0.60	1.02	-	1.597	-	0.71	0.403	0.560	0.62	0.942	1.419	0.35

A.4 Additional major-minor element bivariate plots from the case study tephras

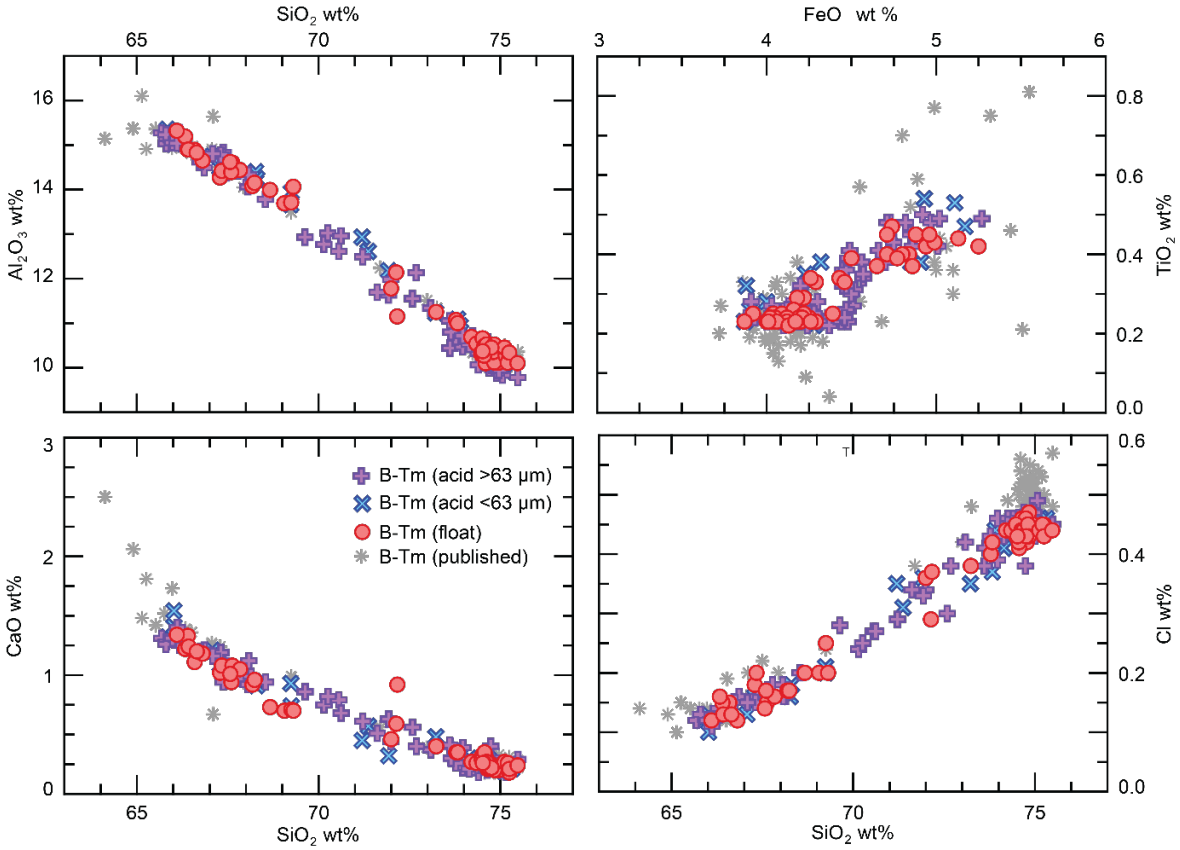

Figure A.1: Bivariate plots of selected major oxide totals (wt%) from the BTm tephra and comparative published values (Hughes *et al.,* 2013; McLean *et al.,* 2016).

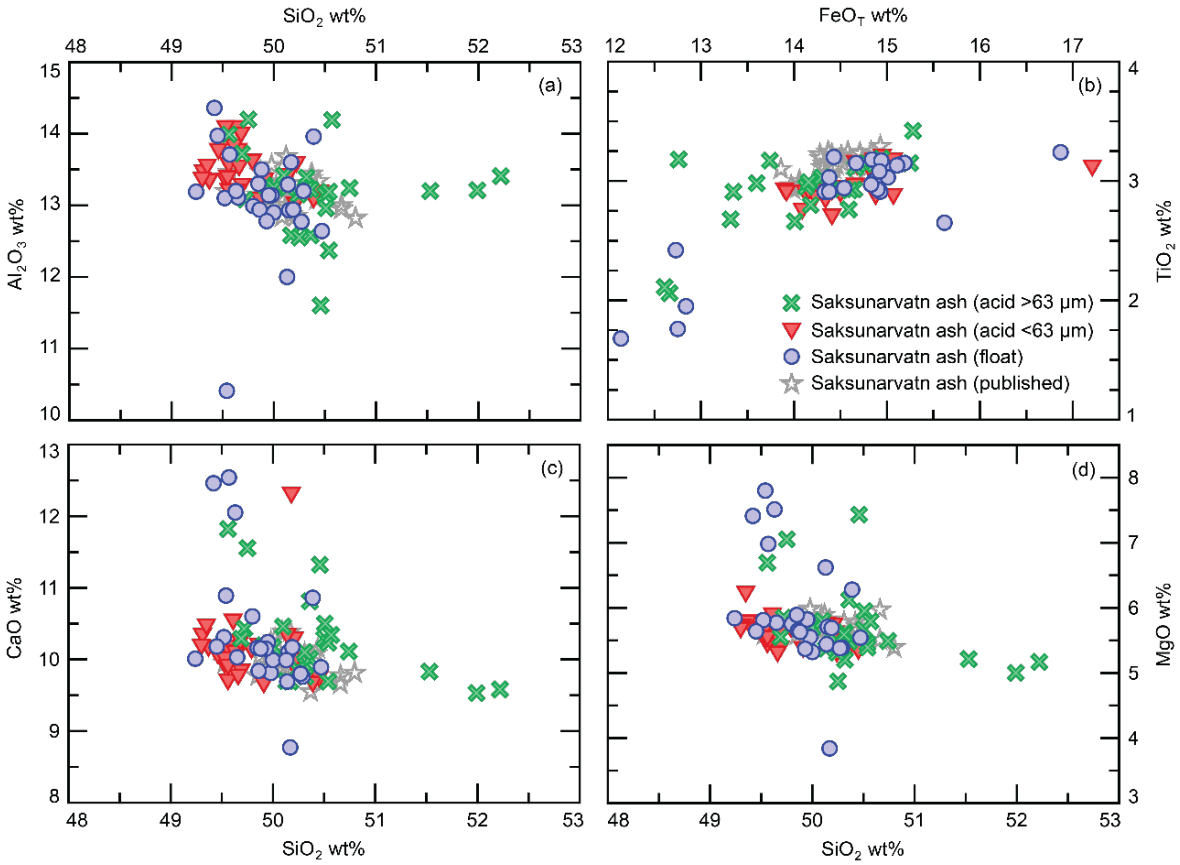

Figure A.2: Bivariate plots of selected major oxide totals (wt%) from the Saksunarvatn ash and comparative published values (Wastegård *et al.,* 2018).

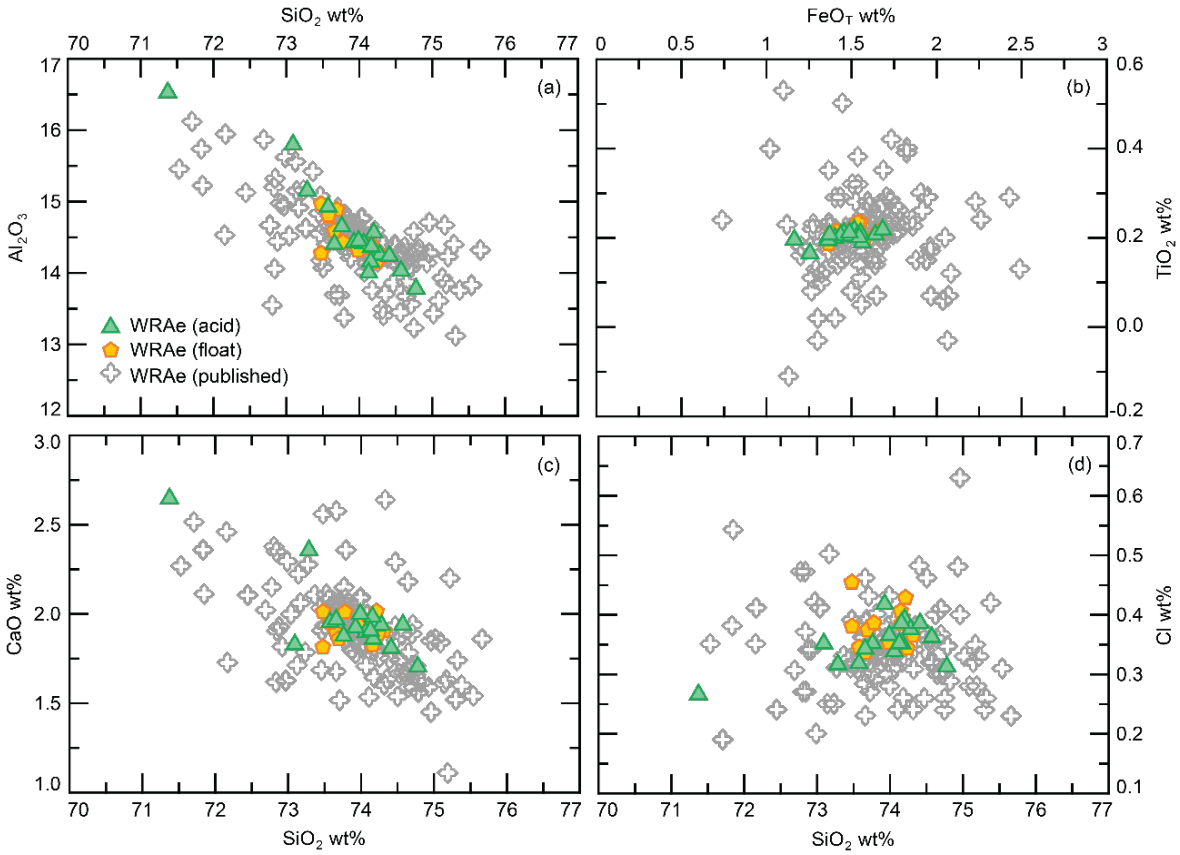

Figure A.3: Bivariate plots of selected major oxide totals (wt%) from the White River Ash (WRAe) tephra and comparative published values (Pyne-O'Donnell *et al.,* 2012; Jensen *et al.,* 2014; Davies *et al.,* 2016).

A.5 Similarity coefficients for case study tephras

Table A.4: Similarity coefficient values for tephra samples analysed in this study and published values. B-Tm (a) includes rhyolitic shard analyses, B-Tm (b) includes trachytic shard analyses. BPB = Baby Pond Bog, PND = Pound Cove Bog. As no P_2O5 was recorded in the B-Tm higher SiO_2 population by Hughes *et al*. (2013) this was removed when calculating similarity coefficients.

	B-Tm (a) float	B-Tm (a) acid (>63 um)	B-Tm (a) acid (<63 um)	B-Tm (a) (Hughes *et al.,* 2013)	
B-Tm (a) floated		0.96	0.94	0.96	
B-Tm (a) acid (>63 um)	0.96		0.95	0.92	
B-Tm (a) acid (<63 um)	0.94	0.95		0.93	
B-Tm (a) (Hughes *et al.,* 2013)	0.96	0.92	0.93		
	B-Tm (b) float	B-Tm (b) acid (>63 um)	B-Tm (b) acid (<63 um)	B-Tm (b) (Hughes *et al.,* 2013)	
B-Tm (b) floated		0.96	0.93	0.85	
B-Tm (b) acid (>63 um)	0.96		0.96	0.88	
B-Tm (b) acid (<63 um)	0.93	0.96		0.90	
B-Tm (b) (Hughes *et al.,* 2013)	0.85	0.88	0.90		
	Saksunarvatn float	Saksunarvatn acid (>63 um)	Saksunarvatn acid (<63 um)	Saksunarvatn (Wastegård *et al.,* 2018)	
Saksunarvatn float		0.98	0.96	0.95	
Saksunarvatn acid (>63 um)	0.98		0.97	0.95	
Saksunarvatn acid (<63 um)	0.96	0.97		0.98	
Saksunarvatn (Wastegård *et al.,* 2018)	0.95	0.95	0.98		
	WRAe float (BPB)	WRAe acid (BPB)	WRAe float (PND)	WRAe acid (PND)	WRAe (Jensen *et al.,* 2014)
WRAe float (BPB)		0.97	0.92	0.95	0.93
WRAe acid (BPB)	0.97		0.92	0.96	0.94
WRAe float (PND)	0.92	0.92		0.89	0.91
WRAe acid (PND)	0.95	0.96	0.89		0.93
WRAe (Jensen *et al.,* 2014)	0.93	0.94	0.91	0.93	

A.6 Cellulase tephra extraction protocol

Outlined here is the methodology for experiments testing effects of cellulase enzyme on peat. These experiments were carried out with the aim of developing a tephra extraction protocol based on the breakdown of cellulose in the walls of plant cells.

Cellulase from *Aspergillus niger* was added to 50 mL of deionised water until saturation was reached. Two 1 cm^3 samples of *Sphagnum* peat were then placed into 100 mL beakers containing this solution and stirred to disaggregate the material. One of these beakers was placed in an incubator at 37 ^oC, while the other was remained at room temperature. Both beakers were left for 24 before being decanted though a 10 µm sieve mesh. Finally, samples from the treated peat were mounted in glycerol and compared with a control sample under a high power microscope.

Appendix B Paper II

B.1 New radiocarbon dates included in Paper II

Table B.1: New radiocarbon dates developed for Paper II. Ages were calibrated using OxCal 4.2.3 (Bronk Ramsey, 2017), and the IntCal13 calibration curve (Reimer *et al*., 2013).

Site	Depth (cm)	Material	^{14}C Age	±	Age (cal yr BP)
Southwest Pond Bog	224	*Sphagnum* stems	2778	34	2955-2787
Southwest Pond Bog	336	*Sphagnum* stems	3504	30	3860-3695
Southwest Pond Bog	430	*Sphagnum* stems	3923	30	4436-4248
Long Pond Bog	224	*Sphagnum* stems	2900	26	3144-2955
Long Pond Bog	368	*Sphagnum* stems	4107	29	4813-4523
Long Pond Bog	501.5	*Sphagnum* stems	5217	36	6174-5908

B.2 EPMA glass shard analyses included in Paper II

Appendix B.2 includes major-minor oxide concentrations (wt%) of individual glass shards from the case study tephra deposits described in Paper II. Shards were analysed at the University of Alberta, using a JEOL 8900 (Jensen *et al*., 2008), or at the University of Edinburgh using a Cameca SX 100 (Hayward, 2012) alongside known secondary standards. Data from standards sets 1-9 are presented in Table B.4. Table B2 does not include analyses from Petite Bog, which were undertaken separately to this thesis as part of the PRECIP project (NERC grant: NER/B/S/2001/00885).

Table B.2: Individual, glass, major-minor oxide concentrations from tephra deposits (wt%) analysed in Paper II.

Tephra ID/Standard sets/Site	Sample	SiO_2	TiO2	Al_2O_3	FeO_T	MnO	MgO	CaO	Na_2O	K_2O	P_2O_5	Cl	Total
WRAe	NL_234	71.76	0.21	14.34	1.59	0.05	0.43	2.03	4.30	3.10	0.05	0.36	98.22
Sets 1,2,3,4 and 5.	NL_234	72.76	0.22	13.86	1.57	0.03	0.40	1.79	4.14	3.06	0.09	0.33	98.25
Nuangola Lake	NL_234	72.99	0.20	14.11	1.52	0.04	0.40	1.89	4.40	3.13	0.05	0.35	99.09
	NL_234	71.07	0.20	13.74	1.44	0.03	0.37	1.88	4.11	3.15	0.05	0.39	96.45
	NL_234	73.72	0.21	13.92	1.54	0.05	0.43	1.74	4.37	3.27	0.06	0.34	99.65
	NL_234	73.16	0.20	13.87	1.41	0.05	0.40	1.90	4.28	3.19	0.07	0.32	98.84
	NL_234	73.13	0.21	14.10	1.62	0.05	0.39	1.91	4.38	3.17	0.07	0.35	99.37
	NL_234	73.27	0.21	14.27	1.56	0.05	0.41	1.97	4.26	3.02	0.06	0.33	99.42
	NL_234	72.56	0.24	14.21	1.70	0.05	0.58	2.21	4.19	3.00	0.07	0.29	99.10
	NL_234	73.95	0.22	14.33	1.46	0.04	0.44	1.87	4.18	3.18	0.06	0.37	100.11
	NL_234	73.18	0.22	14.06	1.55	0.05	0.37	1.84	4.12	3.02	0.08	0.32	98.81
	NL_234	72.46	0.21	13.64	1.55	0.04	0.35	1.88	4.26	3.10	0.07	0.34	97.90
	NL_234	72.77	0.22	13.93	1.55	0.04	0.39	1.94	4.22	3.16	0.05	0.36	98.62
	NL_234	72.43	0.21	13.78	1.49	0.05	0.39	1.99	4.42	3.01	0.06	0.39	98.23
	NL_234	73.05	0.21	14.08	1.68	0.05	0.40	2.00	4.17	3.09	0.05	0.34	99.12

	Mean:	72.82	0.21	14.02	1.55	0.05	0.41	1.92	4.25	3.11	0.06	0.35	98.75
	StDev:	0.72	0.01	0.22	0.08	0.01	0.05	0.11	0.10	0.08	0.01	0.02	0.87
Newberry Pumice	*NL_234*	*68.74*	*0.19*	*13.30*	*1.59*	*0.05*	*0.33*	*1.77*	*4.05*	*3.09*	*0.05*	*0.46*	*93.58*
(reworked)	*NL_234*	*73.34*	*0.21*	*13.93*	*2.12*	*0.05*	*0.19*	*0.91*	*5.05*	*3.99*	*0.03*	*0.14*	*100.02*

Tephra ID/Standard sets/Site	**Sample**	**SiO_2**	**TiO2**	**Al_2O_3**	**FeO_T**	**MnO**	**MgO**	**CaO**	**Na_2O**	**K_2O**	**P_2O_5**	**Cl**	**Total**
Mazama ash	NL_638	72.78	0.41	14.26	1.86	0.06	0.49	1.69	5.32	2.79	0.06	0.18	99.90
Sets 1,2,3,4 and 5.	NL_638	71.06	0.43	13.56	1.84	0.05	0.48	1.74	5.08	2.79	0.06	0.19	97.28
Nuangola Lake	NL_638	72.26	0.42	14.06	1.91	0.05	0.45	1.64	5.33	2.73	0.07	0.18	99.10
	NL_638	72.19	0.41	13.96	1.96	0.06	0.49	1.63	5.09	2.78	0.07	0.20	98.85
	NL_638	73.40	0.42	14.13	1.90	0.05	0.48	1.65	5.28	2.82	0.08	0.18	100.38
	NL_638	73.25	0.41	14.02	1.85	0.05	0.47	1.55	5.04	2.78	0.07	0.18	99.68
	NL_638	71.17	0.42	13.36	1.80	0.06	0.39	1.61	4.92	2.66	0.06	0.20	96.65
	NL_638	72.63	0.42	13.77	1.64	0.05	0.47	1.69	5.03	2.75	0.07	0.18	98.71
	NL_638	73.16	0.48	14.05	1.75	0.04	0.39	1.49	5.13	2.72	0.07	0.19	99.49
	NL_638	71.57	0.42	13.67	1.91	0.05	0.46	1.55	5.13	2.68	0.07	0.19	97.69
	NL_638	71.15	0.49	14.75	2.19	0.07	0.63	1.82	5.45	2.50	0.12	0.19	99.34
	NL_638	71.42	0.41	13.95	1.88	0.06	0.48	1.66	5.06	2.88	0.07	0.19	98.08
	NL_638	72.55	0.42	14.22	1.79	0.05	0.47	1.63	5.22	2.77	0.07	0.20	99.38
	NL_638	73.98	0.43	14.25	1.71	0.05	0.48	1.58	5.23	2.71	0.06	0.19	100.67
	NL_638	73.98	0.44	13.86	1.90	0.05	0.44	1.71	5.28	2.73	0.08	0.19	100.66
	Mean:	72.44	0.43	13.99	1.86	0.05	0.47	1.64	5.17	2.74	0.07	0.19	99.06
	StDev:	1.00	0.02	0.33	0.12	0.01	0.05	0.08	0.14	0.09	0.01	0.01	1.21
	NL_638	*68.51*	*0.40*	*13.19*	*1.73*	*0.04*	*0.41*	*1.47*	*4.91*	*2.68*	*0.07*	*0.16*	*93.62*

Tephra ID/Standard sets/Site	**Sample**	**SiO_2**	**TiO2**	**Al_2O_3**	**FeO_T**	**MnO**	**MgO**	**CaO**	**Na_2O**	**K_2O**	**P_2O_5**	**Cl**	**Total**
Newberry Pumice	LPB_32	73.22	0.21	13.81	1.96	0.06	0.16	0.83	5.19	3.87	0.04	0.14	99.50

Sets 3, 4 and 5.	LPB_32	72.77	0.21	13.55	1.86	0.06	0.13	0.85	4.98	3.93	0.03	0.14	98.51
Long Pond Bog	LPB_32	72.81	0.22	13.13	1.88	0.07	0.18	0.84	4.76	4.06	0.04	0.16	98.15
	LPB_32	70.90	0.21	13.22	1.78	0.05	0.20	0.91	4.85	3.95	0.03	0.15	96.25
	LPB_32	72.75	0.22	13.62	2.02	0.06	0.17	0.84	4.90	3.89	0.02	0.16	98.65
	LPB_32	71.39	0.22	13.80	1.91	0.06	0.17	0.86	4.96	3.89	0.03	0.14	97.44
	LPB_32	73.10	0.21	13.76	1.91	0.06	0.17	0.90	5.03	3.99	0.04	0.15	99.31
	LPB_32	69.46	0.20	12.88	1.77	0.05	0.20	0.92	4.82	3.68	0.05	0.23	94.25
	LPB_32	72.80	0.22	14.05	1.83	0.06	0.20	0.93	4.96	3.81	0.04	0.14	99.04
	LPB_32	72.90	0.22	13.77	2.05	0.05	0.18	0.80	4.84	3.90	0.03	0.14	98.88
	Mean:	72.21	0.21	13.56	1.90	0.06	0.18	0.87	4.93	3.90	0.03	0.15	98.00
	StDev:	1.23	0.01	0.37	0.09	0.01	0.02	0.04	0.12	0.10	0.01	0.03	1.63

Tephra ID/Standard sets/Site	**Sample**	**SiO_2**	**TiO2**	**Al_2O_3**	**FeO_T**	**MnO**	**MgO**	**CaO**	**Na_2O**	**K_2O**	**P_2O_5**	**Cl**	**Total**
Mazama ash	PND_551	70.15	0.44	13.45	1.78	0.04	0.44	1.48	4.23	2.60	-	0.19	94.78
Sets 6,7,8 and 9.	PND_551	70.41	0.40	14.11	1.91	0.07	0.49	1.53	4.40	2.60	-	0.19	96.07
Pound Cove Bog	PND_551	71.68	0.42	14.25	1.75	0.05	0.40	1.46	4.91	2.87	-	0.18	97.92
	PND_551	72.01	0.38	14.20	1.88	0.04	0.48	1.52	5.14	2.82	-	0.19	98.61
	PND_551	71.88	0.36	14.22	1.85	0.06	0.44	1.48	5.52	2.74	-	0.17	98.67
	PND_551	71.25	0.49	14.25	1.75	0.07	0.46	1.55	5.07	2.83	-	0.16	97.84
	PND_551	71.98	0.34	14.52	1.86	0.05	0.51	1.56	5.12	2.79	-	0.18	98.86
	PND_551	71.03	0.44	14.02	1.88	0.02	0.46	1.54	5.26	2.76	-	0.20	97.57
	PND_551	72.51	0.44	14.45	1.75	0.01	0.38	1.42	5.52	3.02	-	0.17	99.63
	PND_551	72.05	0.39	14.63	1.89	0.06	0.48	1.58	5.18	2.75	-	0.16	99.13
	PND_551	71.73	0.46	14.36	1.90	0.04	0.47	1.58	5.09	2.92	-	0.20	98.71
	PND_551	73.14	0.47	14.64	1.90	0.08	0.49	1.63	5.43	2.82	-	0.15	100.71
	PND_551	70.57	0.42	14.33	1.81	0.03	0.43	1.56	5.30	2.64	-	0.16	97.23
	PND_551	71.56	0.37	14.68	1.87	0.04	0.50	1.56	5.10	2.80	-	0.18	98.63
	PND_551	69.00	0.39	14.01	1.76	0.05	0.48	1.55	5.13	2.66	-	0.16	95.15

PND_551	70.74	0.36	14.20	1.92	0.03	0.41	1.61	5.37	2.90	-	0.17	97.66
PND_551	72.06	0.43	14.50	1.85	0.09	0.48	1.64	5.51	2.81	-	0.18	99.50
PND_551	70.31	0.36	14.14	1.79	0.05	0.46	1.60	5.69	2.70	-	0.20	97.25
PND_551	70.16	0.36	14.23	1.82	0.02	0.49	1.61	5.47	2.77	-	0.19	97.07
PND_551	72.24	0.44	14.59	1.91	0.08	0.47	1.63	5.62	2.84	-	0.21	99.97
PND_551	70.86	0.35	14.46	1.81	0.08	0.45	1.57	5.60	2.79	-	0.17	98.10
PND_551	70.99	0.40	14.48	1.81	0.07	0.44	1.57	5.66	2.81	-	0.20	98.38
PND_551	70.89	0.43	14.09	1.88	0.03	0.47	1.67	5.39	3.33	-	0.20	98.31
PND_551	71.03	0.47	14.24	1.78	0.08	0.49	1.60	5.66	3.08	-	0.19	98.57
Mean:	71.26	0.41	14.29	1.84	0.05	0.46	1.56	5.27	2.82	-	0.18	98.10
StDev:	0.93	0.04	0.27	0.06	0.02	0.03	0.06	0.37	0.16	-	0.02	1.40
PND_551	*66.50*	*0.44*	*13.45*	*1.91*	*0.06*	*0.48*	*1.53*	*5.38*	*2.82*	-	*0.17*	*92.71*
PND_551	*67.90*	*1.00*	*13.65*	*4.01*	*0.06*	*0.88*	*2.75*	*4.39*	*3.06*	-	*0.15*	*97.81*
PND_551	*75.90*	*0.23*	*12.88*	*1.28*	*0.07*	*0.39*	*1.89*	*4.10*	*1.55*	-	*0.14*	*98.41*

Tephra ID/Standard sets/Site	**Sample**	**SiO_2**	**TiO2**	**Al_2O_3**	**FeO_T**	**MnO**	**MgO**	**CaO**	**Na_2O**	**K_2O**	**P_2O_5**	**Cl**	**Total**
Unknown	PND_53	74.39	0.00	13.07	0.37	0.09	0.04	0.78	3.85	4.47	-	0.08	97.12
Sets 6, 7, 8 and 9.													
Pound Cove Bog													

Tephra ID/Standard sets/Site	**Sample**	**SiO_2**	**TiO2**	**Al_2O_3**	**FeO_T**	**MnO**	**MgO**	**CaO**	**Na_2O**	**K_2O**	**P_2O_5**	**Cl**	**Total**
Unknown	PND_186	69.87	0.49	15.00	2.37	0.14	0.50	1.71	6.05	3.02	-	0.26	99.34
Sets 6, 7, 8 and 9.	PND_186	70.87	0.21	14.55	1.16	0.02	0.40	2.04	4.20	1.94	-	0.11	95.48
Pound Cove Bog													

Tephra ID/Standard sets/Site	**Sample**	**SiO_2**	**TiO2**	**Al_2O_3**	**FeO_T**	**MnO**	**MgO**	**CaO**	**Na_2O**	**K_2O**	**P_2O_5**	**Cl**	**Total**
WRAe	SWP_99	72.02	0.22	14.07	1.50	0.07	0.37	1.85	4.22	3.18	-	0.35	97.78
Sets 6, 7, 8 and 9.	SWP_99	73.01	0.21	14.20	1.43	0.02	0.39	1.84	4.56	3.20	-	0.37	99.15
Southwest Pond Bog	SWP_99	72.30	0.18	14.12	1.60	0.05	0.41	1.88	4.40	3.17	-	0.37	98.39

	SWP_99	70.52	0.25	13.77	1.42	0.09	0.44	1.82	4.24	3.21	-	0.33	96.03
	SWP_99	72.75	0.22	14.36	1.44	0.05	0.43	1.91	4.53	3.15	-	0.34	99.11
	SWP_99	72.01	0.19	14.18	1.56	0.04	0.43	1.80	4.57	3.17	-	0.33	98.20
	SWP_99	71.36	0.24	14.19	1.57	0.08	0.41	1.85	4.57	3.12	-	0.38	97.67
	SWP_99	70.43	0.31	14.33	1.33	0.06	0.44	1.80	4.40	3.16	-	0.38	96.56
	SWP_99	71.70	0.29	14.03	1.49	0.02	0.39	1.81	5.19	3.23	-	0.34	98.41
	Mean:	71.79	0.24	14.14	1.48	0.05	0.41	1.84	4.52	3.18	-	0.35	97.92
	StDev:	0.90	0.04	0.18	0.09	0.03	0.02	0.04	0.28	0.03	-	0.02	1.06
	SWP_99	*73.04*	*0.09*	*13.37*	*1.00*	*0.06*	*0.26*	*1.48*	*4.55*	*3.28*	-	*0.35*	*97.41*
	SWP_99	*66.14*	*0.17*	*12.73*	*1.39*	*0.01*	*0.42*	*1.74*	*4.24*	*2.95*	-	*0.38*	*90.09*

Tephra ID/Standard sets/Site	**Sample**	**SiO_2**	**TiO2**	**Al_2O_3**	**FeO_T**	**MnO**	**MgO**	**CaO**	**Na_2O**	**K_2O**	**P_2O_5**	**Cl**	**Total**
Mazama Ash	SWP_502	72.30	0.43	14.31	1.86	0.05	0.47	1.49	4.84	2.85	-	0.13	98.70
Sets 6, 7, 8 and 9.	SWP_502	71.52	0.45	14.16	1.83	0.04	0.42	1.52	4.86	2.85	-	0.21	97.81
Southwest Pond Bog	SWP_502	69.87	0.40	13.94	1.81	0.04	0.45	1.43	4.84	2.72	-	0.18	95.63
	SWP_502	70.25	0.44	14.16	1.83	0.00	0.43	1.51	5.07	2.75	-	0.18	96.57
	SWP_502	70.41	0.39	14.35	1.81	0.04	0.40	1.51	4.97	2.74	-	0.22	96.81
	SWP_502	71.24	0.37	14.49	1.89	0.03	0.46	1.49	5.13	2.74	-	0.19	98.01
	SWP_502	70.67	0.42	14.41	1.74	0.01	0.44	1.51	5.09	2.80	-	0.18	97.24
	SWP_502	70.02	0.39	14.04	1.85	0.04	0.47	1.54	5.14	2.79	-	0.18	96.42
	SWP_502	70.68	0.42	14.36	1.89	0.02	0.46	1.52	5.29	2.73	-	0.19	97.52
	SWP_502	72.36	0.44	14.75	1.82	0.08	0.48	1.51	4.79	3.50	-	0.23	99.92
	SWP_502	72.01	0.47	14.98	1.91	0.02	0.48	1.61	5.17	2.65	-	0.19	99.45
	SWP_502	70.00	0.43	14.26	1.72	0.03	0.50	1.54	5.44	2.67	-	0.18	96.71
	Mean:	70.89	0.25	13.58	1.62	0.04	0.22	0.90	4.52	4.07	-	0.12	96.19
	StDev:	1.10	0.03	0.08	0.01	0.04	0.02	0.02	0.40	0.19	-	0.01	0.99
KS1 (reworked)	*SWP_502*	*70.84*	*0.46*	*14.63*	*3.55*	*0.19*	*0.60*	*2.74*	*4.98*	*1.20*	-	*0.17*	*99.33*
	SWP_502	*70.35*	*0.39*	*14.57*	*3.52*	*0.14*	*0.66*	*2.63*	*5.29*	*1.29*	-	*0.17*	*98.97*

	SWP_502	*69.77*	*0.49*	*14.67*	*3.66*	*0.15*	*0.68*	*2.80*	*4.89*	*1.30*	-	*0.19*	*98.55*
	Mean:	*70.32*	*0.45*	*14.62*	*3.58*	*0.16*	*0.65*	*2.72*	*5.05*	*1.26*	-	*0.18*	*98.95*
	StDev:	*0.54*	*0.05*	*0.05*	*0.08*	*0.03*	*0.05*	*0.09*	*0.21*	*0.05*	-	*0.01*	*0.39*
East Lake tephra	*SWP_502*	*72.16*	*0.24*	*13.67*	*1.61*	*0.03*	*0.22*	*0.91*	*4.06*	*4.29*	-	*0.13*	*97.29*
(reworked)	*SWP_502*	*70.19*	*0.22*	*13.52*	*1.63*	*0.01*	*0.20*	*0.88*	*4.70*	*3.95*	-	*0.10*	*95.37*
	SWP_502	*70.33*	*0.28*	*13.56*	*1.63*	*0.08*	*0.23*	*0.92*	*4.80*	*3.98*	-	*0.11*	*95.91*
	Mean:	*70.89*	*0.25*	*13.58*	*1.62*	*0.04*	*0.22*	*0.90*	*4.52*	*4.07*	-	*0.12*	*96.19*
	StDev:	*1.10*	*0.03*	*0.08*	*0.01*	*0.04*	*0.02*	*0.02*	*0.40*	*0.19*	-	*0.01*	*0.99*
	SWP_502	*68.27*	*0.21*	*13.25*	*1.60*	*0.04*	*0.21*	*0.89*	*4.27*	*4.03*	-	*0.10*	*92.82*
	SWP_502	*70.93*	*0.27*	*13.62*	*1.55*	*0.05*	*0.28*	*1.11*	*5.02*	*2.83*	-	*0.16*	*95.77*
	SWP_502	*71.15*	*0.37*	*14.09*	*1.86*	*0.06*	*0.45*	*1.51*	*4.35*	*4.45*	-	*0.20*	*98.45*
	SWP_502	*66.60*	*0.38*	*13.86*	*1.89*	*0.10*	*0.43*	*1.56*	*4.78*	*2.68*	-	*0.21*	*92.46*
	SWP_502	*68.13*	*0.60*	*15.14*	*4.62*	*0.15*	*1.06*	*3.55*	*4.86*	*1.22*	-	*0.17*	*99.46*
	SWP_502	*66.55*	*1.05*	*13.45*	*3.72*	*0.03*	*0.94*	*4.17*	*4.21*	*3.04*	-	*0.14*	*97.28*
	SWP_502	*75.91*	*0.16*	*11.83*	*1.15*	*0.07*	*0.17*	*1.22*	*4.06*	*2.18*	-	*0.17*	*96.90*

B.3 Known comparative data run alongside samples from Paper II

Table B.3: Individual, glass, major-minor oxide concentrations from Mazama ash reference material (wt%) run alongside unknown samples in Paper II. Data from standards sets 6 and 7 are presented in Table B.4.

Tephra ID / Standard sets	Sample	SiO_2	TiO2	Al_2O_3	FeO_T	MnO	MgO	CaO	Na_2O	K_2O	Cl	Total
Mazama ash	UA 1573	72.19	0.42	14.10	1.91	0.07	0.48	1.57	5.05	2.69	0.18	98.62
Sets 6 and 7.	UA 1573	72.66	0.42	14.57	1.89	0.06	0.47	1.55	4.93	2.81	0.17	99.47
	UA 1573	71.07	0.30	14.29	1.91	0.08	0.41	1.50	4.95	2.82	0.20	97.49
	UA 1573	71.67	0.40	14.42	1.92	0.05	0.44	1.54	5.03	2.73	0.16	98.32
	UA 1573	71.14	0.38	14.33	1.88	0.07	0.43	1.55	4.99	2.76	0.20	97.69
	UA 1573	71.43	0.37	14.44	1.88	0.08	0.45	1.53	5.03	2.78	0.19	98.14
	UA 1573	71.93	0.43	14.53	1.93	0.06	0.47	1.57	4.95	2.87	0.16	98.86
	UA 1573	70.38	0.47	14.30	1.83	0.05	0.45	1.55	4.77	2.84	0.20	96.80
	UA 1573	71.92	0.40	14.44	2.01	0.08	0.42	1.54	5.26	2.72	0.18	98.93
	UA 1573	72.18	0.41	14.47	1.95	0.08	0.44	1.53	5.25	2.88	0.18	99.32
	UA 1573	70.96	0.41	14.28	1.89	0.03	0.49	1.55	5.14	2.79	0.20	97.68
	UA 1573	70.97	0.42	14.33	1.83	0.09	0.46	1.48	5.32	2.70	0.19	97.74
	UA 1573	71.59	0.43	14.53	1.95	0.03	0.48	1.54	5.07	2.83	0.19	98.60
	UA 1573	69.28	0.50	14.25	1.79	0.00	0.41	1.43	4.98	2.65	0.17	95.42
	UA 1573	71.32	0.50	14.55	1.93	0.07	0.46	1.52	5.09	2.70	0.19	98.28
	UA 1573	71.33	0.42	14.50	1.97	0.02	0.46	1.52	5.17	2.78	0.16	98.30
	UA 1573	71.19	0.45	14.53	2.01	0.02	0.46	1.60	5.16	2.68	0.17	98.23
	UA 1573	71.29	0.41	14.25	1.84	0.06	0.42	1.54	5.59	2.84	0.18	98.39
	UA 1573	71.66	0.39	14.40	2.00	0.07	0.47	1.53	5.43	2.81	0.19	98.90
	UA 1573	70.85	0.43	14.46	1.91	0.06	0.48	1.60	5.17	2.74	0.19	97.85
	UA 1573	70.03	0.39	14.08	1.92	0.08	0.45	1.48	5.35	2.82	0.17	96.74

UA 1573	70.44	0.43	14.52	1.87	0.06	0.47	1.57	5.05	2.82	0.12	97.33
UA 1573	71.33	0.42	14.62	1.96	0.00	0.46	1.63	5.14	2.88	0.21	98.60
UA 1573	70.76	0.44	14.51	1.94	0.02	0.42	1.55	5.36	2.78	0.21	97.93
UA 1573	65.34	0.77	15.60	4.36	0.09	1.54	3.28	5.45	2.30	0.17	98.87
Mean:	71.00	0.43	14.45	2.01	0.05	0.50	1.61	5.15	2.76	0.18	98.10
StDev:	1.38	0.08	0.28	0.49	0.03	0.22	0.35	0.19	0.11	0.02	0.89

B.4 EPMA secondary standards included in paper II

Table B.4. Individual, glass, major-minor oxide concentrations from secondary standards (wt%) analysed in Paper II. Standard sets are denoted by number. Instrument refers to either a Cameca SX 100 electron probe micro-analyser, housed at the University of Edinburgh, or a JEOL 8900 held at the University of Alberta.

Standard set/Instrument	Sample	SiO_2	TiO2	Al_2O_3	FeO_T	MnO	MgO	CaO	Na_2O	K_2O	P_2O_5	Cl	Total
1	BCR2g	54.22	2.29	13.44	12.10	0.20	3.64	7.16	3.17	1.79	0.27	-	98.27
Edinburgh/Cameca	BCR2g	54.58	2.26	13.62	12.64	0.20	3.65	7.17	3.37	1.92	0.27	-	99.68
	Mean:	54.40	2.27	13.53	12.37	0.20	3.65	7.17	3.27	1.85	0.27	-	98.98
	StDev:	0.26	0.02	0.13	0.38	0.00	0.01	0.01	0.14	0.09	0.00	-	1.00
	Lipari	74.77	0.08	12.88	1.64	0.08	0.00	0.69	3.97	5.10	0.01	-	99.22
	Lipari	74.59	0.07	12.66	1.58	0.06	0.04	0.71	4.07	5.18	0.01	-	98.98
	Lipari	73.67	0.08	13.75	1.45	0.08	0.02	0.81	4.04	5.11	0.01	-	99.03
	Lipari	73.85	0.07	13.31	1.66	0.07	0.03	0.75	4.14	5.21	0.01	-	99.11
	Mean:	74.22	0.08	13.15	1.59	0.07	0.02	0.74	4.06	5.15	0.01	-	99.08
	StDev:	0.54	0.00	0.48	0.10	0.01	0.02	0.05	0.07	0.05	0.00	-	0.11
	BCR2g	54.18	2.29	12.94	12.34	0.20	3.65	7.28	3.27	1.83	0.35	0.01	98.34
	BCR2g	54.60	2.28	13.43	11.84	0.20	3.59	7.05	3.13	1.89	0.35	0.01	98.38
	BCR2g	53.93	2.27	13.67	12.13	0.19	3.63	7.28	2.98	1.83	0.35	0.02	98.27
	Mean:	54.24	2.28	13.35	12.10	0.20	3.62	7.21	3.13	1.85	0.35	0.01	98.33
	StDev:	0.34	0.01	0.37	0.25	0.01	0.03	0.13	0.15	0.04	0.00	0.00	0.05
	Lipari	73.61	0.07	13.03	1.44	0.07	0.04	0.75	4.11	5.12	0.01	0.37	98.61
	Lipari	73.90	0.07	12.60	1.77	0.08	0.01	0.79	4.02	5.12	0.02	0.37	98.74
	Lipari	73.59	0.08	13.10	1.53	0.06	0.04	0.75	4.19	5.30	0.01	0.37	99.02
	Lipari	74.04	0.08	13.06	1.43	0.07	0.06	0.71	4.05	5.28	0.01	0.35	99.15
	Lipari	74.21	0.08	12.85	1.50	0.07	0.01	0.74	4.06	5.15	0.02	0.36	99.05
	Mean:	73.87	0.08	12.93	1.53	0.07	0.03	0.75	4.08	5.19	0.02	0.36	98.92

	StDev:	0.27	0.00	0.21	0.14	0.01	0.02	0.03	0.07	0.09	0.00	0.01	0.23

Standard set/Instrument	Sample	SiO_2	TiO2	Al_2O_3	FeO_T	MnO	MgO	CaO	Na_2O	K_2O	P_2O_5	Cl	Total
2	Lipari	74.09	0.08	12.71	1.62	0.06	0.04	0.74	4.12	5.19	0.00	0.36	99.01
Edinburgh/Cameca	Lipari	74.88	0.08	12.72	1.60	0.08	0.05	0.76	4.08	5.14	0.01	0.36	99.77
	Lipari	75.58	0.08	12.91	1.67	0.07	0.04	0.79	4.08	5.48	0.01	0.36	101.07
	Lipari	73.12	0.07	12.56	1.57	0.06	0.06	0.69	4.19	5.18	0.02	0.36	97.89
	Mean:	74.42	0.08	12.73	1.62	0.07	0.05	0.74	4.12	5.25	0.01	0.36	99.44
	StDev:	1.06	0.00	0.15	0.04	0.01	0.01	0.04	0.05	0.15	0.01	0.00	1.34

Standard set/Instrument	Sample	SiO_2	TiO2	Al_2O_3	FeO_T	MnO	MgO	CaO	Na_2O	K_2O	P_2O_5	Cl	Total
3	BCR2g	54.59	2.29	13.56	12.30	0.19	3.68	7.33	3.24	1.92	0.35	0.01	99.46
Edinburgh/Cameca	BCR2g	53.31	2.27	13.72	12.48	0.18	3.69	7.30	3.12	1.85	0.36	0.01	98.28
	BCR2g	55.06	2.30	13.53	11.74	0.20	3.57	7.26	3.23	1.77	0.35	0.01	99.01
	BCR2g	54.21	2.26	13.53	12.51	0.19	3.58	7.14	3.09	1.75	0.35	0.01	98.62
	BCR2g	54.21	2.28	13.50	12.41	0.19	3.56	7.16	3.02	1.82	0.38	0.00	98.54
	BCR2g	53.44	2.30	13.46	12.06	0.19	3.59	7.25	3.32	1.87	0.36	0.01	97.84
	Mean:	54.13	2.28	13.55	12.25	0.19	3.61	7.24	3.17	1.83	0.36	0.01	98.62
	StDev:	0.67	0.02	0.09	0.30	0.01	0.06	0.08	0.11	0.07	0.01	0.00	0.56
	Lipari	73.91	0.08	12.73	1.58	0.06	0.02	0.79	4.20	5.36	0.01	0.37	99.13
	Lipari	73.81	0.07	12.70	1.44	0.06	0.04	0.65	3.96	5.29	0.01	0.36	98.39
	Lipari	73.48	0.08	12.83	1.49	0.06	0.05	0.80	4.08	5.27	0.02	0.37	98.53
	Lipari	73.74	0.08	12.74	1.61	0.06	0.04	0.73	3.98	5.33	0.02	0.38	98.71
	Lipari	74.50	0.08	12.67	1.57	0.07	0.06	0.85	4.16	5.25	0.01	0.38	99.61
	Lipari	73.91	0.08	12.83	1.55	0.08	0.06	0.71	3.93	5.19	0.01	0.37	98.72
	Lipari	73.24	0.08	12.45	1.70	0.07	0.03	0.70	4.29	5.18	0.01	0.37	98.13
	Mean:	73.80	0.08	12.71	1.57	0.06	0.04	0.75	4.09	5.27	0.01	0.37	98.74

	StDev:	0.40	0.00	0.13	0.08	0.01	0.01	0.07	0.14	0.07	0.00	0.01	0.49

Standard set/Instrument	Sample	SiO_2	TiO2	Al_2O_3	FeO_T	MnO	MgO	CaO	Na_2O	K_2O	P_2O_5	Cl	Total
4	BCR2g	54.22	2.29	13.27	12.07	0.19	3.57	7.27	3.15	1.87	0.37	0.01	98.27
Edinburgh/Cameca	BCR2g	54.05	2.28	13.60	12.08	0.20	3.56	7.39	3.12	1.83	0.35	0.01	98.46
	BCR2g	54.70	2.29	13.40	12.54	0.20	3.64	7.46	3.29	1.72	0.38	0.01	99.64
	BCR2g	54.35	2.30	13.43	12.46	0.20	3.55	7.22	3.30	1.81	0.37	0.01	99.01
	BCR2g	54.93	2.28	13.78	12.25	0.20	3.61	7.29	3.29	1.80	0.37	0.01	99.82
	BCR2g	54.56	2.30	13.90	12.10	0.20	3.66	7.35	3.18	1.80	0.37	0.01	99.43
	Mean:	54.47	2.29	13.56	12.25	0.20	3.60	7.33	3.22	1.80	0.37	0.01	99.10
	StDev:	0.32	0.01	0.24	0.21	0.00	0.05	0.09	0.08	0.05	0.01	0.00	0.63
	Lipari	73.76	0.08	12.89	1.56	0.06	0.04	0.71	4.10	5.22	0.01	0.37	98.80
	Lipari	74.25	0.08	13.11	1.56	0.07	0.05	0.69	3.98	5.08	0.01	0.37	99.26
	Lipari	76.42	0.08	13.24	1.41	0.07	0.08	0.81	4.27	5.33	0.01	0.37	102.08
	Lipari	74.56	0.06	13.15	1.45	0.06	0.05	0.74	4.00	5.14	0.02	0.37	99.59
	Lipari	74.39	0.08	12.89	1.55	0.06	0.06	0.70	4.23	5.29	0.02	0.36	99.63
	Lipari	74.19	0.07	12.86	1.59	0.07	0.02	0.75	3.92	5.32	0.01	0.37	99.18
	Mean:	74.59	0.08	13.02	1.52	0.07	0.05	0.73	4.08	5.23	0.01	0.37	99.76
	StDev:	0.93	0.01	0.16	0.08	0.01	0.02	0.04	0.14	0.10	0.00	0.00	1.18
	Old Crow	73.57	0.29	12.67	1.53	0.06	0.27	1.48	3.67	3.65	0.03	0.26	97.50
	Old Crow	72.63	0.28	12.10	1.60	0.06	0.25	1.50	3.79	3.65	0.04	0.29	96.20
	Old Crow	72.68	0.28	12.06	1.58	0.07	0.28	1.46	3.71	3.77	0.03	0.29	96.20
	Mean:	72.96	0.29	12.28	1.57	0.06	0.27	1.48	3.72	3.69	0.03	0.28	96.63
	StDev:	0.53	0.01	0.34	0.03	0.00	0.02	0.02	0.06	0.07	0.00	0.02	0.75

Standard set/Instrument	Sample	SiO_2	TiO2	Al_2O_3	FeO_T	MnO	MgO	CaO	Na_2O	K_2O	P_2O_5	Cl	Total
5	BCR2G	54.13	2.26	13.43	12.74	0.19	3.62	7.21	3.12	1.78	0.35	0.01	98.84

Edinburgh/Cameca	BCR2G	54.18	2.26	13.51	12.79	0.20	3.66	7.30	3.21	1.82	0.38	0.01	99.31
	BCR2G	54.38	2.27	13.35	12.29	0.20	3.63	7.33	3.14	1.74	0.37	0.01	98.72
	BCR2G	55.14	2.29	12.91	12.81	0.19	3.65	7.23	3.20	1.80	0.36	0.01	99.61
	BCR2G	54.87	2.30	13.09	12.42	0.20	3.61	7.30	3.32	1.80	0.38	0.01	99.27
	BCR2G	54.31	2.28	12.79	12.27	0.19	3.59	7.11	3.26	1.77	0.37	0.01	97.95
	Mean:	54.50	2.28	13.18	12.55	0.20	3.63	7.25	3.21	1.78	0.37	0.01	98.95
	StDev:	0.41	0.01	0.29	0.26	0.00	0.03	0.08	0.07	0.03	0.01	0.00	0.59
	Lipari	74.23	0.08	12.84	1.60	0.07	0.03	0.70	3.74	5.25	0.02	0.37	98.92
	Lipari	74.43	0.08	12.96	1.61	0.06	0.04	0.75	3.61	5.25	0.03	0.36	99.18
	Lipari	74.17	0.08	12.96	1.55	0.08	0.03	0.75	3.89	5.20	0.02	0.37	99.09
	Lipari	74.34	0.08	12.61	1.71	0.08	0.03	0.77	3.96	5.39	0.02	0.38	99.35
	Lipari	74.61	0.08	12.88	1.42	0.07	0.01	0.71	3.61	5.15	0.02	0.37	98.94
	Lipari	74.69	0.08	12.95	1.62	0.07	0.02	0.75	4.01	5.09	0.01	0.37	99.66
	Mean:	74.41	0.08	12.87	1.58	0.07	0.03	0.74	3.80	5.22	0.02	0.37	99.19
	StDev:	0.21	0.00	0.14	0.10	0.01	0.01	0.03	0.17	0.10	0.01	0.01	0.28
	OlD Crow	72.26	0.29	12.31	1.49	0.06	0.26	1.54	3.63	3.76	0.03	0.30	95.94
	OlD Crow	73.31	0.29	12.05	1.59	0.05	0.30	1.44	3.77	3.71	0.02	0.29	96.82
	OlD Crow	73.82	0.30	12.28	1.71	0.06	0.29	1.50	3.76	3.81	0.03	0.26	97.82
	OlD Crow	73.30	0.29	12.46	1.70	0.06	0.26	1.54	3.63	3.62	0.03	0.29	97.17
	OlD Crow	72.22	0.28	12.02	1.76	0.05	0.29	1.38	3.54	3.78	0.03	0.28	95.62
	OlD Crow	72.16	0.27	12.47	1.65	0.06	0.32	1.44	3.69	3.75	0.02	0.29	96.14
	Mean:	72.85	0.28	12.27	1.65	0.06	0.29	1.48	3.67	3.74	0.03	0.28	96.58
	StDev:	0.72	0.01	0.19	0.10	0.01	0.03	0.06	0.09	0.07	0.00	0.01	0.83

Standard set/Instrument	**Sample**	**SiO_2**	**TiO2**	**Al_2O_3**	**FeO_T**	**MnO**	**MgO**	**CaO**	**Na_2O**	**K_2O**	**P_2O_5**	**Cl**	**Total**
6	ID 3506_001	74.41	0.09	12.97	1.50	0.09	0.03	0.74	3.91	5.15	-	0.30	99.13
Alberta/JEOL	ID 3506_002	74.50	0.08	13.22	1.55	0.09	0.02	0.71	4.02	5.27	-	0.36	99.73
	ID 3506_003	73.78	0.06	13.04	1.65	0.09	0.05	0.69	4.07	5.11	-	0.36	98.82

ID 3506_004	74.12	0.08	12.90	1.55	0.10	0.04	0.74	4.29	5.25	-	0.33	99.32
ID 3506_005	74.49	0.10	13.30	1.60	0.07	0.02	0.74	3.85	5.14	-	0.38	99.60
Mean:	74.26	0.08	13.09	1.57	0.09	0.03	0.72	4.03	5.18	-	0.35	99.32
StDev:	0.31	0.02	0.17	0.06	0.01	0.01	0.02	0.17	0.07	-	0.03	0.36
ID 3506_006	74.37	0.09	13.19	1.57	0.07	0.06	0.72	3.86	5.14	-	0.36	99.35
ID 3506_008	74.05	0.16	13.14	1.56	0.10	0.07	0.75	3.79	5.23	-	0.33	99.09
ID 3506_009	74.41	0.04	13.07	1.53	0.05	0.02	0.71	4.05	5.23	-	0.32	99.35
ID 3506_010	74.31	0.10	13.36	1.65	0.09	0.03	0.73	4.10	5.17	-	0.30	99.78
Mean:	74.29	0.10	13.19	1.58	0.08	0.04	0.73	3.95	5.19	-	0.33	99.39
StDev:	0.16	0.05	0.13	0.05	0.02	0.02	0.02	0.15	0.04	-	0.02	0.29
ID 3506_011	73.73	0.08	13.14	1.52	0.08	0.02	0.73	3.79	5.24	-	0.32	98.57
ID 3506_012	73.95	0.10	13.16	1.66	0.06	0.02	0.73	3.98	5.21	-	0.33	99.13
ID 3506_013	75.11	0.08	13.12	1.59	0.08	0.06	0.75	4.13	5.21	-	0.33	100.38
ID 3506_014	74.39	0.08	13.12	1.49	0.09	0.04	0.71	4.61	5.23	-	0.32	100.01
ID 3506_015	74.15	0.09	13.20	1.49	0.08	0.05	0.68	4.09	5.20	-	0.33	99.28
Mean:	74.27	0.09	13.15	1.55	0.08	0.04	0.72	4.12	5.22	-	0.33	99.48
StDev:	0.53	0.01	0.03	0.07	0.01	0.02	0.03	0.31	0.02	-	0.00	0.72
ID 3506_001	74.73	0.10	13.06	1.49	0.09	0.01	0.74	4.14	5.22	-	0.34	99.85
ID 3506_017	73.77	0.05	13.11	1.50	0.09	0.05	0.72	4.19	5.09	-	0.29	98.79
ID 3506_018	74.32	0.08	13.05	1.49	0.10	0.02	0.70	4.35	5.19	-	0.31	99.55
ID 3506_019	74.31	0.08	13.12	1.58	0.07	0.03	0.73	4.13	5.24	-	0.32	99.54
ID 3506_020	74.58	0.11	13.16	1.54	0.07	0.04	0.71	4.26	5.14	-	0.34	99.87
ID 3506_021	74.79	0.08	13.15	1.54	0.06	0.04	0.74	4.21	5.28	-	0.31	100.13
Mean:	74.42	0.08	13.11	1.52	0.08	0.03	0.72	4.21	5.19	-	0.32	99.62
StDev:	0.37	0.02	0.04	0.03	0.02	0.01	0.02	0.08	0.07	-	0.02	0.46

Standard set/Instrument	Sample	SiO_2	TiO2	Al_2O_3	FeO_T	MnO	MgO	CaO	Na_2O	K_2O	P_2O_5	Cl	Total
7	Old Crow_001	73.98	0.34	12.65	1.55	0.02	0.30	1.42	4.16	3.79	-	0.31	98.45

Alberta/JEOL	Old Crow_002	72.46	0.32	12.50	1.56	0.04	0.30	1.35	3.77	3.47	-	0.24	95.96
	Old Crow_003	73.69	0.25	12.74	1.57	0.05	0.29	1.38	4.06	3.78	-	0.26	98.03
	Old Crow_004	71.63	0.25	12.59	1.64	0.08	0.30	1.41	3.74	3.75	-	0.24	95.55
	Old Crow_005	72.11	0.31	12.41	1.59	0.08	0.29	1.41	3.59	3.62	-	0.24	95.60
	Mean:	72.77	0.29	12.58	1.58	0.05	0.30	1.39	3.86	3.68	-	0.26	96.72
	StDev:	1.02	0.04	0.13	0.03	0.03	0.01	0.03	0.24	0.14	-	0.03	1.40
	Old Crow_006	71.59	0.24	12.70	1.55	0.09	0.28	1.34	3.83	3.71	-	0.23	95.50
	Old Crow_007	70.91	0.29	12.60	1.63	0.04	0.29	1.39	3.86	3.73	-	0.29	94.96
	Old Crow_008	72.51	0.29	12.49	1.60	0.09	0.29	1.37	3.66	3.70	-	0.30	96.23
	Old Crow_009	72.10	0.34	12.54	1.54	0.06	0.31	1.45	3.85	3.64	-	0.28	96.05
	Old Crow_010	71.81	0.29	12.68	1.67	0.08	0.30	1.39	3.79	3.71	-	0.26	95.93
	Mean:	71.78	0.29	12.60	1.60	0.07	0.30	1.39	3.80	3.70	-	0.27	95.73
	StDev:	0.60	0.04	0.09	0.06	0.02	0.01	0.04	0.08	0.04	-	0.03	0.51
	Old Crow_011	72.14	0.32	12.70	1.66	0.06	0.22	1.38	3.81	3.52	-	0.28	96.03
	Old Crow_014	70.89	0.32	12.51	1.57	0.00	0.28	1.33	3.67	3.40	-	0.24	94.15
	Old Crow_015	71.62	0.29	12.70	1.61	0.06	0.30	1.34	3.64	3.57	-	0.28	95.34
	Mean:	71.55	0.31	12.63	1.61	0.04	0.27	1.35	3.71	3.50	-	0.27	95.17
	StDev:	0.62	0.01	0.11	0.05	0.04	0.04	0.03	0.09	0.09	-	0.02	0.95
	Old Crow_017	71.72	0.30	12.56	1.69	0.04	0.30	1.40	3.92	3.72	-	0.29	95.88
	Old Crow_018	72.49	0.35	12.57	1.59	0.05	0.26	1.42	4.22	3.73	-	0.25	96.87
	Old Crow_019	73.57	0.24	12.83	1.58	0.05	0.39	1.35	4.21	3.46	-	0.28	97.88
	Old Crow_020	72.43	0.28	12.59	1.56	0.06	0.29	1.41	4.07	3.58	-	0.25	96.47
	Old Crow_021	72.67	0.29	12.80	1.67	0.07	0.28	1.36	4.11	3.55	-	0.27	97.00
	Mean:	72.58	0.29	12.67	1.62	0.05	0.31	1.39	4.11	3.61	-	0.27	96.82
	StDev:	0.66	0.04	0.13	0.06	0.01	0.05	0.03	0.12	0.12	-	0.02	0.74

Standard set/Instrument	**Sample**	**SiO_2**	**TiO2**	**Al_2O_3**	**FeO_T**	**MnO**	**MgO**	**CaO**	**Na_2O**	**K_2O**	**P_2O_5**	**Cl**	**Total**
8	ID 3506_001	73.89	0.05	13.11	1.52	0.09	0.03	0.69	4.08	5.26	-	0.31	98.95

Alberta/JEOL	ID 3506_002	73.78	0.05	13.12	1.60	0.04	0.03	0.73	4.09	5.20	-	0.34	98.91
	ID 3506_003	73.39	0.09	13.08	1.47	0.06	0.02	0.75	4.16	5.04	-	0.35	98.35
	ID 3506_004	73.52	0.07	12.95	1.55	0.06	0.04	0.75	4.08	5.36	-	0.32	98.61
	ID 3506_005	73.49	0.09	13.18	1.54	0.13	0.03	0.71	3.88	5.14	-	0.32	98.42
	Mean:	73.62	0.07	13.09	1.54	0.08	0.03	0.73	4.06	5.20	-	0.33	98.65
	StDev:	0.21	0.02	0.08	0.05	0.04	0.01	0.03	0.11	0.12	-	0.02	0.27
	ID3506_006	73.87	0.02	12.99	1.53	0.03	0.04	0.72	3.94	5.21	-	0.34	98.61
	ID3506_007	73.76	0.06	13.01	1.59	0.04	0.04	0.74	3.86	5.22	-	0.33	98.58
	ID3506_008	74.05	0.14	13.00	1.61	0.06	0.06	0.73	4.15	5.31	-	0.34	99.37
	ID3506_009	74.06	0.05	13.12	1.57	0.08	0.04	0.73	4.22	5.31	-	0.35	99.45
	ID3506_010	74.66	0.06	13.21	1.52	0.07	0.03	0.72	3.92	5.14	-	0.36	99.60
	Mean:	74.08	0.06	13.06	1.57	0.06	0.04	0.73	4.02	5.24	-	0.34	99.12
	StDev:	0.35	0.04	0.09	0.04	0.02	0.01	0.01	0.16	0.07	-	0.01	0.49
	ID306_011	73.22	0.08	13.08	1.58	0.06	0.05	0.71	4.00	5.23	-	0.33	98.25
	ID306_012	73.58	0.07	12.97	1.56	0.06	0.05	0.68	4.11	5.36	-	0.31	98.69
	ID306_013	73.22	0.06	13.07	1.63	0.06	0.04	0.69	4.11	5.27	-	0.34	98.40
	ID306_014	73.68	0.11	13.16	1.53	0.06	0.04	0.70	4.16	5.30	-	0.34	99.00
	ID306_015	73.91	0.05	13.11	1.65	0.05	0.03	0.75	4.46	5.15	-	0.33	99.42
	Mean:	73.52	0.07	13.08	1.59	0.06	0.04	0.70	4.17	5.26	-	0.33	98.75
	StDev:	0.30	0.02	0.07	0.05	0.00	0.01	0.03	0.18	0.08	-	0.01	0.47

B.5 Similarity coefficients used in paper II

Table B.5 Similarity coefficients (Borchardt *et al*., 1972) between cryptotephra deposits identified in Paper II and published values for ash bed they are linked with. Data sources: MSH-We: Pyne-O'Donnell *et al*. (2012); WRAe: Jensen *et al*. (2014); Newberry Pumice: Pyne-O'Donnell *et al*. (2012); Mazama ash: this study; KS_2 rhyolitic values: Plunkett *et al*. (2015).

	PTB_82	**PTB_155**	**PTB_354a**	**PTB_354b**	**NL_234**	**NL_638**	**LPB_82**	**SWP_99**	**SWP_502a**	**SWP_502b**
MSH-We	**0.95**	0.85	0.67	0.87	0.85	0.81	0.79	0.87	0.83	0.60
WRAe	0.86	**0.93**	0.70	0.90	**0.97**	0.84	0.79	**0.90**	0.82	0.62
Newberry Pumice	0.75	0.80	0.62	0.74	0.77	0.76	**0.97**	0.75	0.74	0.59
Mazama ash	0.75	0.85	0.79	0.75	0.82	**0.95**	0.77	0.76	**0.93**	0.75
KS2	0.56	0.62	0.77	0.54	0.60	0.68	0.56	0.55	0.67	**0.93**

B.6 The tephrostratigraphy of eastern North America – summary

Table B.6: The tephrostratigraphy of eastern North America – summary table used in Paper II.

Cryptotephra deposit	Site	Study	Depth (cm)	Median age (cal yr BP)	Maximum age (cal yr BP)	Minimum age (cal yr BP)	EPMA?	Correlation
SB-1 & SB-2	Sidney Bog (Booth)	Jensen *et al*. (in prep)	3	-9	236	-72	Y	Unknown
SB04_27	Sidney Bog	Jensen *et al*. (in prep)	27	182	342	30	Y	Mt St Helens T
FBB12_31	Framboise Bog	Mackay *et al*. (2016)	31	220	411	-5	Y	St Helens T?
SCH10_42	Sacco Heath Bog	Mackay *et al*. (2016)	42	304	454	110	Y	St Helens T?
VDB12_42	Villagedale Bog	Mackay *et al*. (2016)	42	339	443	189	Y	Villagedale tephra
FBB12_47	Framboise Bog	Mackay *et al*. (2016)	47	415	526	202	Y	St Helens T?
SCH10_57	Sacco Heath Bog	Mackay *et al*. (2016)	57	419	506	319	Y	Villagedale tephra
BB-1	Bloomingdale Bog	Jensen *et al*. (in prep)	41	434	597	243	Y	Unknown
SB04_57.5	Sidney Bog	Jensen *et al*. (in prep)	55-60	437	500	327	Y	Mt St Helens W
VDB12_53	Villagedale Bog	Mackay *et al*. (2016)	53	442	572	287	Y	Japanese?
JRB12_71	Jefery's Bog	Mackay *et al*. (2016)	71	488	610	328	Y	St Helens W
LPB16_42	Long Pond Bog	This study	42	488	1042	-33	N	Not analysed
PTB04_82	Petite Bog	This study	82	537	636	393	Y	Mt St Helen We
SB_21	Sidney Bog (Booth)	Jensen *et al*. (in prep)	21	548	675	377	Y	Mt St Helens We
SB-3	Sidney Bog (Booth)	Jensen *et al*. (in prep)	23	628	682	437	Y	Mono Crater
NDN_95	Nordan's Pond Bog	Pyne-O'Donnell *et al*. (2012)	99	639	1029	356	Y	St. Helens set W
SWP16_65	Southwest Pond	This study	60-65	703	1602	-59	N	Not analysed
BB_56	Bloomingdale Bog	Jensen *et al*. (in prep)	56	855	1229	523	Y	WRAe
LPB16_69	Long Pond Bog	This study	69	870	1572	199	N	Not analysed
VDB12_90	Villagedale Bog	Mackay *et al*. (2016)	90	945	1086	810	Y	Mexican
ISB_54	Irwin Smith Bog	Jensen *et al*. (in prep)	54	978	1170	824	Y	WRAe

VDB12_100	Villagedale Bog	Mackay *et al*. (2016)	100	1054	1214	908	Y	WRAe
LPB16_82	Long Pond Bog	This study	82	1055	1790	332	Y	Newberry Pumice
SB_44	Sidney Bog (Booth)	Jensen *et al*. (in prep)	44	1081	1160	1000	Y	Jala Pumice
JRB12_131	Jefery's Bog	Mackay *et al*. (2016)	131	1084	1246	971	Y	WRAe
BB_57	Bloomingdale Bog	Jensen *et al*. (in prep)	57	1097	1264	692	Y	Newberry Pumice
SCH10_18	Sacco Heath Bog	Mackay *et al*. (2016)	118	1102	1213	1003	Y	WRAe
ISB_55	Irwin Smith Bog	Jensen *et al*. (in prep)	55	1106	1352	921	Y	Newberry Pumice
SB04_128	Sidney Bog	Jensen *et al*. (in prep)	128	1114	1239	989	Y	WRAe
SB_49	Sidney Bog (Booth)	Jensen *et al*. (in prep)	49	1121	1175	1070	Y	WRAe
PND01_53	Pound Cove Bog	Monteath *et al*. (2019)	53	1171	7787	7441	Y	WRAe
SCH10_131	Sacco Heath Bog	Mackay *et al*. (2016)	131	1176	1320	1066	Y	WRAe (reworked)
FBB12_70	Framboise Bog	Mackay *et al*. (2016)	70	1178	1264	1075	Y	WRAe
SCH10_150	Sacco Heath Bog	Mackay *et al*. (2016)	132	1187	1333	1071	Y	WRAe (reworked)
PTB04_155	Petite Bog	Jensen *et al*. (2014)	155	1204	1275	1087	Y	WRAe
SB_59	Sidney Bog (Booth)	Jensen *et al*. (in prep)	59	1207	1344	1096	Y	Newberry pumice
SWP16_99	Southwest Pond	This study	99	1216	2227	239	Y	WRAe
SB04_145	Sidney Bog	Jensen *et al*. (in prep)	145	1301	1423	1190	Y	WRAe (reworked)
ISB-1	Irwin Smith Bog	Jensen *et al*. (in prep)	56	1316	1709	928	Y	Mono Crater
NDN_160	Nordan's Pond Bog	Pyne-O'Donnell *et al*. (2012)	163	1329	1707	885	Y	WRAe
SB-5	Sidney Bog (Booth)	Jensen *et al*. (in prep)	83	1441	1574	1366	Y	Mono Crater
SB04_163	Sidney Bog	Jensen *et al*. (in prep)	163	1503	1681	1374	Y	Mono Crater
BB-2	Bloomingdale Bog	Jensen *et al*. (in prep)	62	1517	1693	1296	Y	Mono Crater
NDN_185	Nordan's Pond Bog	Pyne-O'Donnell *et al*. (2012)	185-190	1583	1811	1214	Y	Newberry Pumice
FBB12_105	Framboise Bog	Mackay *et al*. (2016)	105	1614	2008	1444	Y	WRAe reworked
PTB04_202	Petite Bog	This study	202	1722	1946	1447	Y	WRAe (reworked)
BB-3	Bloomingdale Bog	Jensen *et al*. (in prep)	66	1863	2284	1497	Y	KS-1
VDB12_176	Villagedale Bog	Mackay *et al*. (2016)	176	1922	2090	1721	Y	KS1
SWP16_152	Southwest Pond	This study	152	1960	2805	1007	Y	WRAe reworked

LPB16_155	Long Pond Bog	This study	155	2088	2771	1393	N	Not analysed
ISB_69	Irwin Smith Bog	Jensen *et al*. (in prep)	68-69	2281	2731	1964	Y	Ruppert tephra + Mt St Helens P
NDN_230	Nordan's Pond Bog	Pyne-O'Donnell *et al*. (2012)	235	2366	2914	1820	Y	Ruppert Tephra
BB_73	Bloomingdale Bog	Jensen *et al*. (in prep)	73	2382	2687	2119	Y	Ruppert tephra
PND01_97	Pound Cove Bog	This study	97	2403	9796	9603	N	Not analysed
SB04_229	Sidney Bog	Jensen *et al*. (in prep)	229	2452	2595	2352	Y	Ruppert Tephra
SB_129a	Sidney Bog (Booth)	Jensen *et al*. (in prep)	129	2705	2989	2129	Y	Mt St Helens P
SB_129b	Sidney Bog (Booth)	Jensen *et al*. (in prep)	129	2705	2989	2129	Y	Ruppert tephra
SB04_257.5	Sidney Bog	Jensen *et al*. (in prep)	255-260	2775	2955	2578	Y	Shiveluch
SB-7	Sidney Bog (Booth)	Jensen *et al*. (in prep)	131	2833	3030	2301	Y	Medicine Lake
FBB12_162	Framboise Bog	Mackay *et al*. (2016)	162	3015	4077	2254	Y	Japanese?
ISB-2,3,4	Irwin Smith Bog	Jensen *et al*. (in prep)	82	3033	3973	2709	Y	Unknown
PTB04_354	Petite Bog	This study	354	3216	3430	2868	Y	2xUnknown
NDN_300	Nordan's Pond Bog	Pyne-O'Donnell *et al*. (2012)	300-305	3514	3957	3079	Y	Aniakchak CFE II
SWP16_315	Southwest Pond	This study	310-315	3611	3838	3238	N	oxcal
SB04_343	Sidney Bog	Jensen *et al*. (in prep)	343	3685	3824	3592	Y	Mt St Helens Yn
BVB04_160	Burnt Village Bog	Hughes *et al*. (in prep)	160	3686	3822	3551	Y	Mt St Helen Yn
PND01_186	Pound Cove Bog	This study	186	3697	3936	3472	Y	Unknown
SB_174	Sidney Bog (Booth)	Jensen *et al*. (in prep)	174	3722	3933	3528	Y	Mt St Helens Yn
PTB04_404	Petite Bog	This study	404	3758	3973	3403	Y	Unknown
BB-4	Bloomingdale Bog	Jensen *et al*. (in prep)	104	3818	4246	3376	Y	Shiveluch
SWP16_360	Southwest Pond	This study	355-360	3886	4167	3709	N	Not analysed
LPB16_304	Long Pond Bog	This study	303	3905	4406	3428	N	Not analysed
SB-8	Sidney Bog (Booth)	Jensen *et al*. (in prep)	187	3909	4064	3712	Y	Shiveluch
PTB04_428	Petite Bog	This study	428	3975	4323	3835	Y	Unknown
NDN_345	Nordan's Pond Bog	Pyne-O'Donnell *et al*. (2012)	340-345	4159	4550	3925	N	Not analysed
ISB_96	Irwin Smith Bog	Jensen *et al*. (in prep)	96	4259	4709	4004	Y	Unknown

BB-5	Bloomingdale Bog	Jensen *et al*. (in prep)	120	4351	4420	4241	Y	Unknown
SB-9	Sidney Bog (Booth)	Jensen *et al*. (in prep)	224	4446	4606	4303	Y	Unknown
NDN_365	Nordan's Pond Bog	Pyne-O'Donnell *et al*. (2012)	360-365	4464	4955	4049	Y	Unknown
SWP16_465	Southwest Pond	This study	460-465	4700	4850	4572	N	Not analysed
PTB04_508	Petite Bog	This study	508	4928	5232	4587	Y	Unknown
NDN_410	Nordan's Pond Bog	Pyne-O'Donnell *et al*. (2012)	405-140	4978	5382	4493	Y	Unknown
BB-6	Bloomingdale Bog	Jensen *et al*. (in prep)	138	5093	5283	4921	Y	Unknown
SWP16_502	Southwest Pond	This study	502	5107	5270	4968	Y	Mazama ash+KS1
NDN_430	Nordan's Pond Bog	Pyne-O'Donnell *et al*. (2012)	425-430	5227	5451	4796	Y	Unknown
BVB04_301	Burnt Village Bog	Hughes *et al*. (in prep)	301	5263	5427	5078	N	Not analysed
SB-10	Sidney Bog (Booth)	Jensen *et al*. (in prep)	312	5500	5576	5359	Y	Unknown
NDN_455	Nordan's Pond Bog	Pyne-O'Donnell *et al*. (2012)	450-455	5543	6140	5311	Y	Unknown
BB-7	Bloomingdale Bog	Jensen *et al*. (in prep)	150	5846	5953	5753	Y	Unknown
SB04_442.5	Sidney Bog	Jensen *et al*. (in prep)	440-445	5858	6056	5593	Y	Illinsky
SB-11	Sidney Bog (Booth)	Jensen *et al*. (in prep)	338	5918	6041	5761	Y	Illinsky
BVB04_397.5	Burnt Village Bog	Hughes *et al*. (in prep)	395-400	5981	6171	5911	N	Not analysed
SB_12	Sidney Bog (Booth)	Jensen *et al*. (in prep)	364	6323	6610	6080	Y	Unknown
PND01_466	Pound Cove Bog	This study	466	6456	6616	6262	N	Not analysed
NDN_490	Nordan's Pond Bog	Pyne-O'Donnell *et al*. (2012)	485-490	6527	6859	5869	Y	East Lake Tephra
SB-13	Sidney Bog (Booth)	Jensen *et al*. (in prep)	400	7011	7099	6883	Y	Unknown
BB_179	Bloomingdale Bog	Jensen *et al*. (in prep)	179	7079	7562	6491	Y	Mazama ash
PTB04_622.5	Petite Bog	This study	620-625	7229	8173	6442	N	Not analysed
NDN_545	Nordan's Pond Bog	Pyne-O'Donnell *et al*. (2012)	550	7255	7695	6847	Y	Mazama ash
SB04_540	Sidney Bog	Jensen *et al*. (in prep)	540	7658	7787	7441	Y	Mazama ash
PND01_551	Pound Cove Bog	This study	551	7705	8008	7374	Y	Mazama ash
CP_1368.5	Crocker Pond	Pyne-O'Donnell *et al*. (2016)	1368.5	13131	13301	12967	Y	Glacier Peak B+ Mt St Helens J+ Glacier Peak G

CP_1372.5	Crocker Pond	Pyne-O'Donnell *et al*. (2016)	1372.5	13286	13528	13117	Y	Glacier Peak B+ Mt St Helens J+ Glacier Peak G
TI_587	Thin-Ice Pond	Pyne-O'Donnell *et al*. (2016)	587	13481	13574	13287	Y	Glacier Peak B+ Mt St Helens J
VL_841	Veinot Lake	Pyne-O'Donnell *et al*. (2016)	841	14079	14294	13976	Y	Glacier Peak B+ Mt St Helens J+ Glacier Peak G
VL_846	Veinot Lake	Pyne-O'Donnell *et al*. (2016)	846	14352	14604	14259	Y	Mt St Helens J+ Glacier Peak G
NL17_234	Nuangola Lake	This study	234	Undated	Undated	Undated	Y	WRAe
NL17_638	Nuangola Lake	This study	638	Undated	Undated	Undated	Y	Mazama ash

Appendix C Paper III

C.1 EPMA glass shard analyses included in Paper III

Appendix C.1 includes major-minor oxide concentrations (wt%) of individual glass shards from the case study tephra deposits described in Paper II. Shards were analysed at the University of Alberta, using a JEOL 8900 superprobe using a 5 µm focused beam, with a 15 KeV accelerating voltage, and 6 nA current (Jensen *et al*., 2008).

Table C.1: Individual, glass, major-minor oxide concentrations from tephra deposits (wt%) analysed in Paper III.

Mt. Burney type

Sample	SiO_2	TiO2	Al_2O_3	FeO_T	MnO	MgO	CaO	Na_2O	K_2O	Cl	Total	Date	Instrument
HP_14-17b	76.20	0.23	12.87	1.20	0.00	0.32	1.39	4.53	1.71	0.12	98.54	12/04/2018	JEOL
HP_14-17b	75.78	0.14	12.97	0.98	0.03	0.24	1.04	4.40	1.79	0.19	97.51	05/04/2018	Cameca
HP_14-17b	75.45	0.15	12.80	1.03	0.07	0.21	1.24	3.71	1.80	0.22	96.61	05/04/2018	Cameca
HP_14-17b	75.31	0.21	12.61	1.13	0.03	0.29	1.33	3.88	1.84	0.20	96.78	12/04/2018	JEOL
HP_14-17b	77.70	0.17	13.11	0.86	0.05	0.25	1.12	4.37	2.04	0.20	99.82	05/04/2018	Cameca
HP_14-17b	74.31	0.20	12.52	1.02	0.03	0.25	1.24	3.94	1.99	0.21	95.66	12/04/2018	JEOL
HP_14-17b	77.72	0.14	12.96	1.09	0.00	0.29	1.15	4.41	2.10	0.21	100.01	12/04/2018	JEOL
HP_14-17b	73.48	0.15	12.46	1.00	0.03	0.26	1.03	4.03	2.04	0.22	94.64	12/04/2018	JEOL
HP_14-17b	74.27	0.15	12.74	0.88	0.02	0.23	1.01	4.11	2.06	0.25	95.66	05/04/2018	Cameca
HP_14-17b	75.62	0.20	13.02	0.98	0.06	0.24	1.29	4.13	2.26	0.19	97.95	05/04/2018	Cameca
Mean:	75.58	0.17	12.81	1.02	0.03	0.26	1.18	4.15	1.96	0.20	97.32		
StDev:	1.39	0.03	0.22	0.10	0.02	0.03	0.13	0.27	0.17	0.03	1.79		

Detrital glass

Sample	SiO_2	TiO2	Al_2O_3	FeO_T	MnO	MgO	CaO	Na_2O	K_2O	Cl	Total	Date	Instrument
HP_14-17	74.13	0.33	14.62	1.44	0.06	0.32	1.75	4.62	1.45	0.25	98.92	05/04/2018	Cameca
HP_14-17	74.69	0.17	13.52	0.76	0.08	0.09	0.45	3.54	5.23	0.16	98.66	05/04/2018	Cameca
HP_14-17	70.88	0.46	13.85	1.93	0.06	0.39	1.46	4.08	3.99	0.18	97.22	05/04/2018	Cameca
HP_14-17	76.26	0.10	12.33	0.91	0.03	0.01	0.69	2.26	4.20	0.13	96.89	05/04/2018	Cameca
HP_14-17	73.41	0.23	12.81	1.88	0.03	0.08	0.74	3.21	4.24	0.19	96.77	05/04/2018	Cameca
HP_14-17	74.78	0.07	12.35	1.09	0.06	0.02	0.72	3.49	4.06	0.10	96.71	12/04/2018	JEOL
HP_14-17	72.04	0.18	12.13	1.16	0.03	0.19	0.94	3.11	6.27	0.23	96.25	05/04/2018	Cameca
HP_14-17	74.43	0.10	12.30	0.71	0.09	0.07	0.50	2.98	4.08	0.21	95.42	05/04/2018	Cameca
HP_14-17	74.60	0.15	12.63	1.00	0.03	0.13	1.05	2.14	3.48	0.19	95.36	05/04/2018	Cameca
HP_14-17	74.58	0.24	13.07	0.93	0.03	0.19	0.86	1.46	3.77	0.10	95.21	05/04/2018	Cameca
HP_14-17	74.02	0.10	12.13	1.07	0.04	0.04	0.71	2.39	4.17	0.13	94.77	12/04/2018	JEOL
HP_14-17	73.93	0.07	12.20	0.61	0.09	0.04	0.47	3.16	3.78	0.20	94.51	05/04/2018	Cameca
HP_14-17	74.74	0.12	11.42	1.11	0.04	0.09	0.91	2.27	3.53	0.19	94.38	12/04/2018	JEOL
HP_14-17	73.12	0.19	11.40	1.52	0.04	0.16	1.08	2.24	3.78	0.11	93.61	12/04/2018	JEOL
HP_14-17	72.97	0.09	12.19	0.69	0.02	0.02	0.72	2.35	3.63	0.09	92.75	05/04/2018	Cameca
HP_14-17	71.53	0.13	11.98	1.07	0.00	0.28	1.09	4.13	1.76	0.25	92.16	12/04/2018	JEOL
HP_14-17	72.33	0.11	11.64	1.26	0.07	0.02	0.70	2.18	3.69	0.13	92.09	05/04/2018	Cameca
HP_14-17	67.13	0.40	13.01	3.09	0.12	0.39	1.74	2.98	3.08	0.19	92.09	12/04/2018	JEOL
HP_14-17	71.94	0.15	11.47	1.19	0.02	0.05	0.65	2.36	4.12	0.13	92.06	05/04/2018	Cameca
HP_14-17	73.08	0.10	11.41	1.35	0.01	0.08	0.96	1.48	3.43	0.16	92.02	12/04/2018	JEOL
HP_14-17	71.67	0.22	12.09	1.18	0.05	0.19	1.13	1.80	3.50	0.13	91.94	05/04/2018	Cameca
HP_14-17	72.85	0.19	11.39	1.10	0.01	0.16	0.94	2.14	3.05	0.12	91.93	05/04/2018	Cameca
HP_14-17	72.51	0.16	11.43	1.55	0.08	0.06	0.90	1.49	3.53	0.12	91.80	05/04/2018	Cameca
HP_14-17	71.90	0.18	11.82	0.94	0.05	0.07	0.44	2.32	3.77	0.17	91.62	12/04/2018	JEOL
HP_14-17	72.19	0.06	11.41	1.21	0.04	0.00	0.45	2.07	3.97	0.14	91.51	12/04/2018	JEOL
HP_14-17	69.38	0.20	12.47	0.87	0.14	0.19	0.59	2.85	4.24	0.15	91.07	12/04/2018	JEOL

HP_14-17	69.26	0.21	11.93	1.50	0.03	0.22	1.05	2.07	4.04	0.16	90.45	12/04/2018	JEOL
HP_14-17	68.52	0.28	12.78	1.46	0.10	0.25	1.08	1.71	4.19	0.11	90.44	12/04/2018	JEOL
HP_14-17	69.84	0.50	11.85	2.35	0.07	0.36	1.57	1.24	2.26	0.24	90.23	05/04/2018	Cameca
HP_14-17	70.63	0.18	11.50	1.38	0.06	0.16	0.98	2.63	2.47	0.21	90.14	05/04/2018	Cameca
Mean:	72.44	0.19	12.24	1.28	0.05	0.14	0.91	2.56	3.69	0.16	93.63		
StDev:	2.13	0.11	0.79	0.52	0.03	0.12	0.36	0.84	0.92	0.05	2.59		

Detrital glass

Sample	SiO_2	TiO2	Al_2O_3	FeO_T	MnO	MgO	CaO	Na_2O	K_2O	Cl	Total	Date	Instrument
HP_32	76.92	0.12	13.20	0.85	0.00	0.22	1.22	3.68	2.40	0.07	98.67	05/04/2018	Cameca
HP_32	71.99	0.32	12.59	2.12	0.02	0.26	1.50	3.58	3.74	0.15	96.23	05/04/2018	Cameca
HP_32	74.07	0.08	13.08	1.23	0.07	0.17	0.95	3.66	2.82	0.10	96.21	05/04/2018	Cameca
HP_32	71.97	0.12	12.83	1.54	0.06	0.03	0.69	3.48	4.73	0.28	95.66	05/04/2018	Cameca
HP_32	74.52	0.11	12.36	0.88	0.02	0.09	0.74	2.33	3.78	0.19	94.98	05/04/2018	Cameca
HP_32	73.68	0.21	11.71	1.16	0.04	0.10	0.87	3.23	3.62	0.29	94.85	05/04/2018	Cameca
HP_32	75.68	0.09	12.52	1.04	0.02	0.26	1.24	4.46	2.11	0.22	97.59	13/04/2018	JEOL
HP_32	74.39	0.12	11.85	0.86	0.03	0.16	0.92	3.24	4.06	0.18	95.77	13/04/2018	JEOL
HP_32	73.00	0.11	12.21	0.99	0.08	0.22	1.06	4.64	1.83	0.18	94.29	13/04/2018	JEOL
HP_32	69.81	0.30	12.25	1.91	0.06	0.25	1.31	3.61	3.45	0.16	93.09	13/04/2018	JEOL
HP_32	72.07	0.07	11.95	0.84	0.00	0.12	0.69	2.68	4.42	0.11	92.93	13/04/2018	JEOL
HP_32	71.12	0.11	12.47	0.96	0.05	0.16	1.02	3.13	3.30	0.09	92.37	13/04/2018	JEOL
HP_32	72.44	0.10	11.27	1.19	0.02	0.04	0.67	2.76	3.38	0.18	92.00	13/04/2018	JEOL
HP_32	70.59	0.09	11.41	1.47	0.02	0.05	0.92	2.71	2.79	0.13	90.14	13/04/2018	JEOL
HP_32	72.68	0.13	12.22	0.99	0.03	0.06	0.81	2.46	4.24	0.16	93.76	05/04/2018	Cameca
HP_32	72.10	0.11	12.30	1.06	0.03	0.17	1.37	3.82	2.61	0.16	93.69	05/04/2018	Cameca
HP_32	74.03	0.10	11.91	1.26	0.04	0.05	0.68	1.74	3.77	0.13	93.68	05/04/2018	Cameca
HP_32	73.80	0.09	11.76	1.18	0.04	0.02	0.68	2.32	3.65	0.16	93.67	05/04/2018	Cameca
HP_32	72.65	0.06	12.24	1.36	0.06	0.00	0.81	2.27	3.68	0.15	93.25	05/04/2018	Cameca

HP_32	73.05	0.11	11.97	0.79	0.09	0.03	0.44	2.72	3.79	0.20	93.13	05/04/2018	Cameca
HP_32	73.78	0.11	11.82	1.01	0.05	0.03	0.42	1.76	3.76	0.20	92.89	05/04/2018	Cameca
HP_32	72.91	0.25	11.85	0.86	0.05	0.09	0.92	2.56	3.19	0.13	92.80	05/04/2018	Cameca
HP_32	72.72	0.17	11.42	1.14	0.06	0.09	0.82	2.01	3.99	0.19	92.59	05/04/2018	Cameca
HP_32	72.50	0.02	11.90	0.80	0.02	0.04	0.34	1.93	4.79	0.15	92.44	05/04/2018	Cameca
HP_32	72.89	0.06	11.63	1.03	0.03	0.06	0.67	1.87	3.92	0.18	92.29	05/04/2018	Cameca
HP_32	69.55	0.14	12.10	1.28	0.06	0.19	0.95	4.09	3.45	0.26	92.01	05/04/2018	Cameca
HP_32	71.25	0.18	11.87	1.69	0.08	0.09	1.18	1.89	3.54	0.19	91.91	05/04/2018	Cameca
HP_32	72.04	0.04	11.92	0.82	0.01	0.01	0.73	1.90	4.05	0.11	91.60	05/04/2018	Cameca
HP_32	70.97	0.04	12.21	0.63	0.09	0.07	0.49	2.25	4.58	0.09	91.40	05/04/2018	Cameca
HP_32	71.77	0.11	11.64	1.15	0.02	0.06	0.87	2.31	3.34	0.14	91.37	05/04/2018	Cameca
HP_32	72.61	0.13	11.09	1.15	0.05	0.07	0.89	2.22	2.81	0.18	91.15	05/04/2018	Cameca
HP_32	70.16	0.23	12.02	1.01	0.04	0.17	0.93	2.11	2.94	0.23	89.79	05/04/2018	Cameca
HP_32	67.62	0.19	12.03	1.81	0.07	0.08	0.66	3.01	3.70	0.26	89.37	05/04/2018	Cameca
Mean:	72.46	0.13	12.05	1.15	0.04	0.11	0.86	2.80	3.52	0.17	93.26		
StDev:	1.80	0.07	0.47	0.35	0.03	0.08	0.27	0.81	0.70	0.05	2.12		

Detrital glass

Sample	SiO_2	TiO2	Al_2O_3	FeO_T	MnO	MgO	CaO	Na_2O	K_2O	Cl	Total	Date	Instrument
HP_38	78.26	0.23	14.03	0.88	0.07	0.09	0.97	3.89	3.74	0.16	102.29	05/04/2018	Cameca
HP_38	75.72	0.25	12.88	1.41	0.03	0.25	1.69	3.70	2.52	0.18	98.60	13/04/2018	JEOL
HP_38	74.77	0.19	12.47	1.45	0.02	0.12	0.91	3.95	3.67	0.20	97.72	05/04/2018	Cameca
HP_38	75.58	0.17	12.87	0.99	0.01	0.23	1.14	4.88	1.65	0.19	97.66	05/04/2018	Cameca
HP_38	74.31	0.15	12.64	0.92	0.02	0.20	1.37	4.44	2.11	0.23	96.32	05/04/2018	Cameca
HP_38	72.56	0.55	11.93	2.17	0.06	0.43	1.74	3.18	3.58	0.08	96.27	05/04/2018	Cameca
HP_38	72.56	0.08	12.72	1.39	0.07	0.01	0.79	2.99	5.12	0.28	95.95	05/04/2018	Cameca
HP_38	72.14	0.08	12.51	1.40	0.06	0.02	0.67	3.50	5.11	0.28	95.70	14/04/2018	JEOL
HP_38	74.68	0.20	11.74	0.97	0.04	0.12	0.76	2.04	4.23	0.18	94.93	05/04/2018	Cameca

HP_38	74.73	0.08	11.84	1.07	0.05	0.08	0.65	2.17	3.92	0.18	94.71	05/04/2018	Cameca
HP_38	71.64	0.09	13.48	1.18	0.06	0.22	1.14	3.70	2.91	0.10	94.50	05/04/2018	Cameca
HP_38	72.61	0.04	12.67	0.76	0.09	0.07	0.90	3.13	3.85	0.10	94.20	05/04/2018	Cameca
HP_38	74.33	0.05	12.08	1.01	0.04	0.01	0.62	2.27	3.66	0.14	94.17	05/04/2018	Cameca
HP_38	73.41	0.12	11.98	1.31	0.06	0.05	0.72	1.99	4.10	0.14	93.85	05/04/2018	Cameca
HP_38	72.27	0.15	13.06	1.52	0.07	0.15	1.40	2.70	2.33	0.12	93.75	05/04/2018	Cameca
HP_38	71.28	0.18	12.44	1.40	0.01	0.08	1.14	2.85	3.91	0.16	93.42	05/04/2018	Cameca
HP_38	70.91	0.05	13.09	0.90	0.12	0.08	0.66	3.54	3.96	0.04	93.34	15/04/2018	JEOL
HP_38	73.33	0.12	11.80	0.52	0.07	0.02	0.41	2.33	4.44	0.19	93.19	05/04/2018	Cameca
HP_38	73.51	0.13	11.53	1.06	0.07	0.03	0.73	2.18	3.83	0.15	93.18	05/04/2018	Cameca
HP_38	72.83	0.04	11.44	1.23	0.06	0.05	0.70	2.87	3.77	0.13	93.09	16/04/2018	JEOL
HP_38	73.40	0.14	11.54	0.96	0.07	0.11	0.80	2.31	3.57	0.16	93.02	17/04/2018	JEOL
HP_38	72.70	0.12	11.70	1.34	0.03	0.04	0.79	2.12	4.07	0.14	93.01	05/04/2018	Cameca
HP_38	70.74	0.07	13.19	1.13	0.04	0.15	1.05	3.59	2.81	0.10	92.85	05/04/2018	Cameca
HP_38	69.20	0.31	12.42	2.01	0.03	0.20	1.08	3.64	3.73	0.17	92.77	05/04/2018	Cameca
HP_38	73.64	0.18	11.22	1.21	0.06	0.08	0.80	1.53	3.68	0.20	92.56	05/04/2018	Cameca
HP_38	72.51	0.07	11.99	1.36	0.08	0.04	0.90	2.04	3.38	0.10	92.44	05/04/2018	Cameca
HP_38	72.89	0.07	11.45	1.02	0.06	0.04	0.66	2.18	3.70	0.13	92.16	18/04/2018	JEOL
HP_38	72.48	0.06	11.67	0.79	0.07	0.05	0.34	2.92	3.61	0.18	92.13	19/04/2018	JEOL
HP_38	71.65	0.32	10.63	2.18	0.07	0.31	1.63	2.27	2.47	0.41	91.84	20/04/2018	JEOL
HP_38	72.10	0.08	11.44	1.15	0.07	0.05	0.70	2.57	3.36	0.12	91.61	21/04/2018	JEOL
HP_38	70.29	0.15	12.21	0.79	0.08	0.16	0.89	3.19	3.65	0.21	91.57	05/04/2018	Cameca
HP_38	72.11	0.05	11.91	0.76	0.01	0.00	0.46	2.75	3.38	0.03	91.46	05/04/2018	Cameca
HP_38	70.91	0.09	11.91	0.96	0.07	0.07	0.76	1.81	4.60	0.11	91.28	22/04/2018	JEOL
HP_38	71.33	0.10	11.53	0.99	0.05	0.04	0.69	2.33	3.46	0.16	90.64	05/04/2018	Cameca
HP_38	71.09	0.07	11.31	1.11	0.06	0.04	0.67	2.38	3.33	0.13	90.16	05/04/2018	Cameca
Mean:	72.81	0.14	12.15	1.18	0.05	0.11	0.90	2.85	3.58	0.16	93.90		
StDev:	1.77	0.10	0.73	0.37	0.02	0.10	0.34	0.79	0.75	0.07	2.49		

Detrital glass

Sample	SiO_2	TiO2	Al_2O_3	FeO_T	MnO	MgO	CaO	Na_2O	K_2O	Cl	Total	Date	Instrument
HP_53-56	74.78	0.18	12.97	2.34	0.09	0.17	1.31	2.20	4.55	0.16	98.70	05/04/2018	Cameca
HP_53-56	73.74	0.40	13.42	1.96	0.07	0.32	1.28	4.06	2.98	0.14	98.34	05/04/2018	Cameca
HP_53-56	75.74	0.12	12.54	1.02	0.03	0.22	1.07	5.04	1.92	0.20	97.86	13/04/2018	JEOL
HP_53-56	75.14	0.15	12.88	1.04	0.08	0.24	1.09	4.74	1.86	0.23	97.38	05/04/2018	Cameca
HP_53-56	75.18	0.12	12.43	1.11	0.02	0.17	1.43	4.05	2.49	0.16	97.11	05/04/2018	Cameca
HP_53-56	72.67	0.29	13.19	1.76	0.06	0.18	1.28	3.61	3.75	0.20	96.95	05/04/2018	Cameca
HP_53-56	72.30	0.24	12.22	1.68	0.04	0.18	1.04	3.99	3.83	0.17	95.65	13/04/2018	JEOL
HP_53-56	74.78	0.15	11.50	1.26	0.09	0.05	0.55	3.25	3.66	0.15	95.40	13/04/2018	JEOL
HP_53-56	72.40	0.09	13.22	1.18	0.06	0.19	1.15	4.01	2.96	0.09	95.33	13/04/2018	JEOL
HP_53-56	72.50	0.10	13.44	1.17	0.06	0.18	1.13	3.84	2.81	0.11	95.31	05/04/2018	Cameca
HP_53-56	72.49	0.14	13.26	1.42	0.05	0.17	1.13	3.54	2.98	0.08	95.25	05/04/2018	Cameca
HP_53-56	72.38	0.00	12.95	0.95	0.05	0.02	0.62	3.59	4.09	0.11	94.74	05/04/2018	Cameca
HP_53-56	73.90	0.12	12.20	1.74	0.10	0.02	1.00	1.99	3.53	0.13	94.69	05/04/2018	Cameca
HP_53-56	75.02	0.07	11.68	1.08	0.04	0.05	0.68	2.54	3.14	0.14	94.41	05/04/2018	Cameca
HP_53-56	73.13	0.08	12.01	0.88	0.08	0.01	0.69	2.69	4.38	0.08	94.02	13/04/2018	JEOL
HP_53-56	72.84	0.13	11.80	0.92	0.03	0.16	1.14	3.27	3.24	0.15	93.66	05/04/2018	Cameca
HP_53-56	71.08	0.10	13.24	1.20	0.10	0.22	1.22	3.47	2.79	0.09	93.50	05/04/2018	Cameca
HP_53-56	73.25	0.14	11.87	1.23	0.02	0.09	0.98	1.73	3.87	0.16	93.29	05/04/2018	Cameca
HP_53-56	70.48	0.23	12.45	2.02	0.09	0.19	1.44	3.34	2.46	0.10	92.78	05/04/2018	Cameca
HP_53-56	72.25	0.14	12.28	1.20	0.06	0.11	1.03	1.83	3.74	0.12	92.73	05/04/2018	Cameca
HP_53-56	73.03	0.02	11.77	0.90	0.03	0.05	0.66	2.26	3.80	0.18	92.65	13/04/2018	JEOL
HP_53-56	72.23	0.07	11.59	0.92	0.07	0.03	0.48	2.80	4.33	0.16	92.64	13/04/2018	JEOL
HP_53-56	72.81	0.06	11.67	1.13	0.05	0.00	0.74	2.58	3.50	0.13	92.64	13/04/2018	JEOL
HP_53-56	72.40	0.04	12.04	0.80	0.08	0.01	0.49	2.30	3.87	0.21	92.21	05/04/2018	Cameca
HP_53-56	72.67	0.04	11.85	0.91	0.04	0.00	0.50	2.27	3.67	0.20	92.11	05/04/2018	Cameca

HP_53-56	67.92	0.34	13.23	2.12	0.07	0.42	1.81	2.54	3.44	0.20	92.05	05/04/2018	Cameca
HP_53-56	71.24	0.10	12.65	0.64	0.07	0.06	0.49	1.80	4.65	0.17	91.83	05/04/2018	Cameca
HP_53-56	71.64	0.08	11.79	1.11	0.03	0.01	0.87	2.25	3.76	0.13	91.65	05/04/2018	Cameca
HP_53-56	72.47	0.14	11.48	1.34	0.03	0.11	0.85	1.59	3.47	0.13	91.58	05/04/2018	Cameca
HP_53-56	71.82	0.08	11.88	0.83	0.04	0.07	0.65	1.84	4.04	0.10	91.33	13/04/2018	JEOL
HP_53-56	70.32	0.17	12.21	1.28	0.05	0.12	0.90	2.01	4.11	0.10	91.24	05/04/2018	Cameca
HP_53-56	70.75	0.11	12.05	1.46	0.07	0.11	0.93	1.60	4.02	0.08	91.15	13/04/2018	JEOL
HP_53-56	71.66	0.39	11.11	1.57	0.07	0.25	1.59	1.97	2.40	0.18	91.15	05/04/2018	Cameca
HP_53-56	68.86	0.14	12.25	2.68	0.10	0.13	1.56	1.86	2.60	0.18	90.31	05/04/2018	Cameca
Mean:	72.53	0.14	12.33	1.32	0.06	0.13	0.99	2.84	3.43	0.14	93.87		
StDev:	1.72	0.10	0.65	0.47	0.02	0.10	0.35	0.96	0.72	0.04	2.31		

Detrital glass

Sample	SiO_2	TiO2	Al_2O_3	FeO_T	MnO	MgO	CaO	Na_2O	K_2O	Cl	Total	Date	Instrument
HP_60	76.14	0.15	13.48	1.19	0.05	0.21	2.04	4.07	2.42	0.12	99.83	13/04/2018	JEOL
HP_60	73.04	0.20	13.99	3.08	0.14	0.20	1.86	5.06	1.56	0.17	99.26	13/04/2018	JEOL
HP_60	75.12	0.08	13.68	1.25	0.10	0.18	1.14	3.83	2.90	0.10	98.37	05/04/2018	Cameca
HP_60	75.42	0.13	12.95	1.08	0.08	0.22	1.47	3.90	2.82	0.21	98.23	05/04/2018	Cameca
HP_60	74.64	0.17	12.99	0.94	0.09	0.04	0.22	4.70	3.96	0.19	97.91	05/04/2018	Cameca
HP_60	76.33	0.08	11.99	0.55	0.03	0.02	0.39	3.16	5.04	0.13	97.68	13/04/2018	JEOL
HP_60	75.34	0.13	12.82	0.97	0.03	0.24	1.02	4.53	1.92	0.19	97.14	05/04/2018	Cameca
HP_60	74.98	0.14	12.60	1.01	0.03	0.26	1.23	4.70	2.03	0.19	97.12	13/04/2018	JEOL
HP_60	74.16	0.23	12.72	1.24	0.05	0.36	1.70	4.31	1.56	0.20	96.49	05/04/2018	Cameca
HP_60	75.55	0.10	12.36	1.03	0.06	0.21	1.07	4.05	1.61	0.18	96.18	05/04/2018	Cameca
HP_60	72.55	0.11	13.20	1.14	0.11	0.19	1.15	3.98	2.85	0.11	95.37	05/04/2018	Cameca
HP_60	74.18	0.23	11.97	1.30	0.04	0.20	1.41	2.79	2.62	0.20	94.89	05/04/2018	Cameca
HP_60	70.24	0.27	12.69	1.43	0.06	0.21	1.12	3.65	3.88	0.19	93.70	05/04/2018	Cameca
HP_60	70.38	0.26	12.28	1.47	0.04	0.22	1.07	3.57	3.92	0.17	93.34	13/04/2018	JEOL

HP_60	72.91	0.06	11.93	0.74	0.04	0.06	0.78	1.66	4.92	0.21	93.25	05/04/2018	Cameca
HP_60	73.24	0.20	11.61	0.88	0.05	0.13	0.80	2.19	3.95	0.12	93.13	05/04/2018	Cameca
HP_60	70.69	0.07	12.97	1.26	0.04	0.19	1.15	3.69	2.98	0.12	93.13	05/04/2018	Cameca
HP_60	73.79	0.17	11.25	1.08	0.03	0.09	0.83	1.97	3.57	0.17	92.93	05/04/2018	Cameca
HP_60	73.01	0.05	12.16	0.63	0.06	0.05	0.67	2.21	3.94	0.12	92.88	05/04/2018	Cameca
HP_60	72.49	0.24	11.77	0.99	0.11	0.13	0.59	2.26	3.91	0.20	92.65	13/04/2018	JEOL
HP_60	72.04	0.13	11.96	0.60	0.07	0.05	0.81	2.64	4.10	0.14	92.52	13/04/2018	JEOL
HP_60	72.67	0.09	11.51	1.57	0.03	0.01	1.07	1.62	3.63	0.12	92.31	05/04/2018	Cameca
HP_60	72.12	0.14	11.94	0.95	0.03	0.05	0.59	2.49	3.84	0.17	92.28	05/04/2018	Cameca
HP_60	71.22	0.16	12.45	0.66	0.12	0.14	0.50	2.02	4.73	0.04	92.02	05/04/2018	Cameca
HP_60	71.62	0.09	11.86	0.80	0.05	0.02	0.64	2.24	4.38	0.20	91.83	05/04/2018	Cameca
HP_60	67.75	0.27	12.81	2.17	0.03	0.32	1.68	3.47	3.19	0.17	91.83	13/04/2018	JEOL
HP_60	71.23	0.05	11.88	0.88	0.05	0.02	0.64	2.31	4.64	0.12	91.80	05/04/2018	Cameca
HP_60	71.34	0.12	11.64	1.00	0.07	0.06	0.58	2.74	3.75	0.13	91.39	13/04/2018	JEOL
HP_60	71.91	0.10	11.29	1.50	0.09	0.02	0.71	1.92	3.69	0.08	91.28	05/04/2018	Cameca
HP_60	71.99	0.10	11.53	0.89	0.03	0.07	0.60	2.01	3.66	0.17	90.99	05/04/2018	Cameca
HP_60	69.76	0.16	12.33	0.96	0.06	0.08	0.42	2.12	3.88	0.18	89.91	05/04/2018	Cameca
HP_60	66.23	0.01	13.94	0.04	0.01	0.70	1.44	1.48	3.59	0.00	87.44	05/04/2018	Cameca
Mean:	72.63	0.14	12.39	1.10	0.06	0.15	0.98	3.04	3.42	0.15	94.03		
StDev:	2.33	0.07	0.74	0.52	0.03	0.14	0.45	1.06	0.97	0.05	2.99		

Mt. Burney MB1

Sample	SiO_2	TiO2	Al_2O_3	FeO_T	MnO	MgO	CaO	Na_2O	K_2O	Cl	Total	Date	Instrument
HP_67	76.07	0.12	12.28	0.97	0.03	0.24	1.24	4.44	1.74	0.17	97.27	05/04/2018	Cameca
HP_67	75.03	0.12	12.19	1.07	0.03	0.25	1.14	4.29	1.74	0.17	96.00	12/04/2018	JEOL
HP_67	75.07	0.14	12.53	1.13	0.03	0.25	1.16	4.00	1.83	0.20	96.31	12/04/2018	JEOL
HP_67	76.52	0.12	12.56	0.91	0.06	0.25	1.29	4.77	1.63	0.18	98.26	05/04/2018	Cameca
HP_67	75.74	0.19	12.67	0.98	0.04	0.23	1.07	4.49	1.82	0.19	97.40	05/04/2018	Cameca

HP_67	74.55	0.13	12.49	0.94	0.06	0.21	1.18	4.44	1.82	0.21	95.98	05/04/2018	Cameca
HP_67	76.39	0.10	12.92	0.96	0.07	0.23	1.18	4.67	1.73	0.20	98.41	05/04/2018	Cameca
HP_67	74.61	0.18	12.38	1.03	0.02	0.21	1.22	4.44	1.90	0.19	96.13	05/04/2018	Cameca
HP_67	74.23	0.15	12.48	1.08	0.04	0.26	1.17	4.28	1.85	0.16	95.67	12/04/2018	JEOL
HP_67	74.38	0.13	12.54	1.11	0.03	0.22	1.23	4.22	1.85	0.21	95.87	05/04/2018	Cameca
HP_67	74.58	0.15	12.58	0.91	0.07	0.22	1.15	4.44	1.92	0.20	96.18	05/04/2018	Cameca
HP_67	76.11	0.13	12.77	1.00	0.02	0.21	1.15	4.77	1.85	0.20	98.17	05/04/2018	Cameca
HP_67	73.35	0.16	12.40	1.04	0.03	0.23	1.11	4.44	1.79	0.20	94.71	05/04/2018	Cameca
HP_67	73.77	0.15	12.47	1.00	0.05	0.26	1.18	4.52	1.76	0.16	95.29	12/04/2018	JEOL
HP_67	75.60	0.12	12.65	1.07	0.04	0.27	1.26	4.81	1.67	0.22	97.64	05/04/2018	Cameca
HP_67	75.74	0.20	12.64	1.10	0.03	0.26	1.34	4.78	1.61	0.19	97.84	05/04/2018	Cameca
HP_67	74.52	0.18	12.56	0.98	0.03	0.26	1.02	4.60	1.96	0.21	96.27	12/04/2018	JEOL
HP_67	76.09	0.17	12.78	1.07	0.05	0.25	1.15	4.86	1.73	0.19	98.30	05/04/2018	Cameca
HP_67	74.01	0.15	12.51	1.03	0.05	0.25	1.08	4.67	1.74	0.21	95.64	12/04/2018	JEOL
HP_67	75.91	0.17	12.69	1.28	0.08	0.22	1.10	4.80	1.77	0.20	98.17	05/04/2018	Cameca
HP_67	74.25	0.19	12.69	1.05	0.07	0.27	1.24	4.46	1.78	0.21	96.16	05/04/2018	Cameca
HP_67	74.16	0.13	12.71	0.98	0.07	0.25	1.08	4.73	1.92	0.19	96.19	12/04/2018	JEOL
HP_67	75.56	0.15	12.84	1.08	0.07	0.25	1.08	4.92	1.90	0.19	98.00	05/04/2018	Cameca
HP_67	75.17	0.18	13.02	1.08	0.07	0.16	1.17	4.53	2.01	0.20	97.54	05/04/2018	Cameca
HP_67	74.71	0.26	12.66	1.27	0.03	0.30	1.64	4.53	1.49	0.16	97.02	05/04/2018	Cameca
HP_67	73.21	0.22	12.56	0.98	0.05	0.25	1.05	4.87	1.94	0.19	95.29	12/04/2018	JEOL
HP_67	73.93	0.12	12.86	1.07	0.05	0.27	1.16	4.81	1.89	0.22	96.34	12/04/2018	JEOL
Mean:	74.94	0.16	12.61	1.04	0.05	0.24	1.18	4.58	1.80	0.19	96.74		
StDev:	0.94	0.04	0.19	0.09	0.02	0.03	0.12	0.23	0.12	0.02	1.09		
HP_67	*73.08*	*0.12*	*13.01*	*1.45*	*0.09*	*0.36*	*1.67*	*4.94*	*1.46*	*0.23*	*96.36*	*05/04/2018*	*Cameca*
HP_67	*72.66*	*0.23*	*13.19*	*1.56*	*0.03*	*0.38*	*2.04*	*4.65*	*1.45*	*0.20*	*96.35*	*05/04/2018*	*Cameca*
HP_67	*75.22*	*0.25*	*13.82*	*1.44*	*0.02*	*0.47*	*1.96*	*5.30*	*1.31*	*0.23*	*99.99*	*05/04/2018*	*Cameca*
HP_67	*73.21*	*0.19*	*14.80*	*1.41*	*0.04*	*0.39*	*2.66*	*4.57*	*1.27*	*0.16*	*98.67*	*05/04/2018*	*Cameca*

HP_67	*72.56*	*0.25*	*14.28*	*1.92*	*0.10*	*0.53*	*2.32*	*4.85*	*1.40*	*0.23*	*98.38*	*05/04/2018*	*Cameca*
HP_67	*75.64*	*0.15*	*12.44*	*1.07*	*0.04*	*0.26*	*1.21*	*1.86*	*1.87*	*0.22*	*94.72*	*12/04/2018*	*JEOL*
HP_67	*75.38*	*0.21*	*13.17*	*1.44*	*0.04*	*0.35*	*1.75*	*4.59*	*1.56*	*0.18*	*98.63*	*12/04/2018*	*JEOL*
HP_67	*73.16*	*0.11*	*12.66*	*1.59*	*0.11*	*0.19*	*1.52*	*3.81*	*2.60*	*0.12*	*95.84*	*12/04/2018*	*JEOL*
HP_67	*72.25*	*0.38*	*14.47*	*2.08*	*0.05*	*0.58*	*2.58*	*5.12*	*1.33*	*0.20*	*99.00*	*12/04/2018*	*JEOL*
HP_67	*72.77*	*0.12*	*12.26*	*0.92*	*0.05*	*0.19*	*1.13*	*4.43*	*1.78*	*0.19*	*93.81*	*05/04/2018*	*Cameca*

Reclus R1

Sample	SiO_2	TiO2	Al_2O_3	FeO_T	MnO	MgO	CaO	Na_2O	K_2O	Cl	Total	Date	Instrument
HP_133-135	76.86	0.10	13.28	1.32	0.04	0.23	1.39	4.18	2.84	0.19	100.39	05/04/2018	Cameca
HP_133-135	76.89	0.15	13.21	1.14	0.04	0.26	1.71	3.85	2.37	0.18	99.76	05/04/2018	Cameca
HP_133-135	75.97	0.08	12.88	1.26	0.06	0.21	1.50	3.78	2.64	0.18	98.54	12/04/2018	JEOL
HP_133-135	75.99	0.16	12.80	1.15	0.07	0.18	1.52	3.67	2.65	0.19	98.34	12/04/2018	JEOL
HP_133-135	75.87	0.12	13.00	1.09	0.08	0.19	1.56	3.52	2.62	0.17	98.18	05/04/2018	Cameca
HP_133-135	75.68	0.14	12.45	1.19	0.03	0.15	1.46	3.96	2.59	0.15	97.77	05/04/2018	Cameca
HP_133-135	75.10	0.11	12.66	1.11	0.04	0.25	1.46	4.09	2.42	0.19	97.39	12/04/2018	JEOL
HP_133-135	75.79	0.09	12.57	1.05	0.01	0.20	1.44	3.65	2.30	0.14	97.21	05/04/2018	Cameca
HP_133-135	75.40	0.11	12.48	1.08	0.06	0.18	1.35	3.71	2.53	0.17	97.03	12/04/2018	JEOL
HP_133-135	74.83	0.12	12.72	1.20	0.02	0.21	1.51	3.91	2.33	0.19	97.01	05/04/2018	Cameca
HP_133-135	74.84	0.09	12.55	1.20	0.05	0.17	1.37	3.93	2.58	0.20	96.93	05/04/2018	Cameca
HP_133-135	74.23	0.13	12.68	1.21	0.06	0.22	1.48	4.12	2.63	0.20	96.92	05/04/2018	Cameca
HP_133-135	74.65	0.18	12.60	1.14	0.00	0.20	1.42	3.92	2.52	0.19	96.78	12/04/2018	JEOL
HP_133-135	74.47	0.11	12.79	1.14	0.05	0.23	1.41	3.81	2.59	0.19	96.75	05/04/2018	Cameca
HP_133-135	74.37	0.14	12.64	1.27	0.07	0.20	1.50	3.82	2.54	0.21	96.71	05/04/2018	Cameca
HP_133-135	75.23	0.14	12.44	1.19	0.04	0.17	1.36	3.42	2.49	0.19	96.64	05/04/2018	Cameca
HP_133-135	74.55	0.09	12.73	1.11	0.05	0.19	1.40	3.73	2.57	0.19	96.55	12/04/2018	JEOL
HP_133-135	74.02	0.13	12.92	1.32	0.05	0.23	1.47	3.66	2.53	0.18	96.48	05/04/2018	Cameca
HP_133-135	74.32	0.11	12.76	1.15	0.03	0.19	1.44	3.72	2.42	0.19	96.30	05/04/2018	Cameca

HP_133-135	73.93	0.13	12.85	1.17	0.06	0.20	1.53	3.62	2.66	0.17	96.30	05/04/2018	Cameca
HP_133-135	73.74	0.12	12.75	1.14	0.06	0.19	1.45	3.98	2.70	0.18	96.28	05/04/2018	Cameca
HP_133-135	74.02	0.12	12.65	1.17	0.05	0.19	1.45	3.84	2.58	0.18	96.20	12/04/2018	JEOL
HP_133-135	73.85	0.15	12.62	1.07	0.07	0.20	1.44	3.91	2.67	0.16	96.10	12/04/2018	JEOL
HP_133-135	73.83	0.10	12.47	1.12	0.01	0.17	1.31	3.86	2.84	0.18	95.85	05/04/2018	Cameca
HP_133-135	73.50	0.22	11.70	1.64	0.07	0.19	1.30	4.29	2.72	0.16	95.76	05/04/2018	Cameca
HP_133-135	73.71	0.13	12.43	1.11	0.06	0.21	1.32	3.80	2.60	0.22	95.54	05/04/2018	Cameca
HP_133-135	73.68	0.13	12.62	1.09	0.05	0.22	1.32	3.53	2.75	0.18	95.53	12/04/2018	JEOL
HP_133-135	73.45	0.15	12.48	1.32	0.02	0.17	1.44	3.66	2.63	0.19	95.48	05/04/2018	Cameca
HP_133-135	73.32	0.11	12.48	1.13	0.01	0.22	1.35	3.64	2.66	0.16	95.04	12/04/2018	JEOL
HP_133-135	73.09	0.11	12.64	1.33	0.01	0.14	1.32	3.78	2.38	0.24	95.00	05/04/2018	Cameca
HP_133-135	73.45	0.11	12.22	1.05	0.03	0.20	1.33	3.89	2.57	0.16	94.97	05/04/2018	Cameca
HP_133-135	73.12	0.13	12.51	1.12	0.05	0.18	1.32	3.51	2.76	0.17	94.84	12/04/2018	JEOL
HP_133-135	73.06	0.16	12.41	1.14	0.05	0.19	1.33	3.74	2.57	0.21	94.80	12/04/2018	JEOL
Mean:	74.51	0.13	12.64	1.18	0.04	0.20	1.42	3.80	2.58	0.18	96.65		
StDev:	1.07	0.03	0.28	0.11	0.02	0.03	0.09	0.20	0.13	0.02	1.32		
HP_133-135	*74.57*	*0.19*	*12.05*	*0.69*	*0.01*	*0.06*	*0.60*	*3.25*	*4.63*	*0.20*	*96.20*	*12/04/2018*	*JEOL*
HP_133-135	*72.28*	*0.08*	*12.57*	*0.96*	*0.02*	*0.15*	*1.28*	*3.80*	*2.53*	*0.18*	*93.81*	*12/04/2018*	*JEOL*
HP_133-135	*72.05*	*0.06*	*12.09*	*0.75*	*0.09*	*0.09*	*0.50*	*3.50*	*3.61*	*0.21*	*92.90*	*12/04/2018*	*JEOL*
HP_133-135	*70.02*	*0.22*	*12.20*	*2.23*	*0.07*	*0.26*	*1.46*	*3.03*	*2.80*	*0.24*	*92.47*	*05/04/2018*	*Cameca*
HP_133-135	*71.54*	*0.07*	*12.07*	*1.02*	*0.05*	*0.13*	*1.26*	*3.12*	*2.43*	*0.21*	*91.85*	*05/04/2018*	*Cameca*
HP_133-135	*69.82*	*0.07*	*12.04*	*1.10*	*0.01*	*0.17*	*1.31*	*3.41*	*2.42*	*0.28*	*90.59*	*05/04/2018*	*Cameca*

Detrital glass

Sample	SiO_2	TiO2	Al_2O_3	FeO_T	MnO	MgO	CaO	Na_2O	K_2O	Cl	Total	Date	Instrument
HP_156	72.38	0.19	13.06	2.15	0.09	0.15	1.27	3.42	3.92	0.18	96.76	05/04/2018	Cameca
HP_156	73.87	0.16	11.77	0.84	0.00	0.13	0.74	3.18	4.22	0.26	95.12	12/04/2018	JEOL
HP_156	73.20	0.02	12.64	1.01	0.11	0.10	0.91	3.12	3.84	0.11	95.03	12/04/2018	JEOL

HP_156	73.74	0.16	11.55	1.57	0.06	0.12	1.08	3.49	2.95	0.25	94.91	12/04/2018	JEOL
HP_156	71.23	0.06	12.95	1.22	0.05	0.02	0.68	3.57	4.57	0.12	94.44	05/04/2018	Cameca
HP_156	72.95	0.15	11.85	0.81	0.13	0.11	0.53	2.76	4.98	0.22	94.44	12/04/2018	JEOL
HP_156	72.43	0.17	11.92	1.08	0.02	0.14	1.17	3.39	3.76	0.23	94.26	05/04/2018	Cameca
HP_156	70.72	0.21	12.46	1.92	0.07	0.17	1.06	3.84	3.60	0.17	94.18	12/04/2018	JEOL
HP_156	73.78	0.20	11.46	1.09	0.01	0.19	1.13	3.23	2.87	0.19	94.09	12/04/2018	JEOL
HP_156	72.51	0.30	11.73	1.39	0.09	0.19	1.07	3.14	3.53	0.15	94.07	05/04/2018	Cameca
HP_156	71.42	0.27	11.99	1.94	0.06	0.19	1.21	3.57	3.29	0.11	94.04	12/04/2018	JEOL
HP_156	71.33	0.20	12.56	1.65	0.05	0.17	1.20	3.17	3.54	0.15	93.99	05/04/2018	Cameca
HP_156	71.81	0.19	12.18	1.57	0.03	0.13	0.87	3.30	3.75	0.18	93.97	12/04/2018	JEOL
HP_156	71.29	0.33	12.11	1.52	0.03	0.20	0.94	3.02	4.31	0.19	93.90	05/04/2018	Cameca
HP_156	71.24	0.27	12.38	1.08	0.01	0.18	0.82	3.36	4.32	0.21	93.84	12/04/2018	JEOL
HP_156	72.69	0.16	12.06	0.96	0.07	0.06	0.64	3.55	3.36	0.31	93.79	05/04/2018	Cameca
HP_156	72.41	0.15	11.87	1.01	0.03	0.17	0.99	3.32	3.59	0.22	93.72	12/04/2018	JEOL
HP_156	72.73	0.10	11.61	0.88	0.04	0.16	0.70	2.92	4.36	0.24	93.69	12/04/2018	JEOL
HP_156	71.76	0.15	12.14	1.23	0.09	0.10	0.98	3.83	3.23	0.16	93.63	05/04/2018	Cameca
HP_156	72.47	0.30	11.17	2.08	0.00	0.22	1.41	3.37	2.38	0.24	93.58	12/04/2018	JEOL
HP_156	72.15	0.16	11.88	1.30	0.03	0.05	0.77	3.53	3.59	0.16	93.57	12/04/2018	JEOL
HP_156	71.08	0.14	12.10	1.56	0.07	0.09	1.04	2.80	4.52	0.22	93.57	05/04/2018	Cameca
HP_156	72.96	0.11	11.88	0.72	0.09	0.08	0.67	3.31	3.54	0.22	93.55	05/04/2018	Cameca
HP_156	72.59	0.07	11.94	0.69	0.05	0.04	0.67	3.17	4.14	0.15	93.48	05/04/2018	Cameca
HP_156	70.35	0.26	12.57	2.50	0.10	0.20	1.21	3.29	2.90	0.11	93.46	05/04/2018	Cameca
HP_156	73.03	0.07	11.77	0.78	0.10	0.08	0.52	3.22	3.68	0.21	93.42	12/04/2018	JEOL
HP_156	72.19	0.17	12.08	1.02	0.02	0.19	0.95	3.20	3.39	0.20	93.36	05/04/2018	Cameca
HP_156	69.20	0.34	12.73	2.58	0.07	0.28	1.72	2.90	3.45	0.09	93.34	05/04/2018	Cameca
HP_156	69.77	0.30	12.32	1.87	0.06	0.18	1.20	3.70	3.86	0.12	93.34	05/04/2018	Cameca
HP_156	71.45	0.16	12.01	1.57	0.05	0.13	0.91	3.05	3.82	0.22	93.32	05/04/2018	Cameca
HP_156	69.08	0.23	12.66	1.96	0.07	0.21	1.03	3.47	4.39	0.21	93.25	12/04/2018	JEOL

HP_156	72.22	0.09	12.25	0.65	0.08	0.11	0.63	4.00	2.99	0.19	93.16	12/04/2018	JEOL
HP_156	72.88	0.09	11.97	0.95	0.00	0.02	0.61	2.16	4.34	0.12	93.10	12/04/2018	JEOL
HP_156	72.20	0.20	11.59	0.76	0.00	0.10	0.72	2.94	4.28	0.23	92.96	05/04/2018	Cameca
HP_156	71.94	0.03	12.31	0.99	0.04	0.02	0.63	3.20	3.71	0.11	92.96	12/04/2018	JEOL
HP_156	70.75	0.19	12.34	1.33	0.05	0.23	1.28	3.62	2.87	0.18	92.79	12/04/2018	JEOL
HP_156	69.62	0.35	12.56	2.23	0.08	0.40	1.98	3.11	2.29	0.14	92.72	05/04/2018	Cameca
HP_156	70.24	0.17	12.10	1.17	0.08	0.17	0.87	3.48	4.10	0.23	92.56	05/04/2018	Cameca
HP_156	71.78	0.08	11.51	1.07	0.05	0.11	0.86	3.27	3.56	0.21	92.46	05/04/2018	Cameca
HP_156	70.93	0.20	11.79	1.46	0.08	0.14	0.85	3.21	3.63	0.17	92.42	12/04/2018	JEOL
HP_156	71.45	0.20	11.87	1.56	0.05	0.15	1.11	3.13	2.73	0.17	92.38	12/04/2018	JEOL
HP_156	70.33	0.12	12.89	0.96	0.00	0.06	0.77	3.41	3.68	0.03	92.23	05/04/2018	Cameca
HP_156	69.84	0.30	12.26	2.32	0.11	0.17	1.24	3.00	2.84	0.13	92.17	12/04/2018	JEOL
HP_156	70.16	0.23	12.46	1.40	0.04	0.21	0.89	2.87	3.60	0.25	92.04	12/04/2018	JEOL
HP_156	70.65	0.24	11.52	1.50	0.00	0.15	0.96	3.35	3.50	0.19	92.01	12/04/2018	JEOL
HP_156	71.40	0.26	11.24	1.34	0.02	0.18	1.18	2.74	3.26	0.17	91.75	12/04/2018	JEOL
HP_156	70.57	0.16	11.96	1.51	0.04	0.12	0.90	2.79	3.48	0.22	91.70	12/04/2018	JEOL
HP_156	69.67	0.13	12.28	1.46	0.05	0.04	0.54	4.12	3.13	0.28	91.64	05/04/2018	Cameca
HP_156	72.19	0.11	11.35	0.82	0.09	0.14	0.56	2.31	3.77	0.16	91.44	12/04/2018	JEOL
HP_156	71.00	0.25	11.65	1.41	0.00	0.25	1.32	2.49	2.63	0.21	91.17	12/04/2018	JEOL
HP_156	71.01	0.11	11.51	0.92	0.04	0.08	0.80	2.97	3.36	0.22	90.96	12/04/2018	JEOL
HP_156	70.90	0.28	11.25	1.12	0.06	0.21	0.77	2.43	3.54	0.20	90.71	12/04/2018	JEOL
HP_156	68.68	0.28	12.06	1.84	0.07	0.18	1.44	2.56	2.55	0.20	89.81	05/04/2018	Cameca
HP_156	67.50	0.19	11.06	1.11	0.04	0.10	0.52	3.39	4.64	0.36	88.83	05/04/2018	Cameca
HP_156	65.24	0.16	11.08	1.63	0.06	0.10	0.83	2.72	3.65	0.35	85.73	05/04/2018	Cameca
Mean:	71.33	0.18	12.00	1.36	0.05	0.14	0.95	3.19	3.60	0.19	92.96		
StDev:	1.58	0.08	0.48	0.48	0.03	0.07	0.30	0.40	0.59	0.06	1.67		

C.2 EPMA secondary standards included in paper III

Table C.2: Individual, glass, major-minor oxide concentrations from tephra deposits (wt%) analysed in Paper III.

Sample	SiO_2	TiO2	Al_2O_3	FeO_T	MnO	MgO	CaO	Na_2O	K_2O	Cl	Total	Date	Instrument
Old Crow_001	71.22	0.31	12.69	1.70	0.05	0.24	1.40	3.52	3.52	0.28	94.88	05/04/2018	Cameca
Old Crow_002	70.79	0.33	12.42	1.46	0.06	0.26	1.59	3.46	3.48	0.23	94.03	05/04/2018	Cameca
Old Crow_003	71.39	0.30	12.46	1.62	0.07	0.26	1.36	3.71	3.21	0.28	94.59	05/04/2018	Cameca
Old Crow_004	72.11	0.38	12.78	1.57	0.05	0.25	1.53	3.92	3.68	0.30	96.50	05/04/2018	Cameca
Old Crow_005	72.12	0.33	12.72	1.70	0.08	0.26	1.45	3.54	4.01	0.31	96.46	05/04/2018	Cameca
Old Crow_011	72.16	0.32	12.79	1.59	0.07	0.26	1.37	3.79	3.51	0.27	96.07	05/04/2018	Cameca
Old Crow_012	72.82	0.27	12.59	1.59	0.08	0.30	1.41	3.84	3.77	0.27	96.88	05/04/2018	Cameca
Old Crow_013	71.28	0.27	12.46	1.59	0.08	0.24	1.43	3.76	3.51	0.24	94.81	05/04/2018	Cameca
Old Crow_014	71.24	0.28	12.43	1.49	0.07	0.25	1.34	3.48	3.72	0.28	94.53	05/04/2018	Cameca
Old Crow_015	72.45	0.26	12.78	1.67	0.07	0.28	1.48	3.59	3.27	0.27	96.06	05/04/2018	Cameca
ID 3506_001	73.30	0.07	13.03	1.41	0.08	0.02	0.67	3.75	5.07	0.28	97.62	05/04/2018	Cameca
ID 3506_002	73.96	0.06	13.15	1.53	0.07	0.03	0.77	4.26	5.01	0.34	99.11	05/04/2018	Cameca
ID 3506_003	73.95	0.10	13.05	1.65	0.07	0.02	0.72	4.08	5.09	0.33	98.96	05/04/2018	Cameca
ID 3506_004	73.60	0.06	13.06	1.38	0.09	0.01	0.76	4.29	5.15	0.34	98.65	05/04/2018	Cameca
ID 3506_005	72.72	0.10	12.81	1.49	0.05	0.01	0.76	3.73	5.23	0.35	97.17	05/04/2018	Cameca
ID3506_006	74.92	0.08	13.18	1.57	0.07	0.03	0.78	4.04	5.29	0.31	100.19	05/04/2018	Cameca
ID3506_007	73.05	0.07	13.00	1.42	0.05	0.05	0.69	4.15	5.24	0.36	97.99	05/04/2018	Cameca
ID3506_008	74.01	0.06	13.25	1.43	0.10	0.03	0.70	4.22	5.27	0.31	99.31	05/04/2018	Cameca
ID3506_009	74.73	0.05	13.29	1.67	0.08	0.05	0.78	4.25	5.28	0.36	100.46	05/04/2018	Cameca
ID3506_010	74.25	0.08	13.14	1.52	0.06	0.01	0.74	3.78	5.16	0.33	98.99	05/04/2018	Cameca

ID3506_011	75.05	0.07	13.14	1.52	0.07	0.03	0.72	4.07	5.13	0.32	100.04	05/04/2018	Cameca
ID3506_012	75.09	0.09	13.31	1.54	0.07	0.03	0.75	4.24	5.18	0.32	100.54	05/04/2018	Cameca
ID3506_013	73.20	0.08	12.93	1.52	0.07	0.02	0.74	3.82	5.05	0.37	97.71	05/04/2018	Cameca
ID3506_014	74.00	0.08	13.09	1.64	0.07	0.01	0.70	4.16	4.85	0.35	98.88	05/04/2018	Cameca
ID3506_015	73.74	0.05	12.91	1.59	0.05	0.02	0.71	3.95	4.86	0.33	98.13	05/04/2018	Cameca
Old Crow_001	73.98	0.34	12.65	1.55	0.02	0.30	1.42	4.13	3.79	0.31	98.42	12/04/2018	JEOL
Old Crow_002	72.46	0.32	12.50	1.56	0.04	0.30	1.35	3.74	3.47	0.24	95.94	12/04/2018	JEOL
Old Crow_003	73.69	0.25	12.74	1.57	0.05	0.29	1.38	4.03	3.78	0.26	98.00	12/04/2018	JEOL
Old Crow_004	71.63	0.25	12.59	1.64	0.08	0.30	1.41	3.71	3.75	0.24	95.53	12/04/2018	JEOL
Old Crow_005	72.11	0.31	12.41	1.59	0.08	0.29	1.41	3.56	3.62	0.24	95.57	12/04/2018	JEOL
Old Crow_006	71.59	0.24	12.70	1.55	0.09	0.28	1.34	3.80	3.71	0.23	95.47	12/04/2018	JEOL
Old Crow_007	70.91	0.29	12.60	1.63	0.04	0.29	1.39	3.83	3.73	0.29	94.93	12/04/2018	JEOL
Old Crow_008	72.51	0.29	12.49	1.60	0.09	0.29	1.37	3.63	3.70	0.30	96.20	12/04/2018	JEOL
Old Crow_009	72.10	0.34	12.54	1.54	0.06	0.31	1.45	3.82	3.64	0.28	96.02	12/04/2018	JEOL
Old Crow_010	71.81	0.29	12.68	1.67	0.08	0.30	1.39	3.76	3.71	0.26	95.90	12/04/2018	JEOL
Old Crow_011	72.14	0.32	12.70	1.66	0.06	0.22	1.38	3.78	3.52	0.28	96.01	12/04/2018	JEOL
Old Crow_014	70.89	0.32	12.51	1.57	0.00	0.28	1.33	3.64	3.40	0.24	94.12	12/04/2018	JEOL
Old Crow_015	71.62	0.29	12.70	1.61	0.06	0.30	1.34	3.61	3.57	0.28	95.32	12/04/2018	JEOL
Old Crow_017	71.72	0.30	12.56	1.69	0.04	0.30	1.40	3.89	3.72	0.29	95.85	12/04/2018	JEOL
Old Crow_018	72.49	0.35	12.57	1.59	0.05	0.26	1.42	4.19	3.73	0.25	96.84	12/04/2018	JEOL
Old Crow_019	73.57	0.24	12.83	1.58	0.05	0.39	1.35	4.18	3.46	0.28	97.85	12/04/2018	JEOL
Old Crow_020	72.43	0.28	12.59	1.56	0.06	0.29	1.41	4.04	3.58	0.25	96.44	12/04/2018	JEOL
Old Crow_021	72.67	0.29	12.80	1.67	0.07	0.28	1.36	4.08	3.55	0.27	96.97	12/04/2018	JEOL

ID 3506_001	74.41	0.09	12.97	1.50	0.09	0.03	0.74	3.91	5.15	0.30	99.13	12/04/2018	JEOL
ID 3506_002	74.50	0.08	13.22	1.55	0.09	0.02	0.71	4.02	5.27	0.36	99.73	12/04/2018	JEOL
ID 3506_003	73.78	0.06	13.04	1.65	0.09	0.05	0.69	4.07	5.11	0.36	98.82	12/04/2018	JEOL
ID 3506_004	74.12	0.08	12.90	1.55	0.10	0.04	0.74	4.29	5.25	0.33	99.32	12/04/2018	JEOL
ID 3506_005	74.49	0.10	13.30	1.60	0.07	0.02	0.74	3.85	5.14	0.38	99.60	12/04/2018	JEOL
ID 3506_006	74.37	0.09	13.19	1.57	0.07	0.06	0.72	3.86	5.14	0.36	99.35	12/04/2018	JEOL
ID 3506_008	74.05	0.16	13.14	1.56	0.10	0.07	0.75	3.79	5.23	0.33	99.09	12/04/2018	JEOL
ID 3506_009	74.41	0.04	13.07	1.53	0.05	0.02	0.71	4.05	5.23	0.32	99.35	12/04/2018	JEOL
ID 3506_010	74.31	0.10	13.36	1.65	0.09	0.03	0.73	4.10	5.17	0.30	99.78	12/04/2018	JEOL
ID 3506_011	73.73	0.08	13.14	1.52	0.08	0.02	0.73	3.79	5.24	0.32	98.57	12/04/2018	JEOL
ID 3506_012	73.95	0.10	13.16	1.66	0.06	0.02	0.73	3.98	5.21	0.33	99.13	12/04/2018	JEOL
ID 3506_013	75.11	0.08	13.12	1.59	0.08	0.06	0.75	4.13	5.21	0.33	100.38	12/04/2018	JEOL
ID 3506_014	74.39	0.08	13.12	1.49	0.09	0.04	0.71	4.61	5.23	0.32	100.01	12/04/2018	JEOL
ID 3506_015	74.15	0.09	13.20	1.49	0.08	0.05	0.68	4.09	5.20	0.33	99.28	12/04/2018	JEOL
ID 3506_001	74.73	0.10	13.06	1.49	0.09	0.01	0.74	4.14	5.22	0.34	99.85	12/04/2018	JEOL
ID 3506_017	73.77	0.05	13.11	1.50	0.09	0.05	0.72	4.19	5.09	0.29	98.79	12/04/2018	JEOL
ID 3506_018	74.32	0.08	13.05	1.49	0.10	0.02	0.70	4.35	5.19	0.31	99.55	12/04/2018	JEOL
ID 3506_019	74.31	0.08	13.12	1.58	0.07	0.03	0.73	4.13	5.24	0.32	99.54	12/04/2018	JEOL
ID 3506_020	74.58	0.11	13.16	1.54	0.07	0.04	0.71	4.26	5.14	0.34	99.87	12/04/2018	JEOL
ID 3506_021	74.79	0.08	13.15	1.54	0.06	0.04	0.74	4.21	5.28	0.31	100.13	12/04/2018	JEOL
Old Crow_001	72.07	0.31	12.80	1.56	0.08	0.29	1.38	3.70	3.64	0.28	96.05	13/04/2018	JEOL
Old Crow_002	70.88	0.34	12.33	1.58	0.03	0.28	1.39	3.49	3.75	0.28	94.28	13/04/2018	JEOL
Old Crow_003	72.17	0.32	12.63	1.77	0.09	0.31	1.41	3.86	3.77	0.25	96.51	13/04/2018	JEOL

Old Crow_004	71.44	0.26	12.56	1.59	0.07	0.31	1.38	3.70	3.49	0.26	94.99	13/04/2018	JEOL
Old Crow_005	71.80	0.31	12.57	1.62	0.03	0.28	1.41	3.74	3.68	0.26	95.63	13/04/2018	JEOL
Old crow_006	71.72	0.32	12.50	1.68	0.08	0.27	1.36	3.85	3.67	0.25	95.64	13/04/2018	JEOL
Old crow_007	71.85	0.31	12.51	1.51	0.05	0.28	1.41	3.94	3.62	0.27	95.67	13/04/2018	JEOL
Old crow_008	71.83	0.24	12.61	1.59	0.08	0.32	1.37	3.90	3.53	0.26	95.66	13/04/2018	JEOL
Old crow_009	74.68	0.30	13.00	1.76	0.06	0.29	1.43	3.66	3.76	0.31	99.18	13/04/2018	JEOL
Old crow_010	72.00	0.23	12.52	1.69	0.06	0.29	1.35	3.91	3.63	0.27	95.89	13/04/2018	JEOL
Old Crow_011	72.82	0.25	12.75	1.61	0.05	0.33	1.42	3.88	3.78	0.30	97.14	13/04/2018	JEOL
Old Crow_013	72.52	0.31	12.72	1.63	0.06	0.31	1.43	3.65	3.58	0.26	96.41	13/04/2018	JEOL
Old Crow_015	72.39	0.32	12.47	1.58	0.05	0.29	1.45	3.76	3.73	0.28	96.25	13/04/2018	JEOL
ID 3506_001	73.89	0.05	13.11	1.52	0.09	0.03	0.69	4.08	5.26	0.31	98.95	13/04/2018	JEOL
ID 3506_002	73.78	0.05	13.12	1.60	0.04	0.03	0.73	4.09	5.20	0.34	98.91	13/04/2018	JEOL
ID 3506_003	73.39	0.09	13.08	1.47	0.06	0.02	0.75	4.16	5.04	0.35	98.35	13/04/2018	JEOL
ID 3506_004	73.52	0.07	12.95	1.55	0.06	0.04	0.75	4.08	5.36	0.32	98.61	13/04/2018	JEOL
ID 3506_005	73.49	0.09	13.18	1.54	0.13	0.03	0.71	3.88	5.14	0.32	98.42	13/04/2018	JEOL
ID3506_006	73.87	0.02	12.99	1.53	0.03	0.04	0.72	3.94	5.21	0.34	98.61	13/04/2018	JEOL
ID3506_007	73.76	0.06	13.01	1.59	0.04	0.04	0.74	3.86	5.22	0.33	98.58	13/04/2018	JEOL
ID3506_008	74.05	0.14	13.00	1.61	0.06	0.06	0.73	4.15	5.31	0.34	99.37	13/04/2018	JEOL
ID3506_009	74.06	0.05	13.12	1.57	0.08	0.04	0.73	4.22	5.31	0.35	99.45	13/04/2018	JEOL
ID3506_010	74.66	0.06	13.21	1.52	0.07	0.03	0.72	3.92	5.14	0.36	99.60	13/04/2018	JEOL
ID306_011	73.22	0.08	13.08	1.58	0.06	0.05	0.71	4.00	5.23	0.33	98.25	13/04/2018	JEOL
ID306_012	73.58	0.07	12.97	1.56	0.06	0.05	0.68	4.11	5.36	0.31	98.69	13/04/2018	JEOL
ID306_013	73.22	0.06	13.07	1.63	0.06	0.04	0.69	4.11	5.27	0.34	98.40	13/04/2018	JEOL

ID306_014	73.68	0.11	13.16	1.53	0.06	0.04	0.70	4.16	5.30	0.34	99.00	13/04/2018	JEOL
ID306_015	73.91	0.05	13.11	1.65	0.05	0.03	0.75	4.46	5.15	0.33	99.42	13/04/2018	JEOL

C.3 Similarity coefficients

Table C.3 Similarity coefficients (Borchardt *et al*., 1972) between cryptotephra deposits in Hooker's Point and key regional ash beds.

Reference	**Source**	**Eruption**	**Sample**	**HP_14-17b**	**HP_67**	**HP134**
Stern *et al.,* (2008)	Mt. Burney	MB_2	Stern & Killian, (1996)	0.82	0.80	0.79
Stern *et al.,* (2008)	Mt. Burney	MB_2	110/3	0.78	0.77	0.77
Stern *et al.,* (2008)	Mt. Burney	MB_2	PH-107/3	0.77	0.76	0.75
Stern *et al.,* (2008)	Mt. Burney	MB_2	Kilian, (2003)	0.80	0.79	0.77
Wastegård *et al.,* (2013)	Mt. Burney	MB_1	5022-2T1	**0.93**	**0.96**	0.88
Stern *et al.,* (2008)	Reclus Volcano	Reclus R_1	Stern & Killian, (1996)	0.87	0.85	0.89
Stern *et al.,* (2008)	Reclus Volcano	Reclus R_1	BF636	0.80	0.83	0.89
Stern *et al.,* (2008)	Reclus Volcano	Reclus R_1	CS-103	0.80	0.84	0.88
Stern *et al.,* (2008)	Reclus Volcano	Reclus R_1	PAT-14	0.85	0.86	0.89
Stern *et al.,* (2008)	Reclus Volcano	Reclus R_1	3AR	0.82	0.84	0.86
Stern *et al.,* (2008)	Reclus Volcano	Reclus R_1	Kilian, (2003)	0.81	0.82	0.83
Wastegård *et al.,* (2013)	Reclus Volcano	Reclus R_1	5022-2T4	0.84	0.84	**0.95**
Hall *et al.,* (2001)	Unknown	Unknown	Fox Bay 60-65cm	**0.92**	0.88	0.77

C.4 Supplementary diagrams

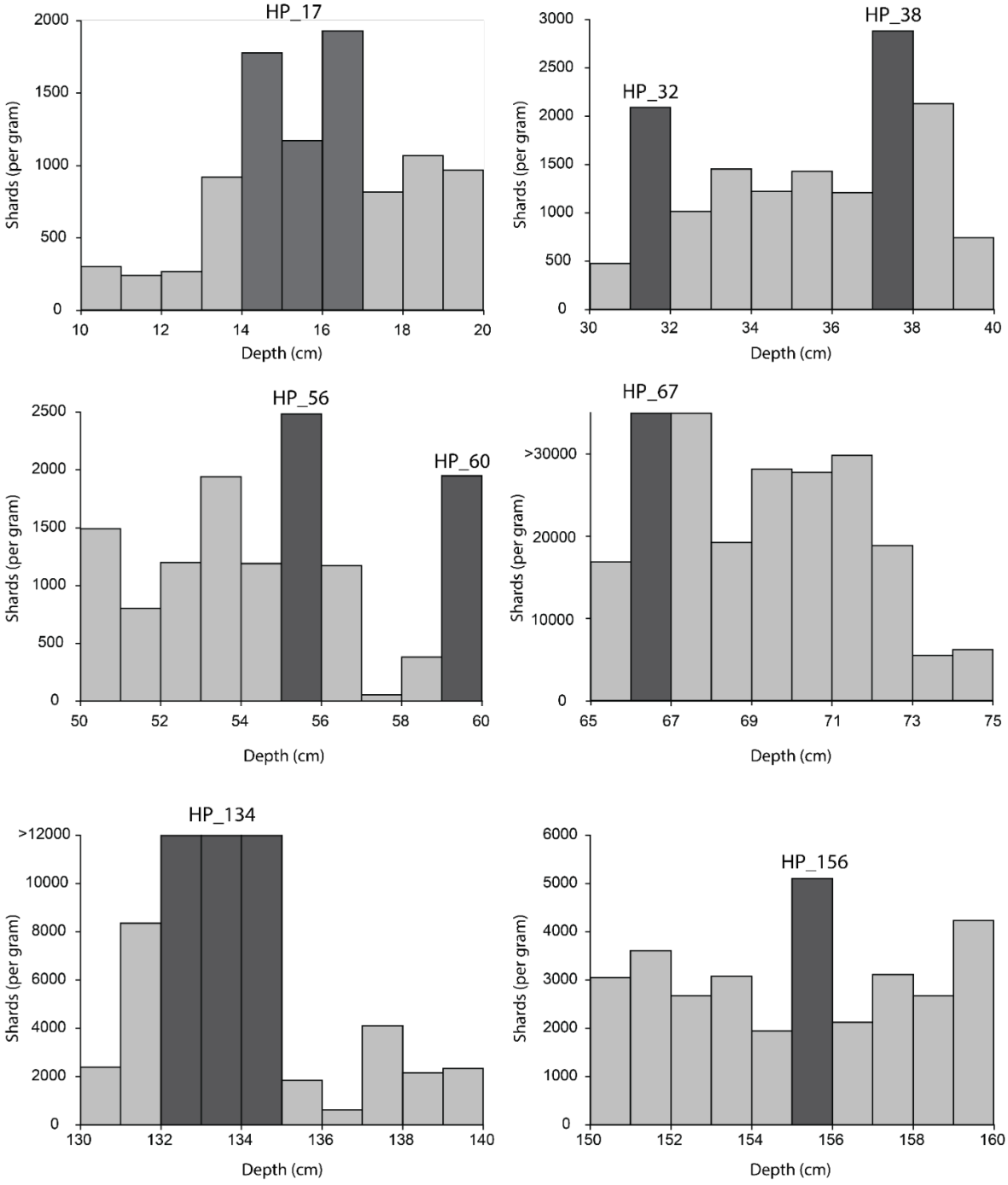

Figure C.1: Cryptotephra shard counts from Hooker's Point at 1 cm resolution. Dark grey bars indicate samples with the highest shard concentrations, which were subsequently analysed for major-minor element compositions.

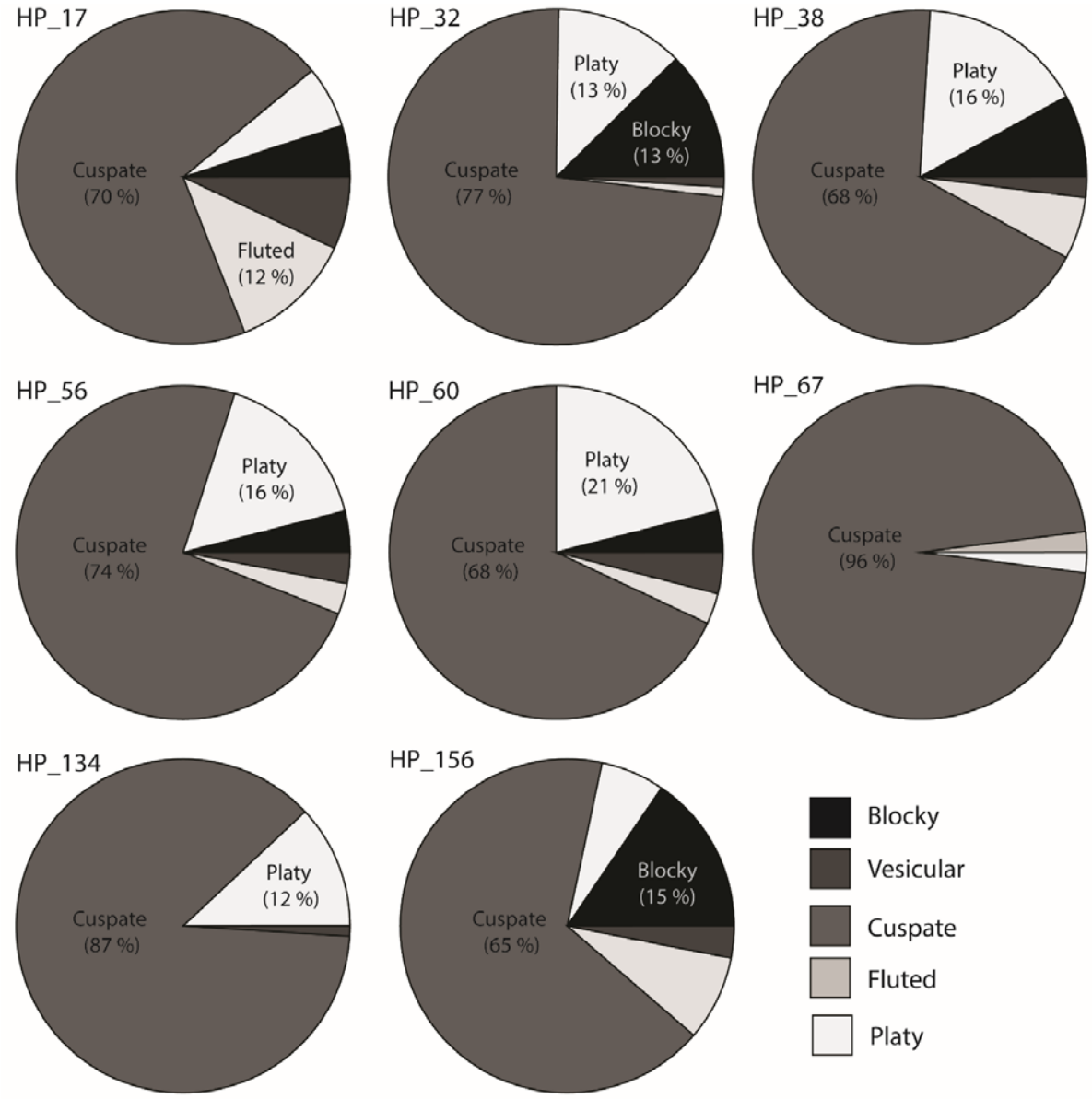

Figure C.2: Pie-chart plots of shard morphologies present in Hooker's Point cryptotephra deposits. With the exception of one brown shards in HP_32, glass shards were exclusively clear in all cryptotephra deposits. Diagrams and percentage values are based on 100 measurements.

Appendix C

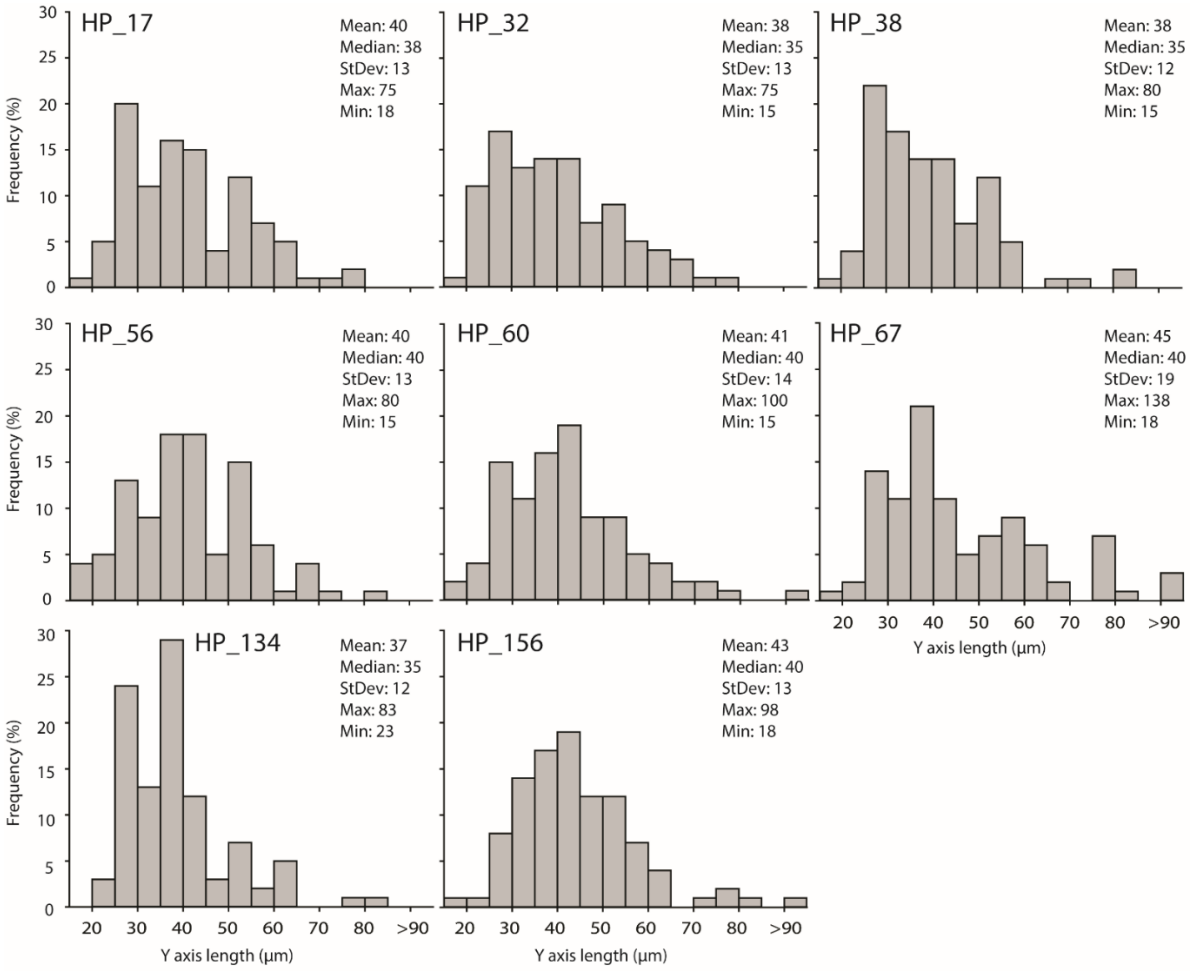

Figure C.3: Histograms and summary statistics of shard long axis (Y) measurements. Diagrams and statistics are based on 100 measurments.

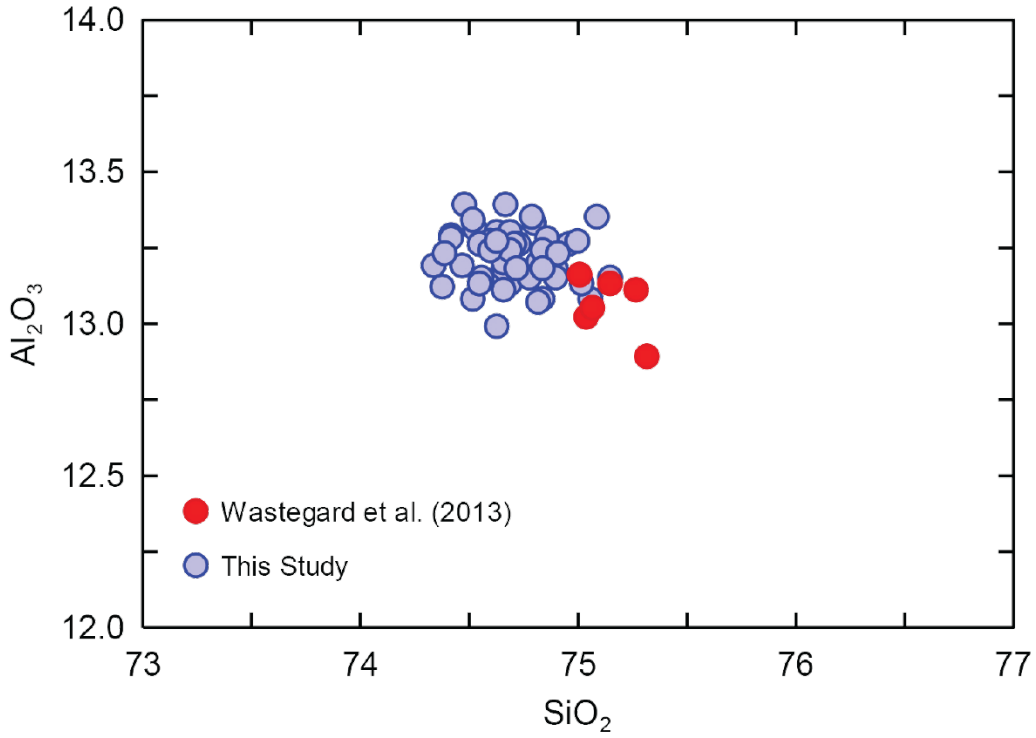

Figure C.4: Bivariate plot of Al_2O_3 and SiO_2 values from Lipari rhyolitic obsidian standards.

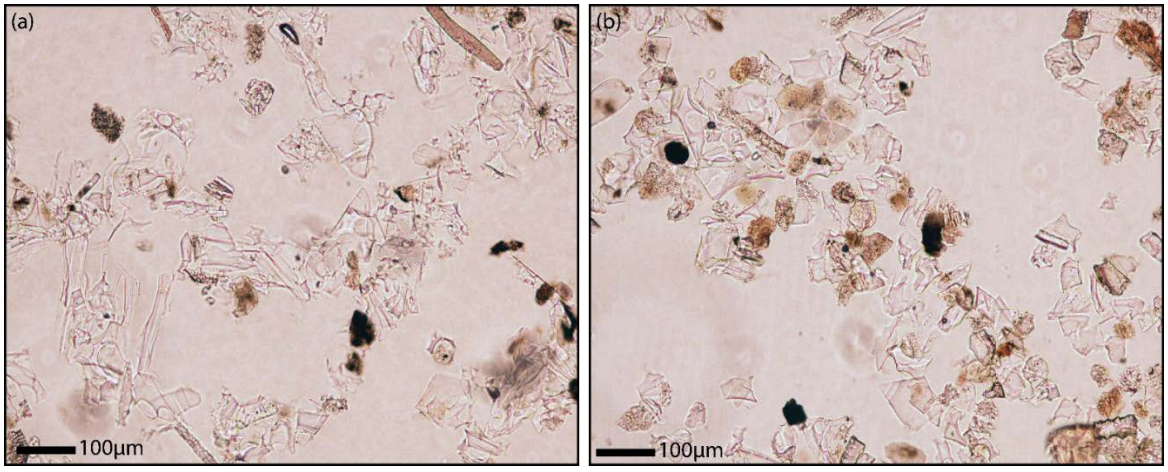

Figure C.5: Tephra shards from (a) HP_67 and (b) HP_134.

Appendix D Paper IV

Appendix D includes supplementary information, including radiocarbon dating and additional diagrams, used in Paper IV.

D.1 Radiocarbon dates

Table D.1 Radiocarbon dates from the Hooker's Point sediment sequence with calibrated two sigma age ranges. Ages were calibrated using OxCal 4.2.3 (Bronk Ramsey, 2017), and the SHCal13 calibration curve (Hogg *et al*., 2013).

Laboratory ID Code	Material	Depth (cm)	Age (14C yr BP)	1 σ Error	Calibrated age range (95.4 %)
Beta-193400	Bulk (peat)	0-2	5700	40	6630-6410
Beta-241334	Plant Macro	42-43	7390	40	8340-8060
Beta-193401	Bulk (peat)	76	9250	80	10650-10240
Beta-241335	Plant Macro	90-91	10030	40	11750-11330
Beta-241336	Wood	94-95	9940	40	11600-11240
Beta-193402	Bulk (peat)	100	10370	60	12520-12000
Beta-241338	Plant Macro	154-155	13320	50	16220-15820
Beta-193403	Bulk (peat)	168	13630	140	16920-16055

D.2 Supplementary diagrams

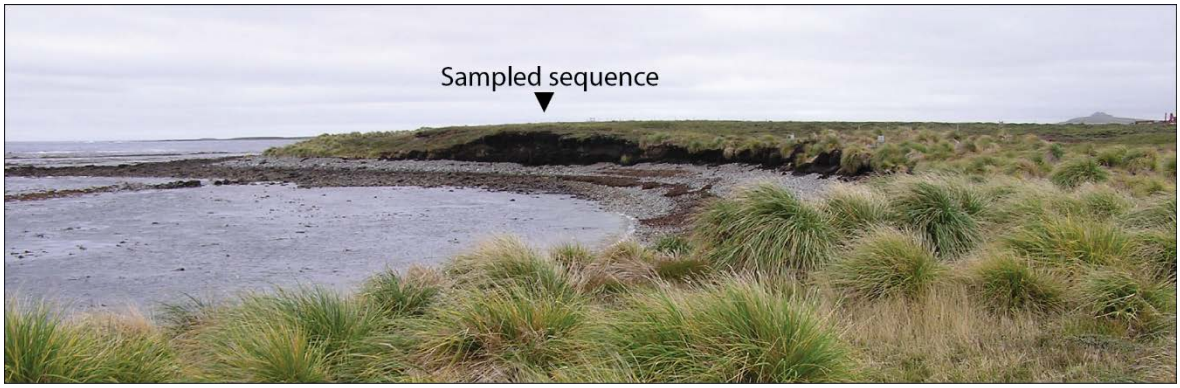

Figure D.1: Hooker's Bay and the surrounding landscape, including the sampled sequence.

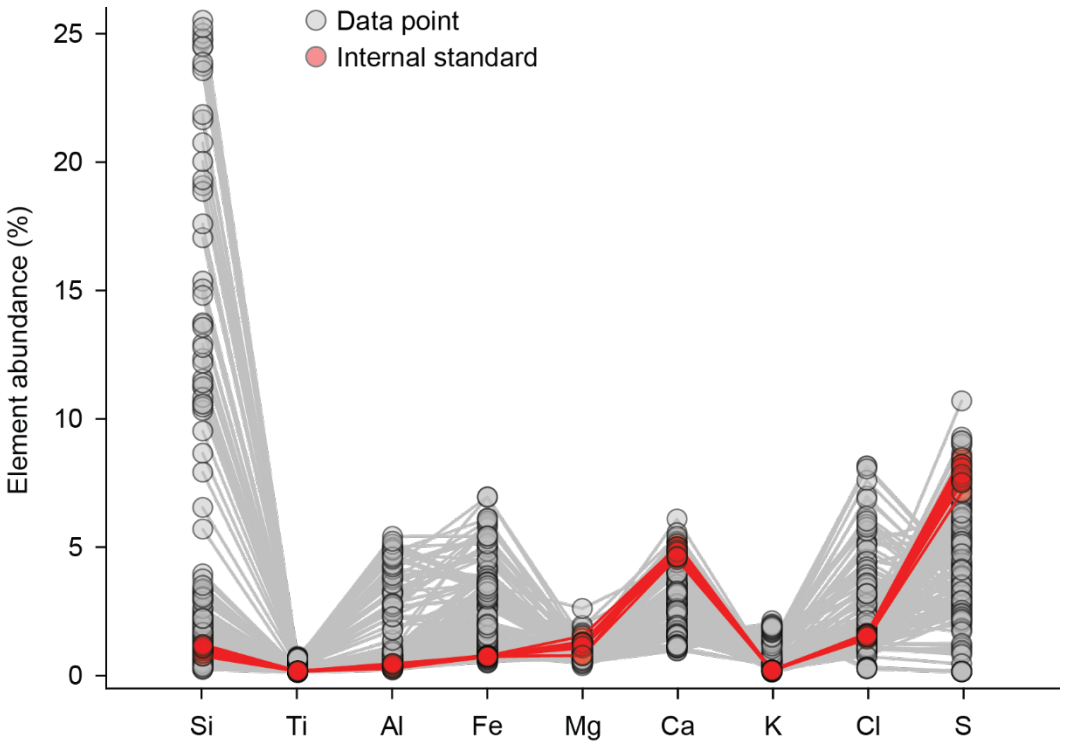

Figure D.2: Repeated analyses of the XRF internal standard plotted (HP_14) plotted against data points taken at one centimetre intervals throughout the Hooker's Point sequence.

Appendix D

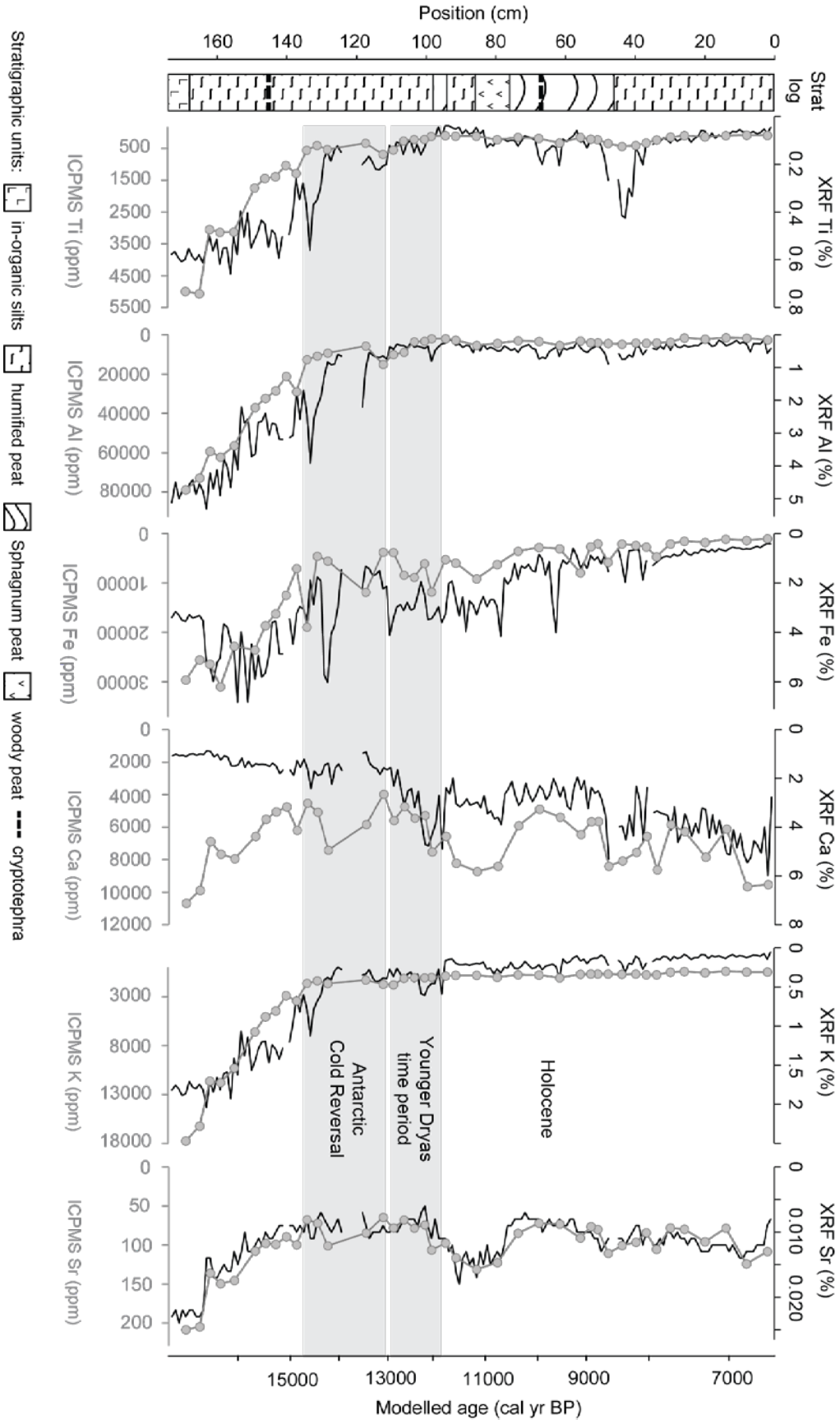

Figure D.3: ICPMS and XRF analyses from Hooker's Point plotted against each other and the plant macrofossil stratigraphy from Scaife *et al*., (2019).

Appendix E The palaeoecology of Hooker's Point

Appendix E includes the accepted paper:

Scaife, R.G., Long, A.J., **Monteath, A.J.,** Hughes, P.D.M., Bentley, M., Stone, P. 2019. The Falkland Islands palaeoecological response to millennial scale climate perturbations during the Pleistocene-Holocene transition: implications for future vegetation stability in Southern Ocean islands. Journal of Quaternary Science. DOI: 10.1002/jqs.3150.

This paper includes data generated during this thesis, and provides palaeoecological interpretation for Paper IV.

JOURNAL OF QUATERNARY SCIENCE (2019) 1–12 ISSN 0267-8179. DOI: 10.1002/jqs.3150

JQS Journal of Quaternary Science QRA Quaternary Research Association

The Falkland Islands' palaeoecological response to millennial-scale climate perturbations during the Pleistocene–Holocene transition: Implications for future vegetation stability in the southern ocean islands

ROBERT G. SCAIFE,[1] ANTONY J. LONG,[2] ALISTAIR J. MONTEATH,[1]* PAUL D. M. HUGHES,[1] MICHAEL J. BENTLEY[2] and PHILIP STONE[3,4]

[1]Geography and Environment, University of Southampton, UK
[2]Department of Geography, Durham University, UK
[3]British Geological Survey, The Lyell Centre Edinburgh, UK
[4]Falkland Islands Department of Mineral Resources, Stanley, Falkland Islands

Received 13 March 2019; Revised 11 September 2019; Accepted 16 September 2019

ABSTRACT: Oceanic island flora is vulnerable to future climate warming, which is likely to promote changes in vegetation composition, and invasion of non-native species. Sub-Antarctic islands are predicted to experience rapid warming during the next century; therefore, establishing trajectories of change in vegetation communities is essential for developing conservation strategies to preserve biological diversity. We present a Late-glacial–early Holocene (16 500–6450 cal a BP) palaeoecological record from Hooker's Point, Falkland Islands (Islas Malvinas), South Atlantic. This period spans the Pleistocene–Holocene transition, providing insight into biological responses to abrupt climate change. Pollen and plant macrofossil records appear insensitive to climatic cooling during the Late-glacial, but undergo rapid turnover in response to regional warming. The absence of trees throughout the Late-glacial–early Holocene enables the recognition of far-travelled pollen from southern South America. The first occurrence of *Nothofagus* (southern beech) may reflect changes in the strength and/or position of the Southern Westerly Wind Belt during the Late-glacial period. Peat inception and accumulation at Hooker's Point is likely to be promoted by the recalcitrant litter of wind-adapted flora. This recalcitrant litter helps to explain widespread peatland development in a comparatively dry environment, and suggests that wind-adapted peatlands can remain carbon sinks even under low precipitation regimes.

KEYWORDS: Falkland Islands; island conservation; palaeoecology; peatland; Southern Westerly Wind Belt

Introduction

Vegetation communities on small oceanic islands are particularly vulnerable to future climate change because of their often-restricted biological diversity, specialised adaptations and limited habitat availability, which impedes species ability to shift ranges (Nurse *et al.*, 2014; Harter *et al.*, 2015). Antarctic and sub-Antarctic islands in the southern oceans are expected to experience rapid temperature rises during the next century (Larsen *et al.*, 2014), and native plant taxa are likely to face increased competition from invasive species as habitats become suitable for a new range of flora (Hellmann *et al.*, 2008; Walther *et al.*, 2009; Thalmann *et al.*, 2015). Understanding the trajectory of change in vegetation communities in these islands is, therefore, essential for developing strategies for future conservation.

The Falkland Islands (Islas Malvinas) archipelago lies north of the polar front within the core of the Southern Westerly Wind Belt (49–53 °S). The islands are an unusual example of a treeless maritime environment which supports rare and endemic plant species (Upson and Lewis, 2014). During the last century, annual mean temperatures have increased by 0.5 °C in Stanley, East Falkland (Lister and Jones, 2015), and are predicted to rise a further 1.8 (±0.34) °C by 2080 (Jones *et al.*, 2013). This warming is likely to lead to decreased soil moisture (Bokhorst *et al.*, 2007) and alter plant distributions across the islands, with limited refugium availability in upland areas (Upson *et al.*, 2016). These projected temperature rises will also affect peatland ecosystems which are extensive in the Falkland Islands. In the northern hemisphere, peatland vegetation succession has been shown to occur rapidly in response to climatic changes (Barber *et al.*, 1994; Hughes *et al.*, 2006; Roland *et al.*, 2014), and is highly sensitive to changes in effective precipitation. The contemporary peatlands of the Falkland Islands exist in what are now marginal conditions for peat accumulation because of limited precipitation, and it is unclear whether these ecological systems are sensitive to changes in temperature or atmospheric moisture availability. Understanding the response of these peatlands to past and future climate variability is therefore important for the conservation of peatland vegetation (and carbon reservoirs) in the Falkland Islands.

Palaeoecology provides an important means to investigate: i) ecosystem resilience, ii) rates of environmental change, and iii) threshold responses; and iv) to test predictions of future vegetation turnover (Mauquoy and Yeloff, 2008; Willis *et al.*, 2010; Nogué *et al.*, 2017). Here we present a Late-glacial–early Holocene (*c.*16 500–6450 cal a BP) palaeoecological record from Hooker's Point (51°42′S, 57°47′W), an exposed coastal peat cliff in East Falkland. This period encompasses the Pleistocene–Holocene transition, a period that was punctuated by both warm and cold millennial-scale climate events, including the Antarctic Cold Reversal (ACR) (14 700–13 000 yr BP), a cooling event widely expressed in

*Correspondence: A. J. Monteath, as above.
E-mail: Ali.monteath@soton.ac.uk

the Antarctic ice cores in Patagonia, and across the southern oceans (Kilian and Lamy, 2013; Pedro *et al.*, 2016). By examining the palaeoecological response to these climate events we aim to assess the potential responses of sub-Antarctic island vegetation to future climate change.

The absence of any higher arboreal or larger shrub vegetation in the Falkland Islands means that palaeo-records here allow the recognition of long distance pollen, including elements from the *Nothofagus* (southern beech) forests of southern South America, such as *Nothofagus* and *Drimys* (Barrow, 1978). Changes in the abundance of these South American pollen components have been used to infer Holocene changes in the strength and/or position of the Southern Westerly Wind Belt (Mayr *et al.*, 2007; Strother *et al.*, 2015; Turney *et al.*, 2016; Thomas *et al.*, 2018). However, this approach has never been applied to Late-glacial deposits in the southern oceans, a period during which the Southern Westerly Wind Belt is suggested to have been particularly dynamic (Moreno *et al.*, 2009, 2012; Vanneste *et al.*, 2015).

Regional setting – the Falkland Islands

Physical setting

The Falkland Islands (51–53°S, 57–61°W) lie about 540 km east of southern South America, in the South Atlantic Ocean (Fig. 1). The archipelago includes over 780 islands, but is dominated by the two largest – West Falkland and East Falkland. Several upland areas occur in excess of 500 m above sea level (a.s.l.); however, the archipelago is characterised by undulating lowlands that are vegetated by acid grassland communities, predominantly whitegrass (*Cortaderia pilosa*) (Davies and McAdam 1989). The underlying, geological setting of the Falkland Islands comprises dominantly Palaeozoic quartzites and sandstones (Aldiss and Edwards, 1999; Stone, 2016). Quaternary glaciation was limited, with small glaciers confined to the highest uplands. However, periglacial deposits and landforms are common across the islands (Wilson *et al.*, 2008).

The present maritime climate of the Falkland Islands is strongly influenced by the cool sea surface temperatures of the surrounding South Atlantic Ocean (annual temperature of *c.* 6 °C; Brandini *et al.*, 2000). Locally, these are controlled by the Falkland (Malvinas) Current, an extension of the northern part of the Antarctic Circumpolar Current. The islands' climate is cool and relatively dry with a narrow range of mean monthly (February 9.5 °C, July 3.8 °C) and mean annual (6.5 °C) temperatures (1987–2000 observations: Mount Pleasant Airport). Precipitation is low (*c.* 500–800 mm yr^{-1}), but evenly distributed throughout the year (Otley *et al.*, 2008; Lister and Jones, 2015). There is some evidence for climatic gradients across the islands; the western coasts of each island receive less precipitation than the eastern coasts (e.g. 430 mm yr^{-1} at West Point Island versus *c.* 600 mm yr^{-1} at Stanley) (Otley *et al.*, 2008). The Falkland Islands lie beneath the central jet of the Southern Westerly Wind Belt with high annual and monthly mean wind speeds (in the range of 6–9 ms^{-1}), which dominantly (74%) come from the sector 200–340° (Clark and Wilson, 1992; Upton and Shaw 2002; Lister and Jones, 2015). These strong winds carry little moisture due to the orographic effect of the Andes, and precipitation is linked with southerly and easterly airflow (Thomas *et al.*, 2018).

Contemporary vegetation and previous work on the palaeoecology of the South Atlantic Islands

Although the vegetation of the Falkland Islands is not as impoverished as the Antarctic islands, the flora is considerably

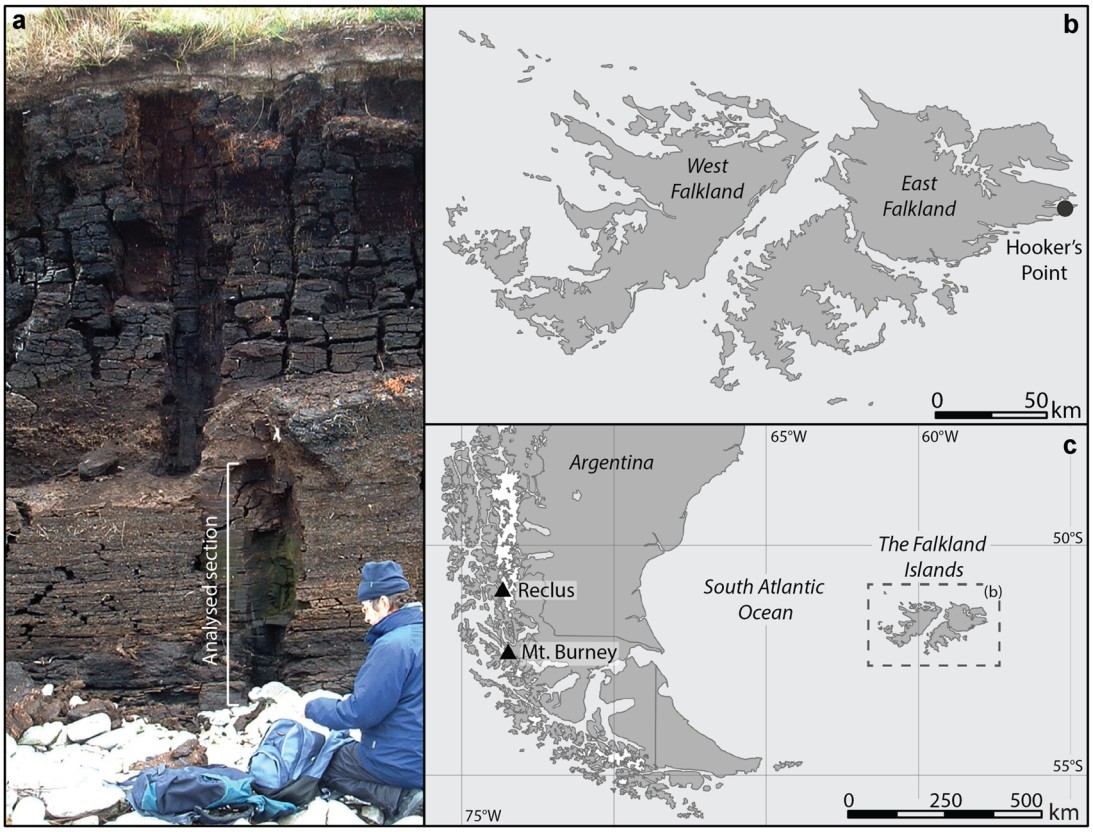

Figure 1. (a) The Hooker's Point peat section (post sampling) shown in relation to (b) the Falkland Islands, (c) southern South America and the volcanic sources (Mt. Burney ad Reclus Volcano) of cryptotephra deposits used to test the Hooker's Point age–depth model. [Color figure can be viewed at wileyonlinelibrary.com].

more restricted than Patagonia and Tierra del Fuego, with only 180 native taxa, including 14 endemic species (Upson and Lewis, 2014). Moore (1983) provides the most authoritative account of the flora and ecology of the South Atlantic islands, and this has been extensively used along with the pollen flora of Heusser (1971) and Barrow (1976) to ascertain possible pollen types and vegetation communities in this study. Other useful ecological flora are those of Moore (1968), Davies and McAdam (1989), Woods (2000) and Upson and Lewis (2014).

The present-day vegetation of coastal regions in the Falkland Islands is characterised by acid grassland, dominated by whitegrass (*Cortaderia pilosa*), and lesser occurrences of dwarf shrub heath. This latter community includes diddle-dee (*Empetrum rubrum*) with mountain berry (*Pernettya pumila),* teaberry (*Myrteola nummularia*) and Christmas bush (*Baccharis magellanica*). Ferns (*Blechnum penna-marina* and *B. magellanicum*) may be important in dry, well-drained areas, including areas of hard dry peat in the coastal zone. Tussac grass (*Poa flabellata*) was once common along the coastal fringe but is now heavily restricted through grazing pressure with an estimated loss of 80% of its range since the introduction of livestock in the 18th century (Otley *et al.*, 2008; Strange et al, 1988). Shallow peatlands occur in low-lying basins, and support communities of whitegrass. Deeper peats are characterised by cushions of *Astelia pumila* along with acidophilous plants such as sundew (*Drosera uniflora*) and, in locally waterlogged areas, *Scirpus* occurs occasionally with cushion grass (*Oreobolus obtusangulus*) and rare patches of bog moss (*Sphagnum*).

Prior to this study, there has been no continuous record of Late-glacial palaeoecology from the Falkland Islands. Barrow (1976, 1978) provides the first pollen data for the Falkland Islands (and South Georgia) and demonstrates a continuity of vegetation throughout the Holocene, and the absence of any higher arboreal or shrub vegetation. The tallest native shrubs are native box (*Hoebe elliptica*), fachine (*Chiliotrichum diffusum*) and the more recently introduced gorse (*Ulex europaea*). Further, mid–late Holocene pollen data are reported by Turney *et al.* (2016) and Thomas *et al.* (2018), while Clark *et al.* (1998) describe the palynology of thin organic horizons with ages of 36 000 to 28 000 ^{14}C yr BP. These organic lenses from Plaza Creek, East Falkland, are interbedded between mass wasting and periglacial deposits and show a grass-steppe environment. The vegetation assemblage throughout the analysed section was remarkably constant, which led Clark *et al.* (1998) to suggest that either there was little change in the environment during the period of sediment accretion or that the assemblage was insensitive to climatic change.

Hooker's Point, East Falkland section

Hooker's Point lies 3.5 km east of Stanley (Fig. 1) and was named after the eminent botanist Sir Joseph Hooker, who visited the Falkland Islands in 1842 as a member of the *Erebus* and Terror Antarctic expedition, led by James Clark Ross. The Hooker's Point peat section (51°42'S, 57°47'W) is a vertical exposure of peat lying immediately behind a small boulder beach, adjacent to Hooker's Point (Fig. 1). The peat overlies grey silt that is located close to rounded beach cobbles that comprise the upper levels of the active beach. The section extends from around 3 m a.s.l. to the present clifftop at around 8 m a.s.l. The Hooker's Point sequence is exposed by eroding wave action and must have formed part of a larger peatland system in the past. Relative sea level around the Falkland Islands reached levels close to present between *c.* 8400 yr BP and *c.* 7000 yr BP (Newton *et al.*, 2014), and therefore, Hooker's Point must have either been partially protected from erosion or have experienced significant shoreline retreat. At the time of sampling, active erosion had created a bench approximately one third of the way up the peat face (Fig. 1). The entire profile was sampled in February 2005 using a series of overlapping 50 cm and 25 cm monolith tins, which were pushed into a cleaned section face and excavated using a spade. Here, we describe the palaeoecology of the lowermost 168 cm of peat from the monolith-sampled sequence (Figs. 1,2).

Materials and methods

Chronology

Eight samples were dated using accelerator mass spectrometer radiocarbon dating (AMS ^{14}C dating): four bulk peat samples, three macrofossil samples and one wood fragment (Table 1). The plant macrofossil remains comprised at least 300 mg wet weight of the above-ground remains from higher plants. Where presence allowed, the stems of *Sphagnum* were preferred as these are representative of *in situ* peat surface. In all cases, plant macrofossils were repeatedly washed in deionised water and cleaned of all fungal hyphae and rootlet material before AMS ^{14}C dating.

A Bayesian age–depth model (Fig. 2) was developed from eight AMS ^{14}C dates using OxCal 4.2.3 (Bronk Ramsey, 2017), and the SHCal13 calibration curve (Hogg *et al.,* 2013). A *P_Sequence* depositional model was run with outlier detection (Bronk Ramsey 2008, 2009a) and a variable *k* factor (depositional events per unit length: cm^{-1}) (Bronk Ramsey and Lee, 2013). One radiocarbon date (Beta-241336) suggests a slight age reversal. This, however, did not reduce the overall model agreement to <60%, and so was retained in the final age–depth model (Bronk Ramsey, 2009b). The final age–depth model was validated against the published age ranges for the Reclus R_1 and Mt. Burney MB_1 ash beds (Fig. 2), which were identified as cryptotephra deposits at Hooker's Point by Monteath *et al.* (2019). Calibrated dates and age ranges are reported at two sigma (95.4%) confidence throughout this study.

Plant macrofossil analysis

Sub-samples of peat measuring 4 cm^3 were prepared for macrofossil analysis by gently heating samples in 4% KOH solution for 10 minutes, before sieving through a 125 μm mesh with a standardised 5 L volume of water. The disaggregated macrofossil remains were examined at x40 to x150 magnification using a dissecting microscope. Identifications of *Sphagnum* branch leaves and monocotyledon epidermal tissues were made at x200 to x400 magnification using transmitted-light microscopy. Plant identifications were checked against the archive collection of fossil and modern type-samples held in the Palaeoecology Laboratory, University of Southampton. Identifications were also made with reference to Davies and McAdam (1989) and Woods (2000) for flowering plants native to the Falkland Islands, and Daniels and Eddy (1990) for *Sphagnum* mosses. Plant macrofossil abundance was assessed using the quadrat and leaf count method of Barber *et al.* (1994) for the main vegetative remains of the peat matrix, and a five-point scale of abundance (Walker and Walker, 1961), where 1 = rare, 2 = occasional, 3 = frequent, 4 = very frequent, 5 = abundant, for fruits, seeds and other small macrofossils. The macrofossil diagram (Fig. 3) was divided into six local plant macrofossil zones (LPMZs) using CONISS in TILIA software (Grimm, 1991).

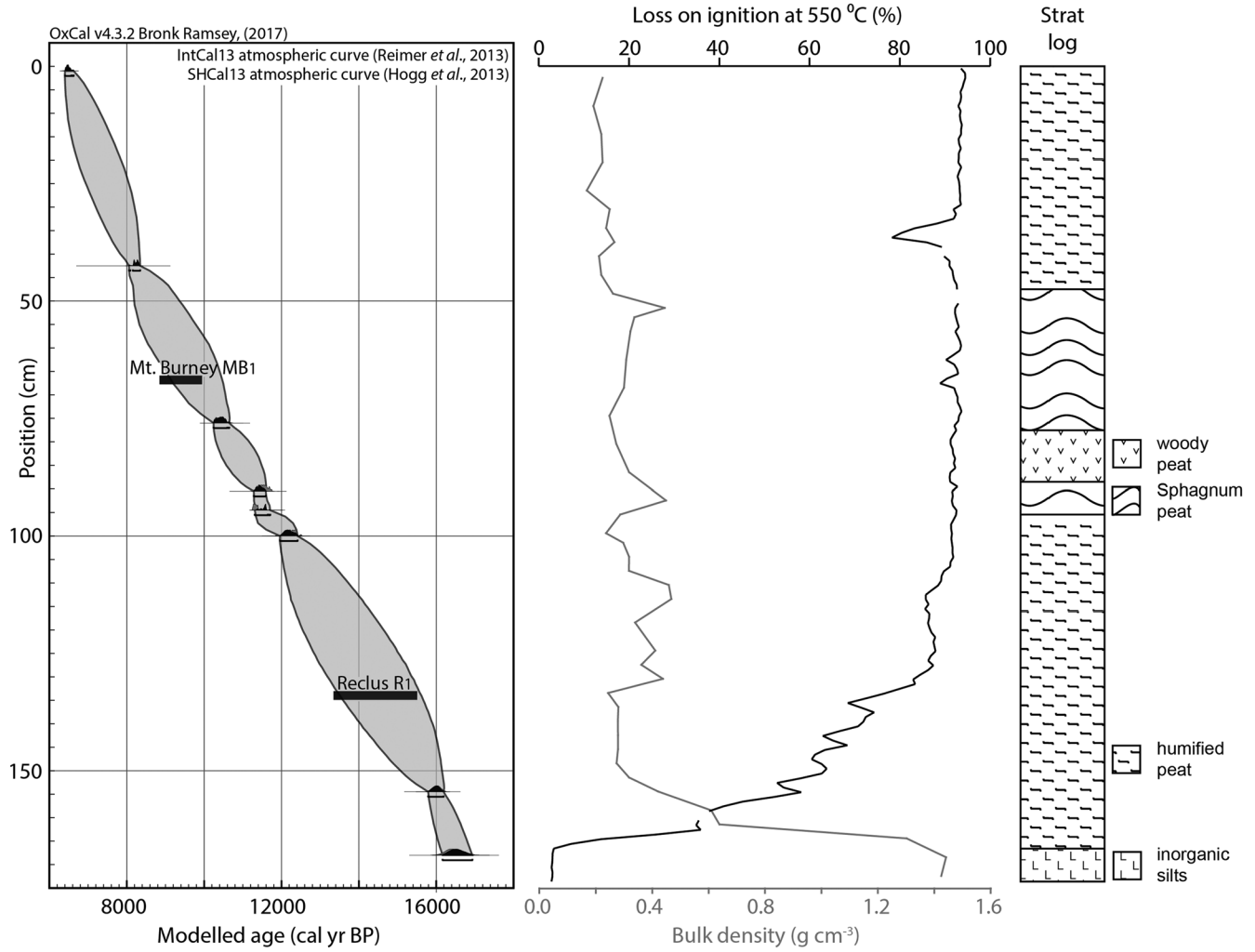

Figure 2. Oxcal age–depth model, loss on ignition values and bulk density data from the Hooker's Point sequence. The published age ranges for the Mt. Burney MB_1 (9950–8850 cal a BP; Stern, 2008) and Reclus R_1 (15 510–14 350 cal a BP; McCulloch *et al.,* 2005) tephra beds are shown as black bars. The position of these cryptotephra deposits in the Hooker's Point sequence are taken from Monteath *et al.* (2019). Bulk density measurements were made from measured 1 cm^3 peat samples.

Pollen analysis

Fifty-two pollen sub-samples taken at sampling intervals of 2 or 4 cm were prepared using standard techniques for the extraction of sub-fossil pollen and spores (Moore *et al.,* 1991). Initially, 10% KOH was used to deflocculate the samples which were sieved (150 µm) to remove coarse organic and inorganic debris. Clay and fine silt was removed using sieving at 10 µm. Hydrofluoric acid (40%vol.) was used to remove any remaining coarser, siliceous material. Samples were acetolysed for removal of plant cellulose and the concentrated pollen was stained using safranine and mounted in glycerol jelly on microscope slides. Pollen counts of 300 land pollen grains were made where possible and pollen frequencies were calculated as a percentage of total land pollen. The pollen diagram (Fig. 4) was divided into six local pollen assemblage zones (LPAZs) based on changes in the major taxa.

Diatom analysis

Samples from the basal 40 cm of the Hooker's Point sequence were examined by Prof. V. Jones (University College, London) for the presence of diatom frustules. The preparation of these samples followed standard protocols for siliceous microfossils (Battarbee *et al.,* 2001).

Table 1. Radiocarbon dates from the Hooker's Point sediment sequence with calibrated two sigma age ranges. Ages were calibrated using OxCal 4.2.3 (Bronk Ramsey, 2017), and the SHCal13 calibration curve (Hogg *et al.,* 2013).

Laboratory ID Code	Material	Position (cm)	Radiocarbon age ($^{14}C \pm 1$ SD yr BP)	13δC (‰)	Calibrated age range (cal a BP) (95.4%)
Beta-193400	Bulk (peat)	0–2	5700±40	−27.0	6628–6405
Beta-241334	Plant Macro	42–43	7390±40	−29.7	8341–8055
Beta-193401	Bulk (peat)	76	9250±80	−26.7	10650–10241
Beta-241335	Plant Macro	90–91	10030±40	−25.0	11749–11330
Beta-241336	Wood	94–95	9940±40	−27.0	11602–11242
Beta-193402	Bulk (peat)	100	10370±60	−27.3	12517–12000
Beta-241338	Plant Macro	154–155	13320±50	−27.1	16217–15822
Beta-193403	Bulk (peat)	168	13630±140	−27.7	16923–16055

Results and interpretation

Chronology

The chronology from the Hooker's Point sequence spans the Late-glacial–early Holocene (*c.*16 500–6450 cal a BP), including the interval of the Antarctic Cold Reversal (14 700–13 000 yr BP). The age–depth model shows close agreement with the published ages of the Mt. Burney MB_1 and Reclus R_1 tephra beds (Fig. 2), and suggests a near constant sedimentation rate throughout the analysed section. The date for earliest peat accumulation at Hooker's Point (*c.* 16 500 cal a BP) is close to that of 13 475 ± 50 BP (calibrated weighted mean:16 160 cal a BP) for the onset of peat growth at Lake Sulivan in West Falkland (Wilson *et al.,* 2002).

Plant macrofossil and pollen data

The results of the palaeoecological analyses from Hooker's Point are presented here and are divided into six vegetation zones based on changes in species abundance. Plant macrofossil data are described in Fig. 3 and Table 2, which are subdivided as LPMZs. The results of the pollen analysis are presented in Fig. 4 and Table 3 which are split into six LPAZs.

Synthesis of palaeoecological evidence from Hooker's Point

Changes in the pollen and plant macrofossil assemblages from the Hooker's Point peat sequence occur at similar points (allowing for slight sampling differences), and six principal phases of vegetation history are recognised between *c.* 16 500 cal a BP and *c.* 6450 cal a BP.

Phase one (pre-16 500 cal a BP) (174–168 cm)

The basal fine-grained (silt and sand) minerogenic sediments contain no pollen or plant macrofossils. The sediment is well sorted, lacks any coarser debris bands indicative of in-wash, and grades upwards sharply into a well humified peat at the boundary with phase two. The diatom assemblage from a sample taken at 172 cm includes aerophilous species (*Hanzschia amphioxys*, *Navicula mutica* and *Pinnularia borealis*), as well as species more characteristic of freshwater (*Brachysira* spp., *Navicula* spp. and *Diploneis* spp.) (Viv Jones, pers coms, 2011). We interpret the original depositional environment as a low-energy, freshwater, shallow-water body that formed under cold conditions at the time of the Last Glacial Maximum.

Phase two (16 500–15 940 cal a BP) (168–154 cm)

Phase two is characterised by the onset of organic accumulation and an amelioration of climate compared with phase one. The diatom assemblage (160 cm) is largely composed of aerophilous species (*Hanzschia amphioxys*, *Navicula mutica* and *Pinnularia borealis*) with additional freshwater taxa (*Amphora veneta*, *Pinnularia* spp., *Navicula* spp.) (Viv Jones, pers coms, 2011).The pollen in LPAZ-1 is dominated by Poaceae with lesser, but significant, numbers of Cyperaceae and Chenopodiaceae. There are woody lignified roots and leaves of *Empetrum* in the lower section of the peat, indicating on-site dwarf shrub development that is not represented in the pollen data, possibly because conditions were too harsh to allow flowering and pollination of these taxa. The low frequencies of Chenopodiaceae and occasional *Armeria*-type pollen grains suggest an arid, cold, steppe environment.

The onset of peat accumulation during phase two is likely to be associated with regional climatic warming beginning *c.* 17 500 cal a BP, coupled with a reduction in the west–east precipitation gradient as the Patagonian ice sheet retreated (McCulloch *et al.*, 2005; Pedro *et al.*, 2011). Organic accumulation, in response to these changes, must have occurred because of an increase in moisture availability and/or temperature. This may have only required a small climatic shift to step across a threshold to tip the accumulation/decay balance towards organic accumulation (Moore and Bellamy, 1974). The earliest phase of peat initiation in de-glaciated

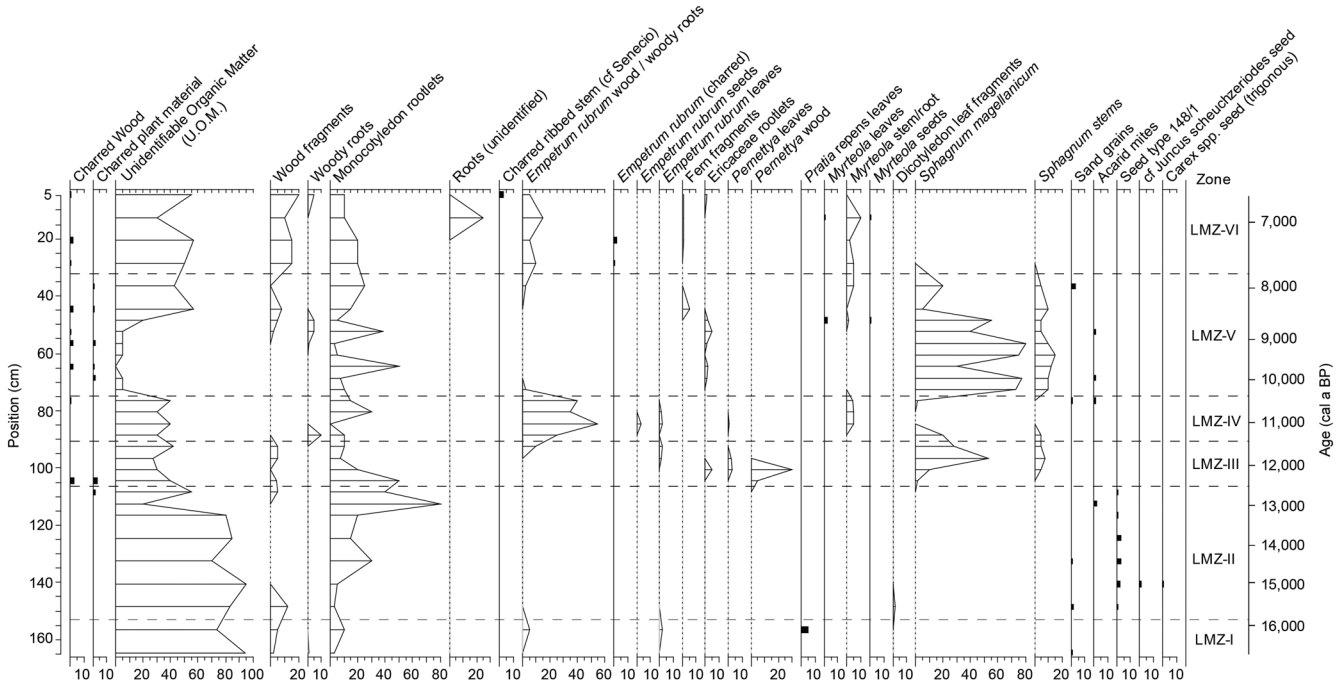

Figure 3. Plant macrofossil profile from the Hooker's Point sequence showing selected taxa. Small macrofossil remains are displayed as unlinked histograms on a scale from 1 (rare) to 5 (abundant). The main peat constituents are quantified as percentage cover of a grid graticule (Barber *et al.,* 1994) and appear as linked histograms.

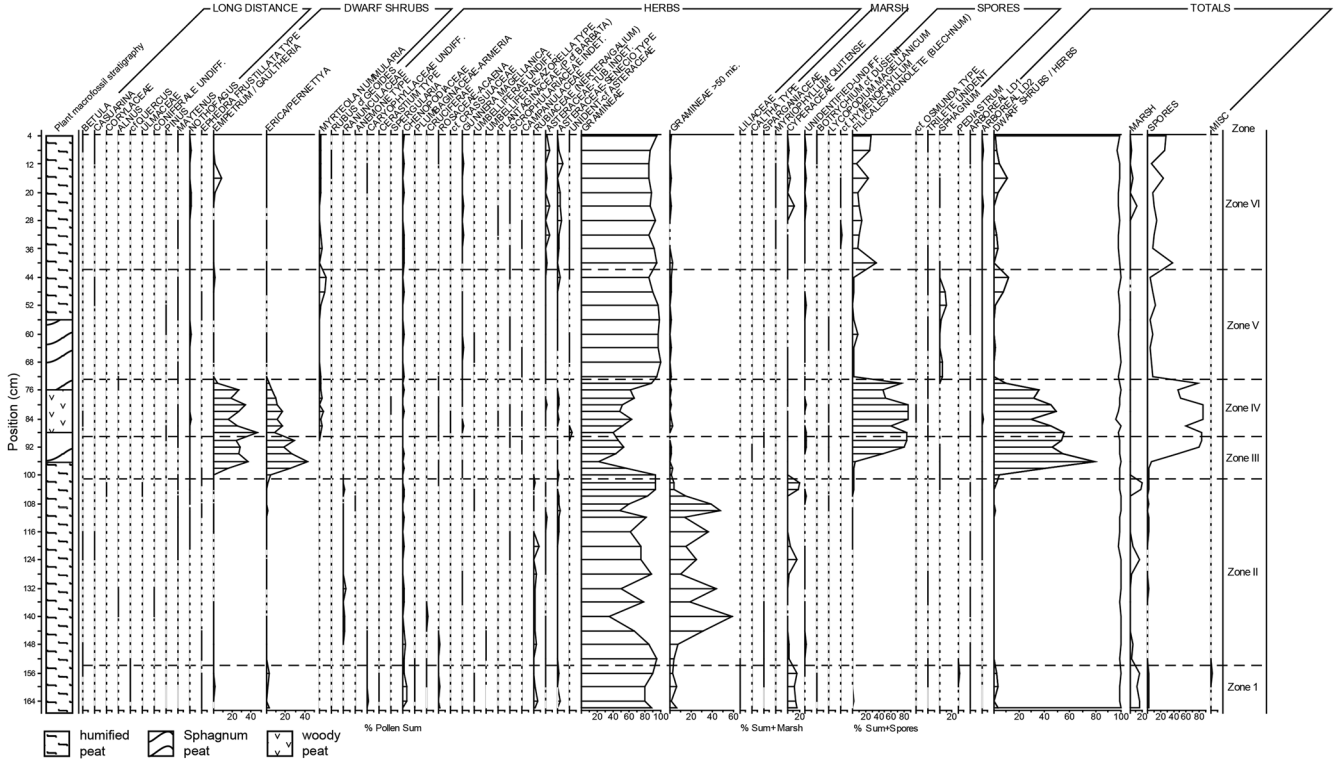

Figure 4. Pollen profile from the Hooker's Point sequence.

regions of Patagonia occurs *c.* 17 000 BP, and is associated with a rise in summer temperatures (Morris *et al.,* 2018).

Phase three (15 940–12 200 cal a BP) (154–101 cm)

Cyperaceae pollen frequencies decline, suggesting a drier local environment than phase two. The pollen assemblage (LPAZ-II) remains dominated by Poaceae and indicates a persistent cold climate, with a locally damp environment surrounded by open grass steppe. A lack of woody macrofossil remains suggests that it was not sufficiently dry to allow heath to become established on site. At *c.* 15 300 cal a BP, there is a sharp increase in the frequencies of a specific grass type of large (>50 μm) size (Poaceae 2) which persists in high values until *c.* 12 690 yr BP, after which they decline. Such large grains (outside of cereal varieties) come from a small number of genera/species (e.g. *Glyceria* and species of a halophytic tendency, including *Elymus*). From data by Barrow (1976), it appears that the Poaceae type 2 grains here are not from *Poa flabellata*, which has a size range of 27–33 μm on the polar axis. Groff (2018) has also noted that *P. flabellata* pollen is not distinguishable from the other grass taxa. However, Graff's measurements include *Elymus magellanicus* (Magellan wheatgrass) which has a size range to 37 μm on the polar axis. These

Table 2. Description of the plant macrofossil content of the Hooker's Point sequence.

Macrofossil zone (position in cm)	Description of the macrofossil content
LPMZ-VI 36–4 cm	Humification increases and the percentage of unidentified organic matter (UOM) remains high, peaking at 57%. Wood fragments dominate, many of which are *Empetrum rubrum*. Fern fragments, monocotyledon rootlets, charred plant remains and *Myrteola nummularia* stems/leaves are also present in the zone.
LPMZ-V 76–36 cm	*Sphagnum magellanicum* remains dominate the lower part of zone V but decline to 20% of the assemblage at 36–37 cm depth. Both monocotyledon rootlets and UOM are poorly represented in the lower part of the zone but increase in importance as the proportion of *Sphagnum* declines. Charcoal and charred leaf fragments occur in most samples. Other macrofossils include Acarid mites and the stems/roots of *Myrteola nummularia*. The top of the zone is marked by the disappearance of *S. magellanicum* which coincides with a sand deposition event.
LPMZ-IV 92–76 cm	*Sphagnum magellanicum* is replaced by the abundant remains of *Empetrum rubrum*, which include the wood, roots, leaves and seeds. The assemblage includes rare leaf fragments of *P. pumila* and the stems of *Myrteola nummularia*. UOM remains at 40% throughout the zone.
LPMZ-III 108–92 cm	This zone is defined by the arrival of *Sphagnum magellanicum* and *Pernettya pumila*. Good macrofossil preservation is shown by the survival of whole *P. pumila* and *Empetrum rubrum* leaves. *S. magellanicum* peaks at 33% of the macrofossil assemblage at the upper zone boundary.
LPMZ-II 156–108 cm	*Carex* and *Juncus* propagules are present together with an increased diversity of other herb taxa. Peat humification remains high. Monocotyledon rootlets increase in occurrence through the zone to a peak of 40% at the upper boundary. Evidence for sand deposition is also present at 132 cm and 148 cm depth. Charred plant material is present at the upper zone boundary at 108–109 cm depth.
LPMZ-I 164–156 cm	Fragments of *Pratia repens* leaf are present together with *Empetrum rubrum* leaves. Macrofossils are strongly humified and mainly composed of UOM and monocotyledon rootlets.

Table 3. Pollen zonation of the Hooker's Point profile.

Pollen zone (position in cm)	Palynological characteristics
LPAZ-VI 42–4 cm	Poaceae remain dominant (90–95%) with important Compositae types (Tubuliflorae indet. and *Senecio* type). *Gunnera magellanica* is consistent (1–2%). Cyperaceae increases in importance mid-zone (from 24 cm) with small numbers of *Myriophyllum cf. quitensis*. Spores of *Blechnum* type again become important with occasional *Hymenophyllum*. Long-distance pollen types recorded include *Nothofagus* and sporadic occurrences of *Meytenus*.
LAPZ-V 73–42 cm	Dwarf shrubs of zone IV reduce to absence. *Myrteola*, however, peaks at 38–40 cm (*c.* 8%). Poaceae attains its highest values (95%). Compositae types become important with Tubuliflorae indet. and *Senecio* type. *Blechnum* spores also diminish to low levels. *Sphagnum* is important in this zone with two separate peaks at *c.* 72 cm and *c.* 50 cm. Long-distance pollen types *Nothofagus* and *Meytenus* are present.
LPAZ-IV 89–73 cm	*Pernettya* declines progressively to low levels. *Empetrum* remains high but declines steeply at the top of the zone. *Myrteola nummularia* is incoming from the base of this zone and *Gunnera magellanica* becomes consistent. Poaceae type 2 (>50 μm) of the preceding zone declines to only occasional occurrences.
LPAZ-III 101–89 cm	Dwarf shrubs expand sharply with *Empetrum/Gaultheria* (45%) and *Pernettya* (45%) followed closely by *Blechnum* (to 90% sum+spores). Poaceae remain important but with reduced values (30%). *Nothofagus* is consistent in this zone at 1–2%. *Maytenus* is absent.
LPAZ-II 154–101 cm	Poaceae type 1 (<50 μm) (to 90%) is dominant with Poaceae type 2 (>50 μm; expanding to 45% declining to <10% at top of zone). There are two small peaks of Cyperaceae (to 20%) at 120 cm and 104 cm. Ranunculaceae are present only in this zone, Chenopodiaceae remain consistent but at reduced levels. Rubiaceae (to 5%) are absent at the top of the zone. The near-continental long-distance pollen types appear at 124 cm with *Maytenus* and *Nothofagus*.
LPAZ-I 168–154 cm	Poaceae are dominant (to 90%) with Cyperaceae (19%). Chenopodiaceae (*cf. Colobanthus*), *Erica/Pernettya* (1–2%), *Ephedra frustillata* and Rubiaceae (4%) represent. Algal *Pediastrum* are present.

grains were mounted in silicone oil, whereas here, glycerol was used and would account for the greater size. Thus, we tentatively attribute Poaceae type 2 to this species. This accords with the coastal distribution of this grass. We do not attribute any palaeoclimate significance to the change in Poaceae frequencies during this interval; however, a more detailed resolution of this taxon is being sought. Long-distance pollen types *Nothofagus* and *Maytenus* first appear in the Hooker's Point sequence during this period (*c.* 13 260 cal a BP).

Phase four (12 200–10 250 cal a BP) (101–73 cm)

The start of phase four saw the onset of a change towards wetter local conditions at Hooker's Point. However, these soon become drier as *Sphagnum. magellanicum* was replaced by *Empetrum rubrum c.* 11 330 cal a BP. Most importantly was the progressive establishment and maturation of a dwarf shrub and fern community. Macrofossil remains of dwarf shrub and ericaceous plants are common and the peat contains larger numbers of fungal hyphae. Initially, *Pernettya* started to expand followed closely by *Empetrum/Gaultheria.* The former is likely to be the evergreen shrub *Pernettya pumila* since abundant (30%) macrofossils of this species occur at this level (Fig. 3). Subsequently, ferns (*Blechnum* spp.) became dominant. This habitat change is also reflected by a substantial reduction in Poaceae and a decline to almost absence of Poaceae type 2. The former may, however, be a within (pollen) sum percentage reduction caused by the expansion of dwarf shrubs. *Sphagnum* spores occur in low frequencies in the pollen record and there are abundant macrofossil remains of *S. magellanicum* throughout this zone. This phase also saw the appearance of *Myrteola nummularia* (teaberry) which is recorded consistently throughout the upper part of the section and in today's vegetation assemblage at the sample site. Its appearance at the start of the Holocene may reflect a change in climate at this time.

Phase five (10 250–8210 cal a BP) (73–42 cm)

This phase records the second shift to wetter conditions recorded at Hooker's Point. The dry ericaceous and fern community was replaced, at least locally, by the development of *Sphagnum* peat. Despite this change, there is clear evidence (charred macrofossils) for repeated burning on the site. *Empetrum rubrum* is resinous and will burn even when damp and, although some of the burning is linked to periods of *Empetrum* heath development, there is also evidence for burning during the *S. magellanicum* bog phase. Similar burning episodes are known from early Holocene peat bogs on West Falkland (Barrow 1978) and in southern South America (Heusser, 1989; Whitlock *et al.,* 2007; Moreno *et al.*, 2018), where they have been attributed to increased aridity and changes in the position of the Southern Westerly Wind Belt. The initial wet shift is followed by a trend towards drier conditions as *Sphagnum* macrofossil frequencies decline and ericaceous communities (notably *Myrteola*) become re-established on site.

Phase six (8210–6450 cal a BP) (42–0 cm)

This period saw the establishment of drier conditions at Hooker's Point, indicated by a decrease in the abundance of *Sphagnum* remains, an increase in unidentified organic matter and Filicales macro-remains, as well as Poaceae and *Myrteola* pollen frequencies.

Discussion

Late-glacial–early Holocene environmental change in the Falkland Islands

The Hooker's Point record demonstrates the persistence of a treeless environment throughout the Late-glacial–early Holocene. Together with Holocene pollen studies (Barrow, 1976, 1978; Turney *et al.*, 2016; Thomas *et al.*, 2018), this record shows that the Falkland Islands have not supported any higher arboreal or large shrub vegetation for at least the last *c.* 16 500 years. While vegetation communities within this environment do appear sensitive to climatic change, the changes in floral composition are subtle relative to those that took place in the northern hemisphere during the time period spanned by the Hooker's Point sequence. It is likely that a combination of continued high wind speeds and shallow soil depths prevented

the establishment of trees in the archipelago, regardless of changes in temperature or precipitation.

The origins of peat accumulation in the Falkland Islands

Peatlands in the Falkland Islands, including Hooker's Point, developed at the edge of the climatic envelope for global peat initiation because of the low annual precipitation (Morris *et al.*, 2018). Despite this, peatlands are extensive across the archipelago, and in some coastal locations (e.g. Beauchêne Island) may form 'extraordinary' sequences exceeding 11 m in depth, characterised by extremely high carbon density (Smith and Clymo, 1984; Evans *et al.*, 2019). We hypothesise that peat accumulation in the Falkland Islands is promoted by the recalcitrant litter quality of the native grass communities, evident in the Hooker's Point macrofossil assemblage (Fig. 3). Species within these communities, such as *Cortaderia pilosa* (whitegrass) and *Poa alopecurus* (bluegrass), are adapted to low nutrient soils and high wind speeds, so produce leaves with thick, fibrous, epidermal layers that are highly resistant to decay (Davies *et al.*, 1990). While whitegrass is dominant in the contemporary setting, bluegrass was far more extensive prior to human disturbance, and was described as 'so harsh and rigid as to be quite unpalatable to cattle' by Hooker (1847). The durable litter produced by these grasses provides a means to tip a catchment balance towards organic accumulation in what would otherwise be a marginal environment for peatland development. Studies of Holocene raised peat accumulation (just after the fen-bog transition) in Europe have also shown that similar litter accumulation processes operated in the northern hemisphere, where peat accumulation following the fen-bog transition often occurred in dry climatic phases during the early to mid-Holocene. In these cases *Eriophorum vaginatum* builds a 'foundation' stratum of highly humified peat. This deposition seems to have been instrumental in providing suitable semi-permeable strata for later development of the domed water tables of Atlantic raised bogs under more humid climatic conditions. (Hughes *et al.*, 2000; Hughes and Barber, 2004).

Due to the comparatively dry climate, peatlands in the Falkland Islands are assumed to be relic systems that formed in the past under wetter conditions (Otley *et al.*, 2008). However, Hooker's Point continued to accumulate organic material at a near linear rate throughout millennial-scale climate perturbations during the Late-glacial, when climate is likely to have been at least as dry as present conditions (Fig. 2). This suggests that peatlands in the Falkland Islands may be continuing to accumulate organic matter, and importantly carbon, under the present climate. Payne *et al.* (2019) report highly variable carbon accumulation rates in Falkland Island peatlands, which suggests that peat systems in the archipelago are affected by a range of drivers; for example, climate change, mineral input, guano input and burning. The study of peatland palaeoecology in drier, marginal, environments such as the Falkland Islands has implications for modelled projections of peatland persistence under different future climate change scenarios (e.g. Ise *et al.*, 2008; Gallego-Sala and Prentice, 2013). In these modelling experiments, continued peat accumulation is often assumed to be dependent on a permanently high water table. However, pollen and plant macrofossil evidence from the Hooker's Point sequence suggests that peat accumulation can continue in comparatively dry environments, where peatland water tables may be low, if the local vegetation is decay-resistant.

Falkland Islands vegetation – climate sensitivity

The Hooker's Point pollen and plant macrofossil records are insensitive to regional cooling during the ACR (14 700–13 000 yr BP), which is widely expressed across the southern hemisphere, and which would have affected the Falkland Islands (Pedro *et al.*, 2016). Glacier, oceanic and terrestrial records in southern South America record the declining temperatures during the ACR, and modelling simulations suggest that the Falkland Islands would have experienced a (0.5 °C) cooling and local drying (Pedro *et al.*, 2016). The apparent climatic insensitivity of the Hooker's Point palaeoecological record during this period suggests that conditions in the Falkland Islands prior to the ACR cooling were already too harsh for the establishment of thermophilous plant species. Instead, cold and wind-adapted grass taxa (e.g. *Cortaderia pilosa* in the contemporary setting) persisted almost throughout the Late-glacial period despite millennial-scale perturbations in climate, which are expressed in regional records (Pedro *et al.*, 2011; Kilian and Lamy, 2013). Conversely, the palaeoecological record from Hooker's Point demonstrates a dynamic vegetation assemblage between 12 200–8 000 cal a BP (Fig. 5), characterised by sharp shifts between wetter (*Sphagnum magellanicum*) and drier (*Erica*) indicators. Turnover between these species occurs during the latter half of the Younger Dryas time period (12 900–11 700 cal a BP) and the Southern Hemisphere Early Holocene Thermal Maximum (11 500–8500 yr BP). These time periods are associated with warming temperatures (Kilian and Lamy, 2013) and shifts in the latitudinal position and/or strength of the Southern Westerly Wind Belt (Vanneste *et al.*, 2015; Moreno *et al.*, 2018), which would have influenced precipitation in the Falkland Islands. These findings show that the flora of the Falkland Islands was sensitive to past climate change, in contrast to previous studies which suggested a stable, unresponsive, vegetation assemblage during the Late-glacial and Holocene (Barrow, 1976, 1978; Clarke *et al.*, 1998). Despite these changes, no new species became established at Hooker's Point during this period (with the exception of *Myrteola nummularia*), suggesting that invasive species remained unable to colonise the local environment despite the increasing temperature and moisture availability, indicated by increases in Ericaceae species and *Sphagnum magellanicum*. It is likely that the exclusion of invasive species is due to a combination of the high wind speeds affecting the archipelago, and its isolation, which limit the establishment of non-wind-adapted flora in the contemporary setting, and may continue to do so even under future climate warming.

Long-distance pollen and the Southern Westerly Wind Belt

The near-continental long-distance pollen component identified at Hooker's Point comprises *Nothofagus* (*N. antarctica, N. pumilla*) and *Maytenus*, which are sourced from southern Chile and Argentina. Similar findings are reported from Holocene records in the Falkland Islands and South Georgia (Barrow, 1978; Strother *et al.*, 2015; Turney *et al.*, 2016; Thomas *et al.*, 2018). Clark *et al.* (1998) also noted a low influx of arboreal pollen (<1%) (mainly of *Nothofagus*) in the Late Pleistocene (*c.* 26 000–36 000 cal a BP) sediments from East Falkland. Changes in the abundance of *Nothofagus* pollen delivered to eastern Patagonia and the Falkland Islands during the Holocene have been interpreted as wind-dependent (Mayr *et al.*, 2007; Turney *et al.*, 2016; Thomas *et al.*, 2018), and it is therefore likely that the first appearance of *Nothofagus* pollen in the Hooker's Point sequence is linked with a change in the

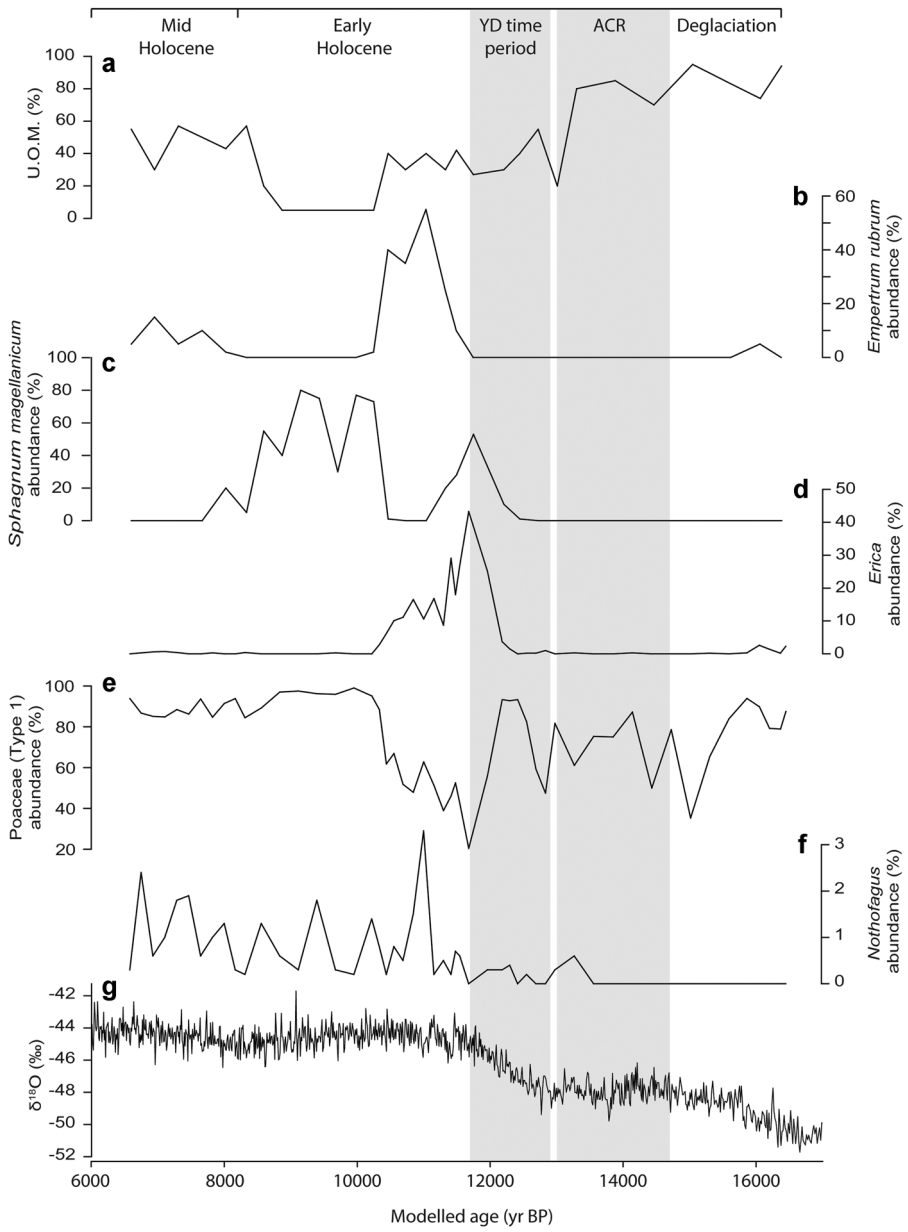

Figure 5. (a–f) Key pollen and plant macrofossil taxa from Hooker's Point plotted against age. (g) The EPICA Dome C $\delta^{18}O$ record (EPICA community members, 2006). YD=Younger Dryas, ACR=Antarctic Cold Reversal; UOM=unidentified organic matter.

strength and/or position of the Southern Westerly Wind Belt. The appearance of *Nothofagus* in Hooker's Point *c.* 13 330 cal a BP (Fig. 5) occurred late in the ACR and coincides with a shift in carbonate isotope values in Laguna Potrok Aike (13 400–11 300 cal a BP; Mayr *et al.,* 2013), and the expansion of *Nothofagus* near Lago Lynch (*c.* 13 300 cal a BP) (Tierra del Fuego) – also linked with a change in the Southern Westerly Wind Belt (Mansilla *et al.,* 2018).

A second 'extra-long-distance' pollen component is present at Hooker's Point which includes *Betula, Casuarina, Alnus,* Coryloid, *cf. Quercus,* Ulmaceae and *Pinus. Quercus* and *Betula* are the earliest extra-long-distance arboreal pollen arrivals with their first occurrences at *c.* 16 200 cal a BP and *c.* 15 860 cal a BP, respectively. Barrow (1978, 1983) also noted *Alnus* in sediment profiles from South Georgia which he suggested may have been a contaminant. However, similar rare occurrences are evident in pollen profiles from both sub-Antarctic islands (Hafsten, 1951; Cranwell, 1969; van der Knaap and van Leeuwen, 1993) and the Antarctic continent (Hafsten, 1951, 1960a, 1960b; Linskens *et al.,* (1991); Linskens *et al.,* 1993). These repeated records of extra-long-distance taxa may represent either: i) ultra-distal atmospheric pollen transport, or ii) contamination. Given the now frequent records, an extra-long-distance, northern hemispheric source for this pollen is plausible. However, replicated results from samples analysed in southern hemisphere control laboratories are needed to test both hypotheses.

Conclusions

The Hooker's Point sequence, in conjunction with Holocene pollen records (Barrow, 1976, 1978; Turney *et al.*, 2016; and Thomas *et al.*, 2018), show that the Falkland Islands have remained treeless for a least the last *c.* 16 500 years. The landscape of the Falkland Islands is, therefore, an unusual example of a maritime environment that has developed without trees and higher shrubs. This rare environmental history provides an interesting ecological control site that may be used for the study of fluvial development under temperate, treeless, conditions.

Peatlands in the Falkland Islands have previously been considered to be relic systems that formed during wetter conditions in the past (Otley *et al.*, 2008). However, continued organic accumulation at Hooker's Point throughout the Late-glacial demonstrates that Falkland Island peatlands have developed under dry conditions in the past, and may continue to do so today. This finding suggests that some peatlands in

marginal environments can remain valuable carbon sinks even under low precipitation regimes.

The vegetation of Hooker's Point appears insensitive to the regional cooling during the ACR, but shifted toward a dwarf shrub-dominated community during the latter half of the Younger Dryas time period and Southern Hemisphere Early Holocene Thermal Maximum. The decline of tussac grass dominance under warming has implications for future vegetation communities in the Falkland Islands which are expected to be subjected to a warmer climate.

The first appearance of long-distance *Nothofagus* pollen in the Hooker's Point sequence *c.* 13 330 cal a BP is likely to be wind-dependant, and occurs late in the ACR. This time period is associated with changes in the strength and/or position of the Southern Westerly Wind Belt, and shifts in wind proxies in Laguna Potrok Aike (Mayr *et al.,* 2013) and Tierra del Fuego (Mansilla *et al.,* 2018) closely overlap the *Nothofagus* pollen record from Hooker's Point.

Acknowledgements. We thank the Shackleton Scholarship Fund for a grant to enable fieldwork in the islands, as well as NE/1022981/1. We are grateful to the Falkland Islands Department of Mineral Resources who provided project support. Alex Blake assisted in sample collection from Hooker's Point. We would also like to thank Professor V. Jones (University College, London) who kindly examined diatoms from selected levels of the peat sequence. The comments of two anonymous reviews helped to improve the focus and clarity of this manuscript.

Abbreviations. ACR, Antarctic Cold Reversal; LPMZs, local plant macrofossil zones; LPAZs, local pollen assemblage zones; UOM, unidentified organic matter.

References

Aldiss DJ, Edwards EJ. 1999. The Geology of the Falkland Islands. Technical Report WC/99/10, British Geological Survey, Keyworth. http://nora.nerc.ac.uk/507542/

Barber KE, Chambers FM, Maddy D *et al.* 1994. A sensitive high-resolution record of late Holocene climatic change from a raised bog in northern England. *The Holocene* **4**: 198–205.

Barrow CJ. 1976. Palynological studies in South Georgia: I Pollen and spore morphology of the native vascular species. *British Antarctic Survey Bulletin* **43**: 63–75.

Barrow CJ. 1978. Postglacial pollen diagrams from South Georgia (sub-Antarctic) and west Falkland Island (South Atlantic). *Journal of Biogeography* **5**: 251–274.

Barrow CJ. 1983. Palynological studies in South Georgia: IV. Profiles from Barff peninsula and Annenkov Island. *British Antarctic Survey Bulletin* **58**: 61–70.

Battarbee, *et al.* 2001. Tracking environmental change using lake sediments, terrestrial, algal and siliceous indicators Smol J. P., Birks H.J., Last W. M. (eds). Kluwer Achademic publishers: Dordrecht; 155–202.

Bokhorst, *et al.* 2007. The effect of environmental change on vascular plant and cryptogam communities from the Falkland Islands and Maritime Antarctic. *BMS Ecology* **7**(1): 15.

Brandini FP, Boltovskoy D, Piola A *et al.* 2000. Multiannual trends in fronts and distribution of nutrients and chlorophyll in the southwestern Atlantic (30-62°S). *Deep-Sea Research Part I* **47**: 1015–1033.

Bronk Ramsey C. 2008. Deposition models for chronological records. *Quaternary Science Reviews* **27**: 42–60.

Bronk Ramsey C. 2009a. Bayesian analysis of radiocarbon dates. *Radiocarbon* **51**: 337–360.

Bronk Ramsey C. 2009b. Dealing with outliers and offsets in radiocarbon dating. *Radiocarbon* **51**: 1023–1045.

Bronk Ramsey C, Lee S. 2013. Recent and planned developments of the program OxCal. *Radiocarbon* **55**: 720–730.

Bronk Ramsey C. 2017. OxCal project, Version 4.3. Retrieved August 2018. https://c14.arch.ox.ac.uk/oxcal/OxCal.html

Clark R, Wilson P. 1992. Occurrence and significance of ventifacts in the Falkland Islands, South Atlantic. *Geografiska Annaler* **74A**: 35–46.

Clark R, Huber UM, Wilson P. 1998. Late Pleistocene sediments and environmental change at Plaza Creek, Falkland Islands, South Atlantic. *Journal of Quaternary Science* **13**: 95–105.

Cranwell LM. 1969. Antarctic and circum-Antarctic palynological contributions. *Antarctic Journal of the United States* **4**: 197–198.

Daniels RE, Eddy A. 1990. *Handbook of European sphagna*. HMSO: London.

Davies TH, McAdam JH. 1989. Wild Flowers of the Falkland Islands: a fully illustrated introduction to the main species and a guide to their identification. Falkland Islands Trust. Bluntisham Books: Huntingdon.

Davies AB, Riley J, Walton DW. 1990. Plant form, tiller dynamics and aboveground standing crops of the range of *Cortaderia pilosa* communities in the Falkland Islands. *Journal of applied ecology* **27**(298): 307.

EPICA community members. 2006. One-to-one coupling of glacial climate variability in Greenland and Antarctica. *Nature* **444**: 195–198.

Evans C, Artz R, Moxley J *et al.* 2019. Implementation of an emission inventory for UK peatlands. In: *Report to the Department for Business, Energy and Industrial Strategy*. Centre for Ecology and Hydrology: Bangor.

Gallego-Sala AV, Prentice IC. 2013. Blanket peat biome endangered by climate change. *Nature Climate Change* **3**: 152.

Grimm EC. 1991. TILIA and TILIAGRAPH software. Illinois State Museum, Springfield.

Groff V. 2018. Modern and Paleoecological Perspectives on a Terrestrial-Marine Linkage in the Falkland Islands. Ph.D. thesis, University of Maine.

Hafsten U. 1951. A pollen-analytic investigation of two peat deposits from Tristan da Cunha. In: *Scientific Results of the Norwegian Expedition to Tristan da Cunha, 1937-1938*, Det Norske Videnskaps Akademi:Oslo; 22.

Hafsten U. 1960a. *Pleistocene development of vegetation and climate in Tristan da Cunha and Gough Island. Årbok for Universitetet i Bergen. Matematisk-naturvitenskapelig serie*. Norwegian Universities Press: Bergen; 20.

Hafsten U. 1960b. The Quaternary history of vegetation in the South Atlantic Islands. *Proceedings of the Royal Society B 152* **5**: 16–629.

Harter DE, Irl SD, Seo B *et al.* 2015. Impacts of global climate change on the floras of oceanic islands–Projections, implications and current knowledge. *Perspectives in Plant Ecology, Evolution and Systematics* **17**: 160–183.

Hellmann JJ, Byers JE, Bierwagen BG *et al.* 2008. Five potential consequences of climate change for invasive species. *Conservation Biology* **22**: 534–543.

Heusser CJ. 1971. *Pollen and Spores of Chile: Modern Types of the Pteridophyta, Gymnospermae, and Angiospermae*. The University of Arizona Press: Tucson AZ; 167.

Heusser CJ. 1989. Late Quaternary vegetation and climate of southern Tierra del Fuego. *Quaternary Research* **31**: 396–406.

Hogg AG, Hua Q, Blackwell PG *et al.* 2013. SHCal13 Southern Hemisphere calibration, 0–50,000 years cal BP. *Radiocarbon* **55**: 1889–1903.

Hooker JD. 1847. Botany of the Antarctic voyage. Vol. I. Flora Antarctica. Pt. 2. Botany of Fuegia, The Falklands, Kerguelen's Land, etc. London, Reeve: 209–574.

Hughes PDM, Mauquoy D, Barber KE *et al.* 2000. Mire-development pathways and palaeoclimatic records from a full Holocene peat archive at Walton Moss, Cumbria, England. *The Holocene* **10**(465): 479.

Hughes PDM, Barber KE. 2004. Contrasting pathways to ombrotrophy in three raised bogs from Ireland and Cumbria, England. *The Holocene* **14**: 65–77.

Hughes PDM, Blundell A, Charman DJ *et al.* 2006. An 8500 cal. year multi-proxy climate record from a bog in eastern Newfoundland: contributions of meltwater discharge and solar forcing. *Quaternary Science Reviews* **25**: 1208–1227.

Ise T, Dunn AL, Wofsy SC *et al*. 2008. High sensitivity of peat decomposition to climate change through water-table feedback. *Nature Geoscience* **1**: 763.

Jones PD, Harpham C, Lister DH. 2013. *Construction of high spatial resolution climate scenarios for the Falkland Islands and southern Patagonia*. Report to UK Falkland Islands Trust.

Kilian R, Lamy F. 2013. A review of Glacial and Holocene paleoclimate records from southernmost Patagonia (49-55ºS). *Quaternary Science Reviews* **53**: 1–23.

Larsen JN, Anisimov OA, Constable A *et al*. 2014. Polar Regions. In *Climate Change 2014: Impacts, Adaptation, and Vulnerability Part B: Regional Aspects Contribution of Working Group II to the Fifth Assessment Report of the Intergovernmental Panel on Climate Change*, Barros VR, Field CB, Dokken DJ (eds). Cambridge University Press: Cambridge; 1654.

Linskens HF, Bargagli R, Focardi S *et al*. 1991. Antarctic moss turf as pollen traps. *Proceedings of the Koninklijke Nederlandse Akademie van Wetenschappen* **94**: 233–241.

Linskens HF, Bargagli R, Cresti M *et al*. 1993. Entrapment of long-distance transported pollen grains by various moss species in coastal Victoria Land, Antarctica. *Polar Biology* **13**: 81–87.

Lister DH, Jones PD. 2015. Long-term temperature and precipitation records from the Falkland Islands. *International Journal of Climatology* **35**: 1224–1231.

Mansilla CA, McCulloch RD, Morello F. 2018. The vulnerability of the Nothofagus forest-steppe ecotone to climate change: Palaeoecological evidence from Tierra del Fuego (~53°S). *Palaeogeography, palaeoclimatology, palaeoecology* **508**: 59–70.

Mauquoy D, Yeloff D. 2008. Raised peat bog development and possible responses to environmental changes during the mid-to late-Holocene. Can the palaeoecological record be used to predict the nature and response of raised peat bogs to future climate change? *Biodiversity and Conservation* **17**: 2139–2151.

Mayr C, Wille M, Haberzettl T *et al*. 2007. Holocene variability of the Southern Hemisphere westerlies in Argentinean Patagonia (52ºS). *Quaternary Science Reviews* **26**: 579–584.

Mayr C, Lücke A, Wagner S *et al*. 2013. Intensified Southern Hemisphere Westerlies regulated atmospheric CO2 during the last deglaciation. *Geology* **41**: 831–834.

McCulloch RD, Fogwill CJ, Sugden DE *et al*. 2005. Chronology of the last glaciation in central Strait of Magellan and Bahía Inútil, southernmost South America. *Geografiska Annaler: Series A, Physical Geography* **87**: 289–312.

Monteath AJ, Hughes PDM, Wastegård S. 2019. Evidence for distal transport of reworked Andean tephra: extending the cryptotephra framework from the Austral Volcanic Zone. *Quaternary Geochronology* **51**: 64–71.

Moore DM. 1968. The Vascular Flora of the Falkland Islands. British Antarctic Survey Scientific Reports 60. Natural Environment Research Council: London.

Moore DM. 1983. Flora of Tierra del Fuego, Anthony Nelson, Oswestry, Shropshire.

Moore PD, Bellamy DJ. 1974. *Peatlands*. Springer-Verlag: New York, NY.

Moore PD, Webb JA, Collison ME. 1991. Pollen analysis. Blackwell scientific publications.

Moreno PI, Kaplan MR, François JP *et al*. 2009. Renewed glacial activity during the Antarctic cold reversal and persistence of cold conditions until 11.5 ka in southwestern Patagonia. *Geology* **37**(375): 378.

Moreno PI, Villa-Martínez R, Cárdenas ML *et al*. 2012. Deglacial changes of the southern margin of the southern westerly winds revealed by terrestrial records from SW Patagonia (52ºS). *Quaternary Science Reviews* **41**: 1–21.

Moreno PI, Videla J, Valero-Garcés B *et al*. 2018. A continuous record of vegetation, fire-regime and climatic changes in northwestern Patagonia spanning the last 25,000 years. *Quaternary Science Reviews* **198**: 15–36.

Morris PJ, Swindles GT, Valdes PJ *et al*. 2018. Global peatland initiation driven by regionally asynchronous warming. *Proceedings of the National Academy of Sciences* **115**: 851–4856.

Newton, T, Gehrels, R, Daley, T *et al*. 2014. Holocene sea-level changes in the Falkland Islands. In: EGU General Assembly Conference Abstracts 16.

Nogué S, de Nascimento L, Froyd CA *et al*. 2017. Island biodiversity conservation needs palaeoecology. *Nature ecology and evolution* **1**: 181.

Nurse LA, McLean RF, Agard J, *et al*. 2014. Small islands. In *Climate Change 2014: Impacts, Adaptation, and Vulnerability. Part B: Regional Aspects. Contribution of Working Group II to the Fifth Assessment Report of the Intergovernmental Panel on Climate Change*, Barros VR, Field CB, Dokken DJ (eds). Cambridge University Press: Cambridge.

Otley H, Munro G, Clausen A *et al*. 2008. Falkland Islands State of the Environment Report. Falkland Islands Government and Falklands Conservation, Stanley, Falkland Islands.

Payne RJ, Ring-Hrubesh F, Rush G *et al*. 2019. Peatland initiation and carbon accumulation in the Falkland Islands. *Quaternary Science Reviews* **2012**: 2013–2218.

Pedro JB, Rasmussen SO, van Ommen TD. 2011. Tightened constraints on the time-lag between Antarctic temperature and CO2 during the last deglaciation. *Climate of the Past* **8**: 1213–1221.

Pedro JB, Bostock HC, Bitz CM *et al*. 2016. The spatial extent and dynamics of the Antarctic Cold Reversal. *Nature Geoscience* **9**: 51.

Roland TP, Caseldine CJ, Charman DJ *et al*. 2014. Was there a '4.2 ka event' in Great Britain and Ireland? Evidence from the peatland record. *Quaternary Science Reviews* **83**: 11–27.

Smith RL, Clymo RS. 1984. An extraordinary peat-forming community on the Falkland Islands. *Nature* **309**: 617.

Stern CR. 2008. Holocene tephrochronology record of large explosive eruptions in the southernmost Patagonian Andes. *Bulletin of Volcanology* **70**: 435–454.

Stone P. 2016. Geology reviewed for the Falkland Islands and their offshore sedimentary basins, South Atlantic Ocean. *Earth and Environmental Science Transactions of the Royal Society of Edinburgh* **106**: 115–143.

Strange, *et al*. 1988. Tussac grass in the Falkland Islands. Falkland Islands Foundation: Brighton.

Strother SL, Salzmann U, Roberts SJ *et al*. 2015. Holocene vegetation and change of westerly winds reconstructed from a high-resolution sub-Antarctic pollen record at Fan Lake, South Georgia. *The Holocene* **25**: 263–279.

Thalmann DJK, Kikodze D, Khutsishvili M *et al*. 2015. Areas of high conservation value in Georgia: present and future threats by invasive alien plants. *Biological Invasions* **17**: 1041–1054.

Thomas ZA, Jones RT, Fogwill CJ *et al*. 2018. Evidence for increased expression of the Amundsen Sea Low over the South Atlantic during the late Holocene. *Climate of the Past* **14**: 1727–1738.

Turney CS, Jones RT, Fogwill CJ *et al*. 2016. A 250-year periodicity in Southern Hemisphere westerly winds over the last 2600 years. *Climate of the Past* **12**: 189–200.

Upson R, Lewis R. 2014. Updated atlas and checklist. Report to Falklands Conservation.

Upson R, Williams JJ, Wilkinson TP *et al*. 2016. Potential impacts of climate change on native plant distributions in the Falkland Islands. *PloS one* 11.

Upton J, Shaw CJ. 2002. An overview of the oceanography and meteorology of the Falkland Islands. *Aquatic conservation: marine and freshwater ecosystems* **12**: 15–25.

van der Knaap WO, van Leeuwen JFN. 1993. A recent pollen diagram from Antarctica (King George Island, South Shetland Islands). *The Holocene* **3**: 169–173.

Vanneste H, De Vleeschouwer F, Martínez-Cortizas A *et al*. 2015. Late-glacial elevated dust deposition linked to westerly wind shifts in southern South America. *Scientific Reports* 5.

Walker D, Walker PM. 1961. Stratigraphic evidence of regeneration in some Irish bogs. *The Journal of Ecology* 169–185.

Walther GR, Roques A, Hulme PE *et al*. 2009. Alien species in a warmer world: risks and opportunities. *Trends in ecology and evolution* **24**: 686–693.

Whitlock C, Moreno PI, Bartlein P. 2007. Climatic controls of Holocene fire patterns in southern South America. *Quaternary Research* **68**: 28–36.

Willis KJ, Bailey RM, Bhagwat SA *et al*. 2010. Biodiversity baselines, thresholds and resilience: testing predictions and assumptions using palaeoecological data. *Trends in ecology and evolution* **25**: 583–591.

Wilson P, Clark R, Birnie J *et al*. 2002. Late Pleistocene and Holocene landscape evolution and environmental change in the Lake Sulivan area, Falkland Islands, South Atlantic. *Quaternary Science Reviews* **21**: 1821–1840.

Wilson P, Bentley MJ, Schnabel C *et al*. 2008. Stone run (block stream) formation in the Falkland Islands over several cold stages, deduced from cosmogenic isotope (^{10}Be and ^{26}Al) surface exposure dating. *Journal of Quaternary Science* **23**: 461–473.

Woods RW. 2000. Flowering Plants of the Falkland Islands. Falklands Conservation; Stanley.

List of references

Abbott, P.M., Davies, S.M., 2012. Volcanism and the Greenland ice-cores: the tephra record. Earth-Science Reviews 115, 173–191.

Abercromby, R., Archibald, E.D., Bonney, T.G., Evans, F.J., Geikie, A., Judd, J.W., Lockyer, J.N., Russell, F.A.R., Scott, R.H., Stokes, G.G., Strachey, R.E., Symons, G.J., Wharton, W.J.L. 1888. The eruption of Krakatoa, and subsequent phenomena. Report of the Krakatoa Committee of the Royal Society. Trübner & Company, London.

Ahrens, C.D., 2012. Meteorology today: an introduction to weather, climate, and the environment. Cengage Learning.

Albert, P.G., Smith, V.C., Suzuki, T., McLean, D., Tomlinson, E.L., Miyabuchi, Y., Kitaba, I., Mark, D.F., Moriwaki, H., Members, S.P., Nakagawa, T., 2019. Geochemical characterisation of the Late Quaternary widespread Japanese tephrostratigraphic markers and correlations to the Lake Suigetsu sedimentary archive (SG06 core). Quaternary Geochronology.

Aldiss, D.T., Edwards, E.J., 1999. The geology of the Falkland Islands. British Geological Survey.

Alloway, B.V., Pearce, N.J.G., Villarosa, G., Outes, V., Moreno, P.I., 2015. Multiple melt bodies fed the AD 2011 eruption of Puyehue-Cordón Caulle, Chile. Scientific reports 5, 17589.

Anderson, R.F., Ali, S., Bradtmiller, L.I., Nielsen, S.H.H., Fleisher, M.Q., Anderson, B.E., Burckle, L.H., 2009. Wind-driven upwelling in the Southern Ocean and the deglacial rise in atmospheric CO2. Science 323, 1443–1448.

Arbogast, A.F., Luehmann, M.D., Miller, B.A., Wernette, P.A., Adams, K.M., Waha, J.D., O'Neil, G.A., Tang, Y., Boothroyd, J.J., Babcock, C.R., Hanson, P.R., 2015. Late-Pleistocene paleowinds and aeolian sand mobilization in north-central Lower Michigan. Aeolian Research 16, 109–116.

Bacon, C.R., Lanphere, M.A., 2006. Eruptive history and geochronology of Mount Mazama and the Crater Lake region, Oregon. Geological Society of America Bulletin 118, 1331–1359.

Basile, I., Petit, J., Touron, S., Grousset, F., Barkov, N., 2001. Volcanic layers in Antarctic (Vostok) ice cores: source identification and atmospheric implications. Journal of Geophysical Research 106, 31915–31931.

Beierle, B., Bond, J., 2002. Density-induced settling of tephra through organic lakesediments. Journal of Paleolimnology 28, 433–440.

Bergman, J., Wastegård, S., Hammarlund, D., Wohlfarth, B., Roberts, S.J., 2004. Holocene tephra horizons at Klocka Bog, west-central Sweden: aspects of reproducibility in subarctic peat deposits. Journal of Quaternary Science 19, 241–249.

Biester, H., Keppler, F., Putschew, A., Martinez-Cortizas, A., Petri, M., 2004. Halogen retention, organohalogens, and the role of organic matter decomposition on halogen enrichment in two Chilean peat bogs. Environmental Science Technology 38, 1984–1991.

Björckl, S. and Clemmensen, L.B., 2004. Aeolian sediment in raised bog deposits, Halland, SW Sweden: a new proxy record of Holocene winter storminess variation in southern Scandinavia? The Holocene, 14(5), pp.677-688.

Björck, S., Rundgren, M., Ljung, K., Unkel, I., Wallin, Å., 2012. Multi-proxy analyses of a peat bog on Isla de los Estados, easternmost Tierra del Fuego: a unique record of the variable Southern Hemisphere Westerlies since the last deglaciation. Quaternary Science Reviews 42, 1–14.

Blanchet, C.L., Thouveny, N., Vidal, L., 2009. Formation and preservation of greigite in sediments from the Santa Barbara Basin: Implications for paleoenvironmental changes during the past 35 ka. Paleoceanography 24.

Blockley, S.P.E., Pyne-O'Donnell, S.D.F., Lowe, J.J., Matthews, I.P., Stone, A., Pollard, A.M., Turney, C.S.M., Molyneux, E.G., 2005. A new and less destructive laboratory procedure for the physical separation of distal glass tephra shards from sediments. Quaternary Science Reviews 24, 1952–1960.

Blockley, S.P.E., Ramsey, C.B., Lane, C.S., Lotter, A.F., 2008. Improved age modelling approaches as exemplified by the revised chronology for the Central European varved lake Soppensee. Quaternary Science Reviews 27, 61–71.

Blockley, S.P., Edwards, K.J., Schofield, J.E., Pyne-O'Donnell, S.D., Jensen, B.J., Matthews, I.P., Cook, G.T., Wallace, K.L., Froese, D., 2015. First evidence of cryptotephra in palaeoenvironmental records associated with Norse occupation sites in Greenland. Quaternary Geochronology 27, 145–157.

Blundell, A., Hughes, P.D. and Chambers, F.M., 2018. An 8000-year multi-proxy peat-based palaeoclimate record from Newfoundland: Evidence of coherent changes in bog surface wetness and ocean circulation. The Holocene 28, 791–805.

List of references

Bonadonna, C., Costa, A., Folch, A., Koyaguchi, T., 2015. Tephra dispersal and sedimentation. In The Encyclopedia of Volcanoes, Academic Press 587–597.

Borchardt, G.A., Aruscavage, P.J., Millard, H.J., 1972. Correlation of the Bishop Ash, a Pleistocene marker bed, using instrumental neutron activation analysis. Journal of Sedimentary Research 42, 301–306.

Boygle, J., 1999. Variability of tephra in lake and catchment sediments, Svınavatn, Iceland. Global and Planetary Change 21, 129–149.

Boyle, J.F., 2002. Inorganic geochemical methods in palaeolimnology. In: Tracking environmental change using lake sediments. Springer, Dordrecht, 83–141.

Braitseva, O.A., Melekestsev, I.V., Ponomareva, V.V., Sulerzhitsky, L.D., 1995. Ages of calderas, large explosive craters and active volcanoes in the Kuril-Kamchatka region, Russia. Bulletin of Volcanology 57, 383–402.

Bromwich, D.H., Toracinta, E.R., Wei, H., Oglesby, R.J., Fastook, J.L., Hughes, T.J., 2004. Polar MM5 simulations of the winter climate of the Laurentide Ice Sheet at the LGM. Journal of Climate 17, 3415–3433.

Bronk Ramsey, C., 2009a. Bayesian analysis of radiocarbon dates. Radiocarbon 51, 337–360.

Bronk Ramsey, C., 2009b. Dealing with outliers and offsets in radiocarbon dating. Radiocarbon 51, 1023–1045.

Bronk Ramsey, C., Lee, S., 2013. Recent and planned developments of the program OxCal. Radiocarbon 55, 720–730.

Bronk Ramsey, C., Albert, P.G., Blockley, S.P., Hardiman, M., Housley, R.A., Lane, C.S., Lee, S., Matthews, I.P., Smith, V.C., Lowe, J.J., 2015. Improved age estimates for key Late Quaternary European tephra horizons in the RESET lattice. Quaternary Science Reviews 118, 18–32.

Bronk Ramsey, C., 2017. OxCal project, Version 4.3. Retrieved April 2018. https://c14.arch.ox.ac.uk/oxcal/OxCal.html.

Brooks, C.E.P., 1932. The movement of volcanic flashover the globe. Met Mag 67, 81.

Brooks, S.J., Matthews, I.P., Birks, H.H., Birks, H.J.B., 2012. High resolution Lateglacial and early-Holocene summer air temperature records from Scotland inferred from chironomid assemblages. Quaternary Science Reviews 41, 67–82.

Brown, R.J., Bonadonna, C., Durant, A.J., 2012. A review of volcanic ash aggregation. Physics and Chemistry of the Earth 45, 65–78.

Bryson, R.A. and Hare, F.K., 1974. Climates of North America, World Survey of Climatology, Volume 11.

Bourne, A.J., Abbott, P.M., Albert, P.G., Cook, E., Pearce, N.J., Ponomareva, V., Svensson, A., Davies, S.M., 2016. Underestimated risks of recurrent long-range ash dispersal from northern Pacific Arc volcanoes. Scientific Reports 6, 29837.

Buizert, C., Sigl, M., Severi, M., Markle, B.R., Wettstein, J.J., McConnell, J.R., Pedro, J.B., Sodemann, H., Goto-Azuma, K., Kawamura, K., Fujita, S., 2018. Abrupt ice-age shifts in southern westerly winds and Antarctic climate forced from the north. Nature 563, 681.

Bullard, J.E., Baddock, M., Bradwell, T., Crusius, J., Darlington, E., Gaiero, D., Gasso, S., Gisladottir, G., Hodgkins, R., McCulloch, R., McKenna-Neuman, C., 2016. High-latitude dust in the Earth system. Reviews of Geophysics 54, 447–485.

Bursik, M., 2001. Effect of wind on the rise height of volcanic plumes. Geophysical Research Letters 28, 3621–3624.

Brown, S.K., Crosweller, H.S., Sparks, R.S.J., Cottrell, E., Deligne, N.I., Guerrero, N.O., Hobbs, L., Kiyosugi, K., Loughlin, S.C., Siebert, L., Takarada, S., 2014. Characterisation of the Quaternary eruption record: analysis of the Large Magnitude Explosive Volcanic Eruptions (LaMEVE) database. Journal of Applied Volcanology 3, 5.

Casadevall, T.J., 1994. The 1989–1990 eruption of Redoubt Volcano, Alaska: impacts on aircraft operations. Journal of volcanology and geothermal research 62, 301–316.

Carey, S., Gardner, J., Sigurdsson, H., 1995. The intensity and magnitude of Holocene plinian eruptions from Mount St. Helens volcano. Journal of Volcanology and Geothermal Research 66, 185–202.

Carn, S.A., Prata, A.J., Karlsdottir, S., 2008. Circumpolar transport of a volcanic cloud from Hekla (Iceland). Journal of Geophysical Research: Atmospheres, 113(D14).

Christiansen, R.L., Peterson, D.W., 1981. Chronology of the 1980 eruptive activity. In: Lipman, P.W., Mullineaux, D.R. (Eds.). The 1980 Eruptions of Mount St. Helens, Washington, vol. 1250. Geological Survey Professional Paper, 17–30.

Clark, R., Wilson, P., 1992. Occurrence and significance of ventifacts in the Falkland Islands, South Atlantic. Geografiska Annaler: Series A, Physical Geography 74, 35–46.

Clynne, M.A., Calvert, A.T., Wolfe, E.W., Evarts, R.C., Fleck, R.J., Lanphere, M.A., 2008. The pleistocene eruptive history of Mount St. Helens, Washington, from 300,000 to 12,800 years before present. In: Sherrod, D.R., Scott, W.E., Stauffer, P.H. (Eds.), A Volcano Rekindled: the Renewed Eruption of Mount St. Helens, 2004-2006. U.S. Geological Survey Professional Paper 1750–28.

Conradt, R., 2008. Chemical durability of oxide glasses in aqueous solutions: A review. Journal of the American Ceramic Society 91, 728–735.

Cook, E., Portnyagin, M., Ponomareva, V., Bazanova, L., Svensson, A., Garbe-Schönberg, D., 2018. First identification of cryptotephra from the Kamchatka Peninsula in a Greenland ice core: Implications of a widespread marker deposit that links Greenland to the Pacific northwest. Quaternary Science Reviews 181, 200–206.

Cooper, C.L., Swindles, G.T., Savov, I.P., Schmidt, A., Bacon, K.L., 2018. Evaluating the relationship between climate change and volcanism. Earth-Science Reviews 177, 238–247.

Coulter, S.E., Pilcher, J.R., Plunkett, G., Baillie, M., Hall, V.A., Steffensen, J.P., Vinther, B.M., Clausen, H.B., Johnsen, S.J., 2012. Holocene tephras highlight complexity of volcanic signals in Greenland ice cores. Journal of Geophysical Research: Atmospheres, 117(D21).

Crosweller, H.S., Arora, B., Brown, S.K., Cottrell, E., Deligne, N.I., Guerrero, N.O., Hobbs, L., Kiyosugi, K., Loughlin, S.C., Lowndes, J., Nayembil, M., 2012. Global database on large magnitude explosive volcanic eruptions (LaMEVE). Journal of Applied Volcanology 1, 4.

Croudace, I.W., Rothwell, R.G. eds., 2015. Micro-XRF Studies of Sediment Cores: Applications of a non-destructive tool for the environmental sciences (Vol. 17). Springer.

Daley, T.J., Barber, K.E., Hughes, P.D.M., Loader, N.J., Leuenberger, M., Street-Perrott, F.A., 2016. The 8.2-ka BP event in north-eastern North America: first combined oxygen and hydrogen isotopic data from peat in Newfoundland. Journal of Quaternary Science 31, 416–425.

Davies, L.J., Jensen, B.J., Froese, D.G., Wallace, K.L., 2016. Late Pleistocene and Holocene tephrostratigraphy of interior Alaska and Yukon: Key beds and chronologies over the past 30,000 years. Quaternary Science Reviews 146, 28–53.

Davies, S.M., Elmquist, M., Bergman, J., Wohlfarth, B., Hammarlund, D., 2007. Cryptotephra sedimentation processes within two lacustrine sequences from west central Sweden. The Holocene 17, 319–330.

Davies, S.M., Larsen, G., Wastegård, S., Turney, C.S., Hall, V.A., Coyle, L., Thordarson, T., 2010. Widespread dispersal of Icelandic tephra: how does the Eyjafjöll eruption of 2010 compare to past Icelandic events? Journal of Quaternary Science 25, 605–611.

Davies, S.M., 2015. Cryptotephras: the revolution in correlation and precision dating. Journal of Quaternary Science 30, 114–130.

Dean, W.E., Forester, R.M., Bradbury, J.P., 2002. Early Holocene change in atmospheric circulation in the Northern Great Plains: an upstream view of the 8.2 ka cold event. Quaternary Science Reviews, 21, 1763–1775.

de Fontaine, C. S., Kaufman, D. S., Anderson, R. S., Werner, A., Waythomas, C. F., Brown, T. A. (2007). Late Quaternary distal tephra-fall deposits in lacustrine sediments, Kenai Peninsula, Alaska. Quaternary Research 68, 64–78.

De Jong, R.D., Björck, S., Björkman, L., Clemmensen, L.B., 2006. Storminess variation during the last 6500 years as reconstructed from an ombrotrophic peat bog in Halland, southwest Sweden. Journal of Quaternary Science 21, 905–919.

Del Carlo, P., Di Roberto, A., D'Orazio, M., Petrelli, M., Angioletti, A., Zanchetta, G., Maggi, V., Daga, R., Nazzari, M. and Rocchi, S., 2018. Late Glacial-Holocene tephra from southern Patagonia and Tierra del Fuego (Argentina, Chile): A complete textural and geochemical fingerprinting for distal correlations in the Southern Hemisphere. Quaternary Science Reviews 195, 153–170.

Deplazes, G., Lückge, A., Peterson, L.C., Timmermann, A., Hamann, Y., Hughen, K.A., Röhl, U., Laj, C., Cane, M.A., Sigman, D.M., Haug, G.H., 2013. Links between tropical rainfall and North Atlantic climate during the last glacial period. Nature Geoscience 6, 213.

Dugmore, A., 1989. Icelandic volcanic ash in Scotland. Scottish Geographical Magazine 105, 168–172.

Dugmore, A.J., Newton, A.J., 1997. Holocene tephra layers in the Faroe Islands. Frodskaparrit 46, 191–204.

Dugmore, A.J., Newton, A.J., 2012. Isochrons and beyond: maximising the use of tephrochronology in geomorphology. Jökull 62, 39–52.

Dugmore, A.J., Newton, A.J., Sugden, D.E., Larsen, G., 1992. Geochemical stability of fine-grained silicic Holocene tephra in Iceland and Scotland. Journal of Quaternary Science 7, 173–183.

Dugmore, A.J., Larsen, G.R. and Newton, A.J., 1995. Seven tephra isochrones in Scotland. The Holocene 5, 257–266.

Durant, A.J., Brown, R.J., 2016. Ash Aggregation in Volcanic Clouds. In Volcanic Ash, Elsevier, 53–65.

Eaton, G.P., 1963. Volcanic ash deposits as a guide to atmospheric circulation in the geologic past. Journal of Geophysical Research 68, 521–528.

Eden, D.N., Froggatt, P.C., Zheng, H., Machida, H., 1996. Volcanic glass found in Late Quaternary Chinese loess: A pointer for future studies? Quaternary International 34, 107–111.

Egan, J., Staff, R., Blackford, J., 2015. A high-precision age estimate of the Holocene Plinian eruption of Mount Mazama, Oregon, USA. The Holocene 25, 1054–1067.

Eriksson, L., Johansson, E., Kettaneh-Wodl, N., Wold, S., 1999. Introduction to Multi and Mega-variate Data Analysis Using Projection Methods (PCA & PLS). Umetrics AB, Umeå.

Finkenbinder, M.S., Abbott, M.B., Steinman, B.A., 2016. Holocene climate change in Newfoundland reconstructed using oxygen isotope analysis of lake sediment cores. Global and Planetary Change 143, 251–261.

Fletcher, M.S., Moreno, P.I., 2012. Have the Southern Westerlies changed in a zonally symmetric manner over the last 14,000 years? A hemisphere-wide take on a controversial problem. Quaternary International 253, 32–46.

Folch, A., 2012. A review of tephra transport and dispersal models: evolution, current status, and future perspectives. Journal of Volcanology and Geothermal Research 235, 96–115.

Fontijn, K., Lachowycz, S.M., Rawson, H., Pyle, D.M., Mather, T.A., Naranjo, J.A., Moreno-Roa, H., 2014. Late Quaternary tephrostratigraphy of southern Chile and Argentina. Quaternary Science Reviews 89, 70–84.

Fontijn, K., Rawson, H., Van Daele, M., Moernaut, J., Abarzúa, A.M., Heirman, K., Bertrand, S., Pyle, D.M., Mather, T.A., De Batist, M., Naranjo, J.A., 2016. Synchronisation of sedimentary records using

tephra: A postglacial tephrochronological model for the Chilean Lake District. Quaternary Science Reviews 137, 234–254.

Fontijn, K., Rawson, H., Van Daele, M., Moernaut, J., Abarzúa, A.M., Heirman, K., Bertrand, S., Pyle, D.M., Mather, T.A., De Batist, M., Naranjo, J.A., 2016. Synchronisation of sedimentary records using tephra: A postglacial tephrochronological model for the Chilean Lake District. Quaternary Science Reviews 137, 234–254.

Fowler, W.B., Lopushinsky, W., 1986. Wind-blown volcanic ash in forest and agricultural locations as related to meteorological conditions. Atmospheric Environment 20, 421–425.

Frölicher, T.L., Sarmiento, J.L., Paynter, D.J., Dunne, J.P., Krasting, J.P., Winton, M., 2015. Dominance of the Southern Ocean in anthropogenic carbon and heat uptake in CMIP5 models. Journal of Climate, 28, 862–886.

Gaiero, D.M., Brunet, F., Probst, J.L., Depetris, P.J., 2007. A uniform isotopic and chemical signature of dust exported from Patagonia: Rock sources and occurrence in southern environments. Chemical Geology 238, 107–120.

Gaiero, D.M., Probst, J.L., Depetris, P.J., Bidart, S.M., Leleyter, L., 2003. Iron and other transition metals in Patagonian riverborne and windborne materials: geochemical control and transport to the southern South Atlantic Ocean. Geochimica et Cosmochimica Acta 67, 3603–3623.

García, J.L., Kaplan, M.R., Hall, B.L., Schaefer, J.M., Vega, R.M., Schwartz, R., Finkel, R., 2012. Glacier expansion in southern Patagonia throughout the Antarctic cold reversal. Geology 40, 859–862.

Garreaud, R.D., Vuille, M., Compagnucci, R., Marengo, J., 2009. Present-day South American climate. Palaeogeography, Palaeoclimatology, Palaeoecology 281, 180–195.

Garreaud, R., Lopez, P., Minvielle, M., Rojas, M., 2013. Large-scale control on the Patagonian climate. Journal of Climate 26, 215–230.

Global Volcanism Program: Smithsonian Institution. https://volcano.si.edu/ (15 March 2018).

Gonzalez, S., Jones, J.M., Williams, D.L., 1999. Characterization of tephras using magnetic properties: an example from SE Iceland. Geological Society, London, Special Publications 161, 125–145.

Grindle, T.J., Burcham Jr, F.W., 2003. Engine damage to a NASA DC-8-72 airplane from a high-altitude encounter with a diffuse volcanic ash cloud. NASA technical report 20030068344.

Greenway, M.E., 1972. The geology of the Falkland Islands 76. British Antarctic Survey.

Gudmundsson, A., 2006. How local stresses control magma-chamber ruptures, dyke injections, and eruptions in composite volcanoes. Earth-Science Reviews 79, 1–31.

Guffanti, M., Mayberry, G.C., Casadevall, T.J., Wunderman, R., 2009. Volcanic hazards to airports. Natural hazards 51, 287–302.

Haberle, S.G., Bennett, K.D., 2004. Postglacial formation and dynamics of North Patagonian rainforest in the Chonos Archipelago, Southern Chile. Quaternary Science Reviews 23, 2433–2452.

Haberzettl, T., Corbella, H., Fey, M., Janssen, S., Lücke, A., Mayr, C., Ohlendorf, C., Schäbitz, F., Schleser, G.H., Wille, M., Wulf, S., 2007. Lateglacial and Holocene wet—dry cycles in southern Patagonia: chronology, sedimentology and geochemistry of a lacustrine record from Laguna Potrok Aike, Argentina. The Holocene 17, 297–310.

Haberzettl, T., Kück, B., Wulf, S., Anselmetti, F., Ariztegui, D., Corbella, H., Fey, M., Janssen, S., Lücke, A., Mayr, C., Ohlendorf, C., 2008. Hydrological variability in southeastern Patagonia and explosive volcanic activity in the southern Andean Cordillera during Oxygen Isotope Stage 3 and the Holocene inferred from lake sediments of Laguna Potrok Aike, Argentina. Palaeogeography, Palaeoclimatology, Palaeoecology 259, 213–229.

Haberzettl, T., Anselmetti, F.S., Bowen, S.W., Fey, M., Mayr, C., Zolitschka, B., Ariztegui, D., Mauz, B., Ohlendorf, C., Kastner, S., Lücke, A., 2009. Late Pleistocene dust deposition in the Patagonian steppe-extending and refining the paleoenvironmental and tephrochronological record from Laguna Potrok Aike back to 55 ka. Quaternary Science Reviews 28, 2927–2939.

Hadley, D., Hufford, G.L., Simpson, J.J., 2004. Resuspension of relic volcanic ash and dust from Katmai: still an aviation hazard. Weather and forecasting 19, 829–840.

Hall, K., 2004. Quaternary glaciation of the sub-Antarctic Islands. In Developments in Quaternary Sciences (2), 339–345).

Hall, M, Hayward, C., 2014. Preparation of micro-and crypto-tephras for quantitative microbeam analysis. Geological Society, London, Special Publications 398, 21–28.

Hall, V.A., Wilson, P., Holmes, J., 2001. A preliminary tephra study of Holocene peats in the Falkland Islands. Dossiers de l'Archäol-Logis 1, 39–44.

Hanebuth, T.J., Henrich, R., 2009. Recurrent decadal-scale dust events over Holocene western Africa and their control on canyon turbidite activity (Mauritania). Quaternary Science Reviews 28, 261–270.

Hayward C. 2012. High spatial resolution electron probe microanalysis of tephras and melt inclusions without beam-induced chemical modification. The Holocene 22, 119–125.

Hildreth, W., 2007. Quaternary magmatism in the Cascades — geologic perspectives. USGS Professional Paper 1744.

Hodgson, D.A., Sime, L.C., 2010. Palaeoclimate: Southern westerlies and CO2. Nature Geoscience 3, 666.

Hodgson, D.A., Graham, A.G., Roberts, S.J., Bentley, M.J., Cofaigh, C.Ó., Verleyen, E., Vyverman, W., Jomelli, V., Favier, V., Brunstein, D., Verfaillie, D., 2014. Terrestrial and submarine evidence for the extent and timing of the Last Glacial Maximum and the onset of deglaciation on the maritime-Antarctic and sub-Antarctic islands. Quaternary Science Reviews 100, 137–158.

Hogg, A.G., Hua, Q., Blackwell, P.G., Niu, M., Buck, C.E., Guilderson, T.P., Heaton, T.J., Palmer, J.G., Reimer, P.J., Reimer, R.W., Turney, C.S., 2013. SHCal13 Southern Hemisphere calibration, 0–50,000 years cal BP. Radiocarbon 55, 1889–1903.

Holmes, J., Hall, V., Wilson, P., 1999. Volcanoes and peat bogs. Geology Today, 15, 60–63.

Huggins, M.L., Sun, K.H., 1943. Calculation of density and optical constants of a glass from its composition in weight percentage. Journal of the American Ceramic Society 26, 4–11.

Hughes, P.D.M., Mallon, G., Brown, A., Essex, H.J., Stanford, J.D., Hotes, S., 2013. The impact of high tephra loading on late-Holocene carbon accumulation and vegetation succession in peatland communities. Quaternary Science Reviews 67, 160–175.

Hughes, P.D.M., Mallon, G., Mauquoy, M., Charman, D.J., Street-Perrot, F.A., Amesbury, M.J., Loader, N.J., Mackay, H., Monteath, A.J., Jensen, B.J., Fontville, T. The impact of Holocene air mass changes across N. America on peatland carbon accumulation and nutrient cycling. In prep.

Jantzen, C.M., Plodinec, M.J., 1984. Thermodynamic model of natural, medieval and nuclear waste glass durability. Journal of Non-Crystalline Solids 67, 207–223.

Jantzen, C.M., 1992. Nuclear waste glass durability: I, predicting environmental response from thermodynamic (Pourbaix) diagrams. Journal of the American Ceramic Society 75, 2433–2448.

Jantzen, C.M., Brown, K.G., Pickett, J.B., 2010. Durable glass for thousands of years. International Journal of Applied Glass Science 1, 38–62.

Jennings, A., Thordarson, T., Zalzal, K., Stoner, J., Hayward, C., Geirsdóttir, Á., Miller, G., 2014. Holocene tephra from Iceland and Alaska in SE Greenland shelf sediments. Geological Society, London, Special Publications 398, 157–193.

Jensen, B.J., Froese, D.G., Preece, S.J., Westgate, J.A., Stachel, T., 2008. An extensive middle to late Pleistocene tephrochronologic record from east-central Alaska. Quaternary Science Reviews 27, 411–427.

Jensen, B.J., Pyne-O'Donnell, S., Plunkett, G., Froese, D.G., Hughes, P.D., Sigl, M., McConnell, J.R., Amesbury, M.J., Blackwell, P.G., van den Bogaard, C., Buck, C.E., 2014. Transatlantic distribution of the Alaskan white river ash. Geology 42, 875–878.

Jensen, B.J., Evans, M.E., Froese, D.G., Kravchinsky, V.A., 2016. 150,000 years of loess accumulation in central Alaska. Quaternary Science Reviews 135, 1–23.

Jensen, B.J., Beaudoin, A.B., Clynne, M.A., Harvey, J., Vallance, J.W., 2019. A re-examination of the three most prominent Holocene tephra deposits in western Canada: Bridge River, Mount St. Helens Yn and Mazama. Quaternary International 500, 83–95.

Jensen, B.J.L., Davies, L., Nolan, C., Monteath, A.J., Plunkett, G., Booth, R., Ponomareva, V., Portnyagin, M., Cook, E., Pyne-O'Donnell, S., Hughes, P.D.M. A late Pleistocene to Holocene cryptotephra framework from northeastern North America: connecting the Pacific to the sub-tropics and north Atlantic. In prep.

Jull, M., McKenzie, D., 1996. The effect of deglaciation on mantle melting beneath Iceland. Journal of Geophysical Research: Solid Earth, 101, 21815–21828.

Kaufman, D.S., Jensen, B.J., Reyes, A.V., Schiff, C.J., Froese, D.G., Pearce, N.J., 2012. Late Quaternary tephrostratigraphy, Ahklun Mountains, SW Alaska. Journal of Quaternary Science 27, 344–359.

Kilian, R., Hohner, M., Biester, H., Wallrabe-Adams, H.J., Stern, C.R., 2003. Holocene peat and lake sediment tephra record from the southernmost Chilean Andes (53-55 S). Revista geologica de Chile, 30, 23–37.

Kilian, R., Lamy, F., 2013. A review of Glacial and Holocene paleoclimate records from southernmost Patagonia (49–55 ^{o}S). Quaternary Science Reviews 53, 1–23.

Kirby, M.E., Mullins, H.T., Patterson, W.P., Burnett, A.W., 2002. Late glacial–Holocene atmospheric circulation and precipitation in the northeast United States inferred from modern calibrated stable oxygen and carbon isotopes. Geological Society of America Bulletin 114, 1326–1340.

Klüser, L., Erbertseder, T., Meyer-Arnek, J., 2012. Observation of volcanic ash from Puyehue-Cordón Caulle with IASI. Atmospheric Measurement Techniques Discussions 5, 4249–4283.

Koffman, B.G., Dowd, E.G., Osterberg, E.C., Ferris, D.G., Hartman, L.H., Wheatley, S.D., Kurbatov, A.V., Wong, G.J., Markle, B.R., Dunbar, N.W., Kreutz, K.J., 2017. Rapid transport of ash and sulfate from the 2011 Puyehue-Cordón Caulle (Chile) eruption to West Antarctica. Journal of Geophysical Research: Atmospheres 122, 8908–8920.

Kuehn, S.C., 2002. Stratigraphy, Distribution and Geochemistry of the Newberry Volcano Tephras. Ph.D. thesis, Washington State University.

Kuehn, S.C., Foit, F.F., 2006. Correlation of widespread Holocene and Pleistocene tephra layers from Newberry Volcano, Oregon, USA, using glass compositions and numerical analysis. Quaternary International 148, 113–137.

Kuehn, S.C., Froese, D.G., Carrara, P.E., Foit, F.F., Pearce, N.J., Rotheisler, P., 2009. Major-and trace-element characterization, expanded distribution, and a new chronology for the latest Pleistocene Glacier Peak tephras in western North America. Quaternary Research 71, 201–216.

Kuehn, S.C., Froese, D.G., 2010. Tephra from Ice—A Simple Method to Routinely Mount, Polish, and Quantitatively Analyze Sparse Fine Particles. Microscopy and Microanalysis 16, 218–225.

Kuehn, S.C., Froese, D.G., Shane, P.A., Participants, I.I., 2011. The INTAV intercomparison of electron-beam microanalysis of glass by tephrochronology laboratories: results and recommendations. Quaternary International 246, 19–47.

Kurbatov, A.V., Zielinski, G.A., Dunbar, N.W., Mayewski, P.A., Meyerson, E.A., Sneed, S.B., Taylor, K.C., 2006. A 12,000 year record of explosive volcanism in the Siple Dome Ice Core, West Antarctica. Journal of Geophysical Research: Atmospheres, 111(D12).

Kutterolf, S., Schindlbeck, J.C., Jegen, M., Freundt, A., Straub, S.M., 2019. Milankovitch frequencies in tephra records at volcanic arcs: The relation of kyr-scale cyclic variations in volcanism to global climate changes. Quaternary Science Reviews 204, 1–16.

Kylander, M.E., Lind, E.M., Wastegård, S., Löwemark, L., 2011. Recommendations for using XRF core scanning as a tool in tephrochronology. The Holocene 22, 371–375.

Kyle, P.R., Ponomareva, V.V., Rourke Schluep, R., 2011. Geochemical characterization of marker tephra layers from major Holocene eruptions, Kamchatka Peninsula, Russia. International Geology Review 53, 1059–1097.

Lacasse, C., Carey, S., Sigurdsson, H., 1998. Volcanogenic sedimentation in the Iceland Basin: influence of subaerial and subglacial eruptions. Journal of Volcanology and Geothermal Research 83, 47–73.

Lacasse, C., Werner, R., Paterne, M., Sigurdsson, H., Carey, S., Pinte, G., 1998. Long-range transport of Icelandic tephra to the Irminger Basin Site 919. Proceedings of the Ocean Drilling Program: Scientific Results 152, 51–65

Lacasse, C., 2001. Influence of climate variability on the atmospheric transport of Icelandic tephra in the subpolar North Atlantic. Global and Planetary Change 29, 31–55.

Lacasse, C., van den Bogaard, P., 2002. Enhanced airborne dispersal of silicic tephras during the onset of Northern Hemisphere glaciations, from 6 to 0 Ma records of explosive volcanism and climate change in the subpolar North Atlantic. Geology, 30, 623–626.

Lamy, F., Kilian, R., Arz, H.W., Francois, J.P., Kaiser, J., Prange, M., Steinke, T., 2010. Holocene changes in the position and intensity of the southern westerly wind belt. Nature Geoscience 3, 695.

Lambert, F., Delmonte, B., Petit, J.R., Bigler, M., Kaufmann, P.R., Hutterli, M.A., Stocker, T.F., Ruth, U., Steffensen, J.P., Maggi, V., 2008. Dust-climate couplings over the past 800,000 years from the EPICA Dome C ice core. Nature 452, 616.

Lane, C.S., Blockley, S.P.E., Lotter, A.F., Finsinger, W., Filippi, M.L., Matthews, I.P., 2012. A regional tephrostratigraphic framework for central and southern European climate archives during the Last Glacial to Interglacial transition: comparisons north and south of the Alps. Quaternary Science Reviews 36, 50–58.

Lane, C.S., Chorn, B.T., Johnson, T.C., 2013. Ash from the Toba supereruption in Lake Malawi shows no volcanic winter in East Africa at 75 ka. Proceedings of the National Academy of Sciences 110, 8025–8029.

Lane, C.S., Brauer, A., Blockley, S.P., Dulski, P., 2013. Volcanic ash reveals time-transgressive abrupt climate change during the Younger Dryas. Geology 41, 1251–1254.

Lane, C.S., Cullen, V.L., White, D., Bramham-Law, C.W.F., Smith, V.C., 2014. Cryptotephra as a dating and correlation tool in archaeology. Journal of Archaeological Science 42, 42–50.

Langdon, P.G., Barber, K.E., 2004. Snapshots in time: precise correlations of peat-based proxy climate records in Scotland using mid-Holocene tephras. The Holocene 14, 21–33.

Lathem, T.L., Kumar, P., Nenes, A., Dufek, J., Sokolik, I.N., Trail, M., Russell, A., 2011. Hygroscopic properties of volcanic ash. Geophysical Research Letters, 38.

Lawson, I.T., Swindles, G.T., Plunkett, G., Greenberg, D., 2012. The spatial distribution of Holocene cryptotephras in north-west Europe since 7 ka: implications for understanding ash fall events from Icelandic eruptions. Quaternary Science Reviews 41, 57–66.

Lerbekmo, J.F., 2008. The White river ash: largest Holocene Plinian tephra. Canadian Journal of Earth Sciences 45, 693–700.

Li, F., Ginoux, P., Ramaswamy, V., 2010. Transport of Patagonian dust to Antarctica. Journal of Geophysical Research: Atmospheres 115.

Lister, D.H., Jones, P.D., 2015. Long-term temperature and precipitation records from the Falkland Islands. International Journal of Climatology 35, 1224–1231.

Longman, J., Veres, D., Ersek, V., Salzmann, U., Hubay, K., Bormann, M., Wennrich, V. and Schäbitz, F., 2017. Periodic input of dust over the Eastern Carpathians during the Holocene linked with Saharan desertification and human impact. Climate of the Past 13, 897–917.

Longman, J., Veres, D., Wennrich, V., 2018. Utilisation of XRF core scanning on peat and other highly organic sediments. Quaternary International 514, 85–96.

Lovenduski, N.S., Gruber, N., Doney, S.C., 2008. Toward a mechanistic understanding of the decadal trends in the Southern Ocean carbon sink. Global Biogeochemical Cycles 22.

Lowe, D.J., Hunt, J.B., 2001. A summary of terminology used in tephra-related studies. Les Dossiers de l'Archaéo-Logis 1, 17–22.

Lowe, D.J., Shane, P.A., Alloway, B.V., Newnham, R.M., 2008. Fingerprints and age models for widespread New Zealand tephra marker beds erupted since 30,000 years ago: a framework for NZ-INTIMATE. Quaternary Science Reviews 27, 95–126.

Lowe, D.J., 2011. Tephrochronology and its application: a review. Quaternary Geochronology 6, 107–153.

Lowe, D.J., Pearce, N.J., Jorgensen, M.A., Kuehn, S.C., Tryon, C.A., Hayward, C.L., 2017. Correlating tephras and cryptotephras using glass compositional analyses and numerical and statistical methods: Review and evaluation. Quaternary Science Reviews 175, 1–44.

Mackay, H., Hughes, P.D., Jensen, B.J., Langdon, P.G., Pyne-O'Donnell, S.D., Plunkett, G., Froese, D.G., Coulter, S., Gardner, J.E., 2016. A mid to late Holocene cryptotephra framework from eastern North America. Quaternary Science Reviews 132, 101–113.

MacLeod, N.S., Sherrod, D.R., Chitwood, L.A., Jensen, R.A., 1995. Geologic Map of Newberry Volcano, Deschutes, Klamath, and Lake Counties. US Geological Survey, Oregon. Miscellaneous Investigations Series Map I-2455, scale, 1(62,500).

Mangerud, J., Lie, S.E., Furnes, H., Kristiansen, I.L., Lømo, L., 1984. A Younger Dryas ash bed in western Norway, and its possible correlations with tephra in cores from the Norwegian Sea and the North Atlantic. Quaternary Research 21, 85–104.

Mansilla, C.A., McCulloch, R.D., Morello, F., 2018. The vulnerability of the Nothofagus forest-steppe ecotone to climate change: Palaeoecological evidence from Tierra del Fuego (~53° S). Palaeogeography, Palaeoclimatology, Palaeoecology 508, 59–70.

Marshall, G.J., 2003. Trends in the Southern Annular Mode from observations and reanalyses. Journal of Climate 16, 4134–4143.

Mayr, C., Wille, M., Haberzettl, T., Fey, M., Janssen, S., Lücke, A., Ohlendorf, C., Oliva, G., Schäbitz, F., Schleser, G.H., Zolitschka, B., 2007. Holocene variability of the Southern Hemisphere westerlies in Argentinean Patagonia (52^{o}S). Quaternary Science Reviews 26, 579–584.

Mayr, C., Lücke, A., Wagner, S., Wissel, H., Ohlendorf, C., Haberzettl, T., Oehlerich, M., Schäbitz, F., Wille, M., Zhu, J., Zolitschka, B., 2013. Intensified Southern Hemisphere Westerlies regulated atmospheric CO2 during the last deglaciation. Geology 41, 831–834.

Mazzocchi, M., Hansstein, F., Ragona, M., 2010. The 2010 volcanic ash cloud and its financial impact on the European airline industry. In CESifo Forum, 92–100.

McCulloch, R.D., Fogwill, C.J., Sugden, D.E., Bentley, M.J., Kubik, P.W., 2005. Chronology of the last glaciation in central Strait of Magellan and Bahía Inútil, southernmost South America. Geografiska Annaler: Series A, Physical Geography 87, 289–312.

McLean, D., Albert, P.G., Nakagawa, T., Suzuki, T., Staff, R.A., Yamada, K., Kitaba, I., Haraguchi, T., Kitagawa, J., Smith, V., 2018. Integrating the Holocene tephrostratigraphy for East Asia using a high-resolution cryptotephra study from Lake Suigetsu (SG14 core), central Japan. Quaternary Science Reviews 183, 36–58.

Mele, D., Dellino, P., Sulpizio, R., Braia, G., 2011. A systematic investigation on the aerodynamics of ash particles. Journal of Volcanology and Geothermal Research, 203, 1–11.

Miller, T. P., Smith, R. L., (1987). Late Quaternary caldera-forming eruptions in the eastern Aleutian arc, Alaska. Geology 15, 434–438.

Monteath, A.J., Hughes, P.D.M., Mackay, H., Amesbury, M.J., Mallon, G., Finkenbinder, M.S., 2017. Spatial and temporal delivery of tephra to the Eastern North American seaboard. In AGU Fall Meeting Abstracts. 2017AGUFM.V12C..07M

Monteath, A.J., van Hardenbroek, M., Davies, L.J., Froese, D.G., Langdon, P.G., Xu, X., Edwards, M.E., 2017. Chronology and glass chemistry of tephra and cryptotephra horizons from lake sediments in northern Alaska, USA. Quaternary Research 88, 169–178. doi:10.1017/qua.2017.38

Monteath, A.J., Hughes, P.D.M., Wastegård, S., 2019. Evidence for distal transport of reworked Andean tephra: Extending the cryptotephra framework from the Austral volcanic zone. Quaternary Geochronology 51, 64–71. doi.org/10.1016/j.quageo.2019.01.003

Monteath, A.J., Teuten, A.E., Hughes, P.D.M., Wastegård, S., The effects of the peat acid digestion protocol on geochemically and morphologically diverse tephra deposits. Journal of Quaternary Science 34, 269–274. doi.org/10.1002/jqs.3104

Moore, D.M., 1968. The Vascular Flora of the Falkland Islands. British Antarctic Survey Scientific Reports 60. Natural Environment Research Council, London.

Moreno, P.I., Villa-Martínez, R., Cárdenas, M.L., Sagredo, E.A., 2012. Deglacial changes of the southern margin of the southern westerly winds revealed by terrestrial records from SW Patagonia (52 S). Quaternary Science Reviews 41, 1–21.

Moreno, P.I., Vilanova, I., Villa-Martínez, R., Dunbar, R.B., Mucciarone, D.A., Kaplan, M.R., Garreaud, R.D., Rojas, M., Moy, C.M., De Pol-Holz, R., Lambert, F., 2018. Onset and evolution of southern annular mode-like changes at centennial timescale. Scientific Reports 8, 3458.

Mortensen, A.K., Bigler, M., Grönvold, K., Steffensen, J.P., Johnsen, S.J., 2005. Volcanic ash layers from the Last Glacial Termination in the NGRIP ice core. Journal of Quaternary Science 20, 209–219.

Mullineaux, D.R., (1996). Pre-1980 Tephra-fall Deposits Erupted from Mount St. Helens. U.S. Geological Survey, Washington 99. Professional Paper 1563.

Naranjo, J.A., Stern, C.R., 2004. Holocene tephrochronology of the southernmost part (42 30'-45 S) of the Andean Southern Volcanic Zone. Revista geológica de Chile 31, 224–240.

Narcisi, B., Petit, J.R., Delmonte, B., Basile-Doelsch, I., Maggi, V., 2005. Characteristics and sources of tephra layers in the EPICA-Dome C ice record (East Antarctica): implications for past atmospheric circulation and ice core stratigraphic correlations. Earth and Planetary Science Letters 239, 253–265.

Narcisi, B., Petit, J.R., Delmonte, B., Scarchilli, C., Stenni, B., 2012. A 16,000-yr tephra framework for the Antarctic ice sheet: a contribution from the new Talos Dome core. Quaternary Science Reviews 49, 52–63.

Natland, J.H., 1993. Volcanic ash and pumice at Shatsky Rise: Sources, mechanisms of transport, and bearing on atmospheric circulation. Proceedings of the Ocean Drilling Program, Scientific Results 132, 57–66.

Neff, P.D., Bertler, N.A., 2015. Trajectory modeling of modern dust transport to the Southern Ocean and Antarctica. Journal of Geophysical Research: Atmospheres 120, 9303–9322.

Nelson, D.M., Hu, F.S., 2008. Patterns and drivers of Holocene vegetational change near the prairie–forest ecotone in Minnesota: revisiting McAndrews' transect. New Phytologist 179, 449–459.

Newton, A.J., Dugmore, A.J., Gittings, B.M., 2007. Tephrabase: tephrochronology and the development of a centralised European database. Journal of Quaternary Science 22, 737–743.

Newton, T.L., 2017. Holocene sea-level changes in the Falkland Islands: new insights into accelerated sea-level rise in the 20th Century. PhD thesis, University of Plymouth.

Oehlerich, M., Mayr, C., Gussone, N., Hahn, A., Hölzl, S., Lücke, A., Ohlendorf, C., Rummel, S., Teichert, B.M.A., Zolitschka, B., 2015. Lateglacial and Holocene climatic changes in south-eastern Patagonia inferred from carbonate isotope records of Laguna Potrok Aike (Argentina). Quaternary Science Reviews 114, 189–202.

Oksanen, J., Blanchet, F.G., Kindt, R., Legendre, P., Minchin, P.R., O'hara, R.B., Simpson, G.L., Solymos, P., Stevens, M.H.H., Wagner, H. Oksanen, M.J., 2013. Package 'vegan'. Community ecology package, version 2, 1–295.

Ohlendorf, C., Fey, M., Gebhardt, C., Haberzettl, T., Lücke, A., Mayr, C., Schäbitz, F., Wille, M., Zolitschka, B., 2013. Mechanisms of lake-level change at Laguna Potrok Aike (Argentina)–insights from hydrological balance calculations. Quaternary Science Reviews, 71, 27–45.

Oppedal, L.T., van der Bilt, W.G., Balascio, N.L., Bakke, J., 2018. Patagonian ash on sub-Antarctic South Georgia: expanding the tephrostratigraphy of southern South America into the Atlantic sector of the Southern Ocean. Journal of Quaternary Science. DOI: 10.1002/jqs.3035

Paul, A., 1982. Chemistry of Glasses. Chapman and Hall: London.

Pausata, F.S., Li, C., Wettstein, J., Kageyama, M., Nisancioglu, K.H., 2011. The key role of topography in altering North Atlantic atmospheric circulation during the last glacial period. Past climate variability: model analysis and proxy intercomparison. Climate of the Past 7, 1089–1101.

Payne, R.J., Kilfeather, A.A., van der Meer, J.J. and Blackford, J.J., 2005. Experiments on the taphonomy of tephra in peat. Suoseura 56, 147-156.

Payne, R., Blackford, J., van der Plicht, J., 2008. Using cryptotephras to extend regional tephrochronologies: an example from southeast Alaska and implications for hazard assessment. Quaternary Research 69, 42–55.

Payne, R., Gehrels, M., 2010. The formation of tephra layers in peatlands: an experimental approach. Catena 81, 12–23.

Payne, R.J., Ring-Hrubesh, F., Rush, G., Sloan, T.J., Evans, C.D., Mauquoy, D., 2019. Peatland initiation and carbon accumulation in the Falkland Islands. Quaternary Science Reviews 212, 213–218.

Pearce, N.J., Bendall, C.A., Westgate, J.A., 2008. Comment on “Some numerical considerations in the geochemical analysis of distal microtephra” by AM Pollard, SPE Blockley and CS Lane. Applied Geochemistry 5, 1353–1364.

Pearce, N.J., Westgate, J.A., Preece, S.J., Eastwood, W.J., Perkins, W.T., 2004. Identification of Aniakchak (Alaska) tephra in Greenland ice core challenges the 1645 BC date for Minoan eruption of Santorini. Geochemistry, Geophysics, Geosystems 5.

Pedro, J.B., Van Ommen, T.D., Rasmussen, S.O., Morgan, V.I., Chappellaz, J., Moy, A.D., Masson-Delmotte, V., Delmotte, M., 2011. The last deglaciation: timing the bipolar seesaw. Climate of the Past 7, 671–683.

Pedro, J.B., Bostock, H.C., Bitz, C.M., He, F., Vandergoes, M.J., Steig, E.J., Chase, B.M., Krause, C.E., Rasmussen, S.O., Markle, B.R., Cortese, G., 2016. The spatial extent and dynamics of the Antarctic Cold Reversal. Nature Geoscience 9, 51.

Peltier, W.R., 2004. Global glacial isostasy and the surface of the ice-age Earth: the ICE-5G (VM2) model and GRACE. Earth Planetary Science 32, 111–149.

Persson, C., 1966. Försök till tefrokronologisk datering av några svenska torvmossar. Geologiska Föreningens i Stockholm Förhandlingar 88, 361–394.

Persson C., 1971. Tephrochronological investigation of peat deposits in Scandinavia and on the Faroe Islands. Geological Survey of Sweden C 656.

Pilcher, J.R., Hall, V.A., 1992. Towards a tephrochronology for the Holocene of the north of Ireland. Holocene 2, 255–259.

Pilcher, J.R., Hall, V.A., McCormac, F.G., 1995. Dates of Holocene Icelandic volcanic eruptions from tephra layers in Irish peats. The Holocene 5, 103–110.

Piva, A., Asioli, A., Schneider, R.R., Trincardi, F., Andersen, N., Colmenero-Hidalgo, E., Dennielou, B., Flores, J.A., Vigliotti, L., 2008. Climatic cycles as expressed in sediments of the PROMESS1 borehole PRAD1-2, central Adriatic, for the last 370 ka. Integrated stratigraphy. Geochemistry, Geophysics, Geosystems 9.

Plunkett, G.M., Pilcher, J.R., McCormac, F.G., Hall, V.A., 2004. New dates for first millennium BC tephra isochrones in Ireland. The Holocene, 14, 780–786.

Plunkett, G., Coulter, S.E., Ponomareva, V.V., Blaauw, M., Klimaschewski, A., Hammarlund, D., 2015. Distal tephrochronology in volcanic regions: challenges and insights from Kamchatkan lake sediments. Global and Planetary Change 134, 26–40.

Plunkett, G., Pilcher, J.R., 2018. Defining the potential source region of volcanic ash in northwest Europe during the Mid-to Late Holocene. Earth-Science Reviews 179, 20–37.

Pollard, A.M., Heron, C.P., (1996). Archaeological Chemistry. Royal Society of Chemistry: Cambridge.

Pollard, A.M., Blockley, S.P.E., Ward, K.R., 2003. Chemical alteration of tephra in the depositional environment: theoretical stability modelling. Journal of Quaternary Science 18, 385–394.

Ponce, J.F., Rabassa, J., Coronato, A., Borromei, A.M., 2011. Palaeogeographical evolution of the Atlantic coast of Pampa and Patagonia from the last glacial maximum to the Middle Holocene. Biological Journal of the Linnean Society 103, 363–379.

Ponomareva, V., Portnyagin, M., Pendea, I.F., Zelenin, E., Bourgeois, J., Pinegina, T., Kozhurin, A., 2017. A full Holocene tephrochronology for the Kamchatsky Peninsula region: applications from Kamchatka to North America. Quaternary Science Reviews 168, 101–122.

Poto, L., Gabrieli, J., Crowhurst, S.J., Appleby, P.G., Ferretti, P., Surian, N., Cozzi, G., Zaccone, C., Turetta, C., Pini, R., Kehrwald, N., 2013. The first continuous Late Glacial–Holocene peat bog multi-proxy record from the Dolomites (NE Italian Alps). Quaternary international 306, 71–79.

Pouget, S., Bursik, M., Cortés, J.A., Hayward, C., 2014. Use of principal component analysis for identification of Rockland and Trego Hot Springs tephras in the Hat Creek Graben, northeastern California, USA. Quaternary Research 81, 125–137.

Praetorius, S., Mix, A., Jensen, B., Froese, D., Milne, G., Wolhowe, M., Addison, J., Prahl, F., 2016. Interaction between climate, volcanism, and isostatic rebound in Southeast Alaska during the last deglaciation. Earth and Planetary Science Letters 452, 79–89.

Prata, F., Rose, B., 2015. Volcanic ash hazards to aviation. In The Encyclopedia of Volcanoes, Academic Press, 911–934.

Pratte, S., Garneau, M., De Vleeschouwer, F., 2017. Increased atmospheric dust deposition during the Neoglacial in a boreal peat bog from north-eastern Canada. Palaeogeography, palaeoclimatology, palaeoecology 469, 34–46.

Pratte, S., De Vleeschouwer, F., Garneau, M., 2017. Geochemical characterization (REE, Nd and Pb isotopes) of atmospheric mineral dust deposited in two maritime peat bogs from the St. Lawrence North Shore (eastern Canada). Journal of Quaternary Science 32, 617–627.

Preece, S.J., McGimsey, R.G., Westgate, J.A., Pearce, N.J.G., Hart, W.K., Perkins, W.T., 2014. Chemical complexity and source of the White River Ash, Alaska and Yukon. Geosphere 10, 1020–1042.

Purich, A., Cai, W., England, M.H., Cowan, T., 2016. Evidence for link between modelled trends in Antarctic sea ice and underestimated westerly wind changes. Nature communications 7, 10409.

Pyne-O'Donnell, S.D., 2011. The taphonomy of Last Glacial–Interglacial Transition (LGIT) distal volcanic ash in small Scottish lakes. Boreas 40, 131–145.

Pyne-O'Donnell, S.D., Hughes, P.D., Froese, D.G., Jensen, B.J., Kuehn, S.C., Mallon, G., Amesbury, M.J., Charman, D.J., Daley, T.J., Loader, N.J., Mauquoy, D., 2012. High-precision ultra-distal Holocene tephrochronology in North America. Quaternary Science Reviews 52, 6–11.

Pyne-O'Donnell, S. D., Cwynar, L. C., Jensen, B. J., Vincent, J. H., Kuehn, S. C., Spear, R., Froese, D. G. (2016). West Coast volcanic ashes provide a new continental-scale Lateglacial isochron. Quaternary Science Reviews 142, 16–25.

Rasmussen, S.O., Andersen, K.K., Svensson, A.M., Steffensen, J.P., Vinther, B.M., Clausen, H.B., Siggaard-Andersen, M.L., Johnsen, S.J., Larsen, L.B., Dahl-Jensen, D., Bigler, M., 2006. A new Greenland ice core chronology for the last glacial termination. Journal of Geophysical Research: Atmospheres, 111(D6).

Rawson, H., Naranjo, J.A., Smith, V.C., Fontijn, K., Pyle, D.M., Mather, T.A., Moreno, H., 2015. The frequency and magnitude of post-glacial explosive eruptions at Volcán Mocho-Choshuenco, southern Chile. Journal of Volcanology and Geothermal Research 299, 103–129.

Reimer, P., Bard, E., Bayliss, A., Beck, J., Blackwell, P., Bronk Ramsey, C., Buck, C., Cheng, H., Edwards, R., Friedrich, M. (2013). IntCal13 and Marine13 radiocarbon age calibration curves 0-50,000 years cal BP. Radiocarbon 55, 1869–1887.

Robock, A., Matson, M., 1983. Circumglobal transport of the El Chichón volcanic dust cloud. Science 221, 195–197.

Roland, T.P., Mackay, H., Hughes, P.D.M., 2015. Tephra analysis in ombrotrophic peatlands: a geochemical comparison of acid digestion and density separation techniques. Journal of Quaternary Science 30, 3–8.

Rose, W.I., Durant, A.J., 2009. Fine ash content of explosive eruptions. Journal of Volcanology and Geothermal Research 186, 32–39.

Riehle, J., Meyer, C., Miyaoka, R., 1999. Data on Holocene tephra (volcanic ash) deposits in the Alaska Peninsula and lower Cook Inlet region of the Aleutian volcanic arc, Alaska. United States Geological Survey Open-file Report 99-135, /www.avo.alaska.edu

Rudnick, R.L., Gao, S., 2003. Composition of the continental crust. Treatise on geochemistry 3, 659.

Scaife, R.G., Long, A.J., Monteath, A.J., Hughes, P.D.M., Bentley, M., Stone, P. 2019. The Falkland Islands palaeoecological response to millennial scale climate perturbations during the Pleistocene-

Holocene transition: implications for future vegetation stability in Southern Ocean islands. Journal of Quaternary Science. DOI: 10.1002/jqs.3150.

Schaetzl, R.J., Krist, F.J., Lewis, C.M., Luehmann, M.D., Michalek, M.J., 2016. Spits formed in Glacial Lake Algonquin indicate strong easterly winds over the Laurentian Great Lakes during late Pleistocene. Journal of Paleolimnology 55, 49–65.

Schiff, C.J., Kaufman, D.S., Wallace, K.L., Ketterer, M.E., 2010. An improved proximal tephrochronology for Redoubt Volcano, Alaska. Journal of Volcanology and Geothermal Research 193, 203–214.

Schneider D.J., Rose, W.I., Kelly, L., 1995.Tracking of 1992 eruption clouds from Crater Peak Vent of Mt. Spurr Volcano, Alaska, using AVHRR data. U.S. Geological Survey Bulletin 2139, 27–36.

Schneider, T., Bischoff, T., Haug, G.H., 2014. Migrations and dynamics of the intertropical convergence zone. Nature 513, 45.

Schofield, J.E., Edwards, K.J., Mighall, T.M., Cortizas, A.M., Rodríguez-Racedo, J., Cook, G., 2010. An integrated geochemical and palynological study of human impacts, soil erosion and storminess from southern Greenland since c. AD 1000. Palaeogeography, Palaeoclimatology, Palaeoecology 295, 19–30.

Shane, P., Hoverd, J., 2002. Distal record of multi-sourced tephra in Onepoto Basin, Auckland, New Zealand: implications for volcanic chronology, frequency and hazards. Bulletin of Volcanology 64, 441–454.

Shuman, B., Bartlein, P., Logar, N., Newby, P., Webb III, T., 2002. Parallel climate and vegetation responses to the early Holocene collapse of the Laurentide Ice Sheet. Quaternary Science Reviews 21, 1793–1805.

Sigurdsson, H., 1990. Assessment of the atmospheric impact of volcanic eruptions. In Global Catastrophes in Earth History, Geological Society of America, 247, 99–110.

Smith, D.G.W., Westgate, J.A., 1968. Electron probe technique for characterising pyroclastic deposits. Earth and Planetary Science Letters 5, 313–319.

Smith, R.E., Smith, V.C., Fontijn, K., Gebhardt, A.C., Wastegård, S., Zolitschka, B., Ohlendorf, C., Stern, C., Mayr, C., 2019. Refining the Late Quaternary tephrochronology for southern South America using the Laguna Potrok Aike sedimentary record. Quaternary Science Reviews 218, 137–156.

Spano, N.G., Lane, C.S., Francis, S.W., Johnson, T.C., 2017. Discovery of Mount Mazama cryptotephra in Lake Superior (North America): implications and potential applications. Geology 45, 1071–1074.

Sparks, R.S.J., 1986. The dimensions and dynamics of volcanic eruption columns. Bulletin of Volcanology 48, 3–15.

Stern, C.R., 2008. Holocene tephrochronology record of large explosive eruptions in the southernmost Patagonian Andes. Bulletin of Volcanology 70, 435–454.

Stern, C.R., Moreno, P.I., Villa-Martinez, R., Sagredo, E.A., Prieto, A., Labarca, R., 2011. Evolution of ice-dammed proglacial lakes in Última Esperanza, Chile: implications from the late-glacial R1 eruption of Reclús volcano, Andean Austral Volcanic Zone. Andean Geology 38, 82–97.

Stevenson, J.A., Loughlin, S., Rae, C., Thordarson, T., Milodowski, A.E., Gilbert, J.S., Harangi, S., Lukács, R., Højgaard, B., Árting, U., Pyne-O'Donnell, S., 2012. Distal deposition of tephra from the Eyjafjallajökull 2010 summit eruption. Journal of Geophysical Research: Solid Earth 117.

Stevenson, J.A., Millington, S.C., Beckett, F.M., Swindles, G.T., Thordarson, T., 2015. Big grains go far: reconciling tephrochronology with atmospheric measurements of volcanic ash. Atmospheric Measurement Techniques Discussions 8.

Stone, P., 2010. The geology of the Falkland Islands. Deposits magazine 23, 38–43.

Streeter, R., Dugmore, A., 2014. Late-Holocene land surface change in a coupled social–ecological system, southern Iceland: A cross-scale tephrochronology approach. Quaternary Science Reviews 86, 99–114.

Strother, S.L., Salzmann, U., Roberts, S.J., Hodgson, D.A., Woodward, J., Van Nieuwenhuyze, W., Verleyen, E., Vyverman, W., Moreton, S.G., 2015. Changes in Holocene climate and the intensity of Southern Hemisphere Westerly Winds based on a high-resolution palynological record from sub-Antarctic South Georgia. The Holocene 25, 263–279.

Sugden, D.E., McCulloch, R.D., Bory, A.J.M., Hein, A.S., 2009. Influence of Patagonian glaciers on Antarctic dust deposition during the last glacial period. Nature Geoscience 2, 281.

Sulpizio, R., Zanchetta, G., Caron, B., Dellino, P., Mele, D., Giaccio, B., Insinga, D., Paterne, M., Siani, G., Costa, A., Macedonio, G., 2014. Volcanic ash hazard in the Central Mediterranean assessed from geological data. Bulletin of Volcanology 76, 866.

Sun, C., Plunkett, G., Liu, J., Zhao, H., Sigl, M., McConnell, J.R., Pilcher, J.R., Vinther, B., Steffensen, J.P., Hall, V., 2014. Ash from Changbaishan Millennium eruption recorded in Greenland ice: implications for determining the eruption's timing and impact. Geophysical Research Letters 41, 694–701.

Swindles, G.T., De Vleeschouwer, F., Plunkett, G., 2010. Dating peat profiles using tephra: stratigraphy, geochemistry and chronology. Mires and Peat Volume 7, 1–9.

Swindles, G.T., Lawson, I.T., Savov, I.P., Connor, C.B., Plunkett, G., 2011. A 7000 yr perspective on volcanic ash clouds affecting northern Europe. Geology 39, 887–890.

Swindles, G.T., Galloway, J., Outram, Z., Turner, K., Schofield, J.E., Newton, A.J., Dugmore, A.J., Church, M.J., Watson, E.J., Batt, C., Bond, J., 2013. Re-deposited cryptotephra layers in Holocene peats linked to anthropogenic activity. The Holocene 23, 1493–1501.

Swindles, G.T., Watson, E.J., Savov, I.P., Lawson, I.T., Schmidt, A., Hooper, A., Cooper, C.L., Connor, C.B., Gloor, M., Carrivick, J.L., 2018. Climatic control on Icelandic volcanic activity during the mid-Holocene. Geology 46, 47–50.

Techer, I., Advocat, T., Lancelot, J., Liotard, J.M., 2001. Dissolution kinetics of basaltic glasses: control by solution chemistry and protective effect of the alteration film. Chemical Geology 176, 235–263.

Timms, R.G., Matthews, I.P., Lowe, J.J., Palmer, A.P., Weston, D.J., MacLeod, A. and Blockley, S.P., 2019. Establishing tephrostratigraphic frameworks to aid the study of abrupt climatic and glacial transitions: a case study of the Last Glacial-Interglacial Transition in the British Isles (c. 16-8 ka BP). Earth-Science Reviews.

Thomas, Z.A., Jones, R.T., Fogwill, C.J., Hatton, J., Williams, A.N., Hogg, A., Mooney, S., Jones, P., Lister, D., Mayewski, P., Turney, C.S., 2018. Evidence for increased expression of the Amundsen Sea Low over the South Atlantic during the late Holocene. Climate of the Past 14, 1727–1738.

Thorarinsson, S., 1981. Tephra studies and tephrochronology: a historical review with special reference to Iceland. In Tephra studies. Springer, Dordrecht.

Thorarinsson S., 1944. Tefrokronologiska studier pa° Island. Geografiska Annaler 26, 1–217.

Turney, C.S.M., 1998. Exatraction of rhyolitic component of Vedde microtephra from minerogenic lake sediments. Journal of Paleolimnology 19, 199–206.

Turner, J.N., Holmes, N., Davis, S.R., Leng, M.J., Langdon, C., Scaife, R.G., 2015. A multiproxy (micro-XRF, pollen, chironomid and stable isotope) lake sediment record for the Lateglacial to Holocene transition from Thomastown Bog, Ireland. Journal of Quaternary Science 30, 514–528.

Turney, C., Jones, R., Fogwill, C., Hatton, J., Williams, A.N., Hogg, A., Thomas, Z., Palmer, J., Mooney, S., 2016. A 250 year periodicity in Southern Hemisphere westerly winds over the last 2600 years. Climate of the Past Discussions 11, 2159–2180.

Unkel, I., Björck, S., Wohlfarth, B., 2008. Deglacial environmental changes on Isla de los Estados (54.4°S), southeastern Tierra del Fuego. Quaternary Science Reviews 27, 1541–1554.

Unkel, I., Fernandez, M., Björck, S., Ljung, K., Wohlfarth, B., 2010. Records of environmental changes during the Holocene from Isla de los Estados (54.4 S), southeastern Tierra del Fuego. Global and Planetary Change 74, 99–113.

Ullman, D.J., LeGrande, A.N., Carlson, A.E., Anslow, F.S., Licciardi, J.M., 2014. Assessing the impact of Laurentide Ice-Sheet topography on glacial climate. NASA technical report 20140011827.

Upton, J., Shaw, C.J., 2002. An overview of the oceanography and meteorology of the Falkland Islands. Aquatic conservation: marine and freshwater ecosystems 12, 15–25.

van den Bogaard, P., Schmincke, H.U., 1985. Laacher See Tephra: A widespread isochronous late Quaternary tephra layer in central and northern Europe. Geological Society of America Bulletin 96, 1554–1571.

van den Bogaard, C., Schmincke, H.U., 2002. Linking the North Atlantic to central Europe: a high-resolution Holocene tephrochronological record from northern Germany. Journal of Quaternary Science 17, 3–20.

van der Bilt, W.G., Lane, C.S., Bakke, J., 2017. Ultra-distal Kamchatkan ash on Arctic Svalbard: towards hemispheric cryptotephra correlation. Quaternary Science Reviews 164, 230–235.

Vanneste, H., De Vleeschouwer, F., Martínez-Cortizas, A., Von Scheffer, C., Piotrowska, N., Coronato, A., Le Roux, G., 2015. Late-glacial elevated dust deposition linked to westerly wind shifts in southern South America. Scientific reports 5, 11670.

Visbeck, M., 2009. A station-based southern annular mode index from 1884 to 2005. Journal of Climate 22, 940–950.

Walker, M., Johnsen, S., Rasmussen, S.O., Popp, T., Steffensen, J.P., Gibbard, P., Hoek, W., Lowe, J., Andrews, J., Björck, S. and Cwynar, L.C., 2009. Formal definition and dating of the GSSP (Global Stratotype Section and Point) for the base of the Holocene using the Greenland NGRIP ice core, and selected auxiliary records. Journal of Quaternary Science 24, 3–17.

Wallace, K., Coombs, M.L., Hayden, L.A., Waythomas, C.F., 2014. Significance of a Near-Source Tephra-Stratigraphic Sequence to the Eruptive History of Hayes Volcano, South-Central Alaska. US Geological Survey Scientific Investigations Report 5133.

Wastegård, S., Davies, S.M., 2009. An overview of distal tephrochronology in northern Europe during the last 1000 years. Journal of Quaternary Science 24, 500–512.

Wastegård, S., Veres, D., Kliem, P., Hahn, A., Ohlendorf, C., Zolitschka, B., 2013. Towards a late Quaternary tephrochronological framework for the southernmost part of South America–the Laguna Potrok Aike tephra record. Quaternary Science Reviews 71, 81–90.

Wastegård, S., Gudmundsdóttir, E.R., Lind, E.M., Timms, R.G., Björck, S., Hannon, G.E., Olsen, J., Rundgren, M., 2018. Towards a Holocene tephrochronology for the Faroe Islands, North Atlantic. Quaternary Science Reviews 195, 195–214.

Watson, E.J., Swindles, G.T., Lawson, I.T., Savov, I.P., 2015. Spatial variability of tephra and carbon accumulation in a Holocene peatland. Quaternary Science Reviews 124, 248–264.

Watson, E.J., Swindles, G.T., Stevenson, J.A., Savov, I., Lawson, I.T., 2016. The transport of Icelandic volcanic ash: Insights from northern European cryptotephra records. Journal of Geophysical Research: Solid Earth 121, 7177–7192.

Watson, E.J., Swindles, G.T., Lawson, I.T., Savov, I.P., 2016. Do peatlands or lakes provide the most comprehensive distal tephra records? Quaternary Science Reviews 139, 110–128.

Watson, E.J., Kołaczek, P., Słowiński, M., Swindles, G.T., Marcisz, K., Gałka, M., Lamentowicz, M., 2017a. First discovery of Holocene Alaskan and Icelandic tephra in Polish peatlands. Journal of Quaternary Science 32, 457–462.

Watson, E.J., Swindles, G.T., Savov, I.P., Lawson, I.T., Connor, C.B., Wilson, J.A., 2017b. Estimating the frequency of volcanic ash clouds over northern Europe. Earth and Planetary Science Letters 460, 41–49.

Watt, S.F., Pyle, D.M., Mather, T.A., 2013. The volcanic response to deglaciation: Evidence from glaciated arcs and a reassessment of global eruption records. Earth Science Reviews 122, 77–102.

Westgate, J.A., Pearce, N.J.G., Perkins, W.T., Preece, S.J., Chesner, C.A., Muhammad, R.F., 2013. Tephrochronology of the Toba tuffs: four primary glass populations define the 75 ka Youngest Toba Tuff, northern Sumatra, Indonesia. Journal of Quaternary Science 28, 772–776.

Weller, D.J., Miranda, C.G., Moreno, P.I., Villa-Martínez, R., Stern, C.R., 2015. Tephrochronology of the southernmost Andean southern volcanic zone, Chile. Bulletin of Volcanology 77, 107.

Weller, D.J., de Porras, M.E., Maldonado, A., Méndez, C., Stern, C.R., 2018. New age controls on the tephrochronology of the southernmost Andean Southern Volcanic Zone, Chile. Quaternary Research 91, 250–264.

Westgate, J.A., Gorton, M.P., 1981. Correlation techniques in tephra studies. In Tephra studies, Springer, Dordrecht, 73–94.

Westgate, J.A., WoldeGabriel, G., Halls, H.C., Bray, C.J., Barendregt, R.W., Pearce, N.J., Sarna-Wojcicki, A.M., Gorton, M.P., Kelley, R.E., Schultz-Fellenz, E., 2018. Quaternary tephra from the Valles caldera in the volcanic field of the Jemez Mountains of New Mexico identified in western Canada. Quaternary Research 91, 813–828.

Wexler, H., 1951. Spread of the Krakatoa volcanic dust cloud as related to the high-level circulation. Bulletin of the American Meteorological Society 32, 48–51.

White, J.D.L., Houghton, B.F., 2006. Primary volcaniclastic rocks. Geology 34, 677–680.

White, W.B., Minser, D.G., 1984. Raman spectra and structure of natural glasses. Journal of Non-Crystalline Solids 67, 45–59.

Williams, J.W., Shuman, B., Bartlein, P.J., Diffenbaugh, N.S., Webb III, T., 2010. Rapid, time-transgressive, and variable responses to early Holocene midcontinental drying in North America. Geology 38, 135–138.

Wilson, L., Huang, T.C., 1979. The influence of shape on the atmospheric settling velocity of volcanic ash particles. Earth and Planetary Science Letters 44, 311–324.

Wilson, P., Clark, R., Birnie, J., Moore, D.M., 2002. Late Pleistocene and Holocene landscape evolution and environmental change in the Lake Sulivan area, Falkland Islands, South Atlantic. Quaternary Science Reviews 21, 1821–1840.

Wilson, T.M., Cole, J.W., Stewart, C., Cronin, S.J., Johnston, D.M., 2011. Ash storms: impacts of wind-remobilised volcanic ash on rural communities and agriculture following the 1991 Hudson eruption, southern Patagonia, Chile. Bulletin of Volcanology 73, 223–239.

Wolff-Boenisch, D., Gislason, S.R., Oelkers, E.H., Putnis, C.V., 2004. The dissolution rates of natural glasses as a function of their composition at pH 4 and 10.6, and temperatures from 25 to 74 C. Geochimica et Cosmochimica Acta 68, 4843–4858.

Yalcin, K., Wake, C.P., Germani, M.S., 2003. A 100-year record of North Pacific volcanism in an ice core from Eclipse Icefield, Yukon Territory, Canada. Journal of Geophysical Research: Atmospheres 108(D1).

Yamaguchi, D.K., (1983). New tree-ring dates for recent eruptions of Mount St. Helens. Quaternary Research 20, 554–557.

Yamaguchi, D.K., (1985). Tree-ring evidence for a two-year interval between recent prehistoric explosive eruptions of Mount St. Helens. Geology 13, 554–557.

Yoshimoto, M., Amma-Miyasaka, M., Takahashi, R., Nakagawa, M., Yoshida K., 2008. Re-evaluation of the pre-1640 A.D. eruptive history of Hokkaido-Komagatake volcano, northern Japan. Journal of the Geological Society of Japan 114, 336–347.

Yoshino, M.M., Tabuchi, H., 1975. Wind variation in the lower troposphere over Japan in the late quaternary period estimated by the distribution of volcanic ashes. WMO Long-term Climatic Fluctuations, 31–38.

Zaragosi, S., Bourillet, J.F., Eynaud, F., Toucanne, S., Denhard, B., Van Toer, A., Lanfumey, V., 2006. The impact of the last European deglaciation on the deep-sea turbidite systems of the Celtic-Armorican margin (Bay of Biscay). Geo-Marine Letters, 26, 317–329.

Zarriess, M., Mackensen, A., 2010. The tropical rainbelt and productivity changes off northwest Africa: A 31,000-year high-resolution record. Marine Micropaleontology 76, 76–91.

Zdanowicz, C.M., Zielinski, G.A., Germani, M.S., 1999. Mount Mazama eruption: Calendrical age verified and atmospheric impact assessed. Geology 27, 621–624.

Zielinski, G. A., Mayewski, P. A., Meeker, L. D., Whitlow, S., Twickler, M. S., 1996. A 110,000-yr record of explosive volcanism from the GISP2 (Greenland) ice core. Quaternary Research 45, 109–118.

Zielinski, G.A., Mayewski, P.A., Meeker, L.D., Grönvold, K., Germani, M.S., Whitlow, S., Twickler, M.S., Taylor, K., 1997. Volcanic aerosol records and tephrochronology of the Summit, Greenland, ice cores. Journal of Geophysical Research: Oceans 102, 26625–26640.

Zolitschka, B., Fey, M., Janssen, S., Maidana, N.I., Mayr, C., Wulf, S., Haberzettl, T., Corbella, H., Lücke, A., Ohlendorf, C., Schäbitz, F., 2019. Southern Hemispheric Westerlies control sedimentary processes of Laguna Azul (south-eastern Patagonia, Argentina). The Holocene 29, 403–420.